

**Science Planning for the DESTINY<sup>+</sup> Dust Analyzer**  
—  
**Leveraging the Potential of a Space Exploration Instrument**

A thesis accepted by the  
Faculty of Aerospace Engineering & Geodesy of the University of Stuttgart  
in partial fulfilment of the requirements for the degree of  
Doctor of Engineering Sciences (Dr.-Ing.)

by  
Maximilian Maria Sommer  
born in Viersen, Germany

Main referee:                      Apl. Prof. Dr.-Ing. Ralf Srama  
Co-referee:                        Prof. Dr. Jürgen Schmidt  
  
Date of defence:                  January 11, 2024

Institute of Space Systems  
University of Stuttgart  
2024



# Abstract

The DESTINY<sup>+</sup> Dust Analyzer (DDA) is a highly sophisticated planetary science instrument to provide cutting-edge in-situ characterization of individual cosmic dust grains, with respect to their composition, as well as their physical and dynamical properties. As such, it constitutes a critical component of the upcoming JAXA mission DESTINY<sup>+</sup>, which is scheduled to launch in 2025. After a three-year cruise phase, the spacecraft will perform a flyby of the target asteroid 3200 Phaethon, with the goal of observing the enigmatic Geminids parent body with two camera instruments, and sampling particles released from its surface with the DDA. Until that flyby, DESTINY<sup>+</sup> will execute a highly diverse, ion-engine-driven flight plan that allows DDA to extensively study the dust environments of the Earth, Moon, and interplanetary space—a breadth of science opportunities that is unique to this mission and instrument.

This dissertation provides a comprehensive study of the dust types and phenomena possibly encountered by DDA during its journey to Phaethon and applies the principles and methods of science planning to prepare for the operational phase of the mission. The work synthesizes technical considerations and scientific analyses of relevant cosmic dust populations, aiming to optimize DDA's scientific potential.

Detailed examinations of spacecraft and instrument factors, such as the dynamic spacecraft attitude during the near-Earth phase or the instrument's two-axis pointing mechanism, lay the groundwork for the scientific planning. The thorough analysis of known (and lesser known) dust populations in the inner solar system and of previous relevant measurements by other dust instruments form the core of the study. Finally, the findings are consolidated into a draft science activity plan for the entire mission, as well as exemplary pointing timelines to be executed by the instrument for optimal scientific return. The latter is accomplished with the DOPE tool, which aids in intuitive and efficient planning of DDA observations, having been developed in the scope of this project.

The presented work builds the foundation for the scientific operations of DDA, setting it up for a successful and scientifically impactful mission. The findings of this study also provide a valuable perspective for other ventures of in-situ dust astronomy to the inner solar system and contribute to the field of cosmic dust as a whole.



# Kurzfassung

Der DESTINY<sup>+</sup> Dust Analyzer (DDA) ist ein hochmodernes Raumsondeninstrument, das darauf ausgelegt ist, einzelne kosmischen Staubkörner hinsichtlich ihrer Zusammensetzung sowie ihrer physikalischen und dynamischen Eigenschaften in-situ zu untersuchen. Es stellt eine entscheidende Komponente der bevorstehenden JAXA-Mission DESTINY<sup>+</sup> dar, deren Start für 2025 geplant ist. Nach einer dreijährigen Flugphase wird die Raumsonde den Asteroiden 3200 Phaethon passieren. Dabei wird sie den mysteriösen Ursprungskörper der Geminiden mit zwei Kamera-Instrumenten untersuchen und Staubpartikel, die von seiner Oberfläche freigesetzt werden, mit DDA analysieren. Bis zu diesem Vorbeiflug verfolgt DESTINY<sup>+</sup> einen außerordentlich vielseitigen Flugplan, der durch den Ionenantrieb der Raumsonde bestimmt ist. Dieser Flugplan ermöglicht DDA eine ausgiebige Untersuchung der Staubumgebungen der Erde, des Mondes und des interplanetaren Raums – eine Vielfalt an wissenschaftlichen Möglichkeiten, die dieses Instrument und diese Mission einzigartig machen.

Diese Dissertation beinhaltet eine umfassende Studie zu den Staubtypen und -phänomenen, die DDA auf seiner Reise zu Phaethon antreffen könnte, und nutzt bewährte Prinzipien und Methoden des wissenschaftlichen Raumsondenbetriebs um die operationale Phase der Mission vorzubereiten. Dabei werden technische Abwägungen mit wissenschaftlichen Analysen von relevanten kosmischen Staubpopulationen kombiniert, um das Potenzial des DDA zu optimieren.

Detaillierte Betrachtungen von Faktoren des Raumfahrzeugs und des Instruments, wie etwa die dynamische Ausrichtung der Raumsonde während der erdnahen Phase oder die steuerbare Zweiachs-Montierung des DDA, legen den Grundstein für die wissenschaftliche Planung. Die sorgfältige Analyse von bekannten (und weniger bekannten) Staubpopulationen im inneren Sonnensystem sowie von früheren Messungen anderer Staubinstrumente stellen den zentralen Teil der Studie dar. Anschließend werden die Erkenntnisse in einem Ablaufplan für die Wissenschaftsaktivitäten während der gesamten DESTINY<sup>+</sup> Mission zusammengeführt. Zusätzlich werden exemplarischen Zeitleisten für die Ausrichtung des Instruments vorgestellt, die einen optimalen wissenschaftlichen Ertrag für bestimmte Observierungsziele gewährleisten. Diese können mithilfe des DOPE-Tools erstellt werden, das im Rahmen dieses Projekts entwickelt wurde und eine intuitive und effiziente Planung der DDA-Beobachtungen ermöglicht.

Die vorgestellte Arbeit schafft die Basis für den wissenschaftlichen Betrieb des DDA und stellt somit die Weichen für eine erfolgreiche und aussagekräftige Forschungsmission. Darüber hinaus bieten die Erkenntnisse dieser Studie eine wertvolle Perspektive für weitere Projekte der In-situ-Staubastronomie und leisten einen wichtigen Beitrag zum Gebiet der kosmischen Staubforschung als Ganzes.



# Acknowledgments

First and foremost, I would like to express my deepest gratitude to my supervisor, Prof. Dr. Ralf Srama, whose exceptional guidance and unwavering support have been constants throughout my academic journey, predating the start of this doctoral project. My trajectory within the cosmic dust group at the University of Stuttgart began with my Bachelor's thesis in 2014, where Dr. Srama, as head of the dust group, consistently supported the evolution of my scientific pursuits. He kept involving me as a student assistant and encouraged me to pursue half-year traineeships in dust and meteoroid science at ESA/ESAC in Madrid and at JAXA/ISAS in Tokyo—experiences that proved invaluable to both my professional and personal development. Finally being given the opportunity to undertake a doctorate under Dr. Srama's guidance has been deeply humbling, and engaging in this exciting and stimulating work has proven even more fulfilling than I could have imagined. Thank you, Ralf, for guiding my path to this point. I will cherish your positivity and kindness as enduring leitmotifs throughout my further career.

In that regard, I would also like to extend my gratitude to those closely tied to the roots of my dust journey, especially Rachel Soja, Nico Altobelli, Eberhard Grün, and Hajime Yano. Your warm mentoring and our insightful discussions on captivating topics have sparked the enthusiasm that set me on this fruitful path.

Moreover, I would like to thank the members of the DDA Science Team, whom I've had the pleasure of working with and receiving guidance from during this doctorate, foremost, Harald Krüger, Peter Strub, and Veerle Sterken, as well as Jürgen Schmidt, who has also kindly made himself available to co-referee my dissertation.

I want to extend my appreciation to my colleagues at IRS, especially those in the cosmic dust group and the satellite technology department, for creating a positive and enjoyable working environment that has made my time at the institute truly pleasant.

I also wish to express my sincere thanks to my friends, with a special mention to my incredible circle from my hometown Viersen, particularly Jonas Hurdalek, for his unwavering companionship. And to all my friends from Stuttgart, including my affectionate and inspiring Möhringen house share community. The time we've spent together and the nurturing habitat we've created will forever shape my ideal of a home. Foremost, I thank my kindred spirit housemate Ariane Exle. Even the all-nighters working on our dissertations side by side I remember fondly.

A very special and heartfelt thanks goes to my parents, Monika and Heiner Sommer, and to my brother Henrik, for their endless love and being steadfast pillars of support throughout every stage and facet of my life.

And I thank you, Katha. Your empathic, attentive, loving, and caring presence has been my unquestioned emotional anchor, guiding me through the ups and downs of this journey.

---

Finally, I would like to thank the German and Japanese taxpayers, whose invaluable contributions make this fundamental research possible. Your support helps uncover the mysteries of our cosmic origins, driving us towards a deeper understanding of our place in the universe.

*“The cosmos is within us. We are made of star-stuff. We are a way for the universe to know itself.”* – Carl Sagan

# Contents

<b>Abstract</b>	<b>i</b>
<b>Kurzfassung</b>	<b>iii</b>
<b>Acknowledgments</b>	<b>v</b>
<b>List of Figures</b>	<b>xi</b>
<b>List of Tables</b>	<b>xv</b>
<b>Nomenclature</b>	<b>xvii</b>
<b>1. Introduction</b>	<b>1</b>
1.1. What is cosmic dust? . . . . .	1
1.2. In-situ dust astronomy . . . . .	2
1.3. The DESTINY <sup>+</sup> mission . . . . .	6
1.3.1. Overview . . . . .	6
1.3.2. A new-generation dust telescope . . . . .	8
1.3.3. Phaethon . . . . .	10
1.3.4. Mission origins . . . . .	12
1.4. Science planning approach . . . . .	12
<b>2. Cosmic Dust in the Solar System</b>	<b>15</b>
2.1. Types . . . . .	15
2.1.1. Circumplanetary dust . . . . .	15
2.1.2. Interplanetary dust . . . . .	16
2.1.3. Interstellar dust . . . . .	18
2.2. Dynamics . . . . .	21
2.3. Relevance for spaceflight . . . . .	26
<b>3. Mission Aspects</b>	<b>29</b>
3.1. Mission phases and trajectory . . . . .	29
3.2. Spacecraft attitude . . . . .	35
3.3. Spacecraft communication . . . . .	36
3.4. Radiation environment . . . . .	37
<b>4. Instrument Aspects</b>	<b>39</b>
4.1. Instrument mounting . . . . .	39
4.2. Sensor geometry . . . . .	40

---

4.3. Sun and bright body avoidance . . . . .	44
4.4. Cover deployment . . . . .	45
4.5. Decontamination . . . . .	45
<b>5. Dust Observability Analysis</b>	<b>47</b>
5.1. Near-Earth dust . . . . .	47
5.1.1. Micro-debris . . . . .	47
5.1.2. Magnetospheric swarms . . . . .	54
5.2. Lunar dust . . . . .	59
5.2.1. Diffuse ejecta exosphere . . . . .	59
5.2.2. Roaming ejecta clouds . . . . .	65
5.2.3. The lunar dust torus . . . . .	68
5.3. Interplanetary dust . . . . .	70
5.3.1. The Grün-flux . . . . .	70
5.3.2. Beta-meteoroids . . . . .	73
5.3.3. Alpha-meteoroids . . . . .	76
5.3.4. The sporadic meteoroid complex . . . . .	86
5.3.5. Cometary streams . . . . .	95
5.3.6. Resonant dust . . . . .	101
5.4. Interstellar dust . . . . .	103
5.4.1. Model predictions . . . . .	105
5.4.2. Conflict with thrusting periods . . . . .	106
5.4.3. Distinguishing interstellar dust . . . . .	107
<b>6. Science and Operations Planning</b>	<b>109</b>
6.1. The Science Themes concept . . . . .	109
6.2. Planning cycles . . . . .	110
6.2.1. Long-term planning . . . . .	112
6.2.2. Medium-term planning . . . . .	113
6.2.3. Short-term planning . . . . .	113
6.3. Science Activity Plan (SAP) - proposal . . . . .	113
6.4. Observation planning tool: DOPE . . . . .	119
6.5. Observation pointing timelines - examples . . . . .	122
6.5.1. Observation of interstellar dust . . . . .	122
6.5.2. Observation of alpha-meteoroids . . . . .	123
6.5.3. Observation of lunar ejecta groups . . . . .	123
6.6. Total dust fluences and significance . . . . .	125
<b>7. Conclusion</b>	<b>127</b>
7.1. Summary . . . . .	127
7.2. Outlook . . . . .	128
7.3. Reflection and final thoughts . . . . .	129
<b>Bibliography</b>	<b>131</b>

---

---

<b>Appendices</b>	<b>151</b>
<b>A. Coordinate Systems</b>	<b>153</b>
<b>B. Correction of Lunar Ejecta Cloud Model</b>	<b>161</b>
<b>C. Absence of <math>\alpha</math>-meteoroid in Dust Models</b>	<b>163</b>
<b>D. Supplementary IMEM Sky Maps</b>	<b>167</b>
<b>E. Supplementary IMEM2 Sky Maps</b>	<b>179</b>
<b>F. DOPE Instructions: Setting Spacecraft Trajectory and Attitude</b>	<b>183</b>



# List of Figures

1.1. Cosmic dust at different scales . . . . .	2
1.2. Cassini Cosmic Dust Analyzer . . . . .	5
1.3. History of impact-ionisation-type dust detectors . . . . .	5
1.4. Trajectories of DESTINY <sup>+</sup> and Phaethon . . . . .	7
1.5. The deployed DESTINY <sup>+</sup> spacecraft and DDA . . . . .	8
1.6. Cut view (generated by Gläser, priv. comm.) and schematic view of DDA. . . . .	9
1.7. Radar images of Phaethon . . . . .	11
2.1. Circumplanetary dust at Saturn . . . . .	15
2.2. Zodiacal Light . . . . .	16
2.3. Zodiacal disc artist's impression . . . . .	17
2.4. Radiant map of sporadic meteor sources . . . . .	18
2.5. Local Interstellar Medium . . . . .	19
2.6. Flow patterns of ISD shaped by solar gravity and solar radiation pressure . . . . .	20
2.7. Flow patterns of ISD shaped by electromagnetic forces . . . . .	20
2.8. Ratio of radiation pressure to gravity as a function of particle mass . . . . .	22
2.9. Evolution of the semi-major axis and eccentricity of particles trapped in MMRs . . . . .	25
2.10. The Anthe Ring Arc . . . . .	26
3.1. Spiralling phase trajectory . . . . .	30
3.2. Spiralling phase evolution of apsides altitude and orbital period . . . . .	30
3.3. Lunar gravity assist phase trajectory . . . . .	31
3.4. Interplanetary trajectory of DESTINY <sup>+</sup> in the Earth-co-rotating frame . . . . .	32
3.5. Interplanetary trajectory of DESTINY <sup>+</sup> with thrusting phases . . . . .	33
3.6. Heliocentric distance of DESTINY <sup>+</sup> during the interplanetary cruise phase . . . . .	33
3.7. Phaethon flyby geometry . . . . .	34
3.8. Extended mission phase heliocentric distance . . . . .	34
3.9. Spacecraft attitude configuration during thrusting . . . . .	35
3.10. Spacecraft theoretical roll rates during spiral phase . . . . .	36
4.1. The two-axis pointing mechanism of DDA . . . . .	39
4.2. Coverage range of the DDA pointing mechanism . . . . .	40
4.3. DDA angle-dependent sensitive area. . . . .	41
4.4. DDA angular impact probability. . . . .	44
5.1. Density distribution of debris dust populations over altitude and object size . . . . .	48
5.2. Spatial density distribution of debris dust as modelled with MASTER . . . . .	49

---

5.3.	Directional debris flux distribution along DESTINY <sup>+</sup> orbit . . . . .	50
5.4.	Flux and velocity comparison of SRM dust and meteoroid-background dust . . . . .	51
5.5.	Variation of micro-debris density with altitude and time . . . . .	52
5.6.	The orbit of HEOS-2 through the magnetosphere. . . . .	55
5.7.	The LDEX lunar dust cloud density model . . . . .	60
5.8.	DESTINY <sup>+</sup> trajectory during lunar flybys. . . . .	62
5.9.	Dust incidence predictions for the lunar flybys of DESTINY <sup>+</sup> . . . . .	63
5.10.	Geometrical information and dust incidence predictions for the lunar flybys . . . . .	64
5.11.	Lunar gravity assist phase trajectory (Moon-centric) . . . . .	66
5.12.	Direction of the Moon during the lunar gravity assist phase . . . . .	67
5.13.	The Grün-flux . . . . .	70
5.14.	The Grün-flux converted to DDA . . . . .	72
5.15.	Orbits and detection scheme of $\alpha$ - & $\beta$ -meteoroids . . . . .	73
5.16.	$\beta$ -meteoroids detectable by DDA . . . . .	75
5.17.	$\beta$ -meteoroids detectable by DDA with parent meteoroid eccentricity constraint . . . . .	76
5.18.	Evolution of eccentricity and perihelion of particles released from JFCs . . . . .	80
5.19.	Evolution of eccentricity and perihelion of particles released from asteroids and from a PR-evolved micrometeoroid . . . . .	81
5.20.	Dikarev model sky maps of the IPD flux at 1 au . . . . .	88
5.21.	DDA incidence rates at certain pointings generated from the Dikarev model . . . . .	91
5.22.	Dikarev model seasonal sky maps of the directional flux of IPD dust along the DES- TINY <sup>+</sup> trajectory . . . . .	92
5.23.	Dikarev model seasonal sky maps of the DDA incidence rate of IPD dust along the DESTINY <sup>+</sup> trajectory . . . . .	93
5.24.	Dikarev model seasonal sky maps of the average velocity of IPD dust along the DES- TINY <sup>+</sup> trajectory . . . . .	94
5.25.	Ratio of meteoroid shower flux to the sporadic flux at different particle sizes . . . . .	96
5.26.	Node predictions of the 1999 Leonids storm, modelled with IMEX-streams . . . . .	97
5.27.	Detection scenario of Kohoutek extended tail particiles by HEOS-2 . . . . .	100
5.28.	The structure of Earth's resonant ring overlaid with the DESTINY <sup>+</sup> trajectory . . . . .	101
5.29.	Radial profiles of the density of Earth's resonant ring at different particle sizes . . . . .	102
5.30.	Simulated infrared images of Earth's resonant ring as seen by a distant observer . . . . .	103
5.31.	ISD flow at Earth schematic . . . . .	104
5.32.	Ram-Sun angle of the idealized ISD flow . . . . .	104
5.33.	Spacecraft attitude during interplanetary thrusting periods . . . . .	106
6.1.	Science Themes concept . . . . .	110
6.2.	DDA operations planning scheme . . . . .	112
6.3.	Science Activity Plan proposal (2025) . . . . .	115
6.4.	Science Activity Plan proposal (2026) . . . . .	116
6.5.	Science Activity Plan proposal (2027) . . . . .	117
6.6.	Science Activity Plan proposal (2028) . . . . .	118
6.7.	DOPE geometry visualization . . . . .	120

---

6.8. Screenshot of the DOPE application . . . . .	121
6.9. Pointing timeline example for ISD C26 . . . . .	122
6.10. Pointing timeline for the observation of $\alpha$ -meteoroids . . . . .	123
6.11. Pointing timeline for lunar ejecta groups observation . . . . .	124
A.1. Ecliptic CS . . . . .	154
A.2. The DESTINY+ spacecraft, deployed and launch configuration . . . . .	155
A.3. DDA Instrument coordinate systems . . . . .	157
A.4. Destiny-centric Orbit Normal CS . . . . .	158
A.5. Destiny-centric Orbit Normal CS . . . . .	159
A.6. Geocentric Solar Ecliptic CS . . . . .	160
C.1. Flux sky maps showing the absence of $\alpha$ -meteoroids in the Divine, Staubach, and Dikarev models. . . . .	165
D.1. Dikarev model sky maps of the JFC flux at 1 au . . . . .	168
D.2. Dikarev model sky maps of the AST flux at 1 au . . . . .	169
D.3. Divine model sky maps of the IPD flux at 1 au . . . . .	170
D.4. Staubach model sky maps of the IPD flux at 1 au . . . . .	171
D.5. DDA incidence rates at certain pointings generated from the Dikarev, Staubach, and Divine models . . . . .	172
D.6. Dikarev model seasonal sky maps of the directional flux of JFC dust along the DES- TINY+ trajectory . . . . .	173
D.7. Dikarev model seasonal sky maps of the DDA incidence rate of JFC dust along the DESTINY+ trajectory . . . . .	174
D.8. Dikarev model seasonal sky maps of the average velocity of JFC dust along the DES- TINY+ trajectory . . . . .	175
D.9. Dikarev model seasonal sky maps of the directional flux of AST dust along the DES- TINY+ trajectory . . . . .	176
D.10. Dikarev model seasonal sky maps of the DDA incidence rate of JFC dust along the DESTINY+ trajectory . . . . .	177
D.11. Dikarev model seasonal sky maps of the average velocity of AST dust along the DESTINY+ trajectory . . . . .	178
E.1. IMEM2 sky maps of the total flux at 1 au(all populations) . . . . .	179
E.2. IMEM2 sky maps of the JFC flux at 1 au . . . . .	180
E.3. IMEM2 sky maps of the AST flux at 1 au . . . . .	181
E.4. IMEM2 sky maps of the HTC flux at 1 au . . . . .	182
F.1. DOPE trajectory selection panel . . . . .	183
F.2. DOPE attitude selection panel (rules-based) . . . . .	184
F.3. DOPE attitude selection panel (kernel-based) . . . . .	185



# List of Tables

4.1. Geometry comparison of impact plasma detectors . . . . .	43
5.1. Comparison of sensor geometries, DDA with HEOS-2 & GORID. . . . .	57
6.1. DDA science themes . . . . .	111
A.1. Exemplary pointings (angles) and their corresponding boresight vectors. . . . .	156



# Nomenclature

## Abbreviations

API	application program interface
AST	asteroid / asteroidal
CAT	Chemical Analyzer Target
CDA	Cosmic Dust Analyzer
CIT	Chiba Institute of Technology
CS	coordinate system
DDA	DESTINY <sup>+</sup> Dust Analyzer
DESTINY <sup>+</sup>	Demonstration and Experiment of Space Technology for INterplanetary voYage with Phaethon fLyby and dUst Science
DESTINY	Demonstration and Experiment of Space Technology for INterplanetary voYage
DLR	German Aerospace Center
DON	DESTINY <sup>+</sup> -centric orbit normal
DOPE	DDA Observation Planning Environment
EGA	Earth gravity assist
EMS	Earth-Moon system
ESA	European Space Agency
FOV	field of view
GEO	geosynchronous orbit
GORID	Geostationary Orbit Impact Detector
GTO	geosynchronous transfer orbit
HEOS-2	Highly Eccentric Orbit Satellite 2
HTC	Halley-type comet
IDE	Interplanetary Dust Experiment
IDEX	Interstellar Dust Experiment

---

IDP	interplanetary dust particle
IID	Impact Ionization Detector
IMAP	Interstellar Mapping and Acceleration Probe
IMEM	Interplanetary Meteoroid Environment Model
IMEX	Interplanetary Meteoroid Environment for eXploration
IMF	interplanetary magnetic field
IPD	interplanetary dust
iPTR	instrument pointing timeline request
IRS	Institute of Space Systems, University of Stuttgart
ISAS	Institute of Space and Astronautical Science
ISD	interstellar dust
ISM	interstellar medium
JAXA	Japan Aerospace Exploration Agency
JFC	Jupiter-family comet
LADEE	Lunar Atmosphere and Dust Environment Explorer
LDEF	Long Duration Exposure Facility
LDEX	Lunar Dust Experiment
LEO	low Earth orbit
LFB	lunar flyby
LTP	long-term planning
LUMIO	LUnar Meteoroid Impacts Observer
MASTER	Meteoroid And Space debris Terrestrial Environment Reference
MCAP	Multiband CAmera for Phaethon
MDC	Munich Dust Counter / Mars Dust Counter
MGA	medium-gain antenna
MMR	mean-motion resonance
MMX	Martian Moons eXploration
MOID	minimum orbit intersection distance
MTP	medium-term planning
NAIF	Navigation and Ancillary Information Facility
NASA	National Aeronautics and Space Administration
NSF	National Science Foundation
PME	pointing mechanism (of DDA)
PR	Poynting-Robertson

---

PRISM	Payloads and Research Investigations on the Surface of the Moon
PROCYON	Proximate Object Close flyby with Optical Navigation
PVDF	polyvinylidene fluoride
S/C	spacecraft
SAP	Science Activity Plan
SMC	sporadic meteoroid complex
SPICE	Spacecraft, Planet, Instrument, Camera-matrix, Events (Observation geometry toolbox developed by the Navigation and Ancillary Information Facility (NAIF))
SRM	solid rocket motor
SSE	selenocentric solar ecliptic
STP	short-term planning
SUDA	Surface Ice Dust Analyzer
TCAP	Telescopic CAmera for Phaethon
TOF	time-of-flight
TS	trajectory sensor
UV	ultraviolet light

---

## Symbols

$a$	semi-major axis
$A$	effective sensitive area of a detector
$A_0$	nominal sensitive area of a detector
$\beta$	ratio of radiation force to gravitational force
$C$	inegral of $da/de$ of a PR-pertrubed orbit (Wyatt and Whipple, 1950)
$e$	orbital eccentricity
$\eta$	angular detection efficiency
$F$	cumulative number flux
$f$	true anomaly
$G$	geometric factor of a detector
$I$	incidence rate onto a detector, calculated as $\frac{N}{T}$
$i$	orbital inclination
$\frac{m}{\Delta m}$	mass resolution (of spectrometer)
$m$	particle mass
$\mu$	standard gravitational parameter (of the Sun)
$N$	total number of detected impact events
$n$	number of particles per unit volume
$\Omega$	solid angle
$\Omega_{\text{tot}}$	total solid angle of a detector
$\Omega_{\text{eff}}$	effective solid angle of a detector
$p$	angular impact probability density function (PDF)
$P$	angular impact cumulative distribution function (CDF)
$\varphi$	azimuthal incidence angle
$q$	perihelion distance
$\rho$	bulk density of a particle
$R_{\oplus}$	Earth radius (6371 km)
$R_{\odot}$	Sun radius (695,700 km)
$R_{\text{Hill}}$	Hill radius
$s$	particle radius
$\mathcal{T}$	total observation time
$\theta$	incidence angle (from detector normal)
$\theta_{\text{max}}$	acceptance angle (from detector normal)
$T$	orbital period
$\theta_{f=\text{max}}$	mode of the angular impact probability
$\theta_{\text{mean}}$	mean of the angular impact probability
$\theta_{\text{median}}$	median of the angular impact probability
$v_{\text{impact}}$	impact velocity

# 1. Introduction

## 1.1. What is cosmic dust?

The vacuum of space is commonly considered to be devoid of matter and, without a doubt, there is substantially less material in it than in the air surrounding us. Had it just 1% the air density of the atmosphere at sea level, space would be opaque enough to block all light coming from the Moon, planets, or even the Sun, not to mention that of distant stars and galaxies.<sup>1</sup> The fact that we can see all those things, tells us that space is indeed very, very empty. Upon thorough investigation, we find that the vacuum of space is, nonetheless, all but a *perfect* vacuum—that is, a complete absence of matter. In fact, the mass density present in the vacuum of space relative to that of the air we breathe is in the order of  $10^{-20}$ . This elusive matter is mostly in the form of single atoms, molecules, and ions, as well as nano- to micrometre-sized aggregates of molecules and/or condensed matter (such as crystalline and amorphous solids), which are referred to as cosmic dust particles. In interplanetary space near the Earth, dust accounts for around half of the mass of the so-called interplanetary medium (Mann et al., 2010). Although this would amount to a number density of merely 10 particles per cubic kilometre with characteristic particle size of 10  $\mu\text{m}$ , it is enough for the Earth to sweep up some 40,000 tons of dust over the course of a year (Love and Brownlee, 1993).

Dust is ubiquitous in the universe. Looking beyond our cosmic neighbourhood, we can observe it in all directions and at all scales: Cometary tails and planetary rings are vibrant representatives of dusty phenomena within our solar system; Protoplanetary discs around newborn stars as well as supernova remnants ejected by aged, collapsing stars are enriched with dust grains; In interstellar space, captivating displays are created by light-years-across dust clouds, manifesting either as shining-bright reflection nebulae or gloomy-dark absorption nebulae. Among the latter is the *Great Rift*, a visible black swath in the southern night sky that obscures the luminous centre of the Milky Way—having inspired the mythology of ancient cultures. Even in active galactic nuclei at the edge of the observable universe or in the vast voids between galaxies, dust is found to be present (e.g., Venemans et al., 2017; Ménard et al., 2010).

As manifold as the locations in which cosmic dust is found in the universe, are the ways it is created. Most dust in our solar system is released from comets as they dissolve in the heat of the Sun and from violent collisions among main-belt asteroids and Kuiper belt objects. On the other hand, these solid building blocks of the solar system themselves stem from the dust in the primordial solar nebula, a collapsing cloud of interstellar medium, enriched with *stardust*. This pristine matter is produced by condensation of heavier elements in cooling stellar ejecta, either the winds of red giants in their latest stage as they shed their hulls into space, or, in the expanding remnants of supernovae—the inconceivably violent deaths of massive stars. Once created, stardust roams the

---

<sup>1</sup>An illustration of this statement can be obtained by a ‘back-of-the-envelope’ calculation using the Beer-Lambert law, which relates the absorption of light to the properties of the medium it travels through.



**Figure 1.1.:** Cosmic dust at different scales: (Left) The dust tail of Comet McNaught over the Pacific Ocean. Image credit: Deiries/ESO (2007). (Right) The Black Eye Galaxy (M64), a spiral galaxy with a prominent, dark band of light-absorbing dust lanes obscuring its luminous centre—similar to way the *Great Rift* blocks our view of the Milky Way centre. Image credit: Schmidt (2020).

galaxy while undergoing heavy processing, such as shattering by supernova shockwaves churning the interstellar medium, just to be rebuilt by accretion of gas-phase heavy elements onto the nanometre-sized fragments (Jones, 1997). The details of the formation and the so-called ‘growth’ of stardust particles are far from understood and, due to their importance in galaxy evolution, continue to be subject of scientific debate (e.g., Osman et al., 2020; Triani et al., 2020). Even the winds of quasars, the most luminous objects known in the universe, have been suggested as production sites of carbon-rich dust, similar to soot (Elvis et al., 2002). This might help explain the abundance of dust in some of the earliest of these hyper-energetic galaxy cores, observed at a time when the universe was essentially devoid of star-bred heavy elements (Bertoldi et al., 2003; Mattsson, 2011; Hirashita et al., 2014).

It is clear that cosmic dust science is all but self-contained. From planetary science to cosmology, building a deep understanding of cosmic dust has far-reaching utility. With our rapidly advancing observational capabilities, dust is assuming ever-bigger roles, for example in the detection of exoplanets around the stars in our neighbourhood (e.g., Isella et al., 2018; Sommer et al., 2022), or in the development of novel standard candles for the determination of distances at high redshifts (Hönig et al., 2017). Even in the unravelling of the origins of life, dust, potentially a key supplier of prebiotic compounds to the Earth (Ehrenfreund et al., 2002), weaves its way.

Intuitively, we are quick to disregard a subject with a title as bland as *dust*, yet the relevance of the scientific field of cosmic dust to our understanding of the cosmos as a whole can hardly be overstated.

## 1.2. In-situ dust astronomy

Cosmic dust particles—much like photons—are messengers, which carry information about their sources, as well as the conditions they evolved in through time and space. This valuable information, contained in their occurrence, their dynamics, their internal structure, as well as their chemical

---

make-up, can effectively be retrieved by space-based in-situ dust detectors. The field concerned with the study of these cosmic dust particles is, in accordance with their analogy to photons, often referred to as *dust astronomy* (e.g., Grün et al., 2019). To distinguish the in-situ analysis of individual dust particles from the observation of formations of dust at a distance via remote sensing techniques (such as infrared astronomy), it will herein be referred to as *in-situ dust astronomy*.

In-situ dust astronomy has been a long-standing and actively developing field, having its roots in the very beginning of the space age. Back then, the largely unknown space environment and the hazards it posed to space flight were the main driver for research of this kind. The abundance of hypervelocity meteoroids (as recognized in the appearance of shooting stars and radar meteors) represented a poorly understood threat, that led to the thorough examination of returned spacecraft surfaces (especially windows) as early as in the Mercury and Gemini programmes (reviewed by Brownlee, 1978). In addition, a variety of sensor concepts were conceived and flown onboard satellites to allow for a more direct way of gauging the micro-particle environment (reviewed by Alexander et al., 1963; Jennison, 1969; McDonnell, 1978), among which were detection methods such as:

- Detection of impact flashes via photomultiplier (Berg and Meredith, 1956)
- Detection of impacts on wire-wrapped surfaces via sensing of impact-induced rupture of the electricity-conducting wires (Manring, 1959)
- Acoustic detection of impacts via piezoelectric crystals connected to a sounding board, e.g., spacecraft surfaces (Dubin, 1960)
- Detection of impacts on thin-film, planar capacitors via sensing of momentary shorts induced by the dielectric-penetrating impactors (Naumann, 1965)
- Detection of foil penetrations via sensing of sunlight behind punctured opaque foils (Jennison et al., 1967)
- Detection of hull penetrations of thin-walled pressurized canisters ('beer cans') via sensing of pressure loss (D'Aiutolo et al., 1967)
- Non-destructive detection of charged grains via sensing of the induced charge they generate when passing near a conductor (Jennison and McDonnell, 1964)
- Detection of impact-generated plasma clouds via sensing of the generated charge, either upon penetration of a conductive film (Berg and Richardson, 1969) or upon impact of a conductive plate target (Auer and Sitte, 1968; Dietzel et al., 1973)

Early on, the focus of these experiments was to determine the quantity or, more specifically, the size-dependent flux of these micrometeoroids in near-Earth space. The data of the different detector types, however, led to inconsistent flux estimates, sometimes disagreeing by up to several orders of magnitude even when placed on the same satellite (e.g., Soberman and della Lucca, 1963). This indicated a tendency to false detections inherent in certain detector types (e.g., the acoustic detectors which turned out to be sensitive to thermal-stress-induced crackling of the spacecraft structure), whereas others, such as the 'beer can' pressure loss sensors, proved to be more reliable (McDonnell, 1978).

As the gained understanding of the meteoroid environment indicated a rather low immanent risk to space flight, the focus shifted to the scientific exploration of the more abundant, smaller dust grains, favouring the use of more sensitive instruments. A high degree of reliability as well as sensitivity could finally be achieved with the impact plasma sensors, which were capable of detecting

---

impacts or penetrations of sub-micron grains. First flown onboard the OGO satellite series and the Pioneer 8/9 probes, the impact (or penetration) plasma sensors allowed for the design of two-stage detector that could directly determine particle speeds via a time-of-flight measurement (Nilsson et al., 1965; Berg and Richardson, 1969). The OGO dust instruments, however, were hampered by their small sensitive area and could not achieve significant scientific output (a result of overestimates of the dust flux stemming from earlier, less reliable sensors, see Nilsson et al., 1969). The Pioneer 8/9 detectors, on the other hand, which featured segmented penetration plasma sensors that could accurately determine particle trajectories, generated highly valuable results during their many-years operation time, yielding the first rigorous characterization of the abundance and dynamics of cosmic dust in near-Earth interplanetary space. Among their most well-regarded findings were the discovery of sub-micron grains on hyperbolic trajectories appearing to emanate from the Sun (called ‘ $\beta$ -meteoroids’, Zook and Berg, 1975). Subsequently, the impact plasma detector continued to be used as the go-to method in a number of different dust instruments, all the while being further matured. Recognizing that the impact plasma could be readily fed into a time-of-flight (TOF) mass spectrometer, Dietzel et al. (1973) devised a detector that performed a mass analysis of the plasma’s ions, thereby allowing investigation of the grain composition. With a successful debut on the DLR-led heliosphere science mission Helios (Dalmann et al., 1977; Grün et al., 1980), the impact plasma mass spectrometer concept expanded the scope of in-situ dust detectors greatly and continued to advance to become implemented in the most sophisticated dust instruments to date: By combining (1) the non-destructive sensing of the particle charge via a set of wire or grid electrodes located at the instrument entry (Jennison and McDonnell, 1964; Auer, 1975) with (2) an impact plasma mass analyser stage, the simultaneous measurement of physical, dynamical, as well as chemical properties of individual dust particles becomes possible. This type of instrument, which has been nicknamed ‘dust telescope’ due to the role it plays for in-situ dust astronomy (Grün et al., 2005; Srama et al., 2004a), was flown onboard the renowned Cassini mission (namely, the Cosmic Dust Analyzer (CDA), see Figure 1.2), investigating the intricate nature of the Saturnian dust complex for over 13 years (Srama et al., 2011). Today, six years after the end of the Cassini mission, the data retrieved by CDA continue to produce high-impact scientific results, for instance, on the age of Saturn’s rings (Kempf et al., 2023) or the habitability of Enceladus’s subsurface ocean (Postberg et al., 2023). New iterations of this highly successful type of instrument are about to set sail onboard deep space missions, such as the Surface Ice Dust Analyzer (SUDA) of the Europa Clipper mission (Kempf, 2018), or the DESTINY<sup>+</sup> Dust Analyzer (DDA), which is the subject of this thesis.

Another viable detector design used extensively in today’s in-situ dust research employs a polarized polymer film that generates a charge pulse upon particle impact (Simpson and Tuzzolino, 1985). For polymer material these foil-type detectors use (polarized) polyvinylidene fluoride (PVDF), hence, they are referred to as PVDF sensors. While they provide minimal constraints on particle dynamics and physique, and no information on chemical make-up (although a two-stage segmented-foil design was demonstrated to be able to retrieve flight vectors of grains larger than 10  $\mu\text{m}$ , see Tuzzolino et al., 2005), PVDF sensors allow for reliable, simple, and light-weight detector systems that can cover large areas on the spacecraft surface (as, e.g., the 0.54  $\text{m}^2$  sensor carried by the solar sail mission IKAROS, see Hirai et al., 2014) and can even be integrated into a spacecraft’s thermal insulation (Funase et al., 2020). This makes PVDF sensors especially suited for small-size missions

and/or when the to-be-encountered dust quantity is the scientific focus. Notable examples include: the PVDF sensor onboard the Stardust mission to record the distribution of dust within the coma of comet Wild 2 (Tuzzolino et al., 2003); the High Rate Detector of Cassini/CDA (Spahn et al., 2006); and the Student Dust Counter onboard New Horizons to study the abundance of dust near Pluto and within the Kuiper belt (Horányi et al., 2008).

In addition, retrievable dust collectors have proven to be a vital tool in in-situ dust astronomy. Aerogel, an ultra-light porous material, can decelerate and ‘catch’ cosmic dust grains moving at relative speeds of several  $\text{km s}^{-1}$ , keeping them largely intact (see review by Burchell et al., 2006).

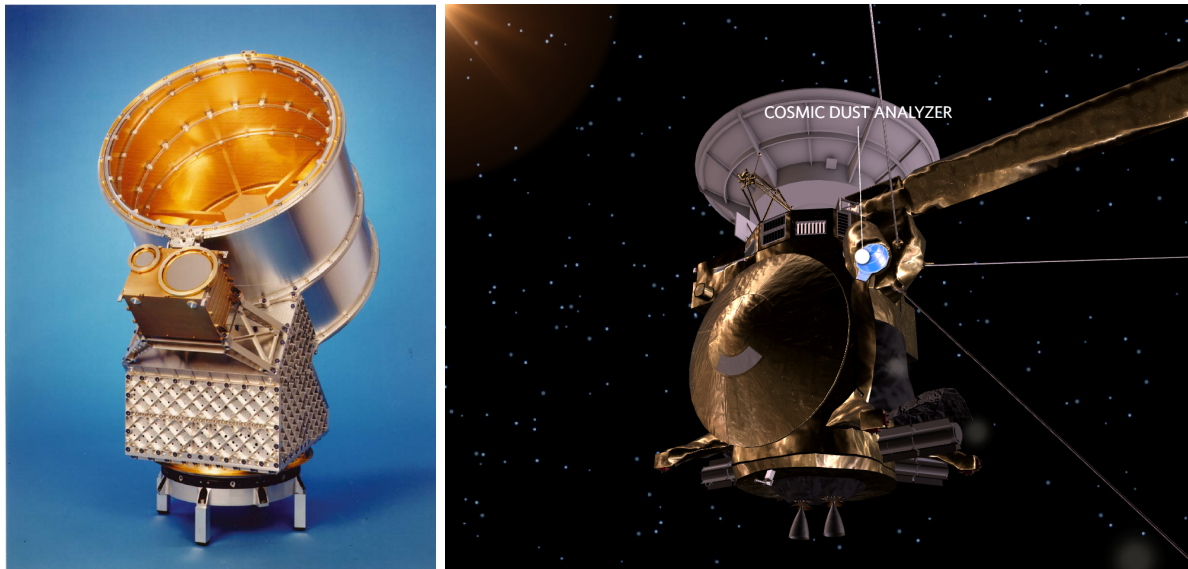


**Figure 1.2.:** (Left) Photo of the Cosmic Dust Analyzer (CDA), taken from Srama et al. (2004b). (Right) Rendered image of the Cassini spacecraft with the mounted CDA, generated with the Cassini spacecraft viewer (NASA, 2023).

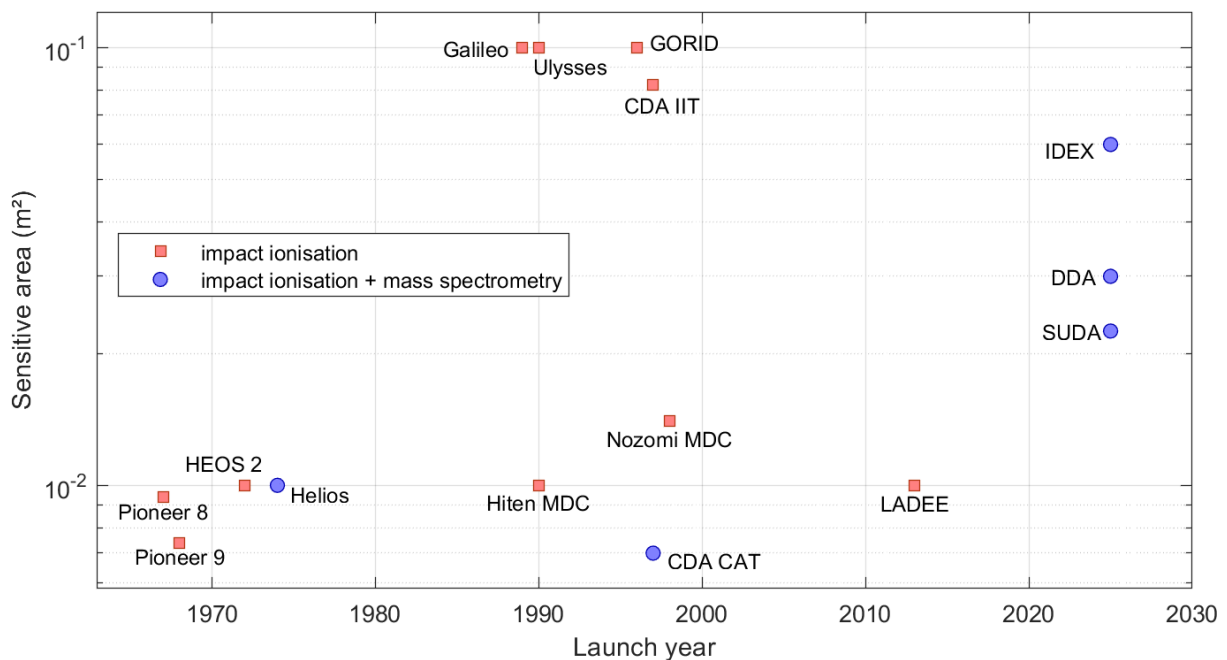


**Figure 1.3.:** History of impact-ionisation-type dust detectors. Sensitive area is the effective sensitive area under normal incidence. Data taken from Janches et al. (2021, Table 2 and references therein), as well as Szalay (priv. comm.) and Goode et al. (2021).

---

Although aerogel collectors demand more complex mission designs (i.e., a way to return the pristine samples to Earth), laboratories on the ground offer far greater analytic capabilities than are achievable onboard spacecraft. Therefore, collectors, such as that carried by the Stardust mission through comet Wild 2's coma, enable a unique way of probing cosmic particulates.

Just as integral to in-situ astronomy as the detector instruments themselves proved to be the capability to simulate hypervelocity cosmic dust experimentally. Among these technologies are the light-gas gun (for grain sizes  $> 100 \mu\text{m}$ ), the plasma drag accelerator (sizes between  $10 \mu\text{m}$  and  $100 \mu\text{m}$ ), and the electrostatic accelerator (sizes between  $10 \text{nm}$  and  $5 \mu\text{m}$ ) (see e.g., Burchell et al., 1999; Maas et al., 1986; Hasegawa et al., 2001; Srama, 2010), all of which have been used in the development, characterization, and calibration of the various aforementioned dust detector types. Relevant for the dust-telescope-type instruments investigated herein is the electrostatic accelerator, which covers the particle size range and the velocities typically targeted with these instruments. In essence, these are electrostatic particle accelerators as used in nuclear physics, which accelerate ions via a static high-voltage electric field. For the purpose of cosmic dust simulation, however, they are equipped with a dust source that feeds charged grains instead of ions into the accelerating field. Development of this cosmic dust simulator occurred concurrently with the development of the impact plasma detectors (Friichtenicht, 1964; Dietzel et al., 1972). Its range of applications has since been expanded to also cover fundamental impact physics (e.g., Lee et al., 2012; Li et al., 2022). Currently, there exist two operational accelerators of this type, located at the University of Colorado Boulder (of the pelletron-accelerator-type, Shu et al., 2012) and at the University of Stuttgart (of the van-de-Graaff-accelerator-type, Mocker et al., 2011; Li et al., 2021). The Stuttgart dust accelerator only recently resumed service after the facility was moved from the Max Planck Institute for Nuclear Physics in Heidelberg, where it had been operational since the late 1960s (e.g., Auer et al., 1968; Dietzel et al., 1972).

With its exceptionally long history, in-situ dust astronomy continues to be highly active field with a number of new developments and instruments on the brink. Especially the dust-telescope-type detectors—one of which being the subject here—with their ability to ‘touch’ and analyse alien worlds and cosmic realms from afar, pose a unique and intriguing window into the nature of the universe.

## 1.3. The DESTINY<sup>+</sup> mission

### 1.3.1. Overview

DESTINY<sup>+</sup> (Demonstration and Experiment of Space Technology for INterplanetary voYage with Phaethon fLyby and dUst Science) is a planetary science mission of the Japanese space agency JAXA. Selected in 2017 as an M-class mission of JAXA's small body exploration programme (Fujimoto and Tasker, 2019; Arai et al., 2018), DESTINY<sup>+</sup> aims to perform a flyby at the active asteroid ‘3200 Phaethon’, the peculiar parent body of the Geminids meteor shower (e.g., Williams and Wu, 1993, see also Section 1.3.3). To meet Phaethon in interplanetary space, DESTINY<sup>+</sup> intends to execute a novel and highly sophisticated mission scheme (Ozaki et al., 2022a): Launched into an elliptical, GTO-like orbit by the Japanese small-class Epsilon rocket, the spacecraft will raise its altitude gradually using its ion engines, until reaching the Moon for a series of gravity assist

manoeuvres and ultimately escaping into a heliocentric orbit. This would allow the spacecraft to forgo a heavier launch vehicle, usually required for interplanetary missions, at the cost of an added near-Earth mission duration of roughly two years. Then, after about another year of interplanetary cruise, the flyby takes place near Phaethon’s crossing of the ecliptic, at a closest-approach distance of 500 km (see Figure 1.4). The current baseline mission schedule foresees a launch in Q1 2025 and a Phaethon flyby in January 2028, the latter being fixed due to Phaethon’s orbit. (A backup scenario with a flyby in November 2030 is available.)

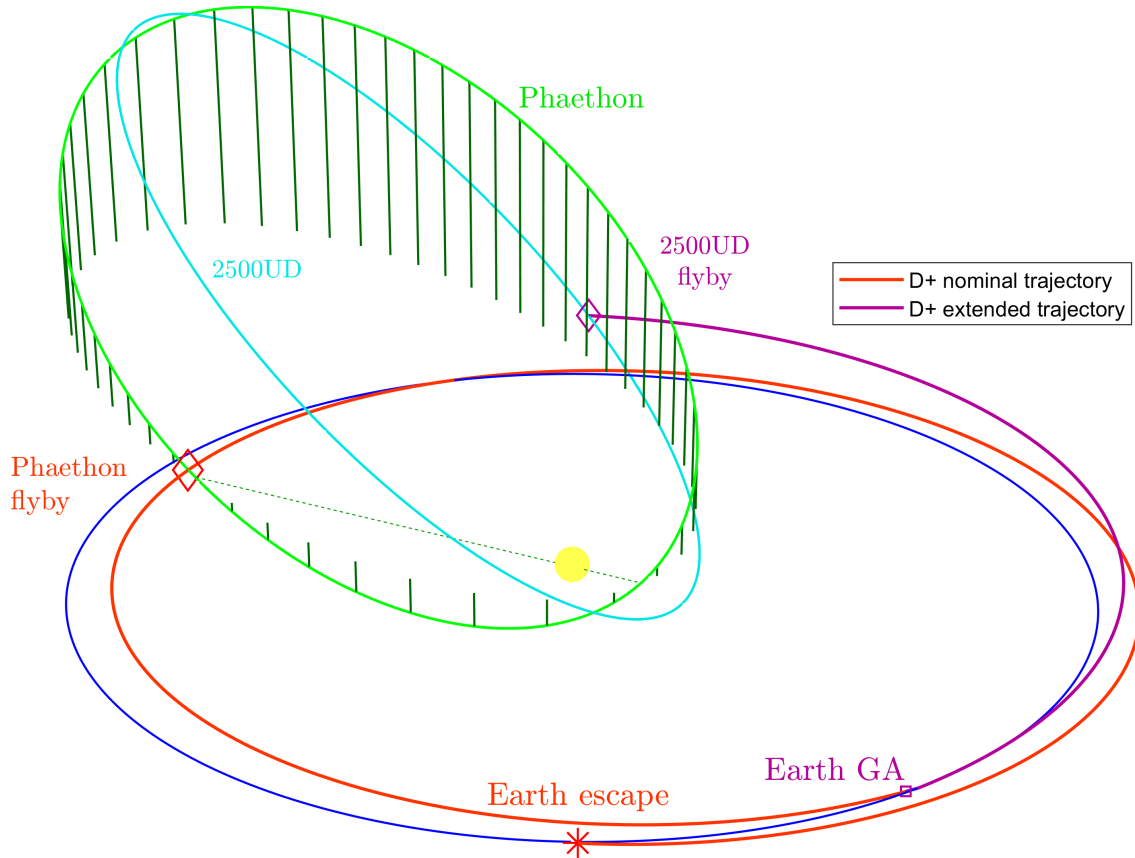


**Figure 1.4.:** Trajectories of DESTINY<sup>+</sup> (red), Phaethon (green), 2005 UD (cyan, potential mission extension target), and Earth (blue). The trajectory corresponds to mission scenario ‘Case #5’ (launch in early 2025) in Ozaki et al. (2022a).

With a launch mass of 480 kg and a xenon propellant mass of 60 kg (in total granting  $\Delta v \approx 4 \text{ km s}^{-1}$ ), the DESTINY<sup>+</sup> probe is size-wise comparable to JAXA’s renowned Hayabusa spacecraft which concluded its asteroid sample retrieval mission in 2010 (see e.g., Kuninaka and Kawaguchi, 2011). DESTINY<sup>+</sup> also draws on Hayabusa heritage for its solar-electric propulsion system, which comprises four ‘ $\mu 10$ ’ electrostatic ion engines. Unlike its predecessors, however, DESTINY<sup>+</sup> will use four instead of three engines simultaneously enabled by advanced power and thermal control systems (Toyota et al., 2017).

DESTINY<sup>+</sup> carries three scientific instruments (see Figure 1.5): (1) the Telescopic CAmera for Phaethon (TCAP), (2) the Multiband CAmera for Phaethon (MCAP), as well as (3) the DESTINY<sup>+</sup> Dust Analyzer (DDA, discussed in the following section). TCAP is a panchromatic, high-focal-length (790 mm) camera with a rotating mirror to track Phaethon during the flyby at a static spacecraft attitude. With a ground resolution down to 3 m per pixel at minimum distance, TCAP

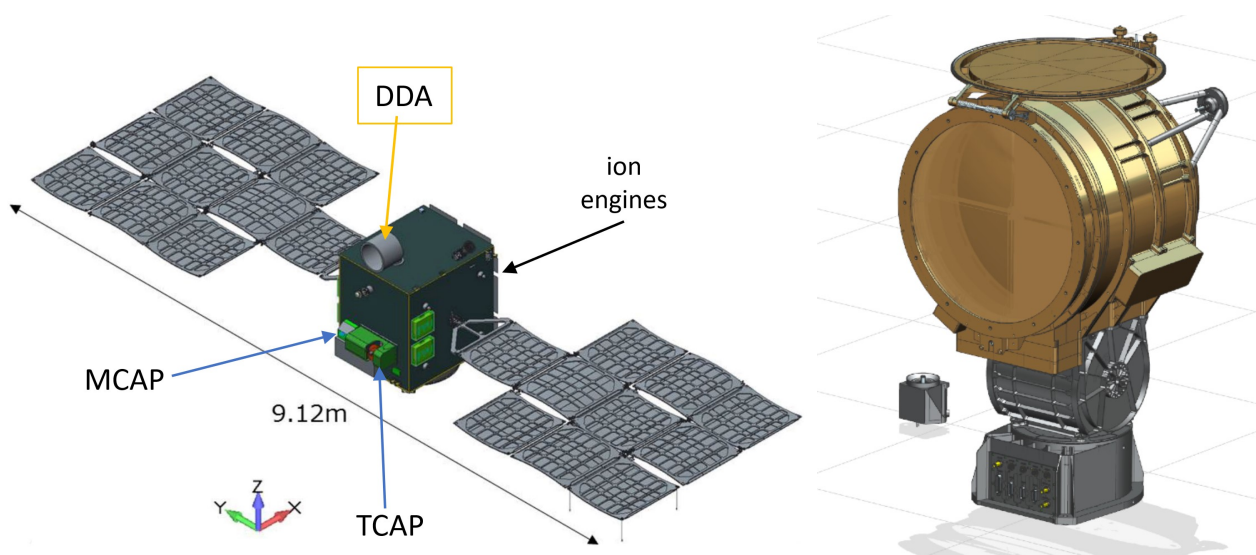


**Figure 1.5.:** (Left) The deployed DESTINY<sup>+</sup> spacecraft. Image credit: JAXA. (Right) Rendered view of the DDA instrument, generated by Gläser (priv. comm.).

will observe Phaethon’s global shape and regional/local surface features, and is also used for optical navigation during the approach. MCAP observes Phaethon in four narrower wavelength bands between 400 nm and 900 nm with a body-fixed optical axis and wider field of view (FOV). Its objective is to map spectral variations to be correlated with surface features imaged by TCAP. For more details on the cameras, see (Ishibashi et al., 2018, 2022). The science mission of DESTINY<sup>+</sup> is coordinated by the Planetary Exploration Research Center (PERC) of the Chiba Institute of Technology (CIT).

### 1.3.2. A new-generation dust telescope

The third instrument, the DESTINY<sup>+</sup> Dust Analyzer (DDA), is a state-of-the-art dust telescope. It incorporates two modules: (1) a non-destructive particle-charge-sensing module and (2) an impact plasma mass spectrometer. These two modules work in tandem to simultaneously measure the physical, dynamical, and chemical properties of individual cosmic dust particles. As such, it draws on heritage of the Cassini CDA (Srama et al., 2004b, 2011). DDA is designed and built at the University of Stuttgart, Institute of Space Systems (responsible for the sensor-head and mounting) and by the private company *von Hoerner & Sulger* (responsible for the electronics), and is funded by the German Aerospace Center (DLR).

DDA is a streamlined version of the dust telescope conceptualized by Grün et al. (2005) and Srama et al. (2004a), which, for the non-destructive particle-charge-sensing stage, employed multiple orthogonally arranged arrays of wire electrodes allowing for the accurate reconstruction of the particle trajectory (directional accuracy of  $\sim 1^\circ$ , see Srama et al., 2007; Sternovsky et al., 2011). This complex and heavy trajectory sensor design, however, which requires one charge-sensitive amplifier (CSA) and measurement channel per wire electrode (at e.g., 64 electrodes in the design of Auer et al., 2008), is not suited for space probes with limited payload capacity such as DESTINY<sup>+</sup>. DDA forgoes the high-accuracy wire electrode trajectory sensor in favour of a simplified, grid-electrode-based version (proposed by Li et al., 2014, 2015, 2017), that reduces complexity and mass greatly at the cost of determined trajectory accuracy. Grid electrodes have the added benefit

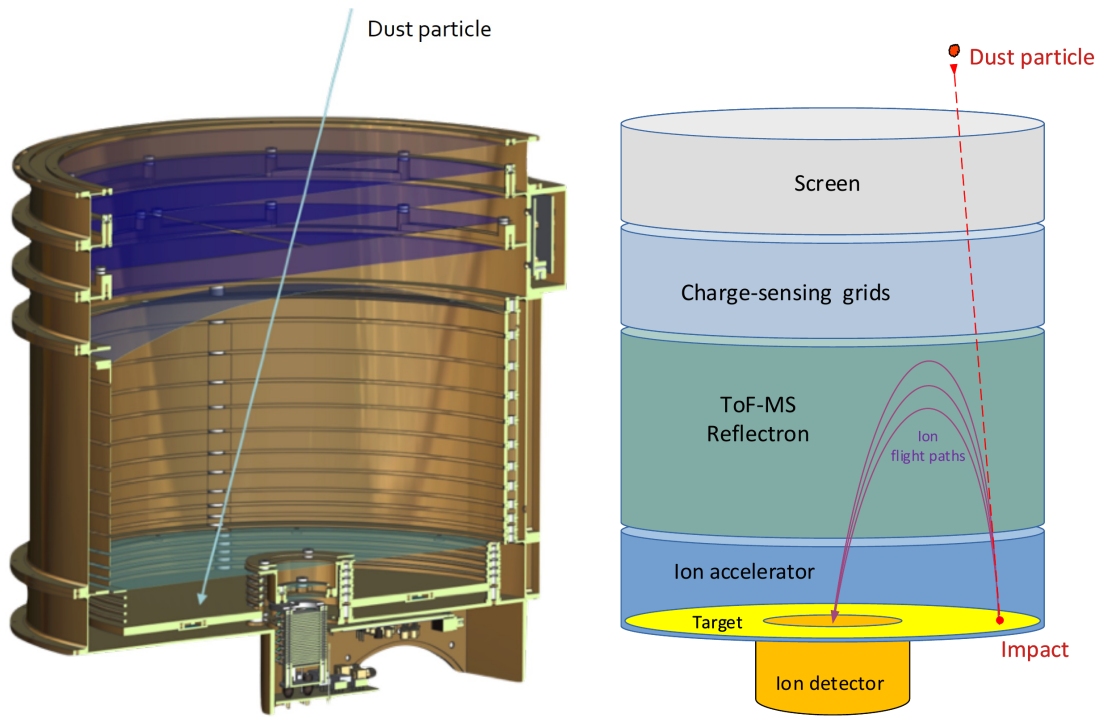


**Figure 1.6.:** Cut view (generated by Gläser, priv. comm.) and schematic view of DDA.

of capturing the particle charge more efficiently than wire electrodes, which benefits sensitivity (Li et al., 2015). For DDA a single-plane, four-segment grid electrode was chosen, therefore, reducing the number of measurement channels to four. Sensing passing dust grains in one of the electrode segments constrains their entry location into the instrument and thus their approach direction. The grain’s velocity is determined via time-of-flight (TOF) measurement between the passing of the entrance grids and the impact on the gold plate target inside the sensor housing.

For the second, destructive detector stage, DDA adopts the working principle of an impact plasma mass spectrometer: The high relative velocity of cosmic dust (typically  $> 1 \text{ km s}^{-1}$ ) causes the grains to decompose into a plasma upon impacting the instrument’s high-purity gold target. Situated within an accelerating electric field, the plasma’s (positively charged) ions are fed into a reflectron-type TOF mass analyser, where they are separated according to their charge-to-mass ratio and focussed onto an ion detector. The ions are registered at the (electron-multiplier-type) ion detector in succession, after a delay according to their charge-to-mass ratio, which allows the determination of their mass number. The derived abundance of ions with respect to their mass numbers forms what is known as the mass spectrum. DDA’s mass resolution, which describes a mass spectrometer’s ability to distinguish between ions of different mass numbers, is at  $\frac{m}{\Delta m} \gtrsim 100$ , roughly a factor of three over CDA and one order of magnitude over Helios (CDA and Helios parameters from Grün et al., 2019). The high mass resolution enabled by the reflectron ion optics as well as the directional analysis enabled by the segmentation of the charge-sensing entrance grid, pose key advancements over DDA’s predecessor, CDA. The recording of a mass spectrum also acts as the unequivocal proof of a true particle impact, an essential advantage of the impact plasma mass spectrometer over other dust detectors types. Furthermore, DDA is mounted on a two-axis pointing mechanism (of DDA), which allows for a certain pointing autonomy even when the spacecraft attitude is determined by operational factors.

---

DDA’s scientific objectives are manifold. For one, it shall sample the dust in Phaethon’s vicinity during the flyby, which is released from its surface through passive (impact-generated) ejection and possibly active ejection mechanisms. In addition, DDA will conduct science operations during the entire three years leading up to the encounter including phases of active propulsion. The flight plan foresees significant amounts of time spent in near-Earth, lunar, and interplanetary space, such that DDA will have exposure to a multitude of cosmic dust populations. Among its objectives are thus also the exploration of the Earth’s dust environment at varying altitudes (expected to be enriched with micro-debris, i.e., human-made dust), the detection of the impact-generated lunar ejecta, the characterization of interplanetary dust at 1 au (with respect to the contribution of different sources, e.g., cometary vs. asteroidal), as well as the study of interstellar dust at 1 au (whose occurrence in the inner solar system due to interaction with the interplanetary magnetic field is expected to be highly solar-cycle-dependent). The evaluation of the various relevant dust populations in the context of observation through DDA will be conducted in the following chapters as the focus of this thesis.

### 1.3.3. Phaethon

Phaethon is a peculiar and highly debated comet-asteroid continuum object that scientists struggle to rank among either one class (Hsieh, 2017). Although dynamically and spectrally an asteroid (Green et al., 1985), it is also, due to its coinciding orbit, unambiguously connected to the Geminids meteoroid stream (meteoroid streams are a phenomenon typically associated with comets). In addition, space-based observations showed that Phaethon repeatedly develops transient cometary-like activity during its perihelion, in the form of brightness outbursts and a tenuous tail, which have been associated with dust production (Jewitt and Li, 2010; Li and Jewitt, 2013; Jewitt et al., 2013; Hui and Li, 2016). Phaethon’s apparent lack in volatile compounds (ices or hydrated minerals, e.g., Takir et al., 2020; Geem et al., 2022) that drive the activity in *true* comets—which has also earned it the name ‘rock comet’—has sparked tremendous debate about how Phaethon’s observed activity (notwithstanding its fathering of the Geminids) could have come about. The proposed mechanisms typically draw on Phaethon’s exceptionally low perihelion distance of only 0.14 au (closer to the Sun than that of any other named asteroid), where its surface temperature is estimated to reach over 1000 K, thus leading to dust production via thermal-stress-induced cracking of rocks (Jewitt and Li, 2010; Jewitt, 2012; Delbo et al., 2014; Molaro et al., 2017). Hypothesized drivers for the emission of such produced regolith include gas production by thermal decomposition of minerals (MacLennan and Granvik, 2023), sublimation of iron and pyroxene (Lisse and Steckloff, 2022), volatilization of mineral-enclosed sodium (Masiero et al., 2021), sublimation of a deep internal ice reservoir (Boice, 2017; Yu et al., 2019), thermal radiation pressure from the asteroid body (Bach and Ishiguro, 2021), as well as electrostatic lofting (Kimura et al., 2022). Responding to the transient nature of Phaethon’s observed activity, others have suggested an impact-driven pseudo-activity (Zubko et al., 2022), or large-scale reshaping and mass-shedding events (Nakano and Hirabayashi, 2020) to take place. Then again, the most recent observational studies by Hui (2023) and Zhang et al. (2023) report Phaethon’s perihelion emissions to be devoid of dust and suggest a purely gaseous activity driven by the thermal desorption of sodium.

Aside from its present-day mass loss, other issues around Phaethon remain similarly strongly

---

contested, such as its affiliation with the Pallas group (León et al., 2010; MacLennan et al., 2021), or a common origin with the asteroids 1999 YC and 2500 UD (Ohtsuka et al., 2006; Ryabova et al., 2019; Devogèle et al., 2020; Kareta et al., 2021), the latter of which is a potential flyby target for a DESTINY+ extended mission.

Phaethon is also classified as a potentially hazardous asteroid (PHA), having a minimum orbit intersection distance (MOID) with Earth of about 0.02 au (or 7.6 Earth-Moon distances). The intersection occurs near Phaethon’s descending node (i.e., the north-to-south ecliptic crossing of its inclined orbit), which is located at a heliocentric distance of 0.87 au. The short MOID permits a flyby point that is relatively easy to reach for spacecraft that can escape Earth’s gravity well, thus enabling the DESTINY+ mission.

In December 2017, Phaethon flew by the Earth at a distance of just 0.07 au, prompting ground-based observation campaigns around the world (e.g., Kim et al., 2018; Devogèle et al., 2018; Jewitt et al., 2019; Lazzarin et al., 2019; Tabeshian et al., 2019; Taylor et al., 2019; Lin et al., 2020; Ye et al., 2021; Kiselev et al., 2022). Among other things, a peculiar reddening of its colour over the course of the flyby (Lazzarin et al., 2019; Tabeshian et al., 2019), as well as a remarkably high degree of polarization (Devogèle et al., 2018; Kiselev et al., 2022) had been found. Furthermore, radar imaging by the Arecibo Observatory revealed a roughly spherical shape of 6 km diameter and confirmed a rapid rotation period of 3.6 hours (Taylor et al., 2019, see Figure 1.7).

Misfits like Phaethon (neither pure asteroid nor comet) have led to the introduction of new taxonomy such as the ‘asteroid-comet continuum’ (see review by Hsieh, 2017), which includes sub-categories such as active asteroids (rock comets), main belt comets, or dormant comets. Although the nature of these poorly understood objects is expected to be highly diverse, the DESTINY+ mission is an auspicious attempt at unveiling some of their mysteries.

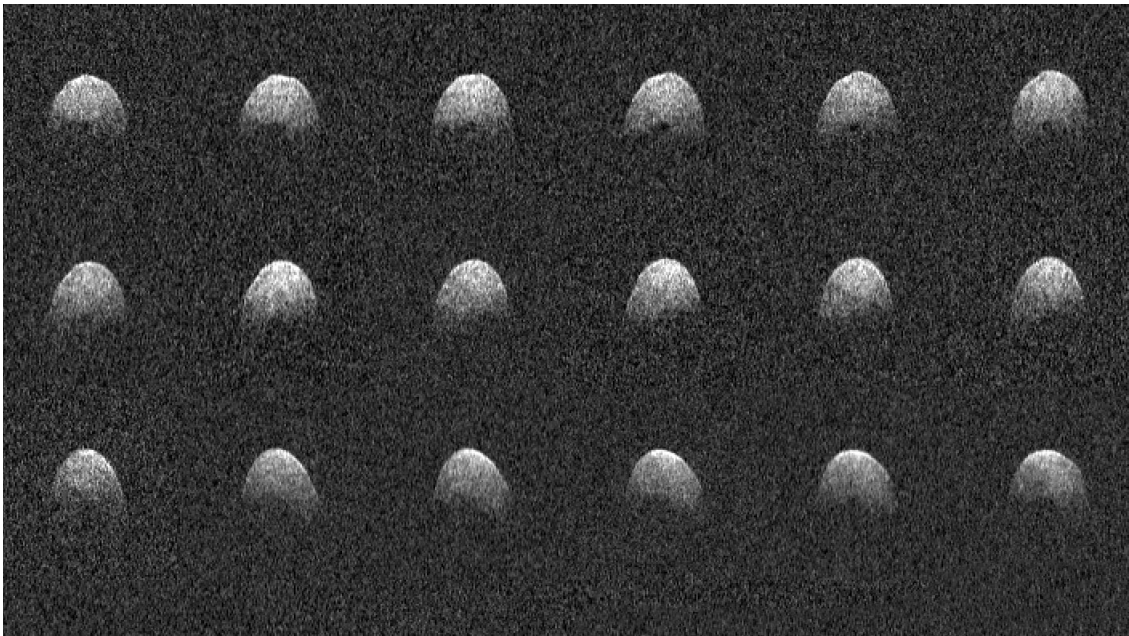


**Figure 1.7.:** Radar images of asteroid Phaethon during its close approach to the Earth in 2017 obtained by the Arecibo Observatory (NASA, 2017; Taylor et al., 2019). Distance:  $10.3 \times 10^6$  km or about 27 Earth-Moon distances; Resolution: 75 m per pixel; Image credit: Arecibo Observatory/NASA/NSF

---

### 1.3.4. Mission origins

The coming about of the DESTINY+ mission deserves some attention as it is untypical for a planetary science mission and, to some extent, affects the selection of science objectives and the planning of science activities for the DDA (see Section 1.4). In fact, DESTINY (Demonstration and Experiment of Space Technology for INterplanetary voYage) was initially conceived as technology demonstration mission that should verify the feasibility of an ambitious mission design, conceived to reach interplanetary space with the small-class/low-cost and all-solid-fuel Epsilon rocket (Kawakatsu and Iwata, 2013). This mission design employs a highly optimized and integrated flight plan, whose execution required a number of technologies to be developed. These novel technologies are centred around the spacecraft's electric propulsion system, including ultra-lightweight solar panels, an advanced thermal control, as well as the implementation of an autonomous operation scheme under the spacecrafts highly dynamic attitude (Zuiani et al., 2013; Fukushima and Mita, 2011; Fukushima, 2012). While the early mission design targeted eventually reaching a halo orbit around the Sun-Earth Lagrange point  $L_2$ , the mission concept kept being refined to include a potential science component in the form a near-Earth asteroid flyby (Sarli et al., 2015; Chen et al., 2016; Iwata et al., 2016; Sarli and Kawakatsu, 2017). Iwata et al. (2016) suggested the DESTINY spacecraft bus to serve as an evolvable platform for a series of low-cost interplanetary space missions, discussing a number of model science payloads and scenarios. In that sense, Sarli et al. (2018) proposed the mission DESTINY+, which would perform a flyby at Phaethon, deploying a reusable (i.e., re-dockable) scouting probe for proximity flyby observations (a derivative of Hayabusa2's PROCYON probe, see Funase et al., 2016). (The acronym DESTINY was thereby appended by a '+', standing for 'Phaethon fLyby with reUSable probe', to form the—comically long—acronym DESTINY+.) However, the deployable probe was subsequently forgone in favour of more sophisticated instrument suite, including the DDA, which expanded the mission's scientific scope to cover the multifaceted field of cosmic dust (Toyota et al., 2017; Arai et al., 2018, 2019). (The meaning of the acronym's '+' was thereby exchanged with 'Phaethon fLyby and dUst Science'.) This mission concept became the finally adopted configuration and the German contribution in form of the DDA was formalized (DLR, 2020).

Compared to typical planetary science missions, the conceptualization of DESTINY+ has (due to its origins) to some extent followed less of a science-objective-driven and more of a platform-capabilities-driven approach. Although DESTINY+ has evolved from its pure technology demonstration roots to a fully fledged science mission, this has arguably resulted in more open-ended scientific ambitions, the closer evaluation of which (or rather those of DDA) is the subject of this thesis.

## 1.4. Science planning approach

Exploration space missions are usually highly geared towards set of specific scientific objectives. The process that tries to ensure these objectives to be met, from defining adequate goals to coordinating their execution, is called 'science planning'. In the general sense of the term, science planning may accompany the whole of a mission life cycle, from conceptualization to mission implementation, and can be deeply intertwined with mission design. This involves identifying research questions that

---

the mission aims to address, selecting the instruments to collect the required data, and determining the optimal configuration and scheduling of observations. Science planning has become a well-established activity at space agencies like ESA (e.g., Hoofs et al., 2004; Titov et al., 2006; Koschny et al., 2010; Vallat et al., 2017) and is vital to mission success.

The purpose of the project presented in this thesis is to tailor and apply the principles and methods of science planning to DDA, with its mission- and instrument-specific factors, to support the DDA science team as well as technical teams. Given the technology-driven origin of the DESTINY+ mission (see Section 1.3.4) and the inherent, highly diverse flight plan exposing DDA to varied environments, DDA functions as an in-situ dust observatory of exploratory nature. Its mission is to investigate all applicable near-Earth and inner solar system dust populations, while using its unprecedented instrumental capabilities to discover them in a new light. In this context, the science planning conducted here will focus on assessing the various occurring dust populations in terms of their observability by DDA, and on devising strategies and the tooling to design and schedule observation campaigns based on their suitability, feasibility, and priority. Notably, we omit the analysis of the Phaethon flyby dust science case, which, on the one hand, require less operational planning effort,<sup>2</sup> and on the other hand, is scientifically already being addressed extensively by members of the DDA science team (e.g., Szalay et al., 2019b; Kimura et al., 2022), as well as by independent researchers (see Section 1.3.3).

We begin by providing a background on the nature of cosmic dust in the solar system, such as its types and dynamics, in Chapter 2. We then discuss the technical aspects that are relevant to DDA science operations, specifically, spacecraft-related factors (such as trajectory and attitude) in Chapter 3, and instrument-related factors (such as the mounting of DDA and the sensor’s geometrical characteristics) in Chapter 4. In Chapter 5, we analyse presumably relevant dust populations based on previous measurements, as well as empirical and physical models, and assess their observability by DDA, taking into account the aforementioned technical considerations. In Chapter 6, we adapt common science planning principles to the case of DDA and introduce tooling developed specifically to enable straightforward design of DDA observation campaigns. Based on our findings and methods, we then derive a tentative high-level science activity timeline for the DESTINY+/DDA mission and instrument pointing timelines as testcases for the operations planning process. Chapter 7 concludes the thesis, providing a summary, an outlook on how to build on the presented work, and final thoughts.

---

<sup>2</sup>The Phaethon flyby is a single, short-duration event, with a fixed spacecraft attitude and fixed dust ram direction, i.e., DDA’s pointing is already determined and will be static during the flyby.



## 2. Cosmic Dust in the Solar System

This chapter provides an overview of the current understanding of cosmic dust in the solar system. Specifically, it outlines the primary dust types and the forces that govern their motion, and it highlights the significance of cosmic dust in the context of spaceflight.

### 2.1. Types

Dust astronomy, today, distinguishes between many different kinds of cosmic dust, doing justice to the diverse forming mechanisms, particle properties, and dynamics that dust grains exhibit. Here, we explain the most fundamental classification of in-space cosmic dust, which comes down to the distinction between circumplanetary, interplanetary, and interstellar dust.

#### 2.1.1. Circumplanetary dust

Circumplanetary dust considers grains that are exclusively found in the immediate vicinity of a planet or moon, typically bound to that body's gravitational field (for a review of the field, see Spahn et al., 2019). This dust may be subject to constant resupply from the body's surface, such as via ejection by meteoroid impacts on the airless Moon or the cryovolcanic activity on the icy moons of the outer solar system. This type of dust may be subject to intricate dynamics, resulting from gravitational interaction with the planet-moon system and the electromagnetic interaction of with the planet's magnetosphere.

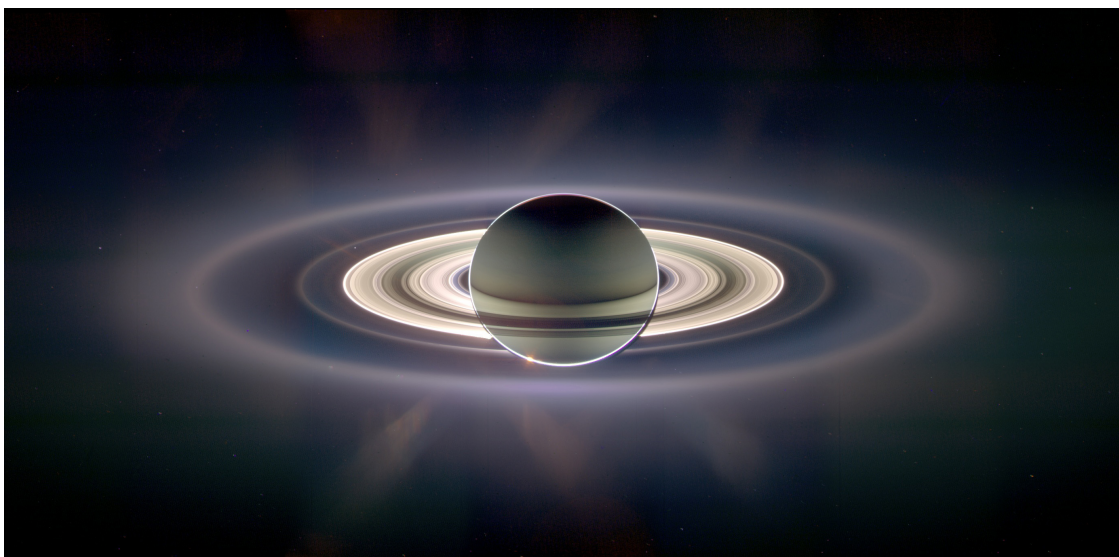


**Figure 2.1.:** Circumplanetary dust at Saturn: The rings of Saturn glowing in the sunlight, imaged by the Cassini spacecraft as the Sun is eclipsed by the planet (NASA, 2006). The outer, diffuse rings are made up of dust grains, generated for example by cryovolcanism on Enceladus.

---

In this thesis, we will consider the circumplanetary dust environments of Earth and the Moon, the only planetary objects visited by DESTINY+. This includes the near-Earth populations of debris dust generated by human spaceflight activities and the magnetospheric particle swarms of yet unknown origin, as well as the lunar impact ejecta environment.

### 2.1.2. Interplanetary dust

Interplanetary dust (IPD) refers to grains that are created within the solar system, liberated from their sources (mainly comets and asteroids) to disperse throughout interplanetary space. This dust forms a tenuous, disc-shaped cloud that encompasses the planets of the solar system, known as the zodiacal cloud. It has its name from the visible phenomenon it generates in the night sky: a faint swath of light along the zodiac constellations caused by the cloud's scattering of the sunlight, the so-called zodiacal light (see Figure 2.2).

In addition to a dominant diffuse component, the zodiacal cloud also contains more structured features, such as toroidal rings, generated for instance by 'recent' large dust production events (e.g., asteroid collisions) or by the dynamical interactions between the disc and the planets. Such a feature-bearing zodiacal cloud is conceptually illustrated in Figure 2.3.

The material of the zodiacal cloud is predominantly supplied by the small bodies of the solar system, which cannot retain once-emitted grains due to their low gravity. For the most part, these are comets dissolving in the heat of the Sun and colliding main-belt asteroids or Kuiper belt objects. Yet, the relative contribution of these sources continues to be a matter of debate: Early considerations estimated a considerable or even dominant contribution from asteroids, as derived from the observed 'zodiacal dust bands'—distinct features in the latitudinal distribution of the infrared zodiacal light, which could be dynamically linked to certain asteroid families (Dermott et



**Figure 2.2.:** The zodiacal light as photographed from the Paranal Observatory. The zodiacal light is the swath of light on the right, next to the Milky Way to the left. Under optimal conditions it is visible by eye just before dawn or just after dusk. It extends along the zodiac (resulting from the dust cloud's alignment with the ecliptic plane), hence its name. Image credit: Horálek et al. (2016).

---

al., 1984; Reach et al., 1997; Kortenkamp et al., 2001). More recent studies, on the other hand, tend to conclude a dominant contribution from Jupiter-family comets (JFCs) and only a minor asteroidal dust component in the range of 1/5th to 1/20th (Nesvorný et al., 2010; Rowan-Robinson and May, 2013; Yang and Ishiguro, 2015; Ueda et al., 2017; Soja et al., 2019). In the outer solar system, dust from the collisional erosion of Kuiper belt objects is thought to be the dominant component (Poppe, 2016; Poppe et al., 2019). A recent investigation by Keller and Flynn (2022) of the age of collected dust particles suggests a significant contribution from the Kuiper belt, even at Earth.

In accordance with their source bodies, the zodiacal cloud components exhibit distinct dynamical properties. Whereas comets can release dust into orbits of considerable eccentricity and inclination, asteroidal or Kuiper-belt dust is expected to be more confined to near-ecliptic and low-eccentricity orbits. This is reflected in the approach directions of the grains at an observer. At Earth, micrometeoroids create radar-observable meteors, allowing one to inspect their radiant distribution in the sky, as seen in Figure 2.4. Several broad radiants of predominant approach directions can be identified, which, via dynamical modelling, can be associated with the respective source body populations (e.g., Jones et al., 2001; Wiegert et al., 2009; Nesvorný et al., 2011a,b; Pokorný et al., 2014): grains from JFCs constitute the so-called helion and anti-helion radiants, which are near the direction of the Sun and away from it, respectively; the north and south toroidal radiants are associated with the meteoroids released from Halley-type comets (HTCs); lastly, the north and south apex radiants are sustained by retrograde particles stemming from HTCs and Oort cloud comets.

Zodiacal discs are also observed around other stars, where they are referred to as ‘exozodis’. Enabled by ongoing advances in observational astronomy, exozodis are an increasingly coveted science target, posing a unique opportunity to study the conditions and architectures of near-habitable-zone planetary systems in our galactic neighbourhood (see, e.g., Stark and Kuchner, 2008; Kennedy and Wyatt, 2013; Rigley, 2022).

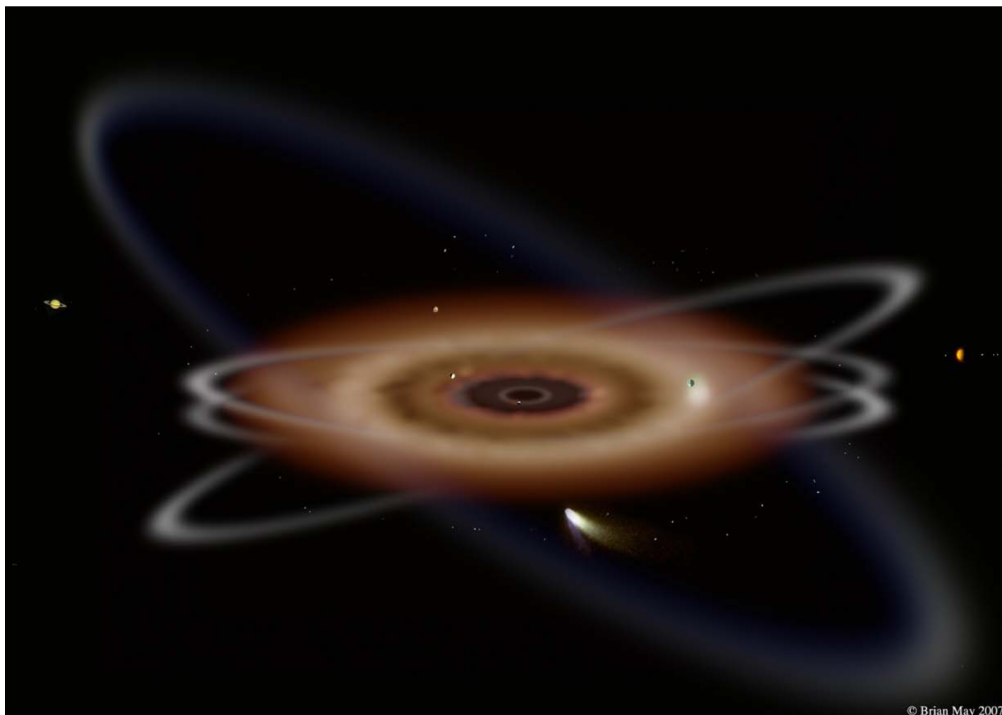


**Figure 2.3.:** The zodiacal cloud with various substructures. Artist's impression by May (2007).

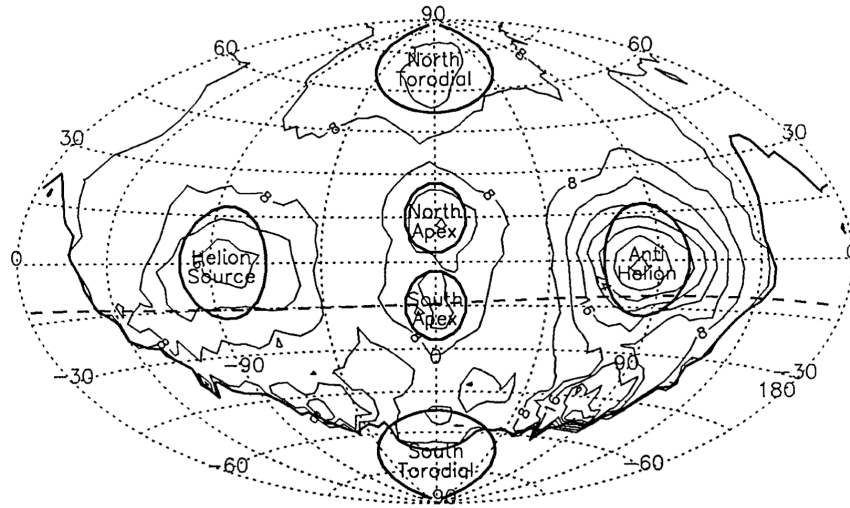


**Figure 2.4.:** Radiant distribution of sporadic meteor sources across the sky. Here, the Earth’s apex (i.e., its heliocentric direction of motion) is at the centre and the direction of the Sun is at a longitude of  $-90^\circ$ . Figure taken from Taylor and Elford (1998).

### 2.1.3. Interstellar dust

Interstellar dust (ISD), on the other hand, is the condensed matter component of the interstellar medium (ISM), which is the gas and dust that fills the space between stars. The ISM—as the primeval material from which stars and planetary systems like the solar system form—is a coveted science object, harbouring essential clues about star formation and galactic evolution processes (e.g., Asano et al., 2013). Within the local ISM, that is, the ISM in our corner of the galaxy, the Sun is moving along the edge of a rather warm and partially ionized cloud, called the local interstellar cloud (Frisch et al., 2011, see also Figure 2.5). Due to the motion of the Sun with respect to the ISM in our immediate surroundings, this material flows into and (to some extent) through the solar system, as our only tangible reference point for the ISM at large. Yet, the detection and analysis of this elusive flow is no easy task. Concerning the dust component (which constitutes around 1% of the mass of the ISM), the first in-situ detection of particles was achieved by the impact plasma detector onboard the Ulysses spacecraft around three decades ago (Grün et al., 1993). To date, however, only a handful of particles seemingly belonging to the flow of ISD could be probed for their chemical make-up (Westphal et al., 2014; Altobelli et al., 2016).

The predominant direction of the ISD flow through the solar system has been constrained by Ulysses and Galileo measurements, yielding an ecliptic longitude and latitude of  $259^\circ$  and  $+8^\circ$ , respectively, for the nominal upstream direction (Frisch et al., 1999).<sup>1</sup> Especially within the inner solar system, however, the flow can significantly deviate from that direction and take a variety of different flow patterns, depending on the size and charge of the particles, which determine their susceptibility to solar radiation pressure and interactions with the interplanetary magnetic field (IMF). This results in a particle-size-dependent and solar-cycle-dependent filtering of the flow, and thus strong variation of the ISD abundance within the inner solar system (Landgraf, 2000; Sterken et al., 2012, 2013). According to the characteristic force shaping the trajectories of the particles, one can loosely define three categories of ISD in the solar system.

<sup>1</sup>A similar nominal upstream direction was found by Albin (2019) for the ISD particles detected by the CDA onboard Cassini:  $263^\circ$  ecl. longitude and  $+9^\circ$  ecl. latitude.

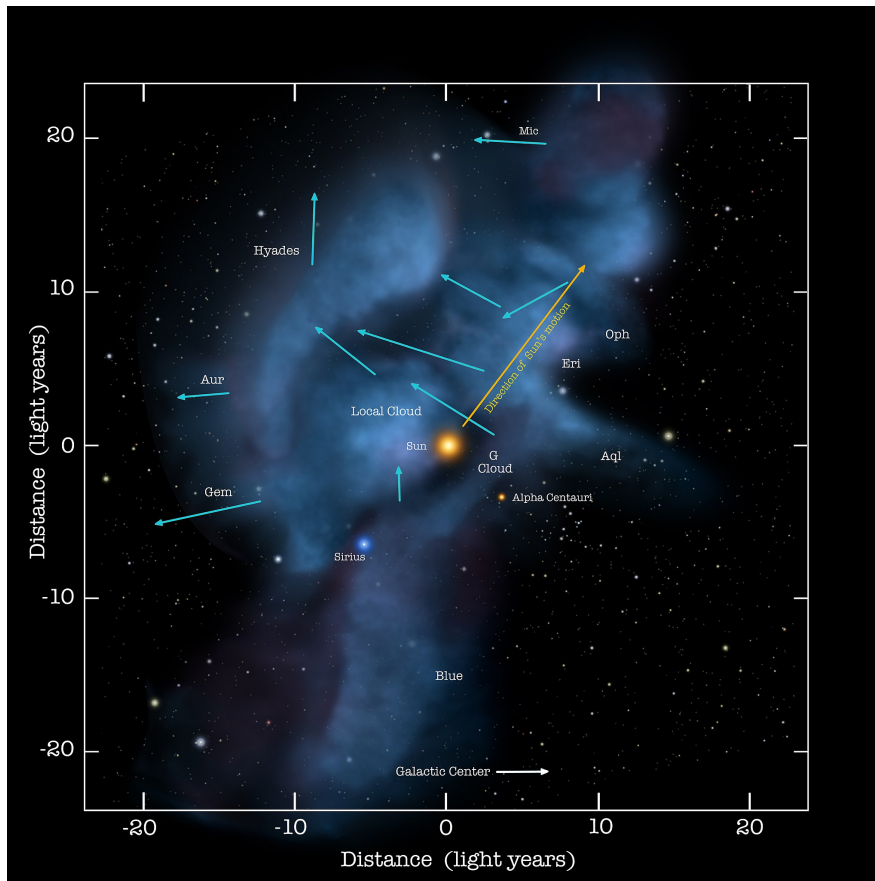


**Figure 2.5.:** Illustration of the Sun in a cluster of interstellar medium clouds. Studies indicate that the Sun is about to leave the ‘local cloud’ within the next few thousand years. Image Credit: NASA/Adler/U. Chicago/Wesleyan (2012).

The largest grains follow paths that are dominantly shaped by solar gravity (herein referred to as G-ISD). As seen in Figure 2.6a, the Sun bends their trajectories towards it, causing them to be concentrated in the downstream direction behind the Sun.

At smaller sizes (smaller than about  $1\ \mu\text{m}$ ), solar radiation pressure may counterbalance and even exceed the gravitational pull of the Sun. (These particles are herein referred to as  $\beta$ -ISD according to their high  $\beta$ -ratio, see Section 2.2.) While particles for which those forces are in equilibrium can traverse the solar system on straight paths, particles dominated by radiation pressure are deflected away from the Sun, forming a cone devoid of such particles in the downstream direction, as seen in Figure 2.6b.

The third category comprises the smallest ISD particles (smaller than  $\sim 200\ \text{nm}$ ), which are again less influenced by radiation pressure (due to their sub-wavelength sizes), yet which are strongly affected by electromagnetic interactions (thus herein referred to as EM-ISD). The steady, predominantly azimuthal field component of the IMF at high heliographic latitude brings about a Lorentz force that acts largely perpendicular to the solar equatorial plane. Because the polarities in the northern and southern hemispheres of the Sun are opposite, particles are accelerated either towards the solar equatorial plane, or away from it, depending on the polarity configuration of the IMF, which changes with the 22-year solar magnetic cycle. This ‘focussing’ of EM-ISD towards the ecliptic occurs during solar cycle minima with negative polarity in the northern hemisphere, whereas the ‘defocussing’ occurs during solar cycle minima with positive polarity in the northern hemisphere

(Morfill and Grün, 1979a; Landgraf, 2000).<sup>2</sup> These two phases are depicted in Figure 2.7. The next focussing phase will occur during the upcoming solar cycle minimum, expected for the time frame around 2030.

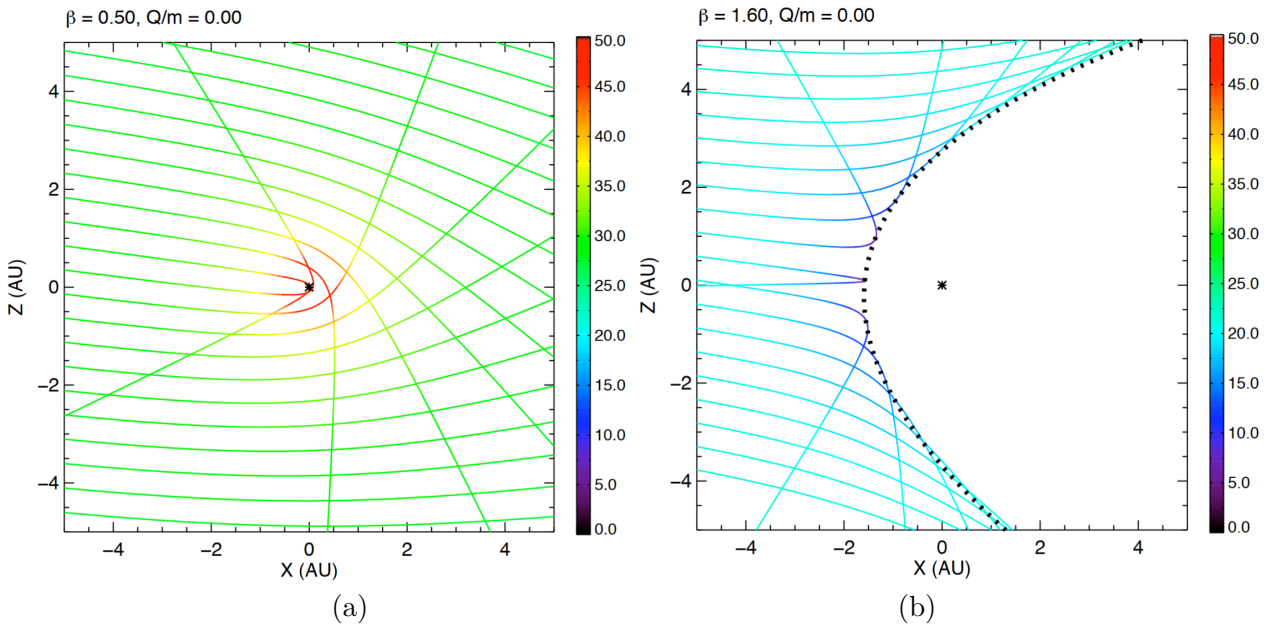


**Figure 2.6.:** Flow patterns of ISD shaped by solar gravity and solar radiation pressure, taken from Sterken et al. (2012). (a): Gravity-dominated particles are concentrated downstream from the Sun. (b): Radiation-pressure-dominated particles that are deflected, forming a cone behind which no particles are found; particle trajectories are concentrated in the cone surface region. Colours indicate the absolute particle speed along the trajectories (colour bar units in  $\text{km s}^{-1}$ ).

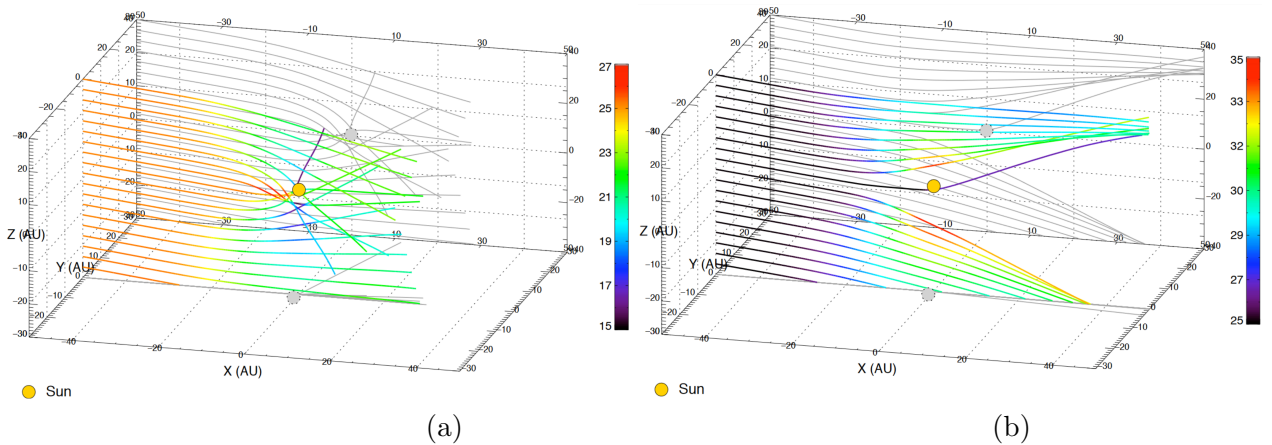


**Figure 2.7.:** Flow patterns of ISD shaped by electromagnetic forces, taken from Sterken et al. (2012). (a): Focussing configuration of the IMF; particles are driven towards the ecliptic (X-Y plane). (b): Defocussing configuration of the IMF; particles are driven away from the ecliptic. Colours indicate the absolute particle speed along the trajectories (colour bar units in  $\text{km s}^{-1}$ ).

<sup>2</sup>During solar cycle maxima, the polarity configuration reverses and no strong averaged field strength is present. Thus, neither strong focussing nor defocussing occur.

---

## 2.2. Dynamics

The motion and ensuing evolution of dust particles across the solar system is influenced by various factors. Depending largely on the size regime of the particles, different forces (or processes) dominate their dynamics thus producing characteristic behaviours of the various populations.

### Gravity

As is the case for bigger celestial bodies, gravity plays the formative role in the motion of cosmic dust grains down to sizes in the order of 1  $\mu\text{m}$ . It binds circumplanetary dust to their central body, and dictates a circumsolar orbital motion for the dust in interplanetary space. These motions can generally be described by Keplerian orbits around a single, central attractor, that is, if the influences from other bodies and forces are negligible, as may be the case for larger particles and/or short observed timescales. For instance, given the extended lifetimes of IPD particles, spanning from 1000s to 100,000s of years, several influences (gravitational and otherwise) render the Keplerian approximation inadequate. Gravitational perturbations affecting IPD grains can be broadly classified into three categories:

- *Secular perturbations*: These refer to gradual changes in a particle's orbit due to sustained gravitational influences from the planets over long distances.
- *Short-term perturbations*: Close encounters with planets trigger abrupt and drastic changes in a grain's orbit, which has the effect of a chaotic scattering of particles.
- *Resonant perturbations*: Arising from mean-motion resonances (MMRs) with planets, these perturbations can significantly influence the dynamics of particles in a more predictable, or orderly, manner. For their peculiar effects on the dust distribution in the zodiacal cloud at large, we will address these in more detail in Section Section 2.2.

Overall, while the Sun is the key player in shaping the orbits of cosmic dust, the secondary contribution from planetary gravitation can have a characterizing role in the orbital evolution of dust grains.

### Solar radiation

Another important factor in the dynamics of cosmic dust is the influence of solar radiation. The absorption and re-emission of photons from the Sun transfers a momentum to the dust grains, resulting in a 'radiation force' that can become substantial in the  $\mu\text{m}$  size regime. Larger particles are generally less affected. This force is (almost entirely) outwardly directed, meaning that it exerts a push on the particle away from the Sun. The strictly radial component of this force is thus also referred to as 'radiation pressure'. Its magnitude is inversely proportional to the square of the heliocentric distance—just as the Sun's gravitational force. Therefore, both forces keep their relative strengths, which effectively reduces the pull towards the Sun by a certain factor. The ratio between the force resulting from radiation pressure and the gravitational force is called  $\beta$ , and (at least for a given star) depends on the particle's properties alone. For a particle of a certain size and material,  $\beta$  may be computed by means of Mie theory. An example of a 'beta curve', showing the typical trend of  $\beta$  over particle size is given in Figure 2.8.

In addition to the radial component, however, there is also a minuscule component of the radiation force that is directed opposite to the particle's motion, resulting from the aberration of the incident

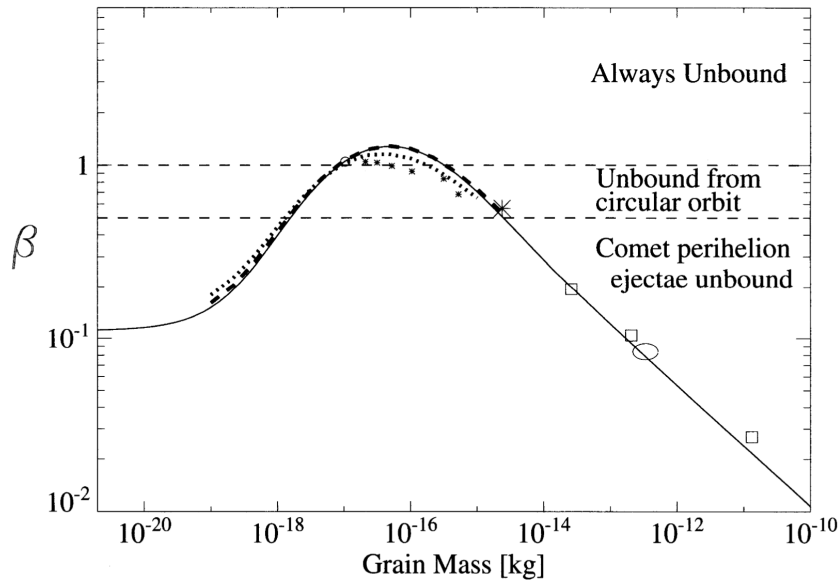


**Figure 2.8.:** Ratio of radiation pressure to gravity,  $\beta$ , as a function of particle mass (from Gustafson et al., 2001). Computed for a particle made of astronomical silicate ( $\rho = 2.5 \text{ g cm}^{-3}$ ). With decreasing particle size, the area to mass ratio increases, which in turn increases the  $\beta$  factor—that is, until the particle size becomes comparable to the wavelength of the incident radiation (i.e., around several 100s of nm). At that point, interaction with the radiation becomes less efficient, causing  $\beta$  to decrease again. In this case, the maximum  $\beta$  is reached at  $\sim 10^{-16}$  kg, roughly corresponding to  $0.4 \mu\text{m}$ . Different lines correspond to differently shaped particles. For more information, see Gustafson et al. (2001).

radiation as well as an asymmetric re-emission of radiation due to the Doppler effect, caused by the high-speed motion of the particle. Since this component scales with the particle’s velocity, it can be effectively considered as a drag force, commonly referred to as Poynting-Robertson (PR) drag (after its discoverers, see Burns et al., 1979, and references therein).<sup>3</sup>

In absolute terms, the PR drag is tiny compared to the radiation pressure component (with a relative magnitude of  $\sim 10^{-4}$ ). Yet, unlike the radial component, the drag continually changes the orbit of the particle by draining its orbital energy. Therefore, the PR drag is a crucial factor in the orbital evolution of dust grains, causing grains to spiral towards the Sun over long timescales. Scaling with velocity, the drag removes orbital energy most effectively at perihelion, thus causing the aphelion to decrease faster than perihelion. This results in a tendency for the orbits of dust grains to circularize, as they decay towards the Sun. Eventually, the conjoint migration toward the Sun causes the particles to be destroyed by mutual collisions or sublimation in the heat of the Sun. Their smaller remnants are then ‘swept out’ by radiation pressure.

For the two-body problem, Wyatt and Whipple (1950) derived analytic solutions for the evolution of the orbital elements of a particle affected by PR drag, which, using the  $\beta$ -factor introduced above,

<sup>3</sup>The net radiation force as a whole may also be referred to as ‘Poynting-Robertson effect’, as promoted by Klačka et al. (2014), who give a critical review of the treatment of the effect in the literature, such as by Burns et al. (1979) who justify their treatment in Burns et al. (2014).

can be written as:

$$\left(\frac{da}{dt}\right) = -\frac{\beta\mu}{c} \cdot \frac{(2+3e^2)}{a(1-e^2)^{3/2}} \quad (2.1)$$

$$\left(\frac{de}{dt}\right) = -\frac{5\beta\mu}{2c} \cdot \frac{e}{a^2(1-e^2)^{1/2}} \quad (2.2)$$

$$\left(\frac{di}{dt}\right) = 0 \quad (2.3)$$

where  $a$  is the semi-major axis of the particle,  $e$  its eccentricity,  $i$  its inclination,  $\mu$  the standard gravitational parameter of the Sun, and  $c$  the speed of light. Note that the inclination is not affected by the drag.

The effect of PR drag governs the evolution of particles as big as 100s of  $\mu\text{m}$ . Beyond those sizes, however, the migration due to PR drag becomes insignificant, as grain-grain collisions take over as the dominant evolutionary factor (as discussed further below).

### Solar wind

Besides electromagnetic radiation, the Sun also emits a stream of charged particles, called solar wind. This plasma stream, which consists of electrons, protons and alpha particles, has a similar effect on dust particles as the electromagnetic radiation, although net transferred momentum is much smaller ( $\sim 2 \times 10^{-4}$ ). However, because the solar wind stream is much slower than the speed of light, the aberration angle of the incident beam is much larger in the case of the solar wind. This results in a net force with a non-negligible drag component, whose magnitude is in the order of 20% to 40% of the PR drag depending on variations in the solar wind speed (Gustafson, 1994). The radial component of the solar wind force, however, remains insignificant compared to the radiation pressure and is usually neglected.<sup>4</sup>

### Charging and Lorentz force

Dust particles in interplanetary space are charged and therefore interact with the interplanetary magnetic field (IMF) carried by the solar wind. The charge is accumulated by the photoelectric effect, which causes the emission of electrons from the particle surface upon absorption of UV photons. Counterbalanced by the absorption of electrons from the solar wind, particles in interplanetary space are expected to assume an equilibrium state at a positive charge of 3–10 V (e.g., Mukai, 1981; Leinert and Grün, 1990).<sup>5</sup>

From their motion through the IMF, the charged dust particles experience a Lorentz force, which is expected to become the dominant force at particle sizes in the order of 100 nm and less (Morfill et al., 1986). In that size regime the strong radiation pressure largely precludes bound orbits around the Sun, but for the unbound ISD particles of that size it indeed plays a formative role, as described in Section 2.1.3. The Lorentz force may also be a factor in the dynamics of the smallest bound IPD particles, causing a stochastic diffusion of orbital elements, as will be discussed in Section 5.3.3.

<sup>4</sup>Solar wind drag is thus often included in dynamical models by scaling the PR drag by a factor of 1.3.

<sup>5</sup>Within the magnetospheres of planets the equilibrium charge varies significantly, depending on the local plasma environment and shadowing by the planet (e.g., Horányi et al., 1988; Horányi, 1996).

---

## Collisions

Collisions and the resulting fragmentation constitute another important evolutionary factor for interplanetary dust particles. With the high relative velocities of particles in interplanetary space, grain-grain collisions can be considered to be always destructive, causing either a break-off of some of their mass (erosive) or a complete break-up into pieces (catastrophic collision), depending on the size ratio of the colliding grains as well as material properties. For meteoroids and IPD in the solar system, the effect of catastrophic collisions dominates over that of erosion, as shown by Dohnanyi (1970). Where it occurs, this process reduces the number of larger particles and injects new smaller particles into the population. In a seminal work, Grün et al. (1985a) consolidate theoretical considerations with in-situ data on the flux and size distribution of micrometeoroids to derive a model for the steady state collisional balance at 1 au. Grün et al. conclude that at particle sizes  $> 100 \mu\text{m}$  the particle evolution is dominated by collisions, meaning they are more likely to suffer collisions than to significantly migrate due to PR drag. Such particles would therefore remain near their source region, until the material is ground up enough by collisions into smaller particles, which then commence their migration towards the Sun. More recent modelling efforts, however, report the necessity of considerable PR evolution at even larger sizes, to match the dynamics of observed by meteor radars (Nesvorný et al., 2010; Pokorný et al., 2014; Soja et al., 2019).

Collisions become important again at short heliocentric distances, where the heightened particle density and velocities increase the collision rate. This causes zodiacal cloud constituents to be ground into a fine dust (i.e., sub-micron collisional fragments) that is then expelled from the solar system by radiation pressure. However, to what extent collisions or other near-Sun loss mechanism (especially sublimation, e.g., Mukai and Yamamoto, 1979; Kobayashi et al., 2009) contribute to the eventual destruction of zodiacal dust is still a matter of debate (see review by Mann et al., 2004).

## Resonances

Another intricate aspect of the dynamics of cosmic dust in the solar system is the presence of mean-motion resonances (MMRs). When a particle moves in a heliocentric orbit with a period that is a rational fraction of that of a planet (e.g.,  $T_{\text{particle}}/T_{\text{planet}} = 5/4$ ), both bodies will periodically assume the same relative position with respect to each other, leading to a repeating gravitational interaction of similar magnitude and geometry. This state is referred to as a MMR. The recurrent pull on the particle, although each individual interaction may be relatively weak, can have a cumulative (and thus significant) effect on its orbit. MMRs may have a stabilizing or destabilizing effect, such that particles can be trapped in the resonance (i.e., the dispersion by other perturbations is counteracted), or conversely, be driven away from the resonance, causing a swift change of orbital elements. For particles that are affected by a dissipative force, such as PR drag, external MMRs (i.e., those where particles have semi-major axes larger than that of the planet) are generally stabilizing, while internal MMRs (i.e., those where particles have semi-major axes smaller than that of the planet) tend to be destabilizing.

As particles migrate inward under PR drag from initial semi-major axes usually much larger than that of the Earth, their steadily shrinking orbits successively assume resonant periods with the planets. This gives them the chance to become trapped at each encountered MMR. This is depicted in Figure 2.9, showing the evolution of the semi-major axis and eccentricity of exemplary particles

originating in the asteroid belt. Once trapped, the resonance counteracts the energy loss by PR drag, allowing a constant semi-major axis to be maintained.<sup>6</sup> The eccentricity, on the other hand, increases, leading the particles onto planet-orbit-crossing trajectories, where a close encounter with the planet eventually causes the resonance to end.

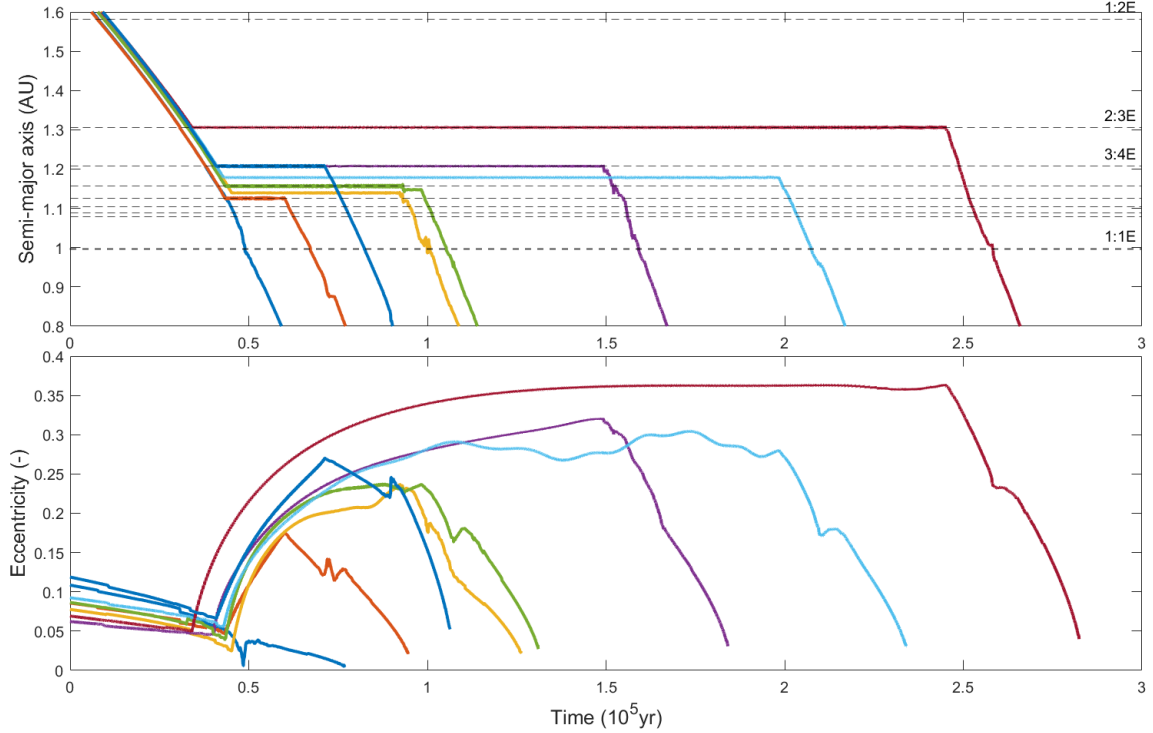


**Figure 2.9.:** Evolution of semi-major axis and eccentricity of exemplary particles becoming trapped in MMRs with Earth. Dashed lines indicate the semi-major axis levels of certain MMRs. The 8 particles were propagated numerically considering Sun & Earth gravity, radiation pressure, and PR drag (at  $\beta=0.01$ ).

Due to their trapping or displacing behaviour, MMRs can have a considerable impact on the density distribution within the zodiacal cloud. Since the semi-major axes corresponding to the most effective trapping MMRs are stacked up in a region just outside the orbit of the planet (roughly between 1.1–1.3 times the planet’s semi-major axis), particles could be expected to accumulate at those distances from the Sun. This was first suggested by Gold (1975), although the effect was more thoroughly characterized by numerical simulations conducted by Jackson and Zook (1989) and Dermott et al. (1994), who coined the term ‘resonant ring’ for the resulting circumsolar, toroidal density enhancement. The existence of such rings near the orbits of Venus and Earth (albeit tenuous and diffuse) has been confirmed by visual and infrared observations of the zodiacal light (e.g., Reach et al., 1995; Leinert and Moster, 2007; Jones et al., 2013), while they continue to be subject of observational and theoretical research. Recently, Sommer et al. (2020) investigated how neighbouring planets (such as those in the inner solar system) interfere with each other’s ability to form these resonant structures.

<sup>6</sup>More correctly, the semi-major axis librates around a constant mean value.

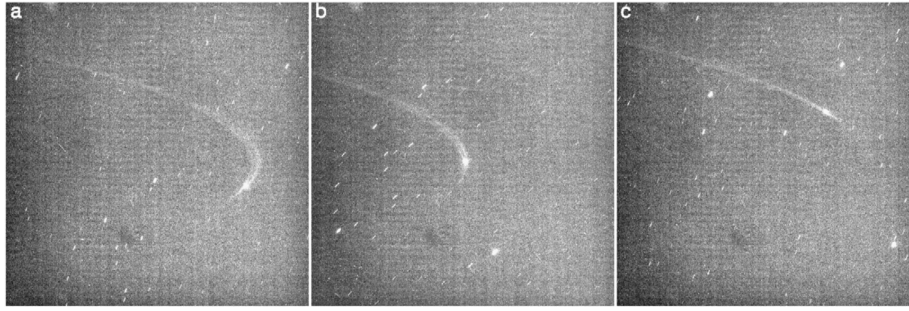


**Figure 2.10.:** Resonant cosmic dust can also be found at more distant places in the solar system. Shown here is the Anthe Ring Arc, a narrow ring of dust particles in the orbit of Saturn’s moon Anthe, confined in azimuthal extent by a 10:11 resonance with the moon Mimas. Taken from Hedman et al. (2009).

### 2.3. Relevance for spaceflight

Cosmic dust is a ubiquitous phenomenon in the solar system, and as such, it is also an aspect that needs to be considered in the context of spaceflight. Covering the surfaces of many planets, moons, and small bodies of the solar system, dust is an infamous factor affecting nearly every surface mission. In particular lunar surface dust became a major concern during the Apollo era, causing a wide range of problems for spacecraft and astronauts alike—a result of the particles’ sharp-edged shapes (due to the absence of weathering) coupled with a strong adhesiveness. These problems include the impairing of spacecraft component functioning (Katzan and Edwards, 1991), as well as skin irritation, and breathing and vision problems for astronauts (Linnarsson et al., 2012). On bodies with considerable dust transport, such as Mars, atmospheric dust deposits onto solar panels and other functional surfaces over time (Perko et al., 2012; Lorenz et al., 2021), having caused the final demise of the Opportunity rover (Callas et al., 2019). Surface dust on small solar system bodies is also of concern, as in the case of Hayabusa2, where dust swirled up by thruster operations during sample collection contaminated the optics of its navigation cameras (Kouyama et al., 2021; Ogawa et al., 2022). These circumstances have prompted a number of studies on technological and operational mitigation techniques for prospective surface exploration missions (e.g., Wagner, 2006; Sharma et al., 2009; Manyapu et al., 2017; Hirabayashi et al., 2023).

However, also orbital dust poses a hazard for spaceflight. With the large impact velocities involved (of up to 10s of  $\text{km s}^{-1}$ ), even micron-sized grains can degrade functional spacecraft surfaces (such as solar panels and radiators, Grossman et al., 2010), damage exposed sensitive elements (such as the imaging sensors of X-Ray telescopes, Carpenter et al., 2008; Li et al., 2022), and cause electrical anomalies aboard spacecraft (Goel and Close, 2015). In one occurrence, the latter effect is thought to have caused the loss of a communications satellite (Caswell et al., 1995).

A special case for concern are the high-density dust environments of cometary comae. During the perihelion activity of comet 67P/Churyumov-Gerasimenko, the Rosetta spacecraft’s star trackers were increasingly unable to determine the spacecraft’s attitude, due to the obscuration of the star field by dust particles. This prompted the spacecraft operators to increase the distance to the comet significantly and to adopt a new, more dynamic science planning scheme that allowed for quicker responses to the changing conditions (Costa et al., 2016b).

Clearly, understanding cosmic dust is not just a scientific endeavour, but also a vital prerequisite for safe and successful space missions. As we expand our presence in the solar system, the knowledge

---

we gain about dust behaviour and properties directly informs spacecraft design and mission planning. Therefore, the field of cosmic dust represents a critical intersection of science and engineering in the realm of space exploration.



## 3. Mission Aspects

This chapter discusses aspects of the DESTINY<sup>+</sup> mission that are relevant to the analysis of DDA’s scientific potential and the planning of its operations. These include the spacecraft’s trajectory and attitude profile across different mission phases, the surrounding radiation environment, and specifics related to spacecraft communication.

### 3.1. Mission phases and trajectory

The DESTINY<sup>+</sup> mission design foresees a number of operationally diverse mission phases, carefully composed to reach Phaethon with the spacecraft’s low-thrust propulsion system starting from an Earth-bound orbit. To assess the scientific potential of DDA in the respective phases, an understanding of their orbital and operational conditions is required. In the following, we present the different phases of the current baseline mission scenario.<sup>1</sup>

#### Launch & early in-orbit phase

DESTINY<sup>+</sup> will be launched from the Uchinoura the Space Center (USC) in Kagoshima, Japan, located at the very south of the Kyushu island (latitude 31.25°N). The USC acts as Japan’s spaceport for suborbital and small-class orbital launch vehicles, in particular for the now-retired M-V rocket, which has launched several Japanese scientific spacecraft, such as the *Hayabusa* mission—the first-ever asteroid sample return (Yoshikawa et al., 2021). DESTINY<sup>+</sup> will be carried to space by the *Epsilon* rocket (specifically, the *Epsilon S* variant) the direct successor of the M-V. With the use of an additional solid-rocket-motor kick-stage, DESTINY<sup>+</sup> will be released into an eccentric Earth orbit (similar to a geosynchronous transfer orbit) with perigee & apogee altitudes of around 230 km × 37,000 km, and an inclination of 31°. The spacecraft will remain in this initial orbit (which has an orbital period is 10 h) for one month, completing system checkout procedures. The current baseline scenario foresees a launch in Q1 2025.

#### Spiralling phase

After completing the initial checkout, DESTINY<sup>+</sup> begins a prolonged period of orbit raising, called the spiralling phase. Using its solar-electric propulsion system, the spacecraft gradually spirals up, aiming to lift its apogee towards the lunar orbit. The spiralling phase takes approximately 22 months and concludes upon reaching an intercept course with the Moon.

The spiralling phase is subdivided into two parts. For the first eight months DESTINY<sup>+</sup> will employ continuous thrusting, with the goal of raising its orbit as fast as possible, minimizing the

---

<sup>1</sup>For a detailed description of the mission design, see Ozaki et al. (2022a). The here presented trajectories correspond to scenario ‘Case #5’ therein.

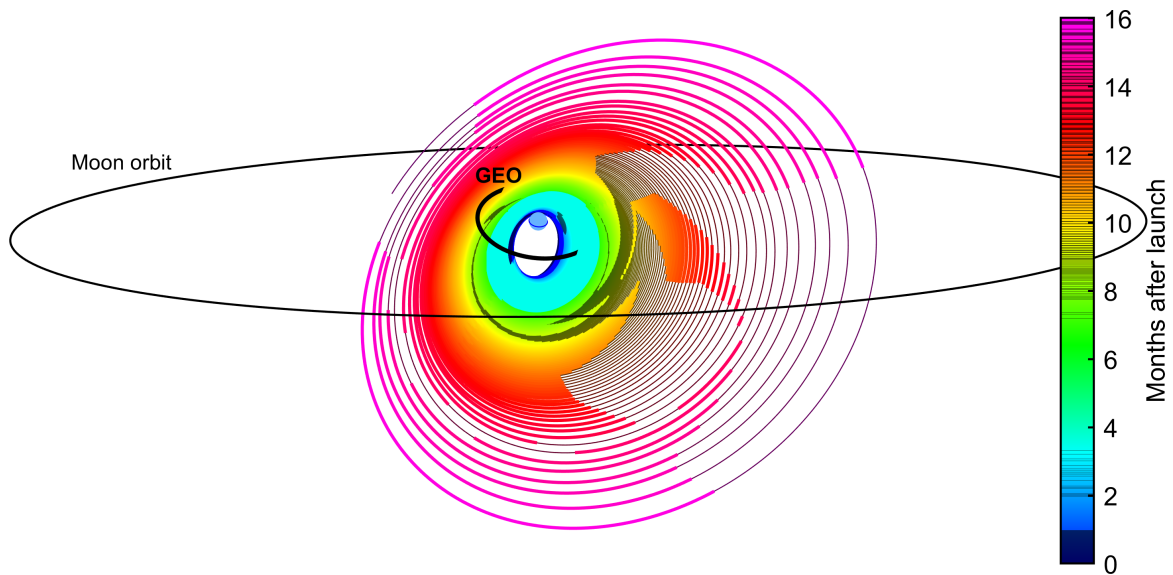


**Figure 3.1.:** Spiralling phase trajectory. Thick lines indicate thrusting arcs, thin lines indicate coasting arcs. Also indicated are the geostationary orbit and the Moon’s orbit.

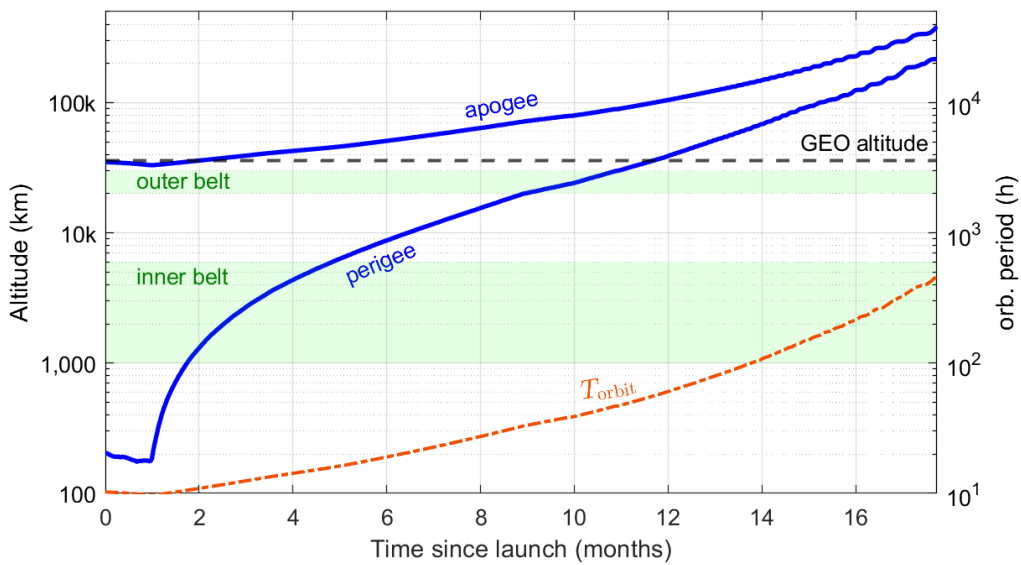


**Figure 3.2.:** Spiralling phase evolution of apses altitude and orbital period. Also indicated are the densest regions of the inner and outer radiation belts (green) and the altitude of the geosynchronous orbit (dashed line).

total time spent inside the Van Allen belts (see also Section 3.4). This is to protect sensitive spacecraft components, such as solar cells, integrated circuits, and sensors, which degrade under the energetic particle radiation. During this radiation belt escape phase, thrusting is only interrupted by periods where the spacecraft moves through the Earth’s shadow (hence lacking power to drive its ion engines). Once the spacecraft has lifted its perigee out of the inner radiation belt, the second part of the spiralling phase begins, during which thrusting is optimized towards more propellant-efficient apogee raising.

### Lunar gravity assist phase

In order to build enough momentum to escape the Earth-Moon system (EMS), DESTINY<sup>+</sup> conducts a series of lunar gravity assist manoeuvres, separated in time by up to several months.<sup>2</sup> The lunar gravity assist phase covers the period from the spacecraft's first entering the lunar sphere of influence until its escape from the EMS. In the baseline scenario presented here, three lunar flybys are foreseen. The first lunar flyby, LFB-1 transfers the spacecraft from its eccentric Earth orbit to a near circular Earth orbit with high inclination, leading the spacecraft through the northern hemisphere of the EMS. The second lunar flyby, LFB-2, sends the spacecraft to a far-out, loosely bound excursion, up to 1.2 Mkm away from Earth. Upon return, LFB-3 finally transfers the spacecraft to an escape trajectory in the anti-sunward direction.

The lunar flybys in the baseline scenario occur between late January and early April 2027: LFB-1: January 24; LFB-2: February 7; LFB-3: April 8.

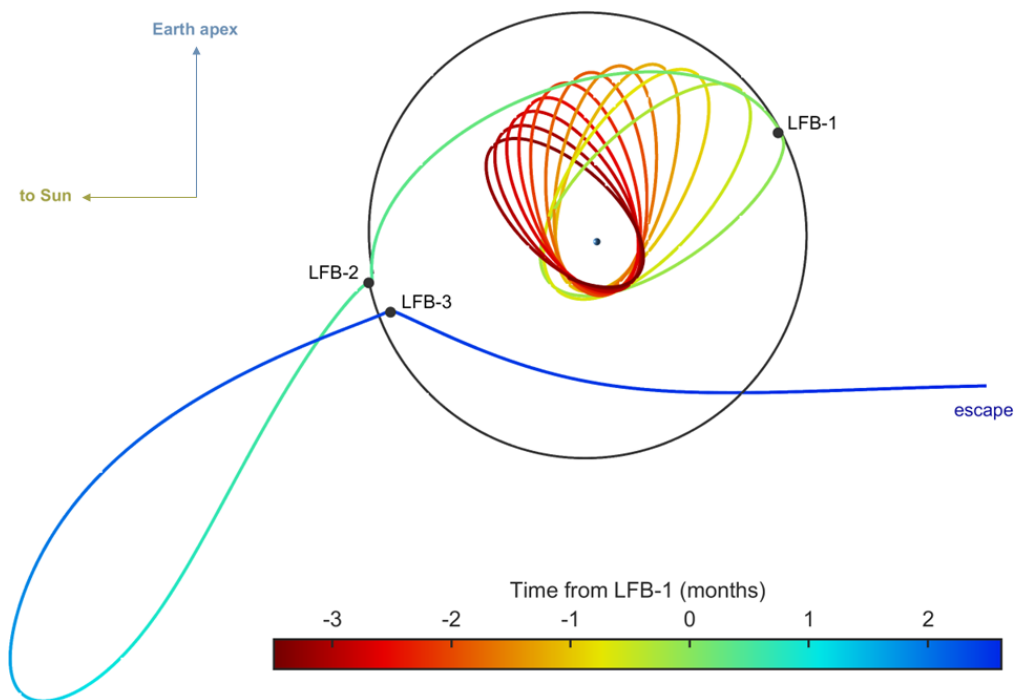


**Figure 3.3.:** Earth centred view of the Lunar gravity assist phase trajectory, including the last few orbits of the spiralling phase.

### Interplanetary cruise phase

After leaving the EMS, the interplanetary cruise phase begins, which is characterized by prolonged thrusting and unthrusting flight periods. In its moderately eccentric orbit ( $e \approx 0.1$ ), DESTINY<sup>+</sup> will begin trailing the Earth up to a maximum distance of 0.36 au (see Figure 3.4). Two thrusting arcs are foreseen in this scenario of about 5.5 months and 1 month, respectively (see Figure 3.5). Only the first thrusting arc occurs in the period before the Phaethon flyby. The second thrusting period is conducted after the Phaethon flyby, to ensure that the trajectory leads back to an encounter with

<sup>2</sup>Such an elaborate Earth escape scheme via multiple lunar gravity assists has been employed before by a Japanese spacecraft, namely the Nozomi mission with the goal of reaching Mars. However in that case, this escape scheme was not foreseen in the original mission design, but was improvised after the spacecraft missed its desired Earth escape trajectory due to a malfunction of its chemical propulsion system (Kawaguchi et al., 2003).

Earth, thereby enabling a potential mission extension to another small body flyby with minimal propellant consumption through an Earth gravity assist manoeuvre.

Staying close the ecliptic plane, the spacecraft will encounter Phaethon slightly ahead of its descending node, which is located at 0.87 au from the Sun (Phaethon has an inclination of  $22.3^\circ$ ). The duration of the nominal interplanetary cruise phase will be about 13.5 months, including 9 months from Earth escape until Phaethon flyby, and another 4.5 months until again reaching Earth.

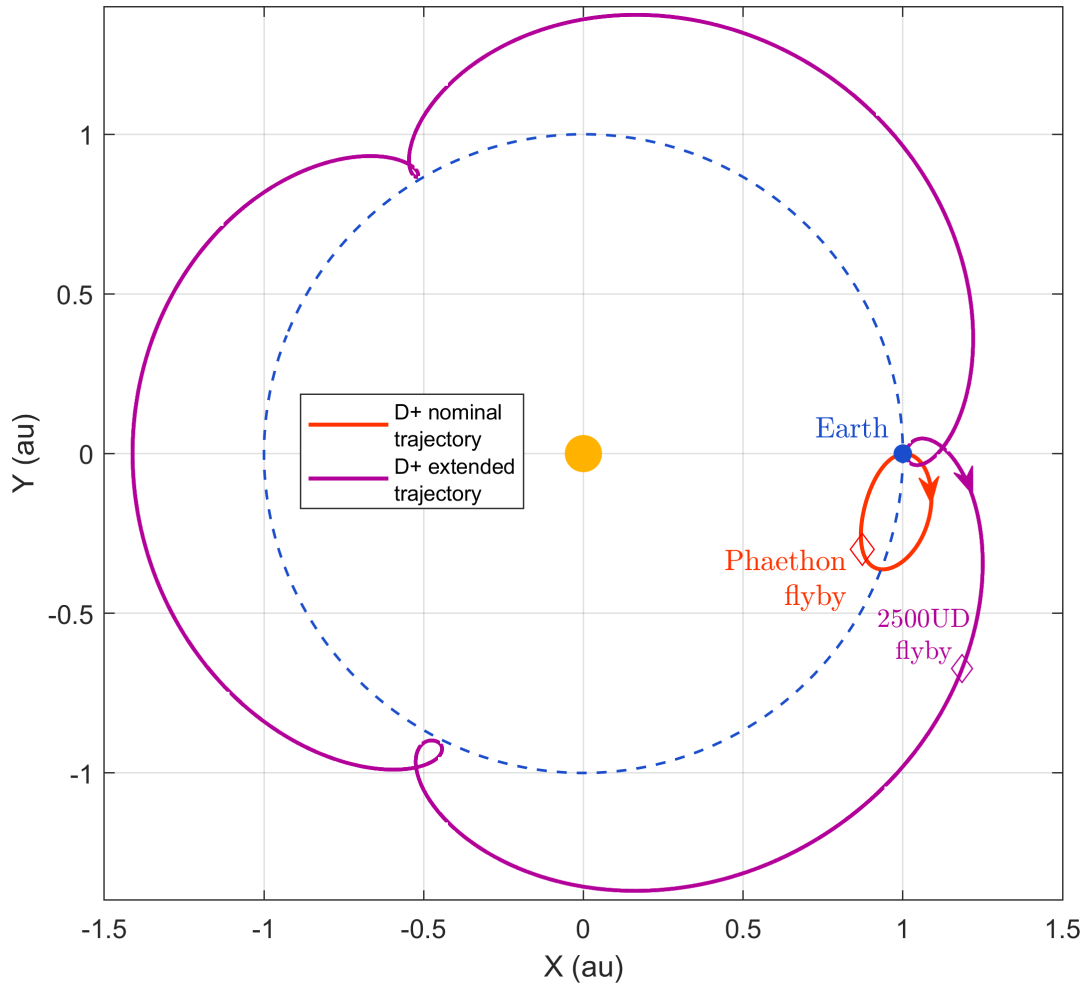


**Figure 3.4.:** Interplanetary trajectory of DESTINY+ in the Earth-co-rotating frame.

### Phaethon Flyby

DESTINY+ encounters Phaethon around 3 years after launch in January 2028. The flyby occurs with a relative velocity of approximately  $34 \text{ km s}^{-1}$  (see Fig. 3.7) and at a targeted flyby distance of 500 km. At the time of the flyby, the distance between Earth and the spacecraft is about 0.32 au. During the flyby all three scientific payloads are active: the two cameras, MCAP and TCAP, as well as DDA.

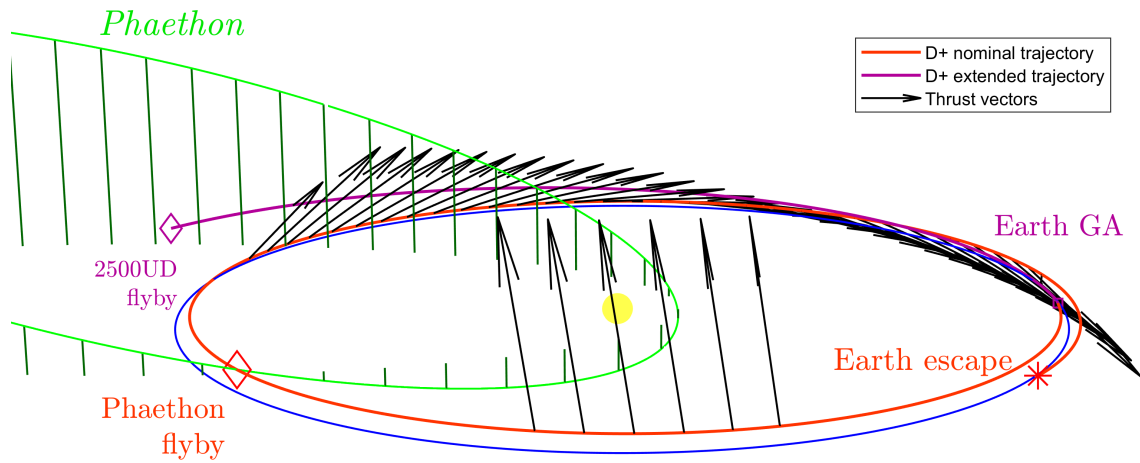


**Figure 3.5.:** Interplanetary trajectory with thrusting phases. Earth orbit is shown in blue.

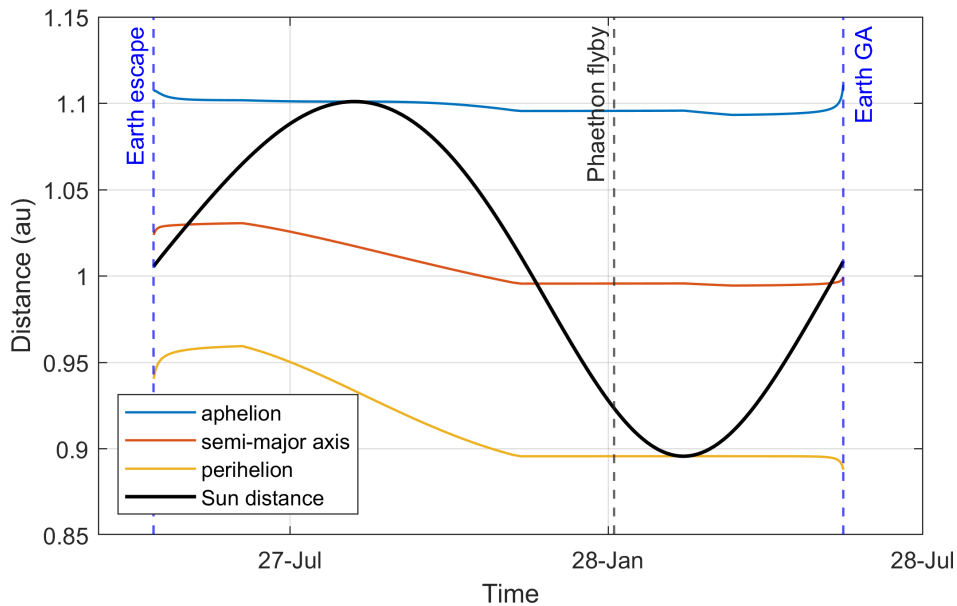


**Figure 3.6.:** Heliocentric distance of DESTINY+ during the interplanetary cruise phase.

### Extended mission

The nominal mission ends with the Earth encounter in April 2028. However, for the case that the spacecraft is still operational at this point, a mission extension is foreseen. Enabled by a gravity assist manoeuvre at Earth, the spacecraft could be put onto an encounter trajectory with another small body. Several options for extended mission targets are currently being considered (Ozaki et al., 2022a). For the current baseline scenario, the intended target is the asteroid 2500 UD, which potentially had a common origin with Phaethon (see Section 1.3.3). To reach 2500 UD, the spacecraft would swing-by the Earth onto a rather eccentric orbit with a considerable aphelion distance near 1.4 au (see Figure 3.8). Furthermore, the extended mission trajectories could be designed in the fashion of an ‘asteroid cyclers’, returning to the Earth after each small body flyby to allow for another Earth gravity assist and yet another flyby target (Ozaki et al., 2022a,b).

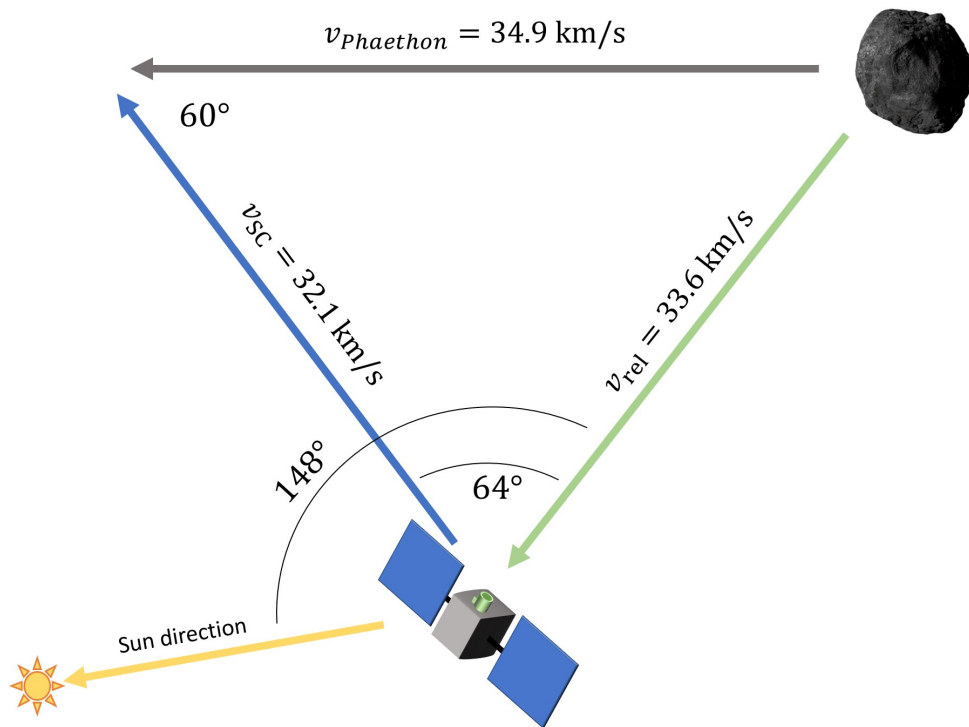


**Figure 3.7.:** Phaethon flyby geometry (spacecraft attitude idealized).

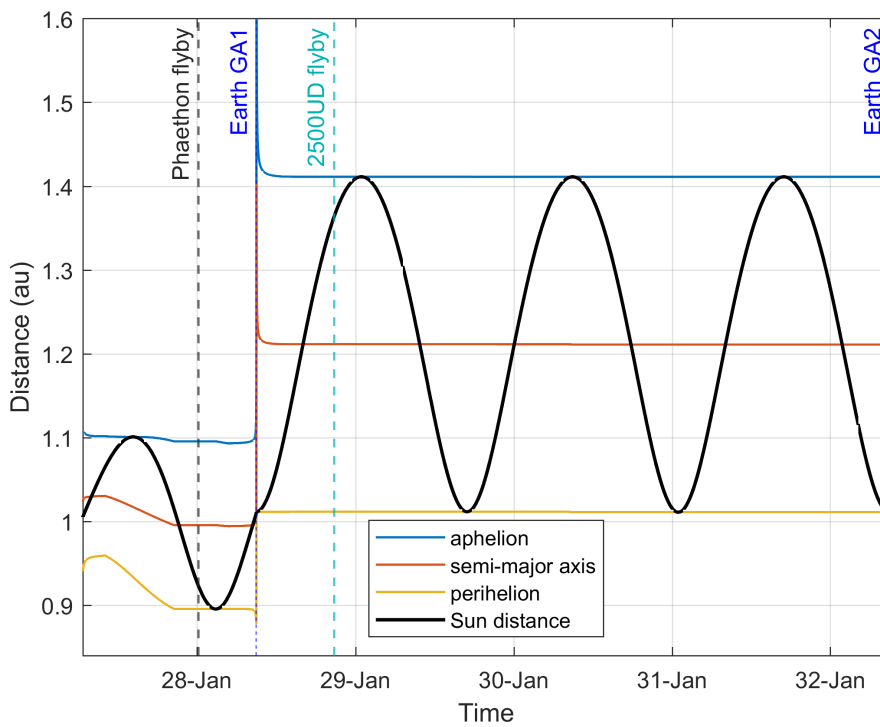


**Figure 3.8.:** Extended mission phase heliocentric distance. Earth-GA1 and Earth-GA2 denote the first and second Earth gravity assist, respectively.

## 3.2. Spacecraft attitude

For the attitude of the DESTINY+ spacecraft two default configurations are foreseen: one for phases of active solar-electric propulsion system thrusting and one for prolonged coasting phases. In the electric propulsion mode, the spacecraft is oriented such that full illumination of the solar panels (i.e., panels pointing normal to the Sun direction) is possible, which is necessary to run the propulsion system at full thrust. This attitude is exemplified in Figure 3.9. (See also Appendix A for a detailed description of the body-fixed spacecraft reference frame.) The spacecraft’s roll angle about the thrust vector (which is parallel the spacecraft  $-X$  axis) is such that the  $Y$ -axis points perpendicular to the Sun direction. Additionally, the  $+Z$  axis shall lie in the anti-sunward hemisphere, such that the radiator-bearing panel of the spacecraft (the ‘ $+Z$  panel’) is never illuminated by the Sun. This determines the spacecraft’s attitude in a way so that the solar panels, which can be actuated about the  $Y$ -axis, can always be oriented to face the Sun at a normal angle. This attitude configuration is used throughout the spiralling phase, and for the thrusting periods during the interplanetary phase.

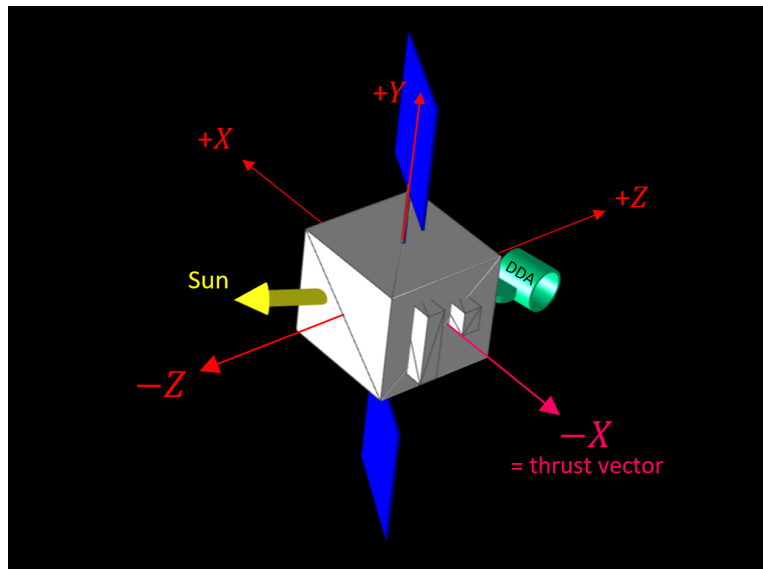


**Figure 3.9.:** Spacecraft attitude configuration during thrusting. The spacecraft roll angle about the thrust vector ( $X$ -axis) is set such that the Sun direction is within the plane spanned by the  $\pm X$  and the  $-Z$  axis of the spacecraft body frame.

In the spiralling phase, the thrust vector is always aligned with the geocentric velocity vector, which changes direction continuously as the spacecraft moves along its orbit. Thus, the spacecraft’s attitude is continuously adjusted to maintain the desired configuration. For periods where angular separation between the thrust vector and the Sun direction is small, which can occur at a low beta angle,<sup>3</sup> this may theoretically require swift roll manoeuvres about the spacecraft  $X$ -axis. This is illustrated in Figure 3.10, which shows the according roll rates about the spacecraft principal axes during the spiralling phase if the attitude configuration were to be strictly maintained. While the beta angle is in a range of  $\pm 10^\circ$ , the roll rate about the  $X$ -axis can reach up to  $0.6^\circ \text{ s}^{-1}$  (and can be even higher depending on the mission scenario). Since the maximum turn rate of the spacecraft is limited to  $0.2^\circ \text{ s}^{-1}$  (Toyota, priv. comm.), a slight deviation from the desired attitude configuration during these periods is expected.

<sup>3</sup>The ‘beta angle’ is defined as the angle between the Sun direction and a geocentric orbital plane.

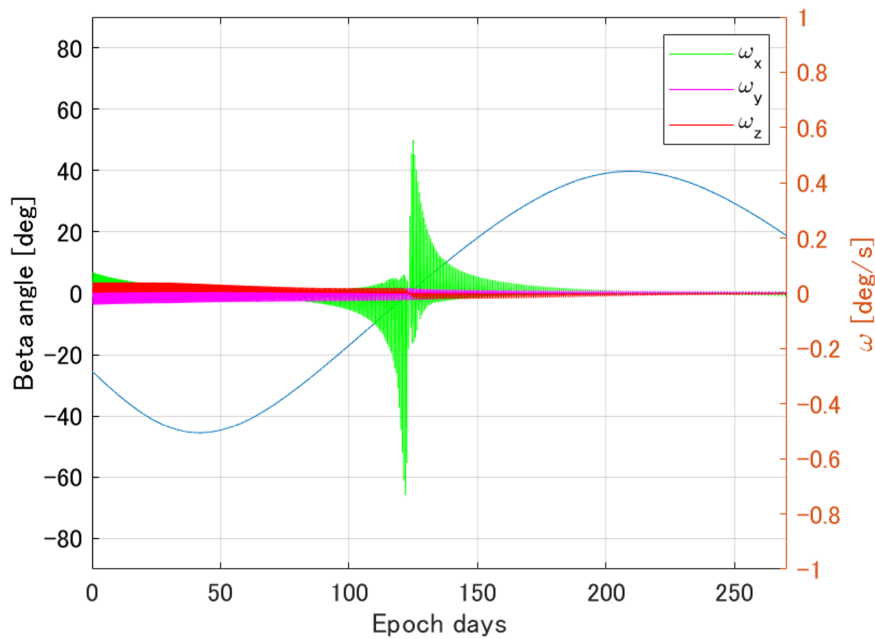


**Figure 3.10.:** Spacecraft beta angle and theoretical roll rates during spiral phase, if the default attitude were to be maintained at all times. The actual roll rates are limited to  $0.2^\circ \text{s}^{-1}$ . Figure received from Hirai (priv. comm.).

On the other hand, the default attitude configuration for prolonged coasting phases, in particular during the coasting in between the lunar flybys is defined as follows: The  $-Z$  axis is aligned with the Sun direction, while the  $-X$  axis will be aligned with the heliocentric velocity vector. This default attitude was requested by the DDA team as it ensures various favourable dust observation directions to be reached solely with the DDA instrument’s pointing mechanism.

### 3.3. Spacecraft communication

DESTINY<sup>+</sup> carries two antennas for communication with ground stations on Earth: a low-gain antenna (LGA) and a medium-gain antenna (MGA). Communication through the LGA requires no specific spacecraft attitude, but is limited to a low data rate. The MGA, which allows higher-bandwidth communication, features a two-axis pointing mechanism enabling it to point in any direction over the ‘ $-Z$  hemisphere’ (i.e., the hemisphere whose zenith is the  $-Z$  axis of the spacecraft body frame).

Downlink is planned to be performed for 4 hours per day, 5 days a week throughout the mission. Given the MGA’s pointing capability, the communication phases are not expected to require significant changes of the spacecraft attitude. Consequently, with regard to spacecraft attitude, the communication phases are not taken into consideration in the science analysis presented herein.<sup>4</sup>

<sup>4</sup>In an earlier development phase of the DESTINY<sup>+</sup> mission, the MGA was intended to be mounted on a one-axis pointing mechanism. This would have required the spacecraft to be reoriented between communication and certain science activities (which, in turn, would have caused a reduction of observation time). However, this design was then abandoned in favour of the two-axis mechanism.

---

### 3.4. Radiation environment

An important factor for the operation of DDA during the early phase of the mission is the radiation environment of the Earth's magnetosphere. Compared with more conventional mission designs, the gradual orbit raising of the DESTINY<sup>+</sup> spacecraft causes a prolonged exposure to the Earth's Van Allen belts and thus relatively high total radiation doses. The Van Allen belts are two toroidal zones with high concentrations of energetic charged particles trapped by the Earth's magnetic field. Although DDA is equipped with high-voltage screening grids to prevent solar wind particles from entering the detector, these cannot deflect the trapped particles of the radiation belts, which have energies of up to 100 MeV (protons in the inner belt) and several MeV (electrons in the outer belt), respectively. These particles can hit the ion detector of the mass spectrometer, potentially causing highly saturated and thereby performance-degrading signals. This is especially problematic due to the exposed position of the ion detector, required for the reflectron-type ion optic configuration.<sup>5</sup> Therefore, it is foreseen to operate the ion detector in a low-gain mode (potentially with integrating readout instead of single pulse counting, as done with CDA) during critical mission phases. Switching off of the ion detector may be necessary during passage of the most intense regions of the radiation belts (especially that of the inner belt), which are located at (variable) altitudes of roughly 1000–6000 km and 20,000–30,000 km, respectively (Van Allen, 1959; Ganushkina et al., 2011). Measurements may thus be impaired or impossible during those periods.

---

<sup>5</sup>DDA's exposed ion detector design is contrary to the more shielded configuration of the CDA instrument with linear ion optic, which may be more suited for high-radiation environments (e.g., Kempf et al., 2012).



## 4. Instrument Aspects

This chapter describes aspects of the DDA instrument that are relevant to the analysis of its scientific potential and the planning of its operations.

### 4.1. Instrument mounting

DDA is situated on the ‘+Z panel’ of the spacecraft body, which is the panel opposite to the launch-adaptor-bearing panel (the ‘top’ panel in the launch-stowed configuration, see also Figure A.2).<sup>1</sup> There, it is mounted on a two-axis pointing mechanism (PME), as depicted in Figure 4.1, allowing for some pointing autonomy from the spacecraft attitude, which is determined by operational factors during large parts of the mission (see Section 3.2). The PME features a pivot articulation with horizontal rotation axis (i.e., parallel to the +Z panel) mounted on top of a turntable with a vertical (i.e., normal to the +Z panel) rotation axis, which connects the structure to the spacecraft body.<sup>2</sup> This setup is akin to the altazimuth mount used for instance with ground-based optical telescopes. Adhering to the corresponding conventions, the angle set by rotation about the vertical and horizontal axis are referred to as azimuth and elevation, respectively.

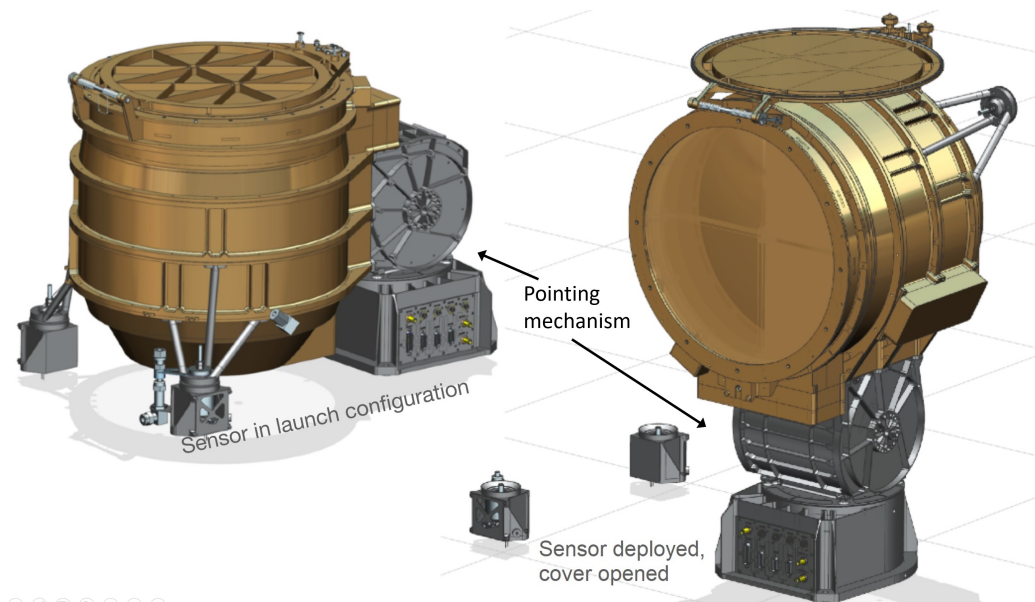


**Figure 4.1.:** The two-axis pointing mechanism of DDA.

The azimuth axis has a range of  $180^\circ$  (from  $-90^\circ$  to  $+90^\circ$ ) centred on the spacecraft’s  $-X$  axis, which is also the thrusting vector of the electric propulsion system. The elevation axis has a range of  $90^\circ$ , from a pointing parallel to the mounting panel ( $0^\circ$ ) to a pointing perpendicular to it ( $90^\circ$ ).

<sup>1</sup>For a description of the spacecraft body-fixed coordinate system, see Appendix A.

<sup>2</sup>For insights into the DDA-PME design and development process, refer to Exle (2023).

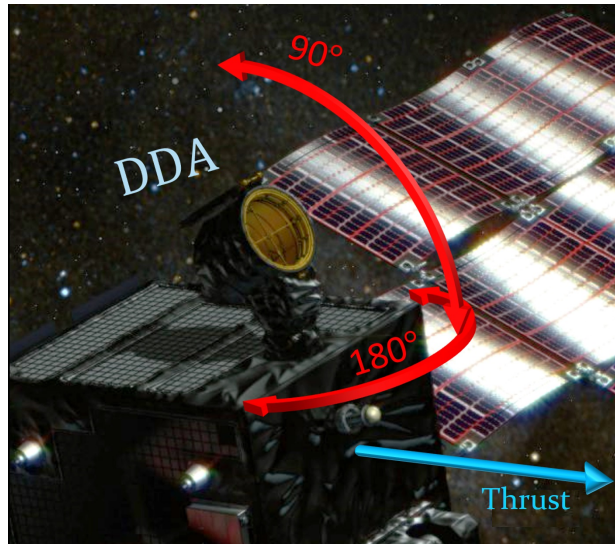


**Figure 4.2.:** Coverage range of the DDA pointing mechanism.

Together, the two axes allow for coverage of 1/4th of the sky (a solid angle of  $1 \pi \text{ sr}$ ), see Figure 4.2. During launch, the instrument is stowed in a position at  $-90^\circ$  azimuth and  $90^\circ$  elevation, such that the boresight points normal to the mounting panel. This is also the direction of the dust ram direction during flybys of the target bodies, which will be aligned with the spacecraft  $+Z$  axis.<sup>3</sup> That way, even if the PME were to fail to operate from the beginning of the mission, the instrument would still be able to perform nominal flyby science operations.<sup>4</sup>

The PME is driven by two stepper motors, which rotate the sensor at a speed of approximately  $13^\circ \text{ min}^{-1}$  in each axis, which is fast enough to be considered instantaneous for the purposes of this study. The PME is designed to reorient the sensor intermittently rather than continuously, as the articulation may impair the highly sensitive measurements of DDA in an unpredictable way. The PME has been tested to perform at least 12,000 actuations, which suffices for roughly hourly (on average) reorientation of the instrument during the attitude-dynamic spiralling phase of the mission.<sup>5</sup>

## 4.2. Sensor geometry

To assess DDA's ability to collect dust of various types, it is necessary to understand the geometry of the detector. One important measure is the nominal sensitive area,  $A_0$ , of the instrument, which is the sensitive area exposed by the instrument to a collimated incident flux normal to the instrument boresight. This is significantly less than the total sensitive area of the gold-coated target plate, due to the number of grid electrodes inside the instruments that particles have to pass before reaching the impact target. With a total transmittance of the seven grids of about 61%, the total target plate area of  $500 \text{ cm}^2$  is reduced to a nominal sensitive area  $A_{0,\text{DDA}} = 302 \text{ cm}^2$ .<sup>6</sup> The nominal sensitive

<sup>3</sup>This orientation is also required for the science operations of the cameras (see Ozaki et al., 2022a).

<sup>4</sup>The transformation from boresight vector pointings to azimuth/elevation combinations as well as exemplary vectors and their corresponding angles are given in Equation A.1 and Table A.1.

<sup>5</sup>The less frequent sensor reorientations during the interplanetary cruise, where the spacecraft attitude is rather static, are no determining factor here, yet are anticipated to occur up to every few days.

<sup>6</sup>The target plate has an annulus shape with an outer radius of 131 mm and an inner cutout radius of 35.5 mm, to accommodate the ion detector.

area, however, lacks information about the acceptance of particles approaching the instrument at an angle to the boresight. In the case of the rotationally symmetric DDA sensor, the exposed sensitive area  $A$  toward a certain direction is a function only of the incidence angle  $\theta$  (i.e., the angle to the boresight), determined by the instrument design. For DDA, an accurate representation of  $A(\theta)$  can be found by ray tracing methods, the result of which is shown in Figure 4.3. With increasing  $\theta$ , the sensitive area of DDA drops steeply to  $0.5 A_0$  at  $\theta \approx 17^\circ$ , and  $0.33 A_0$  at  $\theta \approx 24^\circ$ .<sup>7</sup> At the maximum acceptance angle,  $\theta_{\max} \approx 45^\circ$ , the sensitivity becomes zero.

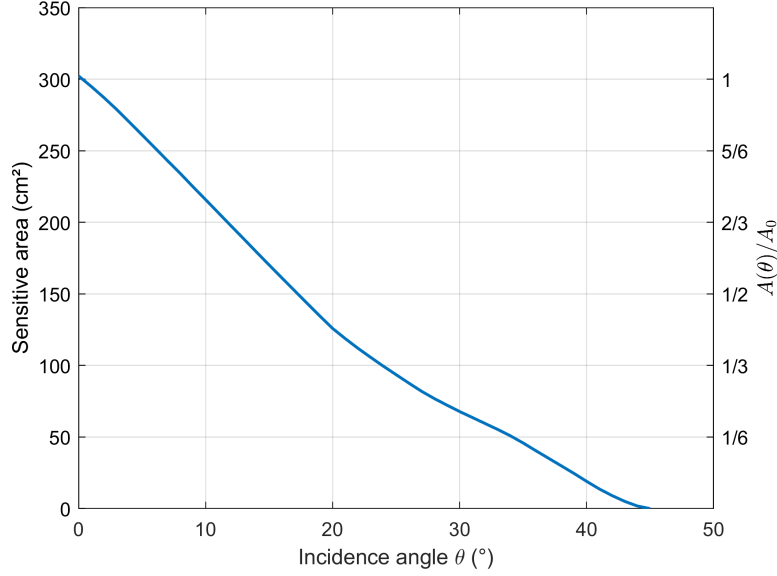


**Figure 4.3.:** The effective sensitive area of DDA as a function of incidence angle  $\theta$  (computed by Srama, priv. comm.).

A single-value parameter that can be derived from  $A(\theta)$  is the effective solid angle  $\Omega_{\text{eff}}$ , which is a measure to describe a detector's sensitivity to off-axis impactors. It may be thought of as the FOV a hypothetical detector with uniform sensitivity across its entire FOV would need in order to match the actual detector's overall ability to detect particles. To find  $\Omega_{\text{eff}}$  we first define the angular detection efficiency  $\eta$  as:

$$\eta(\theta) = \frac{A(\theta)}{A_0} \quad (4.1)$$

and the solid angle interval, which, for an axial symmetric detector, is:

$$d\Omega = \sin \theta \, d\theta \, d\varphi \quad (4.2)$$

where  $\varphi$  is the azimuthal incident angle. The differential effective solid angle is calculated as:

$$d\Omega_{\text{eff}} = \eta \cdot d\Omega \quad (4.3)$$

Then,  $\Omega_{\text{eff}}$  is obtained by integration of  $d\Omega_{\text{eff}}$  over the entire FOV of the instrument:

$$\Omega_{\text{eff}} = \int_0^{2\pi} \int_0^{\theta_{\max}} \eta(\theta) \sin \theta \, d\theta \, d\varphi \quad (4.4)$$

<sup>7</sup>Compare this to typically less steep angular sensitivity functions of other dust detectors, e.g., HEOS-2 (Hoffmann et al., 1975b, Fig. 2), LDEX (Szalay, 2015, Fig. 2.4), Ulysses (Grün et al., 1992b, Fig. 4).

For DDA, we find  $\Omega_{\text{eff}} = 0.48 \text{ sr}$ .

Finally, we can derive a characteristic that includes the detector's ability to detect impactors from off-axis directions, as well as the dimension of the sensitive area. This is the geometric factor  $G$ , obtained simply by:

$$G = A_0 \cdot \Omega_{\text{eff}} \quad (4.5)$$

which yields  $G_{\text{DDA}} = 144 \text{ cm}^2 \text{ sr}$ .<sup>8</sup> As a key instrument parameter, the geometric factor directly describes the gathering power of the detector with respect to an isotropic flux, that is, it relates the intensity of the flux to the resulting incidence rate onto the detector. We may now scale fluxes observed by different instruments by the ratio of their geometric factors to obtain comparable incidence rates.

Table 4.1 presents a comparison of the geometric characteristics derived herein for various flown (and prospective) impact plasma detectors, and relates them to those of DDA. Among its relatives, DDA notably exhibits a rather low  $\Omega_{\text{eff}}$ , which results from its elongated, bucket-like design, having to accommodate the trajectory sensor as well as mass analyser reflectron. However, this can be seen as a trade-off of measurement quality vs. quantity. While a lower  $\Omega_{\text{eff}}$  implies a lower sensitivity to off-axis impactors, and thus, lower overall fluxes, it already provides valuable directional information, simply by the limited FOV covered. Compared to the dust detector onboard Galileo, DDA achieves a threefold improvement in impactor directionality constraint, solely through the different aperture design.

Table 4.1 also lists entries denoted 'DDA (single TS segment)' and 'DDA (aperture)'. The former gives the geometric characteristics for the case where only an incidence through one of the four trajectory sensor (TS) segments is considered, resulting in 1/4th the solid angle and geometrical factor of the full detector. The latter considers essentially a plate detector with an area equal to the aperture area (i.e., opening area) of DDA. This is useful for estimating the number of grid and wall impacts that can be expected. For in isotropic flux, wall impacts would be about one order of magnitude more frequent than target impacts ( $G_{\text{DDA,aperture}}/G_{\text{DDA}} \approx 14$ ), although it is not clear yet whether these will be consistently detectable by DDA.<sup>9</sup>

Lastly, we may additionally consider the probability of impacts occurring under a certain incident angle, in the presence of an isotropic flux. The joint, angular impact probability density function  $p$  is given by the derivative of  $d\Omega_{\text{eff}}$  (Equation 4.3):

$$p(\theta, \varphi) = \frac{d^2\Omega_{\text{eff}}(\theta, \varphi)}{d\theta d\varphi} = \frac{\eta(\theta) \cdot \sin \theta d\theta d\varphi}{d\theta d\varphi} = \eta(\theta) \cdot \sin \theta \quad (4.6)$$

From there, we find the marginal probability density function by integration over  $\varphi$ :

$$p(\theta) = \int_0^{2\pi} p(\theta, \varphi) d\varphi = \int_0^{2\pi} \eta(\theta) \cdot \sin \theta d\varphi = 2\pi \cdot \eta(\theta) \cdot \sin \theta \quad (4.7)$$

<sup>8</sup>See also Fröhlich (2021, student project), who arrived at a similar figure by pure Monte Carlo technique.

<sup>9</sup>The detector's response to wall impacts has not yet been fully investigated. With the impact plasma detectors of Ulysses or Cassini, wall impacts appeared to be detectable at nearly the same sensitivity as target impacts (Stübig, 2002; Altobelli et al., 2004). Considering the less consistent behaviour of wall-impact plasmas within DDA's reflectron ion optics, it is not clear yet whether this will be the case here. Calibration campaigns testing the detector's response to wall impacts may be conducted in the future.

as well as the cumulative distribution function:

$$P(\theta) = \int_0^\theta p(\theta) d\theta = 2\pi \int_0^\theta \eta(\theta) \cdot \sin \theta d\theta \quad (4.8)$$

Figure 4.4 shows  $p(\theta)$  and  $P(\theta)$  for the DDA detector. From these functions, we can also derive a set of informative angles, the mode, median, and mean: The mode, that is the angle of peak impact probability,  $\theta_{f=\max}$ , is simply the angle at which the  $p(\theta)$  reaches its maximum. For DDA, that is  $\theta_{f=\max} = 16.8^\circ$ . The median angle,  $\theta_{\text{median}}$ , separates the probability distribution into two equal halves, meaning that 50% of impacts occur at angles below  $\theta_{\text{median}}$ , and 50% occur at angles above  $\theta_{\text{median}}$ . For DDA,  $\theta_{\text{median}} = 20.3^\circ$ . Finally, the average impact angle,  $\theta_{\text{mean}}$ , is obtained by integrating  $p(\theta)$ , weighted by the angle itself, over the full range of  $\theta$ :

$$\theta_{\text{mean}} = \int_0^{\theta_{\max}} \theta \cdot p(\theta) d\theta \quad (4.9)$$

For DDA, this yields  $\theta_{\text{mean}} = 20.8^\circ$ .

Note, however, that these angles are only valid for an isotropic flux, and that the actual flow of dust is expected to exhibit anisotropy to varying degrees, depending on the type of dust considered (see Chapter 5). Nevertheless, these angles serve as valuable measures to guide our intuition about the behaviour of the DDA detector.

**Table 4.1.:** Geometry comparison of impact plasma detectors.

Instrument	$A_0$ cm <sup>2</sup>	$A_0/A_{0,\text{DDA}}$ —	$\theta_{\max}$ °	$\Omega_{\text{eff}}$ sr	$G$ cm <sup>2</sup> sr	$G/G_{\text{DDA}}$ —
Plate detector (1 m <sup>2</sup> )	10,000	33.1	90	3.14	31,416	218
Galileo <sup>*</sup>	1000	3.31	70	1.45	1450	10.1
CDA-IID <sup>•</sup>	860	2.85	45	0.59	507	3.5
CDA-CAT <sup>•</sup>	170	0.56	28	0.47	80	0.26
DDA	302	1	45	0.48	144	1
DDA (single TS segment)	302	1	45	0.12	36	0.25
DDA (aperture)	647	2.14	90	3.14	2032	14.1
IDEX <sup>§</sup>	600	1.99	50	0.77 <sup>**</sup>	461 <sup>**</sup>	3.2
HEOS-2 <sup>†</sup>	95	0.32	60	1.03	98	0.68
Helios (ecliptic) <sup>i</sup>	54	0.18	65	1.04	57	0.39
Helios (south/north) <sup>i</sup>	67	0.22	73	1.39	92	0.64
LDEX <sup>‡</sup>	76	0.25	68	1.09 <sup>**</sup>	83 <sup>**</sup>	0.27
Pion. 8 (TOF evnt.) <sup>□</sup>	94	0.31	27	0.42	39	0.13
Pion. 9 (TOF evnt.) <sup>□</sup>	74	0.25	27	0.45	33	0.11
MDC/Hiten <sup>*</sup>	100	0.33	74	2 <sup>**</sup>	200 <sup>**</sup>	1.4
MDC/Nozomi <sup>ˆ</sup>	131	0.43	89	2.56	335	2.3

<sup>\*</sup> Values taken/derived from Grün et al. (1992b), GORID & Ulysses detector are equivalent.

<sup>•</sup> Values taken/derived from Srama et al. (2004b).

<sup>§</sup> Values received/derived from Szalay (priv. comm.).

<sup>†</sup> Values taken/derived from Hoffmann et al. (1975b).

<sup>i</sup> Values taken/derived from Grün et al. (1980).

<sup>‡</sup> Values taken/derived from Szalay (2015).

<sup>□</sup> Values taken/derived from Grün et al. (1973).

<sup>ˆ</sup> Values taken/derived from Iglseider et al. (1993)

<sup>ˆ</sup> Values taken/derived from Senger (2007).

<sup>\*\*</sup> Estimated values.

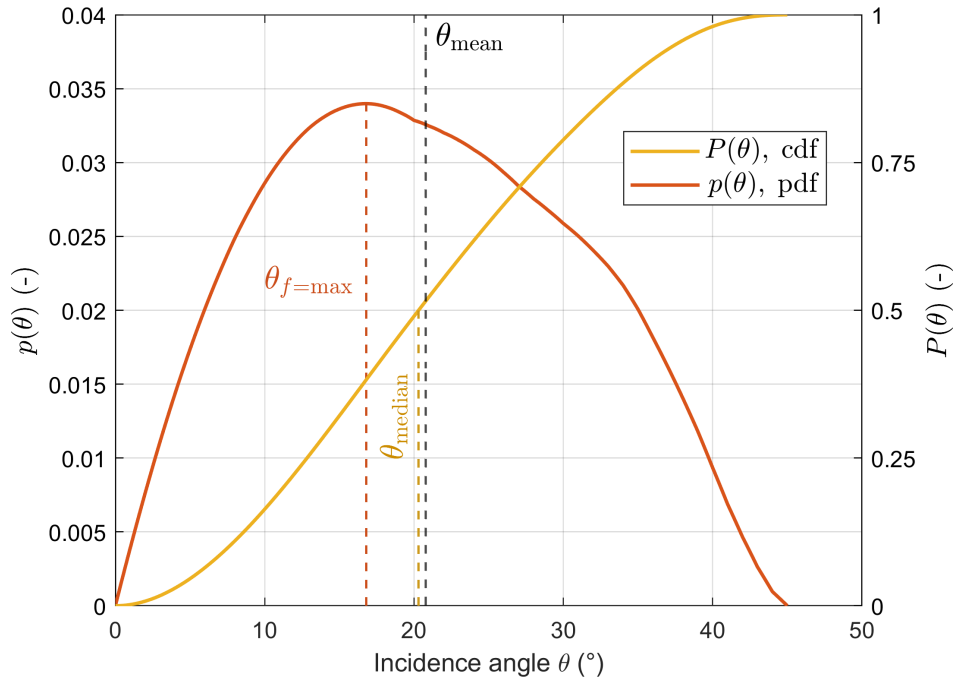


**Figure 4.4.:** The angular impact probability as a function of incidence angle  $\theta$ . Probability density function:  $p(\theta)$ , and cumulative distribution function:  $P(\theta)$ .

### 4.3. Sun and bright body avoidance

One of the paramount constraints of the DDA sensor is the necessary avoidance of direct sunlight in the instrument aperture. For one, sunlight shining on the charge-sensitive electrodes (e.g., those of the trajectory sensor) induces signal noise, as the impinging UV photons cause the emission of electrons via the photoelectric effect. Secondly, there is the apprehension that the radiation can interact with contaminants on the instrument target plate in such a way as to make them difficult to remove, thereby compromising the integrity of the compositional analysis. Thirdly, a large amount of sunlight entering the instrument aperture is thermally unfavourable.<sup>10</sup> Therefore, a flight rule was established, dictating that direct sunlight within the DDA sensor aperture shall be avoided at any time, which means that the angle between the DDA boresight and the Sun direction must not go below  $90^\circ$ . Due to DDA's mounting on the radiator-bearing panel, which is also not to be exposed to direct sunlight by spacecraft flight rule, a 'Sun-safe' position could be defined for DDA, in which sunlight may never enter the instrument aperture (assuming nominal spacecraft operations). The Sun-safe position corresponds to a sensor pointing parallel to the spacecraft +Z axis, that is, any angular state of the PME with an elevation of  $90^\circ$ .

Indirect sunlight (i.e., sunlight reflected from the Earth or the Moon), on the other hand, is less critical. However, it still poses a concern as a potential source of noise through photoelectron production. Thus, we will briefly consider that possibility here. In the Earth's atmosphere, UV-C radiation is almost completely absorbed by the stratospheric ozone, while UV-B is partially absorbed, and UV-A is not absorbed (thus potentially scattered / reflected back into space). DDA's electrode grids, which are made of stainless, have a work function (i.e., a minimum photon energy

<sup>10</sup>Analysis has shown that the temperature of the sensor head structure may rise up to  $105^\circ\text{C}$  in case of direct pointing toward the Sun, which is just  $20^\circ\text{C}$  below the operational limit of the trajectory sensor amplifiers.

---

required to remove an electron from the surface) of around 4.5 eV. This amount of energy is carried by UV-C photons (4.4–12.4 eV), but not by UV-A and UV-B radiation (3.1–3.9 eV and 3.9–4.4 eV, respectively). Thus, we expect that sunlight reflected or scattered back from the Earth, if it enters the instrument aperture, will not cause significant signal noise, due to the filtering of the high-energy UV-C photons.

The Moon, on the other hand, has no absorbing atmosphere and has an albedo in the UV-C in the order of a few percent (Henry et al., 1995; Flynn et al., 1998; Liu et al., 2018). In proximity to the Moon (e.g., during the lunar flybys), reflected sunlight from the lunar surface may, therefore, temporarily impair the performance of the instrument, specifically the sensitivity of the trajectory sensor.

#### 4.4. Cover deployment

To protect the sensor head interior from contamination and damage during ground handling, launch, and the early in-orbit phase, a cover is installed on the DDA sensor aperture. After launch, this cover must be deployed to allow for dust to enter the instrument.<sup>11</sup> However, to avoid contamination of the sensor with outgassing material from the spacecraft, the cover will only be opened after a period of 6–8 weeks after launch, to allow for the outgassing of the spacecraft to subside. During this time the spacecraft’s perigee will have already been raised to approximately 1000 km altitude by the electric propulsion system (see Figure 3.2), precluding the possibility of measurements with DDA below the inner radiation belt.

#### 4.5. Decontamination

To free up volatile contaminants accumulating on the target material over time, the DDA sensor head is equipped with decontamination heaters. These can be activated to heat up the target plate to a temperature of around 100 °C. A decontamination cycle consists of activating the heaters for 10 hours, during which no science activities can be performed. Currently, it is planned to execute a decontamination cycle every 3 months after the cover is released until the end of the mission. Given the infrequency of this procedure, we do not anticipate a significant impact on the science operations.

---

<sup>11</sup>The cover is opened by a release mechanism that is activated by a non-explosive actuator. Contrary to previous instruments of this type, the cover is not jettisoned into space, but remains attached to the sensor head by a hinge. This is to avoid the creation of debris in potentially long-lived Earth orbits, in accordance with the Space Debris Mitigation Guidelines set by the Inter-Agency Space Debris Coordination Committee (IADC).



## 5. Dust Observability Analysis

The design and scheduling of favourable science campaigns for DDA requires thorough analysis of the anticipated cosmic dust populations to be encountered along the foreseen spacecraft trajectory. Such an analysis is presented in this chapter. Incidence and observability of different kinds of dust are assessed qualitatively and quantitatively (that is with respect to their spacecraft-relative dynamics and expectable number fluxes), based on previous measurements, as well as by means of empirical or physical models.

### 5.1. Near-Earth dust

This section addresses the dust populations that are encountered exclusively in the vicinity of the Earth, that is, at altitudes of up to several Earth-radii (or  $\lesssim 100,000$  km). Populations originating outside the Earth-Moon system that are also expected to be present in the near-Earth environment (such as interplanetary dust), are discussed in separate sections. The contents of this section have partially been published in Sommer et al. (2023).

#### 5.1.1. Micro-debris

The dominant component of dust bound to the Earth is artificial in origin: As the only obvious source of particulate matter at moderate altitudes, human activity (whether crewed or robotic) is responsible for the pollution of the near-Earth environment with debris of all sizes. This is supported by the analysis of impactor compositions on retrieved spacecraft surfaces, such as the Hubble Space Telescope solar arrays and satellite thermal control elements, showing that, in LEO, the debris dust flux dominates over the flux of natural dust (Laurance and Brownlee, 1986; Graham et al., 2001; Kearsley et al., 2005). For instance, artificial micron-sized dust is known to be generated in large amounts by solid rocket motors (SRMs). SRMs typically use aluminium as the primary fuel component, which is oxidized in the combustion process. The produced aluminium-oxides leave the motor nozzle mainly in the form of solid, fine-grained  $\text{Al}_2\text{O}_3$  particles with sizes in the submicron to micron range (Akiba and Inatani, 1990; Geisler, 2002), which are referred to as metal oxide smoke or SRM dust. SRM firings at LEO altitudes typically produce sub-orbital dust that reenters the atmosphere promptly (except for historic retrograde burns, which produced orbital dust that could take months to reenter, see Stabroth et al., 2008). Yet, solid-propellant apogee motors, which are used for the orbital insertion of GEO-satellites, are fired at GEO altitudes such that they can produce dust with high enough perigee as to be less effectively deorbited by atmospheric drag (Mueller and Kessler, 1985). Moreover, spacecraft surface material is constantly shed under micrometeoroid bombardment (akin to sandblasting) and decomposition processes, adding to the micro-debris environment (Bariteau and Mandeville, 2000; Johnson and Klinkrad, 2009).

Here, we consider micro-debris in two different ways: first, the diffuse cloud around the Earth, which evolves steadily and shows no distinct features connected to singular events, and second the transient micro-debris clouds and streams, which are connected to singular events (such as fresh GEO-insertion SRM firings) and dissolve over time to become part of the diffuse cloud.

### The diffuse micro-debris cloud

To assess the relevance of the diffuse micro-debris cloud for DDA, we make use of the MASTER model (Meteoroid And Space debris Terrestrial Environment Reference). MASTER is ESA’s tool for assessing the space debris impact risk to Earth-orbiting satellites (Braun et al., 2021). As such, it includes artificial dust with sizes  $> 1 \mu\text{m}$  because of the threat it poses to sensitive spacecraft components (see Section 2.3). MASTER is a physical model, simulating particle populations by means of trajectory propagation and taking into account their actual sources. Here, we use MASTER (version 8.0.3) to understand and evaluate the types, dynamics, and quantities of debris dust that DDA will encounter.

To get an overview of the spatial distribution of debris dust around Earth, we first run the *spatial density* mode of MASTER. Figure 5.1a shows the simulated spatial density as dependent on altitude and object diameter. Note that only three debris populations appear in this plot. Other debris populations modelled by MASTER produce negligible densities in comparison and are thus not further considered in this study. The relevant populations are: ‘ejecta’ (impact-excavated

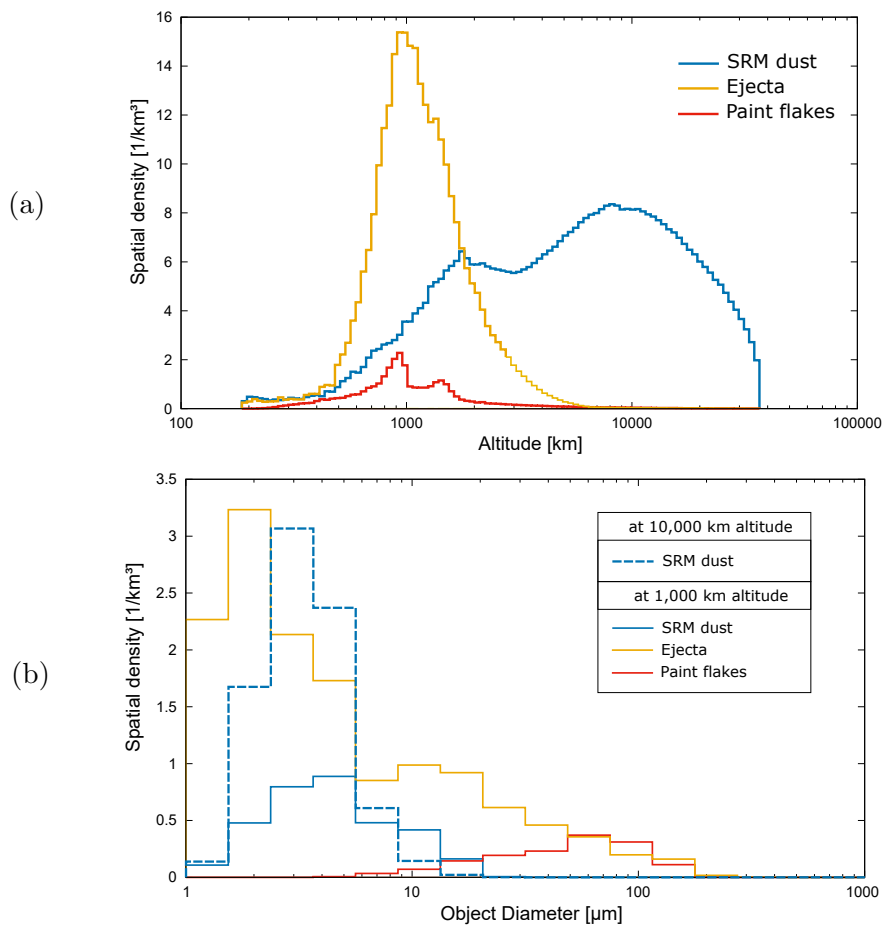


**Figure 5.1.:** Density distribution of debris dust populations: (a) over altitude and (b) over object diameter taken at two different altitudes, modelled with MASTER. Populations other than the ones shown have insignificant densities in comparison and are omitted. At 10,000 km altitude SRM dust is the only significant population density-wise.

surface material of satellites and larger debris), ‘paint flakes’ (particles released from degrading spacecraft surfaces), and SRM dust. Ejecta particles dominate at altitudes below 2000 km with a peak density at 1000 km. Paint flakes show an altitude profile similar to that of ejecta (consistent with their common origin) although at densities roughly one order of magnitude lower. SRM dust on the other hand reaches a peak density at around 10,000 km and drops off to zero at 36,000 km, which is the apogee altitude of dust created in GTO apogee motor firings (Bunte, 2003). Figure 5.1b shows the spatial density over object diameter profile taken at two different altitudes, 1000 km and 10,000 km. The predominant grain size is in the range of a few microns for SRM dust and ejecta, and a few tens of microns for paint flakes. Note that ejecta and paint flakes are not present at 10,000 km. Figure 5.2 shows the density distribution of these three populations over altitude-declination bins. For ejecta and paint flakes the density peaks near the poles, hinting at the predominance of sun-synchronous orbits among LEO satellites. The SRM dust distribution at low altitudes appears to be confined to declinations within  $\pm 40^\circ$ , but becomes uniformly distributed at altitudes above 3000 km. Also indicated are the paths of the DESTINY+ orbit at three different points in time, showing that the spacecraft be exposed to the ejecta and paint flakes populations only for the first few months after launch. The SRM dust population will be encountered for longer, but exposure diminishes once the perigee is raised beyond 20,000 km around the 8th month.

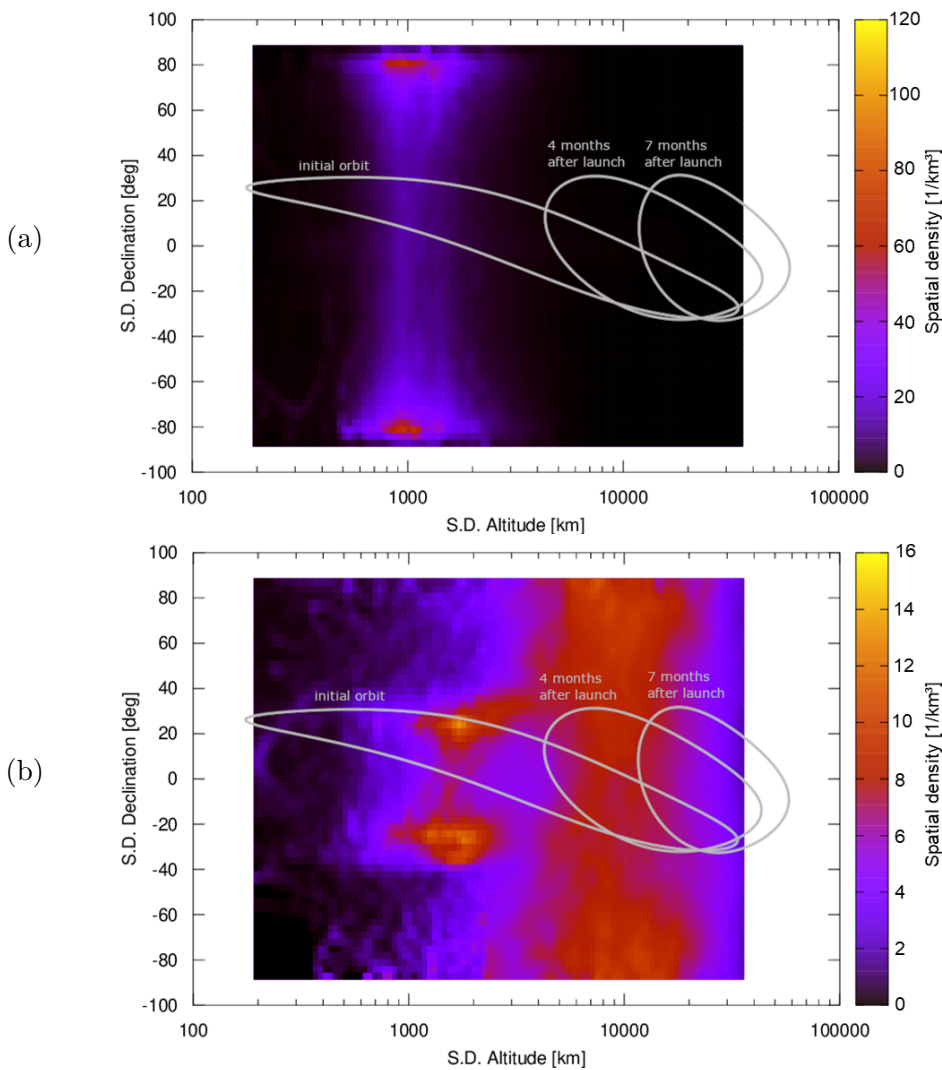


**Figure 5.2.:** Spatial density distribution of debris dust as modelled with MASTER. Dust populations shown are (a) ejecta & paint flakes (which are similarly distributed) and (b) SRM dust. The orbit of DESTINY+ is shown for three points in time.

Considering the short time DESTINY+ will spend at LEO altitudes (see Figure 3.2) and that the DDA cover will remain closed after launch for several weeks, study of the ejecta and paint flakes population will not be possible with DDA. For the flux analysis along the orbit of DESTINY+, we thus focus on the SRM dust population. As an exemplary case, we use the orbit around the 4th month after launch for this MASTER simulation. Figure 5.3 shows the distribution of impact azimuth and elevation along that orbit of DESTINY+, to get a sense of the impact directionality (the underlying coordinate system is the 'Earth-oriented' system used in MASTER). The angular distributions show that the predominant impact direction veers off the spacecraft's (Earth-centred) apex direction, but stays roughly within  $\pm 50^\circ$  from the apex in azimuth and  $\pm 30^\circ$  from the apex in elevation.<sup>1</sup> We see that the flux is minimal around perigee and increases with growing altitude, although it drops off sharply closer to the spacecraft's apogee, which in this case lies beyond the GEO altitude. This is consistent with the density distribution noted earlier, which shows a cut-off at 36,000 km.

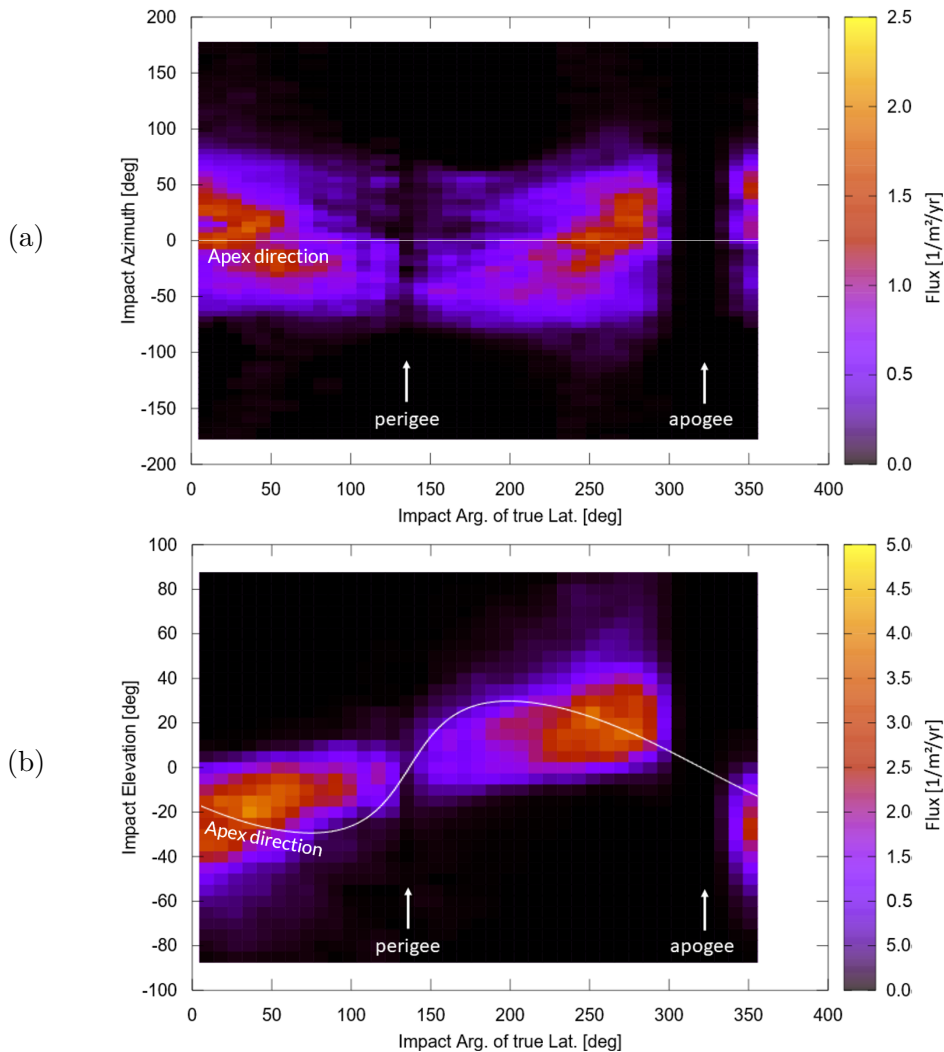


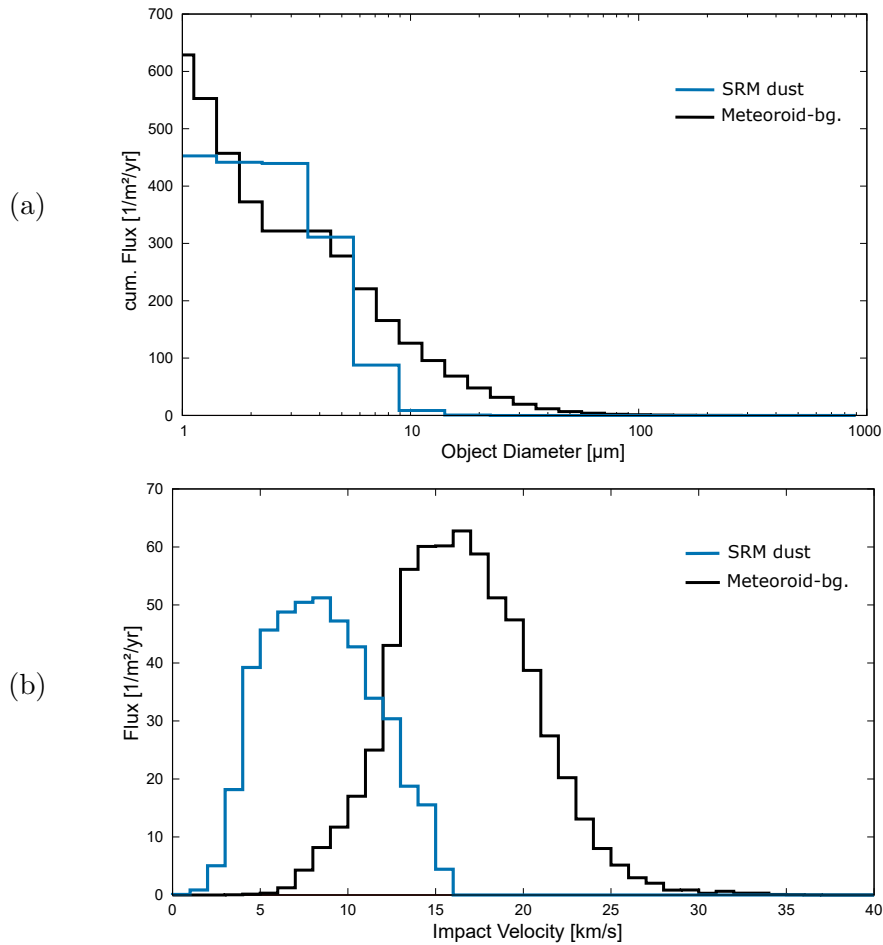
**Figure 5.3.:** Directional debris flux distribution along DESTINY+ orbit, modelled with MASTER. The orbit used to model the flux is that of DESTINY+ 4 months after launch. The coordinate system is the 'Earth-oriented' system used in MASTER, where azimuth and elevation are the angular components of the impact direction inside and outside the local horizontal plane. The spacecraft's (Earth-centric) apex direction is indicated by a white line. The gap in the flux around apogee is due to the absence of debris particles in MASTER beyond GEO altitudes.

<sup>1</sup>Note that these angles (as defined in MASTER) use the same naming convention as the DDA-PME. There is no relation between the two.

To compare the incidence of SRM dust with the meteoroid background, Figure 5.4a shows their cumulated fluxes for a plate that is oriented toward the spacecraft apex during the entire orbit. The SRM size distribution appears to be nearly flat at sizes of a few microns. Thus, the SRM flux is around 30% below the natural flux for grains larger than  $1\ \mu\text{m}$ , yet around 50% higher than the natural flux for grains larger than  $3\ \mu\text{m}$ .

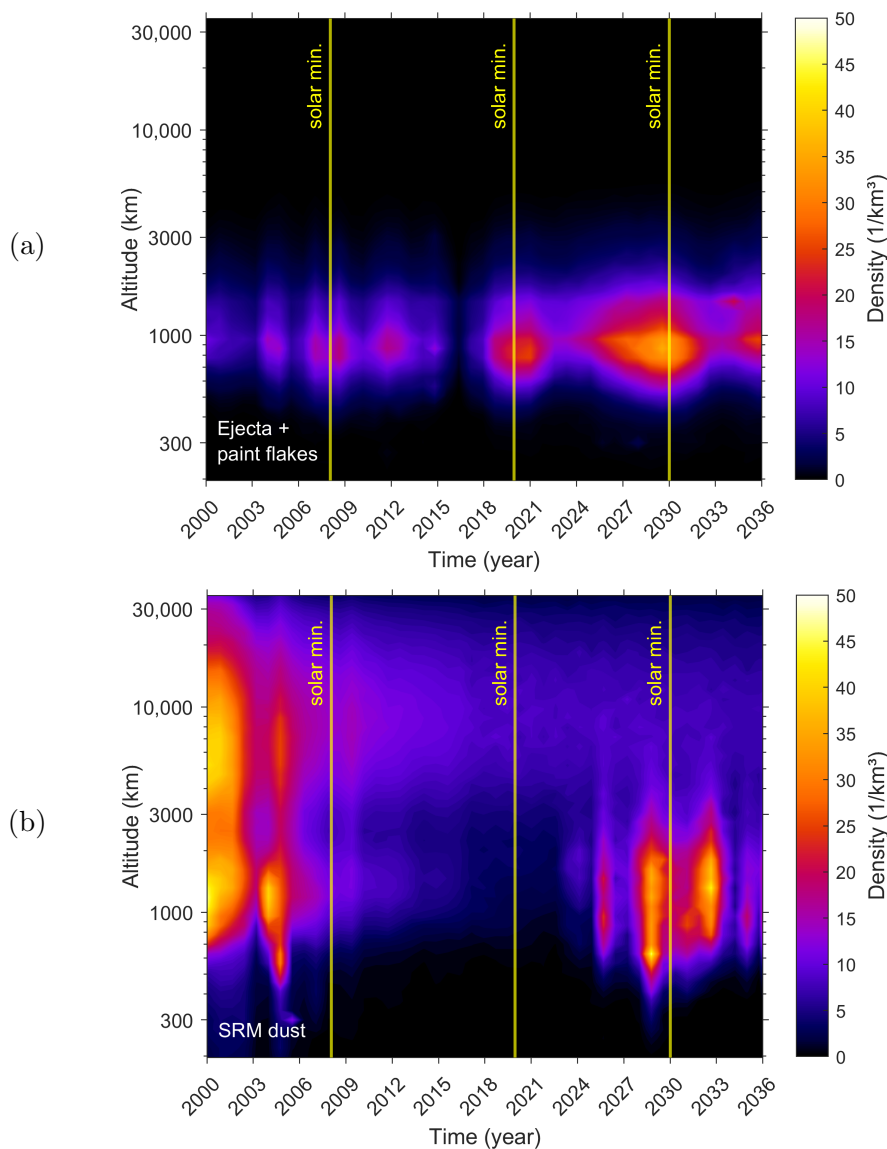
For a rough estimate, the SRM dust plate detector flux of  $450\ \text{m}^{-2}\ \text{yr}^{-1}$  can be multiplied with DDA's sensitive area of  $0.03\ \text{m}^2$ , amounting to an impact rate for DDA of  $13.5\ \text{yr}^{-1}$ . This, however, assumes that all dust influx occurs collimated from the sensor boresight and that DDA points into that flux at all times. Therefore, this incidence rate should be considered as an upper limit. If, instead, we assume the flux to be isotropic—knowing that DDA has a geometric factor of 0.0046 that of a unit plate, see Section 4.2—we obtain an impact rate of  $2.1\ \text{yr}^{-1}$ . This, on the other hand, can be considered a lower limit, as it ignores that the flux has in fact a predominant directionality (seen in Figure 5.3), which DDA will be able to exploit using its pointing mechanism. Notwithstanding the fact that the orbit is not stationary, we can derive that the detection of a few SRM dust grains during the first eight months of the mission is realistic.

Figure 5.4b compares the velocity distribution of SRM dust flux and meteoroid background grains onto the apex-facing plate. The different velocity profiles would help to distinguish grain origin, in case of an ambiguous grain composition.



**Figure 5.4.:** Flux and velocity comparison of SRM dust and meteoroid-background dust along DESTINY<sup>+</sup> orbit, modelled with MASTER. For the meteoroid environment the Divine-Staubach model within MASTER was chosen. The orbit used to model the flux is that of DESTINY<sup>+</sup> 4 months after launch. The Target surface is an apex-facing plate (i.e., surface normal points parallel to the Earth-centric velocity vector of the spacecraft).

It is noteworthy that, although the diffuse micro-debris cloud appears quasi-static on shorter timescales, its density varies significantly with the solar cycle. This is a result of the changing density of the thermosphere, which, due to an increased UV-radiation-induced heating, is around one order of magnitude higher at solar maximum than at solar minimum (at an altitude of 400 km, see Emmert, 2015). The higher thermosphere density increases the atmospheric drag imposed on micro-debris particles at LEO altitudes, which accelerates their orbital decay. Therefore, the abundance of micro-debris also varies with the solar cycle. This effect is considered in MASTER by inclusion of a solar-activity-dependent atmospheric density model for the orbital propagation of objects (Horstmann and Stoll, 2017; Braun et al., 2021). Figure 5.5 shows the MASTER-predicted spatial density of particles over altitude and time. The density variation of the LEO populations (ejecta and paint flakes, shown in Figure 5.5a), show a correlation with the solar cycle, with fluctuations from minima to maxima of roughly a factor of 3 to 5, as well as an overall increase from solar cycle to solar cycle (due to the growth of the LEO-satellite population during the 2000 to 2030 timeframe). The higher altitude SRM dust, on the other hand, shows no obvious



**Figure 5.5.:** Variation of micro-debris density with altitude and time, modelled with MASTER. Considered particle populations are (a) ejecta & paint flakes and (b) SRM dust, larger than  $1 \mu\text{m}$ . Timing of the Solar Cycle 25 minimum indicated as predicted by (Espuña Fontcuberta et al., 2023).

---

dependence on the solar cycle (Figure 5.5b), as expected due to the lesser exposure of these grains to the density-dynamic thermosphere. Their density variations may instead be due to the irregular injection of SRM dust into near-Earth space, caused by infrequent and unevenly-productive orbital SRMs firings. The frequency of SRM firings considered by MASTER decreases from around  $80 \text{ yr}^{-1}$  in the 1980s to  $5 \text{ yr}^{-1}$  in 2020, and to  $\sim 2 \text{ yr}^{-1}$  in 2030 (a prediction based on the ‘mean’ future scenario, see Horstmann et al., 2020). However, in lack of further knowledge about the way SRM firings are considered in the generation of MASTER’s future debris populations, the reason for the temporal fluctuations seen in Figure 5.5b, cannot be definitively resolved. Yet, it may be concluded that at the higher altitudes, where DDA has the highest chance of detecting SRM (e.g., Figure 5.3), fluctuations of the SRM dust density are insignificant, as modelled by MASTER. Therefore, we consider the prediction (as derived from Figure 5.4a) of a few detectable SRM dust particles of the diffuse micro-debris cloud during the DESTINY<sup>+</sup> spiralling phase unaffected by a potential shift in the launch date. It should also be noted, that the diffuse micro-debris cloud may contain submicron particles, which are not considered by MASTER, and thus, are not included in the flux predictions.<sup>2</sup>

### Micro-debris streams

In addition to the diffuse micro-debris cloud, there are transient density features imposed on it, generated by major (yet infrequent) dust-release events, such as satellite collisions and GEO-insertion SRM firings. Before reentering Earth’s atmosphere or mixing into the diffuse cloud, such-released dust may form toroidal streams around the Earth, resulting from Keplerian shearing of the initial cloud (Bunte, 2003). The crossing of a dense-enough stream may cause a number of particles to be registered by an in-situ dust detector, if pointed in the right direction. For instance, the capacitor-type Interplanetary Dust Experiment (IDE) on the LEO-stationed Long Duration Exposure Facility (LDEF), detected repeated event clustering at certain points along its orbit that were attributed to the presence of elliptic toroidal streams around the Earth (Oliver et al., 1995). Indeed, few of the detected streams could be dynamically associated with the firings of specific GEO-insertions (Schobert and Paul, 1997; Stabroth et al., 2007).<sup>3</sup> Similarly, certain event clusters in the data of the plasma impact detector GORID instrument, which is particularly noteworthy due to its higher orbit,<sup>4</sup> were also found to be dynamically linked to known SRM firings (Drolshagen et al., 2001b; Bunte, 2003; Bunte and Drolshagen, 2005). If such an SRM firing were to occur during the DESTINY<sup>+</sup> near-Earth phase, the resulting dust stream could be modelled and checked for intersection with the DESTINY<sup>+</sup> trajectory, in the manner of Bunte (2003). In that case, the novel pointing flexibility of DDA may facilitate the detection of such a directed stream. However, since the days of LDEF and GORID, use of orbital SRMs has plummeted (see Horstmann et al., 2020, Figure 8.3a) (in favour of hydrazine-based and electric propulsion options), making an encounter with a freshly created SRM dust stream highly unlikely.

It should be noted, that neither the LEO-deployed instruments nor the more sensitive impact

---

<sup>2</sup>Although Juhász and Horányi (1997) show that particles in the 100 nm size range are efficiently removed from SRM-dust-typical orbits within months of creation via interaction with the Earth’s magnetosphere.

<sup>3</sup>Further account of the occurrence of clusters and streams at LEO altitudes was given by the instruments Prospero (Bedford et al., 1975), SPADUS (Tuzzolino et al., 2005), DEBIE-1 & 2 (Schwanethal et al., 2005; Menicucci et al., 2013), and SODAD-1 & 2 (Durin and Mandeville, 2009; Durin et al., 2016; Durin et al., 2022). One of the streams detected by SPADUS could be attributed to a known SRM firing (Neish et al., 2004; Bunte and Drolshagen, 2005).

<sup>4</sup>The Geostationary Orbit Impact Detector (GORID) was mounted on the Russian telecom. satellite Express-2.

---

plasma detector GORID had the capability to analyse the composition of detected particles, thus lacking definitive proof that the detected clusters were indeed SRM dust streams. Though plausible, this explanation still leaves other clusters unresolved, that could not be connected to SRM firings. While the occurrence of clusters in the densely-populated LEO region may plausibly be the result of human activity in a number of ways (such as satellite explosions and collisions, as well as destructive anti-satellite weapon tests), the frequent occurrence of clusters in the GEO region is more difficult to explain. The high number of clusters detected by GORID (the average rate of clustered events exceeded the rate of random events by a factor of 5, see Drolshagen, 2006; Graps et al., 2007), which could not be attributed to SRM firings, led Bunte and Drolshagen (2005) and Drolshagen (2006) to conjecture an unknown micro-debris cloud generating mechanism present in GEO. Graps et al. (2004, 2007) speculated that the breakup of larger SRM slag particles via electrostatic fragmentation as a result of magnetospheric interaction could act as such a mechanism.<sup>5</sup>

However, historic data retrieved from dust sensors in near-Earth space up to and beyond GEO also indicate the frequent occurrence of particle clouds that are unlikely to be debris-related. These phenomena, which are plausibly connected to the GORID-detected non-SRM clusters, are further discussed in Section 5.1.2.

### 5.1.2. Magnetospheric swarms

Besides the aforementioned clusters reported by dust detectors in LEO and GEO, which could in part be attributed to human activity, there are accounts of roaming clouds of particles occurring at altitudes beyond GEO—which are largely unused for spaceflight—indicating a non-human-activity-related origin (GEO-insertion SRM dust streams do not significantly extend beyond GEO, see Bunte and Drolshagen, 2005). The HEOS-2 spacecraft, launched in 1972, carried an impact plasma detector on a highly eccentric orbit with varying perigee in a range of 350–3000 km and apogee of 240,000 km, as illustrated in Figure 5.6. Due to that orbit, HEOS-2 could characterize the dust flux over widely varying distances from Earth, from a practically ‘pristine’ interplanetary background flux around its apogee to the near-Earth dust flux present at sub-GEO altitudes. Whereas the interplanetary background flux rate was found to be essentially random, the near-Earth dust flux appeared to be dominated by clusters of impacts, spaced in time only by few minutes (Hoffmann et al., 1975a,b; Fechtig et al., 1979). Encountered at distances of up to 10 Earth radii, which is about the extent of the Earth’s magnetosphere dipole field (about twice the GEO altitude), these ‘magnetospheric swarms’ generated an averaged particle flux rate about one order of magnitude higher than the random background flux rate. Examining different directions perpendicular to the Sun (toward the Earth apex, antapex, ecliptic north, and south), however, HEOS-2 also revealed that the swarms occurred anisotropically in the Sun-Earth-line-fixed ecliptic coordinate system, preferentially coming from the Earth apex.<sup>6</sup> The masses of the individual particles ranged mostly within  $10^{-14}$  g to  $10^{-12}$  g (corresponding to radii of about 100–500 nm), similar to the mass range of the  $\beta$ -meteoroids irradiating from the Sun, which, however, the HEOS-2 sensor was insensitive to, due to its pointing.

The findings of HEOS-2 are reinforced by the data of two other in-situ dust detectors, the MDC

---

<sup>5</sup>SRM slag particles are larger (cm-sized) aluminium-oxide clumps ejected at the end of an SRM burn, such that those produced in GEO-insertions burns have near-GEO orbital parameters.

<sup>6</sup>The Earth apex is the Earth’s direction of motion with respect to the Sun.

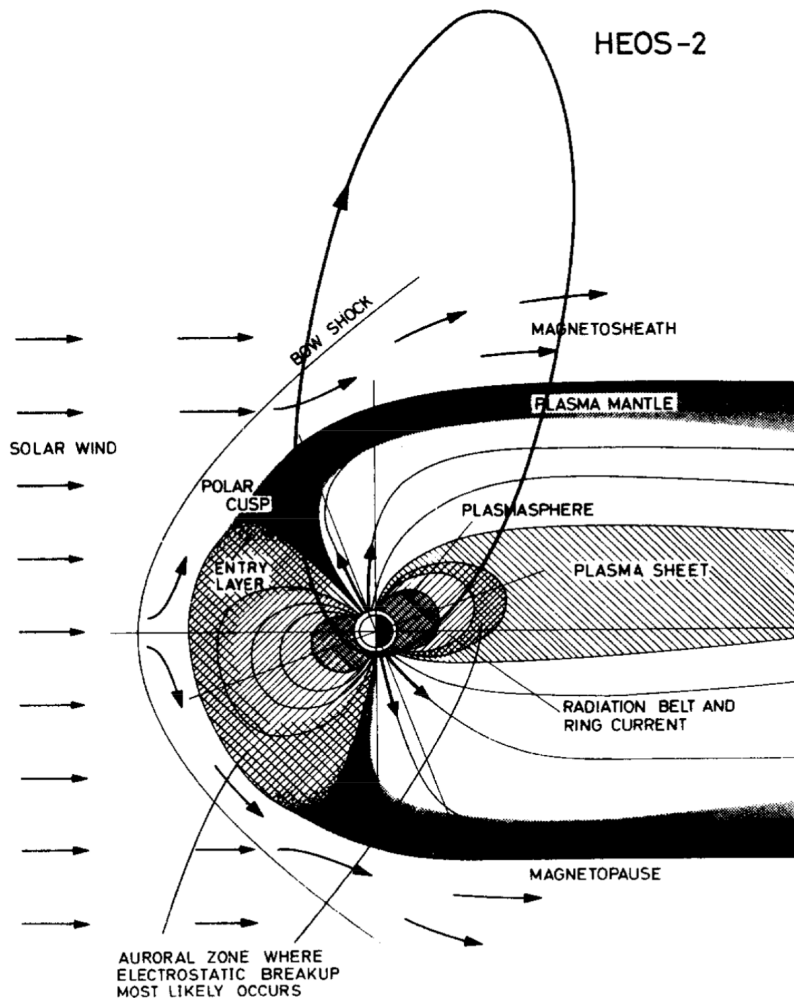


**Figure 5.6.:** Plasma and field regions within the Earth's magnetosphere and a sample orbit of HEOS-2. Taken from Fechtig et al. (1979).

(Munich Dust Counter) and GORID. MDC, carried by the Hiten spacecraft on a (similarly to HEOS-2) highly eccentric orbit, likewise reported a ten-fold increase of flux near Earth (closer than 100,000 km) compared to interplanetary space, as well as the occurrence of clustering (Iglesider et al., 1993, although published details are sparse). The GORID instrument, stationed in GEO, reported an averaged flux of cluster events around 5 times that of random events, with a strong preference for detection around local midnight, that is, when the spacecraft-body-fixed sensor was most sensitive to a flux from apex (Drolshagen et al., 2001a; Graps et al., 2007). The striking similarities in terms of incidence rate and anisotropy of the HEOS-2- and GORID-detected swarms suggest that they pose the same phenomenon. Not considering this relationship, however, Drolshagen et al. (2001a) and Graps et al. (2007) attribute all GORID-recorded event clusters to GEO-activity-related debris phenomena. Although Graps et al. (2007) note that fresh micro-debris clouds originating in GEO would have too low velocities relative to GORID (few  $100 \text{ m s}^{-1}$ ) to be efficiently detected.

Fechtig et al. (1979), on the other hand, suggested that the swarms could be caused by the breakup of fluffy interplanetary grains that fragment due to inner, repulsive electrostatic forces, resulting from the charging of the grains while traversing the Earth's magnetosphere. They argue that, in case of the electrostatic fragmentation origin, the apex-predominance would be consistent with radiants of different types of meteors observed in the Earth's atmosphere. As classified by

---

Ceplecha (1977) (see also Ceplecha et al., 1998), the type III meteors are those with high ablation ability, and accordingly small bulk densities ( $< 1 \text{ g cm}^{-3}$ ), as would be expected for particles prone to electrostatic fragmentation. Among those low-density meteors, the subgroup IIIAi, stemming from highly inclined long-period comets, exhibits a strong anisotropy of trajectories with a concentration of radiants toward the Earth apex. This predominant meteor radiant concentration has since then been identified to be split into two meteor radiants, called the north & south apex radiants (Jones and Brown, 1993). However, meteoroids from these sources have high relative velocities with respect to Earth in excess of  $50 \text{ km s}^{-1}$ , which is incompatible with the low-velocity swarms ( $v_\infty < 20 \text{ km}$ ) as noted by Fechtig et al. (1979). Even considering the large uncertainty in the velocity determination of HEOS-2-detected particles (uncertainty factor of 2, typical for rise-time-determined speeds, see Göller and Grün, 1989), this precludes the possibility that the swarms are formed out of meteoroids from the north & south apex radiants.

Instead, the dynamics of the swarms may hint at another group of interplanetary dust grains as their progenitors, namely, the  $\alpha$ -meteoroids (as originally coined by Grün and Zook, 1980). These particles move on highly eccentric orbits with aphelia near 1 au, where they thus exhibit low heliocentric velocities. A detector moving with the Earth effectively overtakes these slow-moving particles, such that they appear to be coming towards the detector from the Earth apex with relative velocities of  $5\text{--}20 \text{ km s}^{-1}$  (notwithstanding gravitational focussing). Having sizes around  $1 \mu\text{m}$ , they are flux-wise the most abundant bound interplanetary dust grains in the inner solar system (e.g., Grün, 1981, see also Section 5.3.3 for a discussion of the  $\alpha$ -meteoroids). The  $\alpha$ -meteoroids notably exhibit the dynamical properties demanded for swarm progenitors, that is, an approach direction roughly from apex, as well as relative velocities below  $20 \text{ km s}^{-1}$ . Yet, the micron-sized  $\alpha$ -meteoroids are only about an order of magnitude more massive than the swarm particles and, assuming that swarms are generated by fragmentation of a single progenitor, could thus not produce the rich swarms of  $10^{14}$  to  $10^{19}$  individual grains, as estimated from the swarms' spatial dimensions and number densities (Fechtig et al., 1979). A speculative explanation for this discrepancy could be that the swarms are formed by the quasi-simultaneous breakup of a large number of  $\alpha$ -meteoroids in a region of the magnetosphere, due to local fragmentation-inducing variations of the plasma environment (for a review of turbulences of the geomagnetosphere, see Zimbardo et al., 2010).

The magnetospheric swarms are a peculiar phenomenon, which have thus far not been satisfactorily explained by any of the proposed pathways. As a modern dust-telescope, DDA is in a unique position to shed light on their poorly-understood nature. By analysing their composition, definitive proof of their natural or artificial origin may be given. By accurately measuring the impact speeds of the largest swarm particles (having masses of  $10^{-11} \text{ g}$  or  $s \approx 1 \mu\text{m}$ , sufficiently large to allow TOF speed measurements via the DDA trajectory sensor), the true velocity of the swarms within the Earth's magnetosphere may be determined. Together with the mapping of their anisotropy across the antisolar hemisphere, enabled by the DDA-PME, their dynamics may be unambiguously diagnosed. To achieve a conclusive understanding of the magnetospheric swarms, DDA should thus attempt to map the antisolar hemisphere, with particular attention to the apex region, during the first 14 months of the attitude-dynamic spiralling phase (i.e., when DESTINY<sup>+</sup> is still within the inner magnetosphere, see Figure 3.2).

Lastly, one might consider an entirely different explanation for the consistent detection of cluster events by impact plasma detectors within Earth's magnetosphere. A thus far unknown interaction of

this sensor type with the magnetosphere’s turbulent plasma environment may cause the clustered occurrence of genuine-looking noise events. (For a description of identified noise events in the GORID-data that are likely caused by an electrostatic interaction with the spacecraft as well as the operation of the spacecraft’s plasma thrusters, see Drolshagen et al. (2001a)). However, given the scrutiny put in place to distinguish true impact events from noise events (e.g., Grün et al., 1995a, note that GORID is identical to the sensors flown on Ulysses & Galileo), as well as the anisotropic detection of clusters, this explanation seems unlikely. As an impact plasma mass spectrometer, DDA has the essential advantage that the recording of a mass spectrum also acts as the unequivocal proof of a true particle impact, and is thus able to rule out the noise cluster hypothesis.

## Quantitative analysis

Here, we analyse the incidence rate of the magnetospheric swarm particles for DDA, based on the HEOS-2 and GORID measurements. Table 5.1 summarizes the key geometrical characteristics of DDA, the nominal sensitive area  $A_0$  and the geometric factor  $G$ , and relates them to the values of HEOS-2 and GORID. With these relations, we can convert the impact rates determined by HEOS-2 and GORID to DDA-equivalent impact rates (assuming that DDA would have the same orbit, pointings, and sensitivities as HEOS-2 and GORID). For a collimated dust stream and perfect instrument pointing, only the nominal sensitive area  $A_0$  is important, allowing DDA to detect roughly 30% of what GORID and 300% of what HEOS-2 would detect. For an isotropic flow of dust (or a randomly varying instrument pointing) the geometric factor  $G$  is the relevant quantity, such that DDA would pick up about 10% of the flux onto GORID and 147% of the flux onto HEOS-2.

**Table 5.1.:** Comparison of sensor geometries.

Instrument	$A_0$ cm <sup>2</sup>	$A_0/A_{0,DDA}$ –	$\Omega_{\text{eff}}$ sr	$G$ cm <sup>2</sup> sr	$G/G_{DDA}$ –
GORID	1000*	3.31	1.45*	1450	10.1
DDA	300	1	0.48	144	1
HEOS-2	95.4 <sup>†</sup>	0.32	1.03 <sup>†</sup>	98	0.68

\* Taken from Grün et al. (1992b).

<sup>†</sup> Taken from Hoffmann et al. (1975b).

With HEOS-2, a total of 207 swarm particles (split among 15 swarms) have been identified during an accumulated observation time below  $10 R_{\oplus}$  of 70 days (Fechtig et al., 1979). Assuming a randomly varying instrument pointing, we can calculate the corresponding incidence rate for DDA as:

$$I_{\text{DDA,rand}} = \frac{N_{\text{HEOS}, <10 R_{\oplus}}}{\mathcal{T}_{\text{HEOS}, <10 R_{\oplus}}} \cdot \frac{G_{\text{DDA}}}{G_{\text{HEOS}}} \quad (5.1)$$

where  $N_{\text{HEOS}, <10 R_{\oplus}}$  is the number of all swarm particles (or the number of swarms, respectively) detected, and  $\mathcal{T}_{\text{HEOS}, <10 R_{\oplus}}$  is the total observation time, while HEOS-2 was within  $10 R_{\oplus}$ . We thus obtain an incidence rate for DDA of 30 particles per week (split among 2.2 swarms). Converting GORID’s averaged rate of events that were part of clusters ( $2.46 \text{ d}^{-1}$ , Graps et al., 2007) to DDA-equivalent rates in the same manner, we obtain 1.7 impacts per week. (Note that the number of

events per cluster is not evident in the GORID-related publications.) Strikingly, the converted rates of HEOS-2 and GORID differ by an order of magnitude. Assuming that the clusters detected by HEOS-2 and GORID stem for the most part from the same phenomenon (the magnetospheric swarms), the discrepancy may be explained by the following reasons:

- The HEOS-2 sensor was more exposed to the anisotropic flow of swarms than GORID, which both instruments reported to be coming preferentially from the Earth apex: HEOS-2 pointed toward the Earth apex for 40% of the observation time. GORID, on the other hand, was sensitive to a flow from Earth apex only around the local midnight hours on its geostationary orbit (or roughly 25% of the time) and only with a large boresight angle to the ecliptic, between  $42^\circ$  and  $88^\circ$ .<sup>7</sup>
- The HEOS-2 sensor is more sensitive than GORID: The particle mass detection threshold of HEOS-2 is one order of magnitude lower than that of GORID at the same velocity ( $m_{\min, \text{HEOS}} = 10^{-15}$  g and  $m_{\min, \text{GORID}} = 1.5 \times 10^{-14}$  g, both at  $v_{\text{imp}} = 10 \text{ km s}^{-1}$ , see Dietzel et al., 1973; Göller and Grün, 1989). Particle masses derived from HEOS-2 measurements indeed indicate that swarm particles are partially below the GORID threshold (Fechtig et al., 1979).<sup>8</sup>

Given the above considerations, we find the rates as converted from GORID and HEOS-2 to be consistent, reinforcing the assumption that the impact clusters measured by the two instruments stem from the same phenomenon.

Compared to GORID and HEOS-2, DDA will benefit from an increased sensitivity, with a mass threshold expected in the order of  $10^{-16}$  g at comparable speeds, that is, particles of only 10s of nanometres (Simolka and Srama, priv. comm., pending final calibration campaign). For DDA, the estimated incidence rates as converted from data of the more sensitive HEOS-2 sensor can thus be cautiously considered as a lower limit.

Moreover, with the added pointing flexibility of DDA, a high exposure time to the Earth-apex-dominated swarms may be achieved. If we only consider the part of HEOS-2 data while the sensor was pointed toward the Earth apex and assume that all detected swarms had a flow direction exactly from the Earth apex, the incidence rates for a statically apex-pointing DDA can be computed as

$$I_{\text{DDA,apex}} = \frac{N_{\text{HEOS}, <10 R_{\oplus, \text{apex}}}}{\mathcal{T}_{\text{HEOS}, <10 R_{\oplus, \text{apex}}}} \cdot \frac{A_{0, \text{DDA}}}{A_{0, \text{HEOS}}} \quad (5.2)$$

where  $N_{\text{HEOS}, <10 R_{\oplus, \text{apex}}}$  is the number of all swarm particles (or the number of swarms, respectively) detected, and  $\mathcal{T}_{\text{HEOS}, <10 R_{\oplus, \text{apex}}}$  is the total observation time, while HEOS-2 was within  $10 R_{\oplus}$  and pointed in the Earth apex direction. This results in an incidence rate for DDA of 112 swarm particle impacts per week (split among 7 swarms). Given the unrealistically favourable assumption of a parallel flow of swarms, however, this rate should be considered an upper limit estimate. Also note, that the observation time of DDA towards the Earth apex is limited due to dynamic spacecraft attitude, despite the flexibility offered by the pointing mechanism (as will be demonstrated in Section 6.5.2).

<sup>7</sup>GORID's boresight angle to the ecliptic depends on the position along the geostationary orbit as well as the time of year, due to spacecraft-body-fixed mounting at  $25^\circ$  from the equatorial north, see Drolshagen et al. (2001a).

<sup>8</sup>That is, notwithstanding an uncertainty in the mass determination, which, due to the propagation of an increased uncertainty in the velocity determination for impacts near the detection threshold, is in the order of a factor of ten, see Hoffmann (1971) and Fechtig et al. (1979)

---

## 5.2. Lunar dust

The airless lunar surface is directly exposed to hypervelocity meteoroid impacts. With characteristic sizes of 100s of microns, velocities of 10s of  $\text{km s}^{-1}$ , and a mass influx in the order of  $0.1 \text{ g km}^{-2} \text{ d}^{-1}$  (Grün et al., 1985b), these interplanetary projectiles excavate lunar surface material and loft it high above the ground with each impact. In the Moon's low gravity, these lofted lunar soil particles, called ejecta, can easily reach altitudes of 10s or 100s of kilometres, or even escape, depending on the ejection velocity. Here we investigate the prospects of DDA for detecting lunar ejecta during the lunar flybys of DESTINY<sup>+</sup>, as well as while in cis- and translunar space.

We do not consider electrostatically lofted dust, a near-surface phenomenon potentially present in the lunar terminator region. Surface experiments seem to have indicated its presence, although these findings remain controversial (e.g., Grün and Horányi, 2013, and references therein). Despite this, the phenomenon could not be detected by in-situ measurements down to altitudes of 3 km (Szalay and Horányi, 2015b).

### 5.2.1. Diffuse ejecta exosphere

The continuous bombardment of the lunar surface by micrometeoroids results in the permanent lofting of soil particles to significant altitudes, creating a quasi-static, faint cloud of dust around the Moon. This ejecta exosphere has been first theorized by Gault et al. (1963) and its detection from lunar orbit has been attempted by a number of experiments. Not considering the data retrieved from microphone-type detectors (Alexander et al., 1973), which were found to be prone to a high rate of noise-events (Nilsson, 1966; Berg and Gerloff, 1971), the first reliable (yet low-sensitivity) measurements in lunar orbit were carried out by the pressurized-can-type dust detectors onboard the five Lunar Orbiter spacecraft launched in 1966, which (orbiting the Moon between 30 km and 6200 km) found no clear evidence of an ejecta exosphere (Grew and Gurtler, 1971). Similarly, the Hiten probe, carrying the more sensitive impact plasma detector MDC (with perilune altitudes of a few 1000 km) could not detect the lunar ejecta cloud (Iglesider et al., 1996). Finally, with the Lunar Atmosphere and Dust Environment Explorer (LADEE), stationed in low lunar orbit (LLO) from 2013 to 2014 and equipped with the impact plasma detector Lunar Dust Experiment (LDEX), the existence of the lunar ejecta cloud could finally be confirmed (Horányi et al., 2014, 2015). In addition, LDEX discovered the asymmetric shape of the cloud, a result of the anisotropic influx of meteoroids, as well as its dynamic nature, caused by the time-dependent influx of annual meteoroid streams (Szalay et al., 2019a; Pokorný et al., 2019; Bernardoni et al., 2021).

Due to these measurements, the properties of the lunar ejecta dust cloud are fairly well understood in the orbital regime explored by LADEE, that is, around the equatorial region and at altitudes between 20 km and 100 km. Based on the LDEX data, Szalay and Horányi (2015a, 2016b) constructed a steady-state geometrical model for the ejecta cloud density distribution, assuming an idealized, anisotropic influx of sporadic meteoroids from the low-latitude (helion, anti-helion, and apex) meteor radiants. Szalay et al. (2019a) extend the model to higher latitudes by including the toroidal meteor radiants, and quantify the latitudinal-dependant impact gardening of the lunar surface, that is, the net burial or uncovering of regions due to ejecta lofting and re-depositioning.

Here we employ the geometric density model of Szalay et al. (2019a) (with corrected equations, see Appendix B) to estimate the dust density encountered along the DESTINY<sup>+</sup> flyby trajectory.

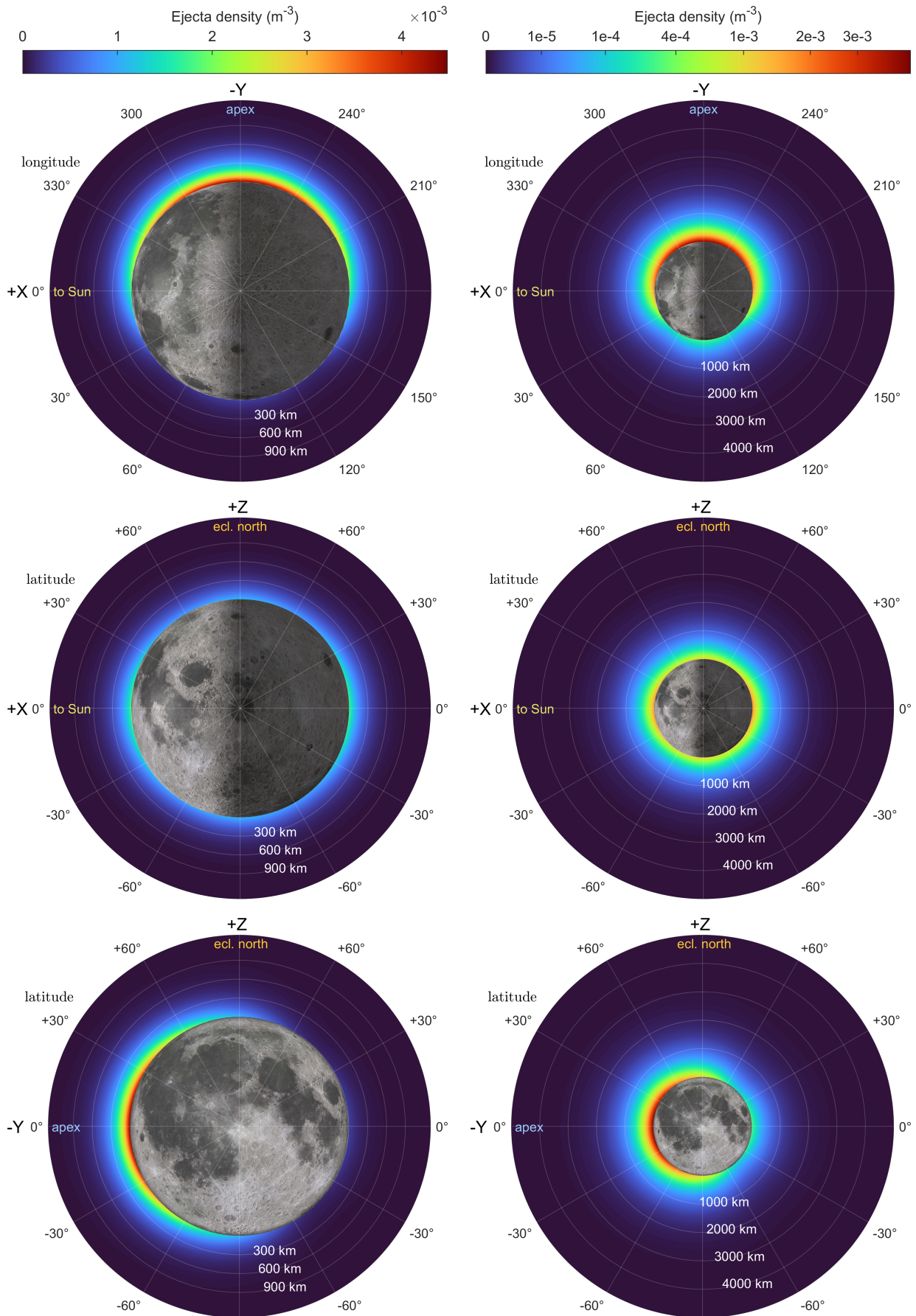


**Figure 5.7.:** Three volumetric cuts of the lunar ejecta cloud density along the X-Y (top), X-Z (middle), and Y-Z plane (bottom) of the SSE system, generated with the geometric density model by Szalay et al. (2019a) at  $s_{\min} = 0.3 \mu\text{m}$ . For each cut, a close-up view (left) with a linear colour scale, and a wider view (right) with a power-law colour scale (exponent of  $1/3$ ) is given.

The model provides a straightforward, steady-state representation of the location-dependant ejecta number density:

$$n = f(h, \phi, \lambda, s_{\min})$$

where  $n$  is the number density of particles per unit volume,  $h$ ,  $\phi$  and  $\lambda$  are the altitude, latitude, and longitude in the SSE system, and  $s_{\min}$  is the minimum particle radius. Figure 5.7 illustrates the density distribution arising from this geometric model with volume cuts at the principal planes of the selenocentric solar ecliptic (SSE) coordinate system.<sup>9</sup> The thus-produced density distribution is significantly canted towards the Earth-apex-facing side, as measured by LDEX. This is consistent with the anisotropic influx of meteoroids, in accordance with the sporadic meteor radiants, namely, the apex, north & south toroidal, and helion & anti-helion radiants, which are located on the Earth-apex-facing hemisphere of the sky (e.g., Campbell-Brown, 2008).<sup>10</sup> We note that, density-wise, a flyby over the Earth apex side is favourable for the detection of the diffuse lunar ejecta exosphere.

Assuming that the velocities of ejecta particles are small with respect to the sensor and that the detector boresight always points into the dust ram direction,<sup>11</sup> the momentary incidence rate onto DDA may be calculated from the local number density  $n$  as:

$$I = n \cdot A_{0,\text{DDA}} \cdot |\vec{v}| \quad (5.3)$$

where  $\vec{v}$  is the spacecraft velocity vector of the spacecraft with respect to the Moon.

We shall now apply this analysis to the lunar flybys performed by DESTINY<sup>+</sup> during the lunar gravity assist phase to escape the Earth-Moon system. Although the lunar trajectory is not yet definitive (depending on a number of not-yet-known factors such as the final launch date and the in-flight performance of the propulsion system, see Ozaki et al., 2022a), we examine the current baseline trajectory (with a launch in Q1 2025, see Section 3.1)<sup>12</sup> to provide a general assessment of DDA's potential to detect the diffuse lunar ejecta cloud and to exemplify flyby science operational aspects.

In this representative mission scenario, three lunar flybys (LFBs) with varying flyby geometries are intended to be performed: The first flyby, LFB-1, occurs at a large distance of 20,000 km from the Moon, whereas LFB-2 & 3 occur at altitudes of 480 km and 1160 km, respectively. Here, we disregard LFB-1 due to its remoteness and focus on the remaining two flybys. The trajectories of LFB-2 & 3 are shown in Figure 5.8. Both flybys occur around new moon, with closest approaches over the southern anti-sunward side (thus also over the nearside) in LFB-2, and over the Earth-apex-facing side in LFB-3.

Figure 5.9a shows the dust density along the two flyby trajectories computed with the Szalay-model, as well as the resulting incidence rate onto DDA calculated with Equation 5.3. As minimum detectable particle size  $s_{\min} = 0.3 \mu\text{m}$  is used, corresponding to the detection threshold of LDEX, from whose data the Szalay-model is derived. However, Szalay and Horányi (2016b) argue that the power-law size distribution observed by LDEX above its threshold may hold true down to sizes of

<sup>9</sup>See Appendix A for a description of the SSE coordinate system.

<sup>10</sup>The model takes the sporadic meteor radiants into account by their specific directions and assigns them relative weights for their mass production potential, to reproduce the LDEX-observed density distribution.

<sup>11</sup>The lunar dust ram direction is equivalent to the Moon-centric spacecraft velocity direction (assuming that the velocity of particles is small compared to the spacecraft velocity).

<sup>12</sup>The lunar gravity assist phase trajectory used here corresponds to Case #5 in Ozaki et al. (2022a); filename: `trj_destiny_2028flyby_interplanetary_20221208.bsp`; received from CIT in Dec. 2022.

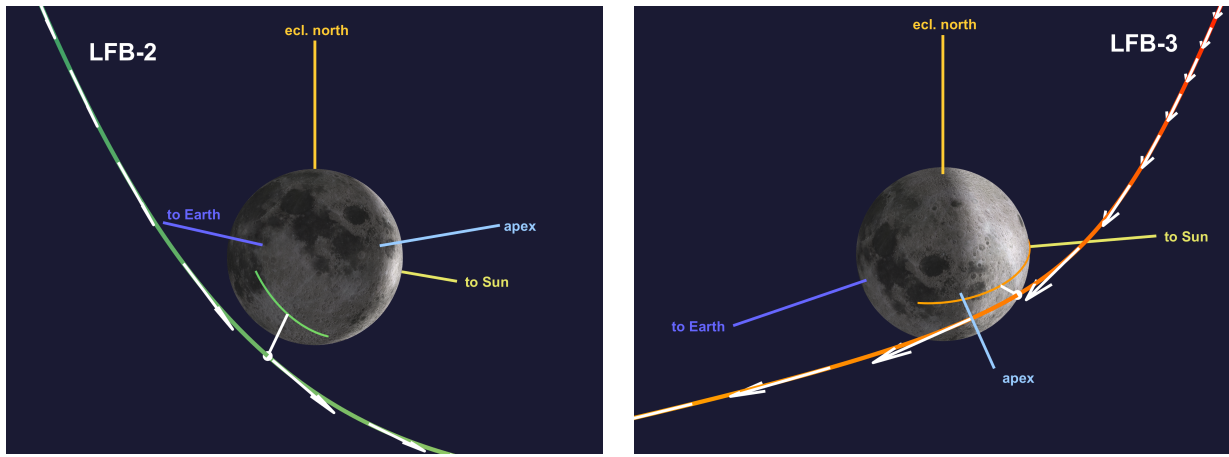


**Figure 5.8.:** Spacecraft trajectory during LFB-2 & 3. Also indicated are the ground track of the spacecraft while below 1500 km altitude, the location of the perilune, the principal directions of the SSE coordinate system (namely, the Sun direction, the Earth apex, and the ecliptic north), as well as the Earth direction during the flyby. White arrows indicate the flight direction.

0.05  $\mu\text{m}$ , which allows us to cautiously extend the model to smaller sizes. For DDA, a reduction of this threshold is anticipated, due to the higher speed at which the lunar dust grains are encountered. Compared to the circular orbital velocity of  $1.7 \text{ km s}^{-1}$  of LADEE, DESTINY<sup>+</sup> reaches speeds of  $2 \text{ km s}^{-1}$  and  $2.6 \text{ km s}^{-1}$  during its hyperbolic flybys LFB-2 & 3, respectively, as seen in the flyby speed profiles in Figure 5.10a.

Figure 5.9b shows the flyby fluences, that is, the cumulated number of particles impacting DDA during the flybys, for two values of  $s_{\text{min}}$ , namely  $0.3 \mu\text{m}$  (LDEX’s threshold) and  $0.2 \mu\text{m}$  (estimated threshold for DDA). Comparing the two flybys at the nominal threshold of  $0.3 \mu\text{m}$ , LFB-2 is found to generate a fluence of less than one particle, meaning no particle would be detected by DDA, whereas LFB-3 yields a fluence of 23 particles. The reduction of  $s_{\text{min}}$  by 50% increases the fluence by a factor of  $\sim 3$ , which increases the number of detected particles to one (LFB-2) and 68 (LFB-3). The difference of nearly two orders of magnitude between the flybys is due to the different flyby altitudes, as well as the favourable location of LFB-3 over the Earth-apex-facing side of the Moon.

However, we also have to consider the technical constraints of DDA, which require the avoidance of direct sunlight entering the instrument aperture (see Section 4.3). To that end, Figure 5.10b shows the angle between the lunar dust ram angle and the Sun direction during the flybys. As long as this ram-Sun angle is  $>90^\circ$ , the instrument can maintain the optimal ram pointing without direct sunlight in the aperture. This requirement is fulfilled for the entire flyby of LFB-3. For LFB-2, on the other hand, the ram-Sun angle is  $<90^\circ$  throughout the encounter. However, the spacecraft flies through the shadow of the Moon while descending to perilune, for a total shadowed period of 36 minutes ending shortly before perilune. Considering the turn-rate of the DDA-PME allowing the instrument to rotate by  $90^\circ$  in 7 minutes (see Section 4.1), observation into the dust ram direction could safely be executed for a duration of at least 22 minutes before turning the instrument away from the Sun and exiting the shadow, even though the fluence prediction for that period is less than one particle for the LFB-2 scenario. Another strategy could involve the partial exposure of the detector to the ram direction, which is sensitive to incidence directions as far as  $45^\circ$  from the boresight, yet, as the ram-Sun angle is  $<45^\circ$  in the case of LFB-2, this is not applicable here. Furthermore, we should note that indirect sunlight reflected from the lunar surface enters

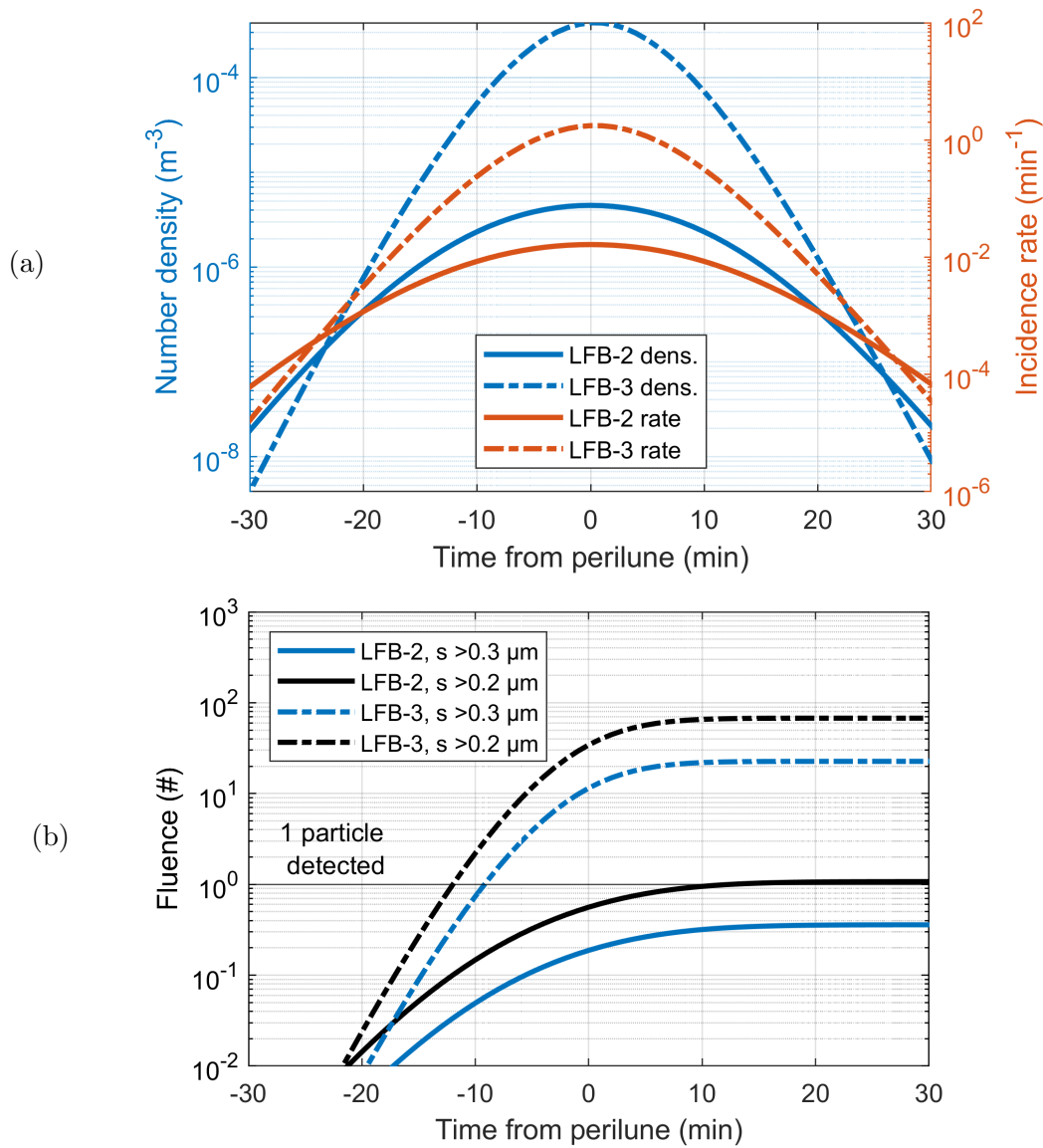


**Figure 5.9.:** Dust incidence predictions along the trajectories of LFB-2 & 3. (a): Dust density and incidence rates onto DDA, computed with the geometrical model by Szalay et al. (2019a). (b): Fluence onto DDA.

the DDA aperture during to descend to perilune in LFB-3, which may degrade the performance of the instrument’s trajectory sensor, such that charge and velocity measurements are affected or prevented.

We can conclude that DDA’s potential to detect the diffuse lunar ejecta cloud highly depends on the specific flyby geometry, namely, the flyby altitude, the location of the closest approach over the lunar surface in the SSE frame, as well as the angular separation between the Moon-centric flight direction and the Sun direction. Although particle detections may not be expected for a specific flyby based on the Szalay-model (as in this case for LFB-2), no-detection measurements are still valuable for constraining the dust density distribution. After all, the predictions made here are based on an extrapolation of the LDEX-data-fitted density profile between 20 km and 250 km.

We should also note, however, that the Szalay-model is designed as a steady-state model representing the annual average densities of the dynamic lunar dust cloud. The daily mean impact rate measured by LDEX showed fluctuations with a factor of up to  $\sim 2$ , some of which could be

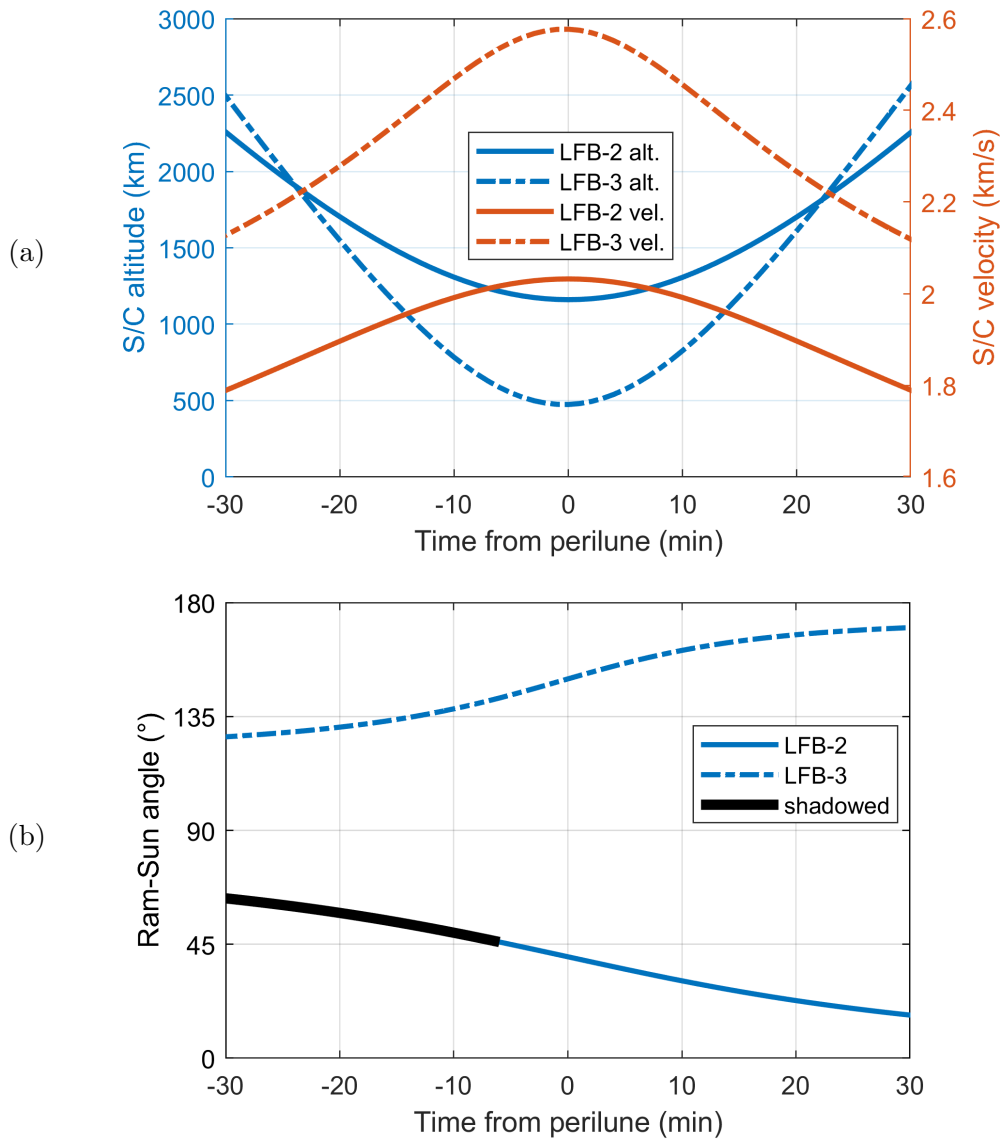


**Figure 5.10.:** Geometrical information along the trajectories of LFB-2 & 3. (a): Spacecraft altitude and velocity relative to the moon. (b): Angle between the dust ram direction (equivalent to the Moon-centric spacecraft velocity vector) and the Sun direction. A value of  $>90^\circ$  between the DDA boresight and the Sun direction is required for observation, excluding periods when shaded by the Moon (which are indicated by a thick black line).

associated with the occurrence of meteor showers (Szalay and Horányi, 2016a). In addition, minute-long outbursts of several 10s of impacts were recorded, presumably due to the stochastic impacts of larger meteoroids creating dense ejecta plumes. Although no major meteor showers are expected during the flyby dates of this representative scenario,<sup>13</sup> this adds to the uncertainty inherent to the estimates given here, and may be the deciding factor between non-detection and plentiful detections of the lunar dust cloud.

<sup>13</sup>The lunar flybys in the representative scenario occur between late January and early April 2027: LFB-1: January 24; LFB-2: February 7; LFB-3: April 8.

---

### 5.2.2. Roaming ejecta clouds

In addition to the diffuse ejecta exosphere in the immediate lunar environment, it can be conceived that parts of ejecta plumes stemming from sporadic, larger individual impacts may escape the lunar gravity well to roam the EMS as a formation of particles, potentially dense enough to be detected as such by an in-situ dust detector. Indication for such detections is given by the HEOS-2 data. Other than the confined swarms it encountered within the magnetosphere, HEOS-2 detected more dispersed ‘groups’<sup>14</sup> of particles occurring at all distances from the Earth (up to the apogee at 240,000 km), occurring predominantly when the Moon was within the sensor’s FOV (Hoffmann et al., 1975a,b). Backtracing of the trajectories taking into account uncertainties in the derived particle dynamics, Hoffmann et al. (1975b) excluded the lunar origin for only one out of the 12 groups. By modelling the motion of escaping ejecta plumes through the EMS, Dohnanyi (1977) further conclude that their spatial dimensions are consistent with HEOS-2’s encounter times of the groups and that lunar impactors in the order of 1 kg could suffice to create the observed group number densities. Using the Grün-model for the interplanetary meteoroid flux (Grün et al., 1985b, see also Section 5.3.1), it can be estimated that around one such meteoroid impacts the lunar surface every day.<sup>15</sup>

Further analysing the HEOS-2 data, Fechtig et al. (1979) find that the averaged flux of group particles for when the Moon was within the sensor FOV, amounted to  $1.6 \times 10^{-4} \text{ m}^{-2} \text{ s}^{-1}$  for a minimum particle mass of  $10^{-15} \text{ g}$ ,<sup>16</sup> with numbers of detected particles per group varying between 2 and 51. Assuming a constant pointing towards the Moon, this corresponds to an averaged incidence rate of group particles onto DDA of  $\sim 3$  per week (although, given the group sizes observed by HEOS-2, it appears likely that the group encounter rate will be less than once per week).

Considering the above-derived incidence rate onto DDA, detection of the roaming ejecta clouds during the two years that DDA will spend in the EMS seems highly likely. Moreover, a sophisticated observation campaign for the detection of such clouds with a high accumulated coverage time of the lunar direction enabled by the DDA-PME could allow for their thorough characterization. Such a campaign could be conducted intermittently throughout the attitude-dynamic spiralling phase, that is, when the direction of the Moon is within the coverage range of the PME and the angular separation of the Moon and the Sun is  $>90^\circ$ . (An example of an according observation sequence is given in Section 6.5.3.) In addition, the coasting phases between the lunar flybys pose viable opportunities for uninterrupted observations of the lunar direction, due to the static spacecraft attitude. The trajectory of the baseline scenario examined here is especially favourable, as is illustrated in Figure 5.11, showing the Moon-centric flight path of DESTINY+ in the SSE reference frame. In between LFB-1 and LFB-2, the spacecraft goes out of the ecliptic reaching 350,000 km over the Moon’s North Pole. LFB-2 sends the spacecraft onto an excursion to translunar space, in a direction between the Earth antapex and Sun direction. Figure 5.12b shows the resulting angular separation of the Moon and Sun as seen from the spacecraft. In between LFB-1 and LFB-2, only

---

<sup>14</sup>Hoffmann et al. (1975a) defined the particle ‘groups’ as clusters of impact events where the ‘spacing in time between to consecutive events is more than 15 minutes but less than 2 hours.

<sup>15</sup>The Grün-flux gives the number flux in the particle mass range of  $10^{-21} \text{ kg}$  to  $0.1 \text{ kg}$  (Grün et al., 1985b), which we extrapolate to  $1 \text{ kg}$  using the constant slope of the distribution found to be valid by Grün et al. for masses  $>10^{-8} \text{ kg}$ , yielding a cumulated flux of meteoroids  $>1 \text{ kg}$  of  $3 \times 10^{-19} \text{ m}^{-2} \text{ s}^{-1}$  onto a spinning plate. Scaling to the surface area of the Moon one obtains an impact rate of  $\sim 1$  per day.

<sup>16</sup>The typical mass of individual group particles consistent with lunar origin were around  $10^{-15} \text{ g}$  to  $10^{-14} \text{ g}$  as determined by HEOS-2 (Hoffmann et al., 1975b).

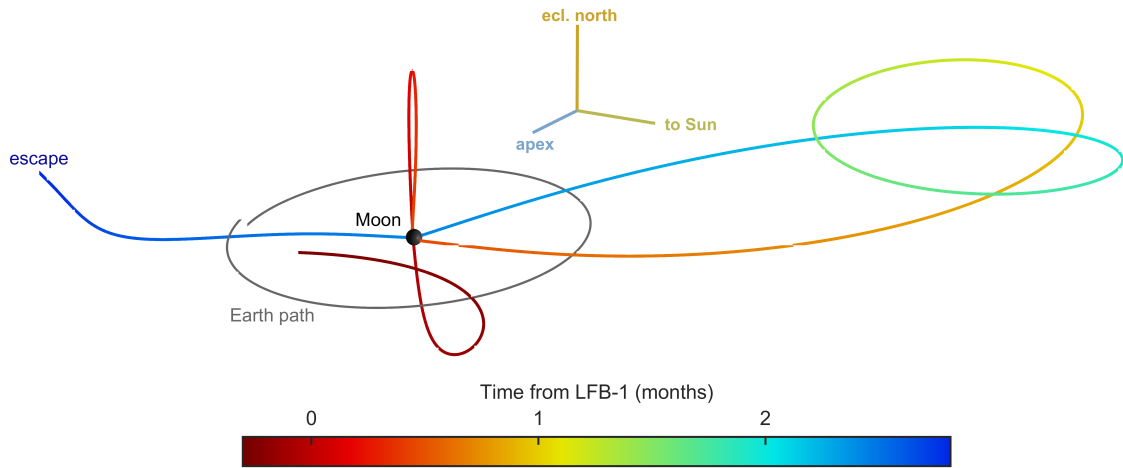


**Figure 5.11.:** Moon-centric view of the lunar gravity assist phase trajectory in the SSE reference frame. The first lunar flyby LFB-1 concludes the spiralling phase, after which the spacecraft enters a largely unpowered flight. In between LFB-1 & 2, the spacecraft goes out of the ecliptic reaching 350,000 km over the Moon’s North Pole. LFB-2 sends the spacecraft onto an excursion to translunar space, in a direction between the Earth antapex and Sun direction.

fractional exposure to the Moon direction would be possible, at a boresight angle of around  $25^\circ$ .<sup>17</sup> Yet, in between LFB-2 and LFB-3 continuous pointing toward the Moon direction is possible. By scaling of the HEOS-2 results, one could derive a total of  $\sim 25$  observable lunar group particles during this phase alone, although this does not take into account the relatively large distance to the Moon during this period (up 1.5 Mkm).

As with the diffuse ejecta cloud science campaign, one might expect periods around the annual meteor showers to be particularly promising for the detection of roaming ejecta clouds, due to the showers’ ability to enhance the flux of larger (i.e., centimetre-sized) meteoroids manifold (rather than that of micrometeoroids, see e.g., Moorhead et al., 2019, Figure 9). Indeed, seismic data from Apollo-deployed instruments on the lunar surface show a modest temporal correspondence of impactors assigned to the sub-kg class with the annual meteor showers (Oberst and Nakamura, 1991). However, in the super-kg impactor class, only marginal clustering was found, suggesting a deficiency of such massive meteoroids in meteoroid streams. Of the four distinct super-kg clusters that were observed, none could be unambiguously associated with a known meteor shower (see Oberst and Nakamura, 1991, Table 3). Yet, large variations in the impact rate still did occur (beyond what would be expected from a Poisson process), suggesting that a fraction of the super-kg meteoroids move as groups through interplanetary space (Duennebier et al., 1976). As for directionality, the rate of seismically-sensed impacts correlated with the experiment’s exposure to the known meteor radiants over the lunar cycle, that is, rates hiked when the territory spanned by the seismic networked faced the helion and anti-helion directions and plummeted when it faced the antapex (Oberst and Nakamura, 1991; Dainty et al., 1975). However, in the super-kg impactor class, this anisotropy disappeared (see Oberst and Nakamura, 1991, Figure 1), which could be explained by less eccentric (e.g., asteroid-like) orbits. The latter would also be consistent with Earth-based observations of meteors, indicating the flux predominance of asteroidal-origin meteoroids in the super-kg class, as found by Halliday et al. (1996). Based on these considerations, we assess the

<sup>17</sup>An off-axis angle of  $25^\circ$  corresponds to a fractional sensitive area of 31%, see Figure 4.3.

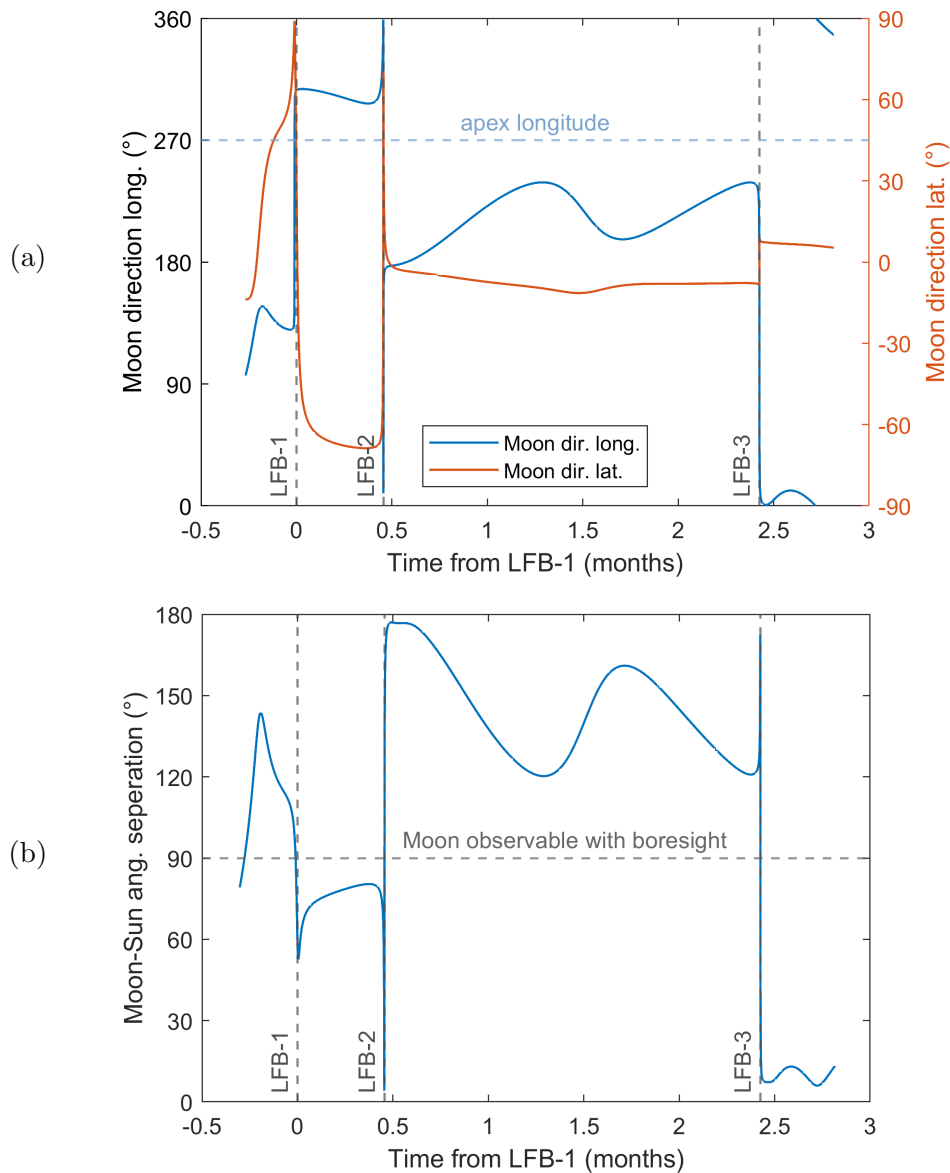


**Figure 5.12.:** Direction of the Moon during the lunar gravity assist phase as seen from the DESTINY+ spacecraft. (a): Longitude and latitude of the Moon direction in the SSE reference frame. The longitude of the Sun is at  $0^\circ$  and the longitude of the apex direction is at  $270^\circ$ . (b): Angular separation between the Moon and Sun direction. At an angular separation  $>90^\circ$  the DDA boresight can be pointed towards the Moon, without sunlight in the aperture.

temporal and directional influx of super-kg meteoroids (although not entirely sporadic) as largely unpredictable, suggesting the maximizing of total observation time of the lunar direction as an effective strategy for the detection of the roaming ejecta clouds.

With the ability to measure their dynamical properties (note that only one particle per group has to be sensed by DDA's trajectory sensor to determine the group velocity and direction), as well as the grain compositions, DDA may finally give unequivocal proof of the lunar origin of the EMS-roaming groups seen by HEOS-2. Moreover, the timing of the DESTINY+ mission may open up a unique opportunity for joint observation of impact processes from diverse vantage points. Enabled by its Commercial Lunar Payload Services (CLPS) initiative, NASA is planning a series of missions under the newly formed Payloads and Research Investigations on the Surface of the Moon (PRISM) programme, the second of which, PRISM-1b, will deliver a seismometer instrument suite

to the farside of the Moon with the intention to sense moonquakes and meteoroid impacts (NASA, 2021; Panning et al., 2022). PRISM-1b—similar to DESTINY<sup>+</sup>—is set to launch in the 2024/2025 timeframe, and the instrument suite is planned to be operated for several months, allowing for the possible correlation of DDA-detected roaming ejecta formations with impacts registered by the seismometers. Such a correlation was also attempted by Fechtig et al. (1979) with the HEOS-2-measured groups, drawing on the data of seismometers deployed by the Apollo missions and operated until 1977. Yet, due to the high number of impacts present in the seismic data combined with the uncertainty in the travel speed of the groups, a 1:1 association could not be achieved. Additional opportunities for joint investigation of this phenomenon may be provided by the observation of lunar impact flashes. Such observations can be conducted from Earth between new moon and half moon (for a total of about one week per lunar cycle) with a sensitivity down to sub-kg impactors (e.g., Melosh et al., 1993; Liakos et al., 2020). In one case, an ejecta cloud of micron-sized particles was detected escaping the Moon as the result of an impact, enabled by favourable viewing conditions near the terminator (Berezhnoy et al., 2019). Currently, JAXA’s EQUULEUS mission, among the first lunar exploration CubeSats, is demonstrating such observations from translunar space, although its operational lifetime is projected to end before the launch of DESTINY<sup>+</sup> (Funase et al., 2020). On the other hand, ESA is considering the (presently in phase-B study) LUnar Meteoroid Impacts Observer (LUMIO), which is a dedicated 12U CubeSat observatory for the Earth-Moon L<sub>2</sub> to scout for lunar farside impact flashes, caused by meteoroids in the 0.1 kg to 1000 kg mass range (Cervone et al., 2022; Merisio and Topputo, 2023). With LUMIO’s operational phase currently foreseen for 2027, correlation of impact flashes with DDA group detections, or even short-term predictions of group encounters by DESTINY<sup>+</sup> and according detector pointing instructions (given the group’s travel time through the EMS of up to several days) may be possible.

### 5.2.3. The lunar dust torus

In addition to the diffuse lunar dust cloud and the roaming lunar ejecta groups, it has been considered that the Moon could sustain an appreciable, diffuse Earth-bound population of lunar ejecta particles, that would take the form of a geocentric toroidal structure. Such a population would be analogous to the faint ‘dust tori’ associated with ejecta generation from other solar system moons, such as the ‘gossamer’ rings of Jupiter (e.g., Burns et al., 1999; Krüger et al., 2009) or the putative Martian dust belts presumably generated by Phobos and Deimos (e.g., Krivov and Hamilton, 1997; Liu and Schmidt, 2021).<sup>18</sup> However, in the case of the Moon, the injection of dust into bound orbits must be expected to be relatively inefficient due to the narrow velocity range required for ejecta to enter bound orbits around the Earth. This inefficiency is a result of the Moon’s comparatively high gravity, effectively retaining too slow ejecta,<sup>19</sup> on the one hand, and the Moon’s large distance to the Earth, facilitating the escape of too fast ejecta into interplanetary space,<sup>20</sup> on the other.

This circumstance led early investigations to conclude that the quantity of lunar ejecta released

<sup>18</sup>Although often referred to as such, these formations technically aren’t tori but rather flared discs around the central planet.

<sup>19</sup>Compare the Moon’s escape velocity of 2.38 km s<sup>-1</sup> to that of Phobos and Deimos, 11.4 m s<sup>-1</sup> and 5.6 m s<sup>-1</sup>, respectively, or that of Jupiter’s Amalthea and Thebe, both <100 m s<sup>-1</sup> (Burns et al., 1999).

<sup>20</sup>Compare the Moon’s location at 0.26 R<sub>Hill</sub> to that of Phobos and Deimos, at 0.0095 R<sub>Hill</sub> and 0.0239 R<sub>Hill</sub>, respectively, or that of Jupiter’s Amalthea and Thebe, at 0.0036 R<sub>Hill</sub> and 0.0044 R<sub>Hill</sub>, respectively. Compare also the local system escape speed at the Moon’s orbit of 1.45 km s<sup>-1</sup> to that at the orbits of Phobos and Deimos, 3.0 km s<sup>-1</sup> and 1.9 km s<sup>-1</sup>, respectively, or at Jupiter’s Amalthea and Thebe, 38 km s<sup>-1</sup> and 34 km s<sup>-1</sup>, respectively.

---

into prolonged geocentric orbits is negligible, and as such, no substantial enhancement of the near-Earth dust abundance due to lunar dust should be expected (Colombo et al., 1966). Recently, Yang et al. (2022) made another attempt to model this quasi-static population, enabled by modern computational resources and insights into the ejecta mass production obtained through the LADEE mission. Yang et al. find that grains smaller than a few microns cannot remain in geocentric orbits for significant durations (i.e., longer than  $\sim 1$  month), particularly due to the perturbing effect of solar radiation pressure. Larger particles, however, were found to sustain a permanent toroidal structure, whose density increases towards the Earth, reaching particle number densities of up to  $1 \text{ km}^{-3}$ . The authors point out that the modelled densities are about four and five orders of magnitude lower than predictions for the tori of Phobos and Deimos, respectively. For an apex pointing plate detector in a circular geocentric orbit at  $10 R_{\oplus}$ , this amounts to a flux of  $50 \text{ m}^{-2} \text{ yr}^{-1}$ , generated particularly by a substantial fraction of lunar ejecta particles in retrograde orbits (around 40%),<sup>21</sup> whose flux is significantly amplified due to the high relative velocities with respect to the prograde observer. The authors note that this is still a factor of several below the IPD flux at comparable particle sizes.

For the DDA sensor geometry, this would translate to an incidence rate of  $1.5 \text{ yr}^{-1}$ , assuming an entirely collimated flux from the sensor boresight,<sup>22</sup> and an incidence rate of  $0.2 \text{ yr}^{-1}$ , assuming a flux entirely isotropic at the spacecraft.<sup>23</sup> Considering these estimates, as well as the uncertainties of the model, it is plausible that DDA might detect one or a few Earth-bound lunar ejecta particles over its entire near-Earth mission phase, although the predictions hardly warrant a dedicated search for such grains. However, since their flux would be expected to occur predominantly from the spacecraft’s Earth-centric apex direction (due to the retrograde orbits) and since the DDA coverage range is centred on the apex direction (due to the changing spacecraft attitude during the spiralling phase, see Section 3.2), the DDA sensor is well suited to detect such particles, should they exist in adequate numbers. Their characteristic dynamics—Earth-bound and retrograde—would also allow for the straightforward identification of ‘lunar torus particles’ with DDA.

---

<sup>21</sup>The retrograde component of the torus is a consequence of radiation pressure perturbation, causing bound particles to oscillate between prograde and retrograde motion (Yang et al., 2022).

<sup>22</sup>Computed as  $50 \text{ m}^{-2} \text{ yr}^{-1} \cdot A_{0,\text{DDA}}$ .

<sup>23</sup>Found by scaling of the incidence rate onto the unit-plate detector with the ratio of the respective geometric factors, i.e.:  $50 \text{ m}^{-2} \text{ yr}^{-1} \cdot A_{0,\text{plate}} \cdot \frac{G_{\text{DDA}}}{G_{\text{plate}}} = 50 \text{ yr}^{-1} \cdot 0.0046$ .

### 5.3. Interplanetary dust

The characterization of the multifaceted interplanetary dust (IPD), which we introduced in Section 2.1.2, is a key objective of the DDA. Here, we analyse different conceptual groups of IPD, depending in large part on their size regime. To get an impression of the abundance of IPD encountered by DDA (in terms of impact rates), we first examine the Grün-flux with respect to the sensor's geometry, before turning to the different types of IPD at 1 au, including the dust component of the sporadic meteoroid complex, the  $\alpha$ - &  $\beta$ -meteoroids, cometary streams, as well as dust trapped in orbital resonances.

#### 5.3.1. The Grün-flux

The Grün-model for the quantitative state of the inner solar system IPD cloud—commonly referred to as the ‘Grün-flux’—is widely recognized as the first consistent and reasonably accurate representation of the IPD flux encountered at cloud at 1 au. Conceived by Grün et al. (1985b) by correlating the size distribution of microcraters on lunar rock (returned by the Apollo missions) with the in-situ data on micrometeoroids gathered by the Pegasus and Helios missions, the Grün-flux is still used as a reference for more recently developed models, if it is not as an integral part of them. Specifically, the Grün-flux gives the cumulative mean number flux of particles over particle mass onto a spinning flat plate detector in a circular heliocentric orbit at 1 au, as seen in Figure 5.13.

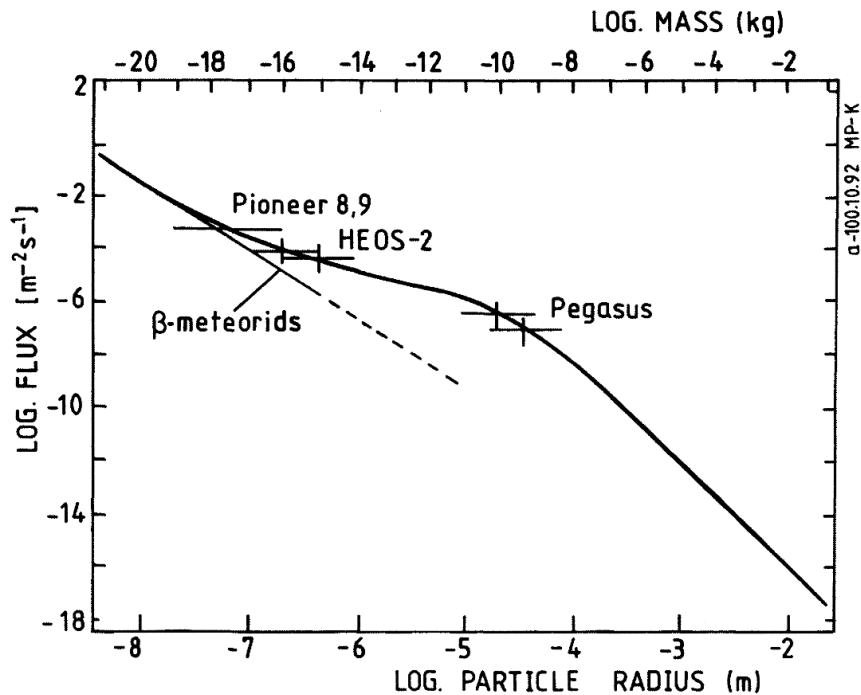


**Figure 5.13.:** The Grün-flux (plot taken from Grün et al., 2001) gives the cumulative flux of IPD particles at 1 au distance from the Sun onto a spinning flat plate detector (with a rotation axis perpendicular to the ecliptic). Particle radii are calculated from the particle masses using a density of  $2.5 \text{ g cm}^{-3}$ .

As DESTINY<sup>+</sup> will remain fairly close to 1 au throughout its nominal mission, the Grün-flux is a valid reference for the number of IPD particles observable by DDA, at different particle sizes. Based on the geometric characteristics derived in Section 4.2, we may convert the Grün-flux to an

equivalent incidence rate onto DDA. Assuming an isotropic flux, the cumulative incidence rate onto DDA is found by scaling the Grün-flux incidence rate onto the unit-plate detector with the ratio of the respective geometric factors, that is:

$$I_{\text{DDA,Grün,iso}} = F_{\text{Grün}} \cdot A_{0,\text{plate}} \cdot \frac{G_{\text{DDA}}}{G_{\text{plate}}} = F_{\text{Grün}} \cdot 1 \text{ m}^2 \cdot 0.0046 \quad (5.4)$$

On the other hand, we may assume an entirely collimated flux to be generating the Grün-flux onto the spinning plate, which may be more realistic in certain size regimes. The flux thus resulting on a plate detector pointing into that collimated flow can be calculated as:

$$F_{\text{Grün,coll}} = F_{\text{Grün}} / \chi_{\text{spin.-plate}} \quad (5.5)$$

where  $\chi_{\text{spin.-plate}}$  is the detection efficiency of the spinning plate detector with respect to the collimated flux.  $\chi_{\text{spin.-plate}}$  is calculated as the normalized average area the plate detector exposes towards a collimated flow (with detector spin rotation axis perpendicular to the flow)<sup>24</sup>:

$$\chi_{\text{spin.-plate}} = \frac{1}{2\pi} \int_{-\pi}^{\pi} \eta_{\text{plate}}(\theta) d\theta \quad (5.6)$$

where  $\eta_{\text{plate}}(\theta)$  is the angular sensitivity of the plate detector (i.e., the projected area under an incidence angle  $\theta$  relative to the total area, see Equation 4.1). For the one-sided plate detector the angular sensitivity is calculated as:

$$\eta_{\text{plate}}(\theta) = \cos(\theta) \cdot H\left(\theta - \frac{\pi}{2}\right) \quad (5.7)$$

where  $H$  is the Heaviside function. Inserting into Equation 5.6 yields:

$$\chi_{\text{spin.-plate}} = \frac{1}{2\pi} \int_{-\pi/2}^{\pi/2} \cos(\theta) d\theta = \frac{1}{\pi} \quad (5.8)$$

Finally, we can calculate  $F_{\text{Grün,coll}}$  with Equation 5.5 and then the incidence rate onto DDA pointing into that flux as:

$$\begin{aligned} I_{\text{DDA,Grün,coll}} &= F_{\text{Grün,coll}} \cdot A_{0,\text{DDA}} = F_{\text{Grün}} \cdot \pi \cdot 0.03 \text{ m}^2 \\ &\approx 20.5 \cdot I_{\text{DDA,Grün,iso}} \end{aligned}$$

Neither of these assumptions is entirely realistic, as none of types of IPD which the Grün-flux represents are completely isotropic or entirely collimated. Rather, they are expected to exhibit varying degrees of anisotropy (as we shall see), which means their actual incidence rates should lie between the incidence rates derived here. In other words, the derived incidence rates can be understood as upper and lower bounds, assuming that knowledge about the anisotropy is used to guide the instrument pointing. In the case of a highly collimated flow of dust and a sensor orientation away from that flow, of course, the incidence rate will be lower than the ‘lower bound’ derived here based on the isotropic flow assumption. The resulting curves are shown in Figure 5.14.

<sup>24</sup>This assumes that the collimated flow is parallel to the ecliptic, which is an adequate assumption for the more directional populations that the Grün-flux incorporates ( $\alpha$  &  $\beta$ -meteoroids).

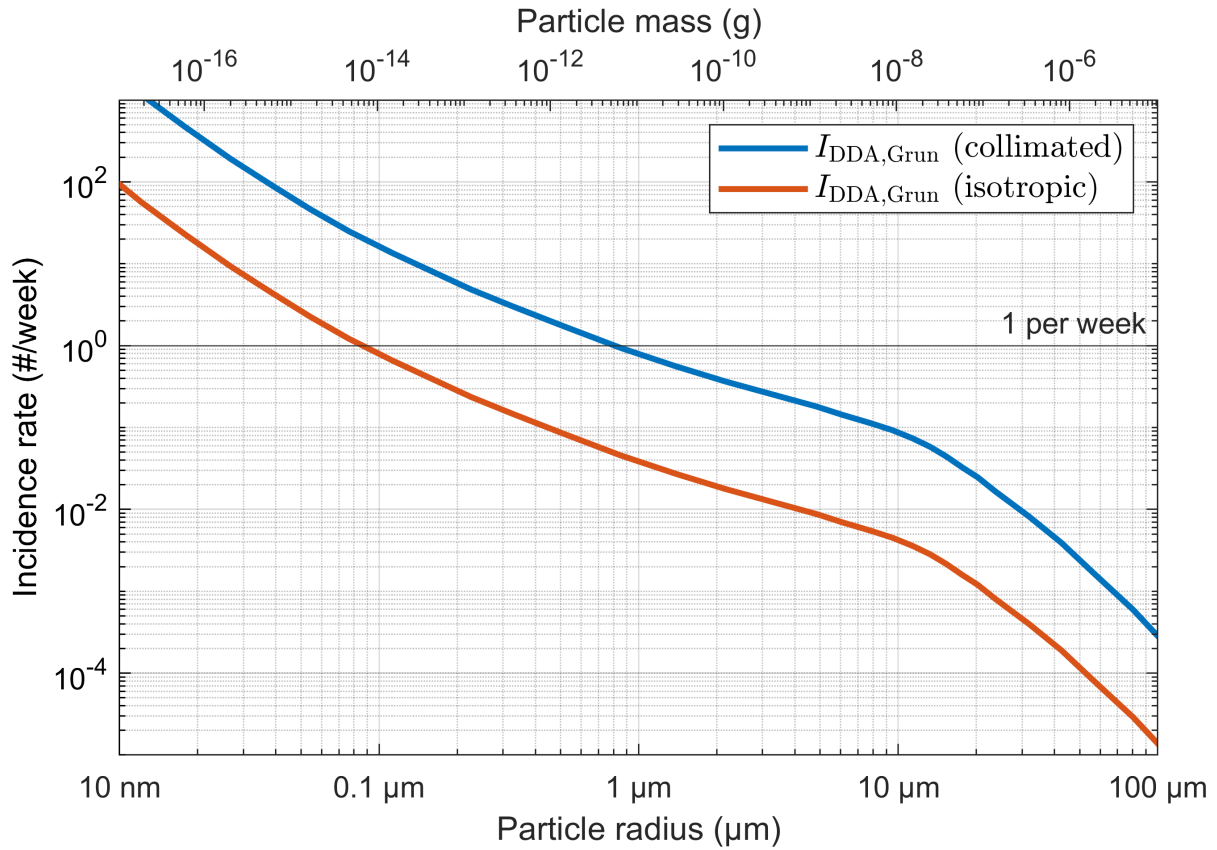


**Figure 5.14.:** The Grün-flux converted to incidence rates for DDA under two different assumptions: (Orange) the Grün-flux is isotropic and the sensor pointing is arbitrary, and (blue) the Grün-flux is collimated and the sensor points straight into the dust flow (see text). Particle radii are converted from the particle masses using a density of  $2.5 \text{ g cm}^{-3}$ .

From the corridor spanned by these curves, we can now estimate the incidence rate onto DDA at different minimum particle sizes. Due to the steepness of the Grün-flux, the incidence rate at any minimum particle size is governed by particles in the size range close to the chosen minimum. In other words, it can be considered that the incidence rate at a given size threshold is mostly in the form of particles with sizes close the threshold. Therefore, it is adequate to consider different size regimes separately with regard to their anisotropy and, thus, resulting incidence rates. For instance, particles with radii  $>5 \mu\text{m}$  may exhibit little anisotropy and, hence, an incidence rate closer to the ‘lower bound’ curve in Figure 5.14 may be anticipated ( $I_{\text{DDA,Grün,iso}}(s>5 \mu\text{m}) \approx 0.01 \text{ week}^{-1}$ ). On the other hand, particles in the one-micron range may be expected to be highly anisotropic, therefore, an incidence rate closer to the ‘upper bound’ curve could be estimated (e.g.,  $I_{\text{DDA,Grün,coll}}(s>0.5 \mu\text{m}) \approx 1.7 \text{ week}^{-1}$ ), if the detector is oriented toward that anisotropic flow.

Indeed, Grün et al. found that different types IPD with distinctive dynamical behaviour generally also occupy different size regimes: By analysis of the data of the first generation of impact plasma detectors, Pioneer 8/9, HEOS-2, and Helios on the dynamics of impacting IPD grains, Grün and Zook (1980) propose a classification scheme into three groups (mass ranges from Grün et al., 1985b):

1.  **$\beta$ -meteoroids:** Grains on hyperbolic trajectories; approach direction from the Sun;<sup>25</sup> Represent the smallest detected particles:  $m < 10^{-13} \text{ g}$ .
2.  **$\alpha$ -meteoroids:** Grains on low-perihelion, highly eccentric orbits; encountered near their

<sup>25</sup>As seen from an observer in a circular heliocentric orbit at 1 au from the Sun.

aphelion and thus exhibiting an approach direction from the apex direction;<sup>25</sup> Represent intermediate detected masses:  $10^{-13} \text{ g} < m < 10^{-11} \text{ g}$ .

3. **Sporadic meteoroids:** Grains on high angular momentum orbits; no pronounced directionality;<sup>25</sup> Represent the largest detected masses:  $m > 10^{-11} \text{ g}$ .

In summary, Grün et al. argue that the first two types,  $\beta$ -meteoroids and  $\alpha$ -meteoroids, are produced in collisions between larger grains at short heliocentric distances (see Figure 5.15). The third type of detected particles they consider to be the lower-mass-end (i.e., the dust component) of the sporadic meteoroid complex, which are meteoroids that have dispersed away from their parent body enough as to not be identified as part of a specific stream (i.e., they are ‘sporadic’), yet which may still retain their dynamical linkage to their parent body family, for instance JFCs or main-belt asteroids.<sup>26</sup> In the following, we dive deeper into the nature of these three types of IPD, as well as their observability through DDA—especially with regard to their dynamics and anisotropy, which are key factors in conceiving a detection and characterization strategy.

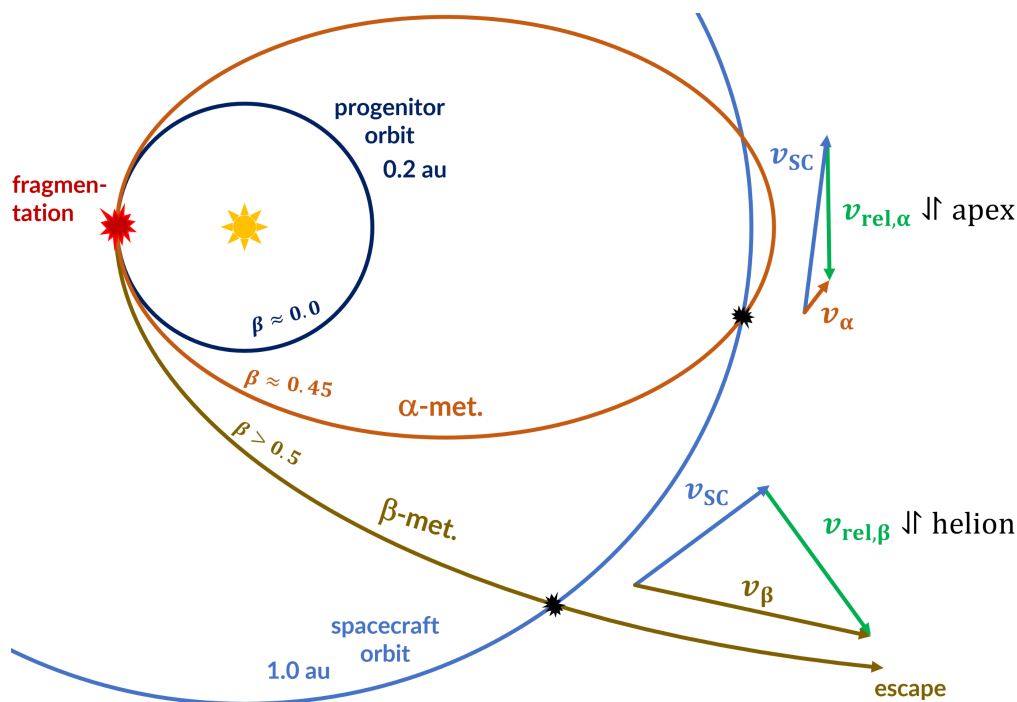


**Figure 5.15.:** Orbits of  $\alpha$ - &  $\beta$ -meteoroids in the sense of Grün and Zook (1980): A progenitor meteoroid close to the Sun fragments into grains with different  $\beta$ -factors, thus released into different orbits, which are either elliptical ( $\alpha$ ) or hyperbolic ( $\beta$ ). Also shown are their typical detection conditions and according velocity vector additions, explaining the different approach direction; from the apex ( $\alpha$ ) and from the Sun ( $\beta$ ).

### 5.3.2. Beta-meteoroids

One of the most well-regarded findings of the first viable, highly sensitive impact plasma detectors flown on the Pioneer 8/9 probes, was the discovery of submicron-sized grains on hyperbolic trajectories appearing to emanate from the Sun (Berg and Grün, 1973). Zook and Berg (1975) showed that the Pioneer 8/9 data is consistent with the production of hyperbolic particles in collisional

<sup>26</sup>Larger sporadic meteoroids are also observable as radar or even visual meteors, which as allowed for the extensive characterization of their anisotropy (at least at sizes  $>100 \mu\text{m}$ ) with the six major, broad radiants: north/south apex, north/south toroidal, helion, and anti-helion (e.g., Campbell-Brown, 2008), see also Section 2.1.2.

---

breakups of meteoroids near the Sun, a mechanism previously proposed by Dohnanyi (1971). As micrometeoroids spiral inward under the Poynting-Robertson (PR) drag, their concentration and relative velocities increase with decreasing solar distance, eventually causing them to suffer grain-grain collisions. Submicron fragments, having much larger area-to-mass ratios than the colliding parent grains, suddenly receive a significant influence from solar radiation pressure, which may sweep them away on unbound trajectories. Denoting the effective strength of the radiation pressure for a given particle as the quantity  $\beta$  (which relates the radiation pressure force to the solar gravitational force), Zook and Berg (1975) introduce the term  $\beta$ -meteoroid for particles whose orbits are significantly shaped by radiation pressure. Since then, the term  $\beta$ -meteoroid has come to be used to refer only to those particles that emanate from the Sun on hyperbolic trajectories.

The escaping  $\beta$ -meteoroids were subsequently confirmed by dust detectors onboard the Helios (Grün et al., 1980) and later Ulysses spacecraft (Baguhl et al., 1995; Wehry and Mann, 1999). Other mechanisms have been proposed to be able to generate  $\beta$ -meteoroids, such as sublimation of grains in the heat of the Sun (e.g., Mukai and Yamamoto, 1979; Kobayashi et al., 2009), or of rotational bursting of grains spun up by solar radiation (e.g., Misconi, 1993; Herranen, 2020). The study of the  $\beta$ -meteoroids thus remains of high scientific interest, being seen as a window of insight into the near-Sun physics that enable their creation.

Since the  $\beta$ -meteoroids approach an observer in a circular heliocentric orbit at 1 au, roughly from the direction of the Sun, and since it is a requirement of DDA not to have direct sunlight fall into the instrument aperture, one is tempted to *a priori* rule out the study of  $\beta$ -meteoroids with DDA. Here, we test this presumption by searching for trajectories of unbound  $\beta$ -meteoroids that are possibly detectable with DDA, without violating its flight rules. To that end, we evaluate the dynamics of particles that impact an apex-pointing plate detector, in dependence of their impact angle and velocity, as well as their  $\beta$ -factor.<sup>27</sup> The result is shown in Figure 5.16 for approach angles between  $90^\circ$  (coming from the Sun direction) and  $0^\circ$  (coming from the apex direction),<sup>28</sup> and impact speeds from  $0$ – $65 \text{ km s}^{-1}$ . White contours separate impactors on bound and unbound, as well as pro- and retrograde trajectories. For the apex-pointing DDA (an orientation that just avoids sunlight in the aperture), only impact angles  $<45^\circ$  (DDA’s maximum entry angle) are detectable, as indicated by a black dashed line. Shaded areas indicate impactor trajectories with perihelia  $>0.5 \text{ au}$ , which we disregard, given the constraint on  $\beta$ -meteoroid perihelion distances to  $0.5 \text{ au}$  indicated by Ulysses measurements (Wehry and Mann, 1999; Wehry et al., 2004).

At  $\beta=0.5$ , unbound grains may only impact at angles  $<45^\circ$  if they are on retrograde orbits. Going to higher  $\beta$ -factors, a growing range of possible impact angle and velocity combinations manifests, that correspond to particles on unbound prograde trajectories. However, these belong to particles that could only be released from progenitor meteoroids moving on highly eccentric orbits ( $e>0.7$ ), which is incompatible with the common assumption that such meteoroids, after having evolved and circularized under PR drag to reach short heliocentric distances, should exhibit low eccentricities (e.g., see review by Mann et al., 2004). In Figure 5.17, impactors stemming from progenitors with

---

<sup>27</sup>This analysis assumes that particles are created from fragmentation of progenitor meteoroid orbits that move within the ecliptic (i.e., inclinations of  $0^\circ$  or  $180^\circ$ ) at an arbitrary eccentricity.

<sup>28</sup>Approach directions from ‘behind’ (incidence angles onto the apex-facing plate of  $>90^\circ$ ) are disregarded, as they require particles to be ejected from progenitor meteoroids moving on highly eccentric orbits, with perihelia close to  $1 \text{ au}$ , which is incompatible with the known low perihelia of the  $\beta$ -meteoroids, as derived from previous observations (Wehry et al., 2004).

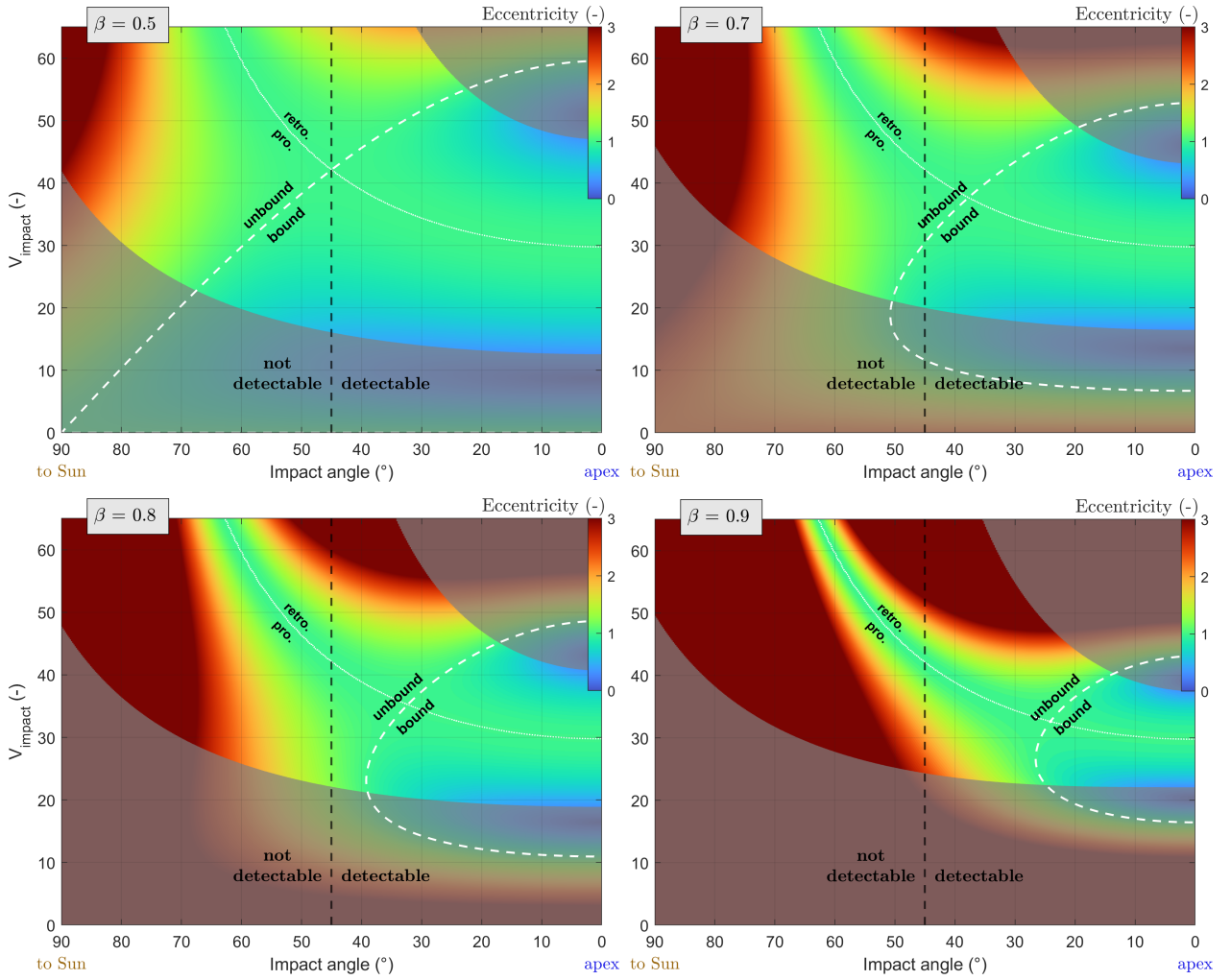


**Figure 5.16.:** Dynamics of particles impacting an apex-facing plate detector in a circular heliocentric at 1 au, dependent on impact angle, impact velocity, and  $\beta$ -factor. White contours separate impactors on bound and unbound, as well as pro- and retrograde trajectories. Impact angles  $< 45^\circ$  (right side of the dashed black line) are detectable by the apex-facing DDA. Shaded areas indicate impactor trajectories with perihelia  $> 0.5$  au.

$e > 0.7$  (calculated assuming that fragmentation occurs at perihelion) are additionally excluded (shaded). This puts little constraint on impactors of  $\beta = 0.8$  (Figure 5.17-left), but for  $\beta = 0.9$  virtually no impact angle and velocities combinations corresponding to unbound prograde particles remain at impact angles  $< 45^\circ$ . From Figure 5.17 one could infer that certain  $\beta$ -meteoroids, with  $\beta \approx 0.8$ , are detectable by DDA at approach angles of around  $40^\circ$  from the apex direction. Yet, with a fractional sensitivity of the sensor at such large entrance angles in the order of 10% (see Section 4.2), detection efficiency must be considered negligible.

Thus, we conclude that, as expected, prograde  $\beta$ -meteoroids are nearly undetectable by DDA, without allowing sunlight to enter the instrument aperture. Retrograde  $\beta$ -meteoroids may be detected by the apex-facing DDA at impact angles  $> 20^\circ$ . While a fraction of the Ulysses-measured  $\beta$ -meteoroids are compatible with a retrograde motion, Wehry and Mann (1999) argue that, due to selection effects of the sensor, the detected  $\beta$ -meteoroids should move predominantly on prograde trajectories.

For completeness, estimates for the incidence rate of  $\beta$ -meteoroids for DDA pointing into the flow of  $\beta$ -meteoroids may still be given: Evaluating the DDA incidence rates derived from the Grün-flux

(Figure 5.14) at  $\beta$ -meteoroid masses of  $m > 10^{-15}$  g (see Wehry and Mann, 1999, Figure 5) yields  $I_{\text{DDA,Grün,iso}} \approx 2.5 \text{ week}^{-1}$  and  $I_{\text{DDA,Grün,coll}} \approx 45 \text{ week}^{-1}$ . Considering the strong anisotropy of the  $\beta$ -meteoroid flow, one could thus expect a detection rate in the 10s of particles per week, if DDA were to point toward the Sun.

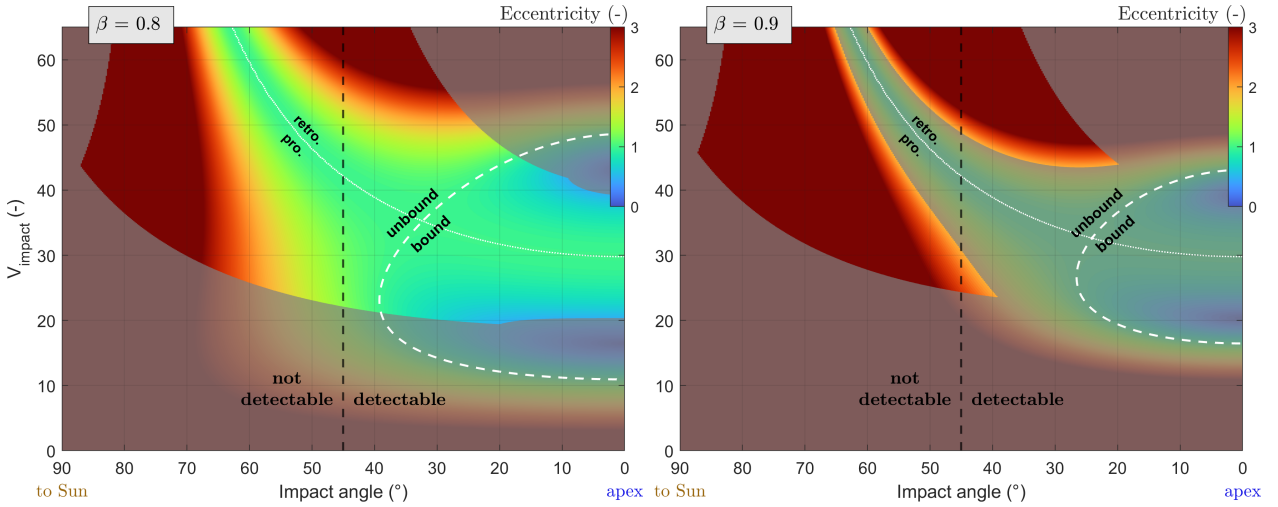


**Figure 5.17.:** Dynamics of particles impacting an apex-facing plate detector in a circular heliocentric at 1 au, dependent on impact angle, impact velocity, and  $\beta$ -factor. White contours separate impactors on bound and unbound, as well as pro- and retrograde trajectories. Impact angles  $< 45^\circ$  (black line) are detectable by the apex-facing DDA. Shaded areas indicate impactor trajectories with perihelia  $> 0.5$  au, as well as impactors stemming from parent bodies with  $e > 0.7$ .

Nonetheless, the dynamics of impactors shown in Figures 5.16 and 5.17, also reveal bound prograde orbits emerging from the fragmentation of the  $\beta$ -meteoroid progenitors, that the apex-facing DDA is sensitive to. These belong to the group of the  $\alpha$ -meteoroids, as defined by Grün and Zook (1980), which we turn our attention to in the next section.

### 5.3.3. Alpha-meteoroids

Originally, the term  $\beta$ -meteoroid was introduced by Zook and Berg (1975) not only to describe the unbound submicron dust particles, but all particles whose orbits trajectories were significantly altered by radiation pressure from purely gravitational orbits. In particular, this referred to fragments produced along with the hyperbolic  $\beta$ -meteoroids that are slightly too massive to be expelled by radiation pressure and that would instead be launched onto highly eccentric orbits with low perihelia, as illustrated in Figure 5.15. At a heliocentric distance of 1 au such particles would be on their outer orbital arc, moving at velocities much lower than the circular orbital speed. A detector at 1 au would thus ‘overtake’ these particles on its path around the Sun, detecting them as coming from around the apex direction of the observer’s orbit. Those that are created with aphelia near 1 au would be the most massive particles of this kind detectable, with an apparent approach most closely from the apex direction.

This is consistent with the data of the Pioneers, showing that, while impactors from the Sun direction are the most numerous (the hyperbolic  $\beta$ -meteoroids), the average energy per impact reaches a maximum centred at the apex direction (Zook and Berg, 1975, Figure 1). Moreover, the highest energy impactors reached a second sensor after penetrating the first, allowing for a TOF speed measurement, indeed revealing the highly eccentric orbits of the prograde, bound population

---

(Berg and Gerloff, 1970; Berg and Gerloff, 1971; Wolf et al., 1976). These measurements were reinforced by the HEOS-2 data, indicating an excess of apex flux of one order of magnitude over the anti-apex, ecliptic north, and south directions, as well as an average impact velocity of these ‘apex particles’ of  $10 \text{ km s}^{-1}$ , consistent with particles being outpaced near their aphelion (Hoffmann et al., 1975a,b).

After Pioneer 8/9 and HEOS-2, the Helios spacecraft, orbiting the Sun on eccentric orbits between 0.3 au and 1 au, delivered more revealing in-situ dust data (Grün et al., 1980). Interpreting the consistent findings of Pioneer 8/9, HEOS-2, and Helios, Grün and Zook (1980) come to the conclusion that the apex particles constitute a distinct class of meteoroids for which they introduce the term  $\alpha$ -meteoroids. In subsequent works, the Helios data are further analysed to characterize the  $\alpha$ -meteoroids, yielding: their mass range  $10^{-13} \text{ g} \lesssim m \lesssim 10^{-11} \text{ g}$ ;<sup>29</sup> their (broadly distributed) low semi-major axes and high eccentricities with averages of  $\bar{a} \approx 0.6 \text{ au}$  and  $\bar{e} \approx 0.6$ ; as well as a constraint on their average inclination of  $\bar{i} < 30^\circ$  (Grün, 1981; Grün et al., 1985a).

Here we investigate the  $\alpha$ -meteoroids as a scientific objective for DDA. It stands to reason that, due to their predominance in the datasets of Pioneer 8/9, HEOS-2, and Helios, they will also be the most numerous IPD type detectable by DDA. Before quantifying their detectability by DDA, however, we first spotlight a terminological confusion around the  $\alpha$ -meteoroids, which has led to a transition of meaning of the term, and, consequentially, to the original  $\alpha$ -meteoroids being overlooked by contemporary in-situ dust research. Then we assess their dynamics with respect to possible creation pathways to point out the incompatibility of the original  $\alpha$ -meteoroids with the adopted meaning of the term. This is also to stress the importance of the further characterization of the  $\alpha$ -meteoroids, to come to terms with their classification and nature. For the details on the literature around the term  $\alpha$ -meteoroids, the dynamical assessments, as well as the implications of the existence for other in-situ dust experiments the reader is referred to Sommer (2023), a focussed, qualitative investigation of the  $\alpha$ -meteoroids, of which the most important parts are summarized here.

### **Ambiguity of the term ‘ $\alpha$ -meteoroid’**

After their characterization by the Helios mission, interest in the  $\alpha$ -meteoroids subsided, owing to the growing popularity of in-situ cosmic dust research on the outer solar system and the interstellar component, for instance, onboard Galileo (Grün et al., 1992b; Krüger et al., 1999), Ulysses (Grün et al., 1992a; Krüger et al., 2007), and Cassini (Srama et al., 2004b; Altobelli et al., 2016). Only few publications take up the  $\alpha$ -meteoroid term in the sense of Grün and Zook (1980) (e.g., Shestakova and Tambovtseva, 1995; Wehry and Mann, 1999), whereas others adopt the term ‘apex particles’ to refer to this class of in-situ-measured grains, having identified them in datasets of MDC, as well as GORID (e.g., Igenbergs et al., 1991; Iglseider et al., 1993, 1996; Svedhem et al., 2000; McDonnell et al., 2001).

However, the  $\alpha$ -/ $\beta$ -meteoroid terminology is then adopted in the domain of circumsolar disc modelling, where it is used to describe the two components of discs in general, that is, bound and unbound dust (Artymowicz and Clampin, 1997; Artymowicz, 1997, 2000; Krivova et al., 2000b; Krivova et al., 2000a; Krivov et al., 2000, 2006; Mann et al., 2006; Freistetter et al., 2007; Krivov,

---

<sup>29</sup>The  $\alpha$ -meteoroids mass range corresponds to radii between  $0.2 \mu\text{m}$  and  $1 \mu\text{m}$  at  $\rho = 2.5 \text{ g cm}^{-3}$ .

---

2010; Kral et al., 2017). Thereby, meaning of the term  $\alpha$ -meteoroids is extended to collisionally evolving grains of all sizes—instead of only those significantly affected by radiation pressure. More recently, this usage is transpiring back into the context of in-situ dust detection (Mann and Czechowski, 2021; Pusack et al., 2021; Szalay et al., 2021). In the solar system’s zodiacal cloud, the broad size regime covered by the adopted meaning arguably includes grains that evolve and circularize under PR drag, after having been released from their cometary or asteroidal source bodies (or from larger, collisionally evolving meteoroids whose orbital properties are still similar to those of their source bodies). Therefore, under the new definition, the  $\alpha$ -meteoroids are generally considered to have circular orbits, such as by Szalay et al. (2021), who use a two-component ( $\alpha/\beta$ ) zodiacal cloud model of bound (circularized) and unbound particles to simulate the influx onto the Parker Solar Probe.

The new usage is in contrast to the grains originally referred to as  $\alpha$ -meteoroids (or apex particles), which have a narrow size range and exhibit large eccentricities with low perihelia. The attained ambiguity of the term  $\alpha$ -meteoroid is not easily resolved, though one might be tempted to use a different name for the originally referred-to particles: The term ‘apex particles’ seems straightforward and descriptive, but carries meaning only in the context of in-situ detection from certain orbits. The Helios probe, itself on a high-eccentricity orbit (with peri- and aphelion of roughly 0.3 au and 1 au), observed this population to impact from the apex direction only when sufficiently far from aphelion. Around its low-momentum aphelion, relative velocities with respect to the apex particles diminished, causing them to lose their directional signature (Grün et al., 1985a). This term also bears the risk of confusing the particles with the meteoroids that approach the Earth from the apex direction, generating the north/south apex radiants seen in radar meteors. These grains move on retrograde orbits, stemming from Halley-type and Oort cloud comets (e.g., Nesvorný et al., 2011a; Pokorný et al., 2014), and have no dynamical relation with the apex particles discussed here. A suitable replacement for the original  $\alpha$ -meteoroid term may be ‘bound  $\beta$ -meteoroids’, which is descriptive and conveys the relatedness to the hyperbolic  $\beta$ -meteoroids. However, for the purpose of brevity, this author still favours a return to the original  $\alpha$ -meteoroid meaning. Throughout this thesis, the term  $\alpha$ -meteoroids is thus used in the sense of Grün and Zook (1980), referring to the micron sized grains on eccentric, low-perihelion orbits.

### Origin of the $\alpha$ -meteoroids

The limited coverage of the original  $\alpha$ -meteoroids warrants a new and closer look at the dynamics and possible origins of the dust particles at hand, which we will take in this section. The determined particle mass range of  $10^{-13} \text{ g} < m < 10^{-11} \text{ g}$  suggests that the motion of the  $\alpha$ -meteoroids is characterized by the radiation pressure PR drag. The PR drag causes a particle’s orbit to decay towards the Sun, while additionally circularizing eccentric orbits, as discussed in Section 2.2. Understanding how this connects to the low perihelia and high eccentricities present in the  $\alpha$ -meteoroids—which are their defining qualities—is essential when investigating their nature.

Already with the first direct speed measurements of particles impacting the Pioneer sensors, Berg and Gerloff (1970) note an incompatibility with direct asteroidal or cometary origin, and Zook and Berg (1975) as well as Grün and Zook (1980) conclude that the derived dynamics favour a collisional origin close to the Sun, akin to the generation of hyperbolic  $\beta$ -meteoroids. The underlying

argument is this: Since the PR drag circularizes orbits before substantially lowering perihelia, the low-perihelion and high-eccentricity orbits of the  $\alpha$ -meteoroids, could not have evolved from initially asteroidal or cometary orbits. To illustrate this proposition, we can analyse the evolution of perihelion and eccentricity of particles released from different sources.

For a particle evolving under the PR effect the semi-major axis and eccentricity decrease with time, while, as shown by Wyatt and Whipple (1950), the quantity  $C$  remains constant:

$$C = a e^{-4/5} (1 - e^2) = \text{constant} \quad (5.9)$$

where  $a$  and  $e$  are the semi-major axis and eccentricity of the particle at any arbitrary time. The above formulation of  $C$  is obtained by dividing and integrating the analytically derived time derivatives of semi-major axis and eccentricity of a PR-perturbed orbit, namely,  $da/dt$  (Equation 2.1) and  $de/dt$  (Equation 2.2). Note that, although  $C$  is in the dimension of  $a$ , it has no straightforward geometric representation. Since  $a = q / (1 - e)$ , where  $q$  is the perihelion distance, we can write

$$C = q e^{-4/5} (1 + e) = \text{constant} \quad (5.10)$$

Once a particle is released from a source body and assumes a new semi-major axis and eccentricity at the onset of solar radiation pressure, its evolution under the PR effect now follows a constant value of  $C$ . The evolutionary track is independent of the particle's  $\beta$ -factor, which only determines the speed at which the particle progresses along the track.

Due to their high eccentricity coupled with low perihelia, the  $\alpha$ -meteoroids are characterized by their low  $C$ -values. Thus, for assessing whether dust particles released from a certain source can assume the dynamical properties of the  $\alpha$ -meteoroids, the minimum  $C$ -value that particles can obtain upon release without becoming hyperbolic ( $e > 1$ ) is critical. In this way, we examine four different sources, JFC-type, Encke-type, asteroidal (via eccentricity-pumping resonances), as well as fragmenting, PR-evolved micrometeoroids near the Sun with respect to their ability to generate the  $\alpha$ -meteoroids. To that end, Figures 5.18 and 5.19 show the evolutionary tracks of dust particles released from the different sources in  $e$ - $q$  space, alongside the ' $\alpha$ '  $e$ - $q$  region, spanning the Pioneer 8/9-TOF-measured  $\alpha$ -meteoroid (indicated in yellow), which notably exhibit  $C < 1$  au.

**Jupiter-family comets (JFCs)** Figure 5.18a shows the evolution of a dust grain of JFC origin, thought to be the predominant dust source in the inner solar system (e.g., Nesvorný et al., 2010; Soja et al., 2019). Here, the comet 67P is used as a representative object of the JFC population. The analysed grain may be released from the comet directly or from larger fragments released by the comet, which evolve collisionally rather than under PR drag, and still share the orbital characteristics of the comet. Once released, the dust grain's orbit is changed due to the effect of radiation pressure suddenly becoming relevant. The resulting perihelion and eccentricity depend on the  $\beta$ -value of the particle, as well as the location along the source orbit at which the particle is released. The range of possible  $e$ - $q$  combinations is indicated by the 'release zone', which encompasses the  $e$ - $q$  coordinate of the source body. Within the release zone, contours mark constant values of  $\beta$ , as well as constant values of true anomaly at which the release occurred (contours corresponding to release at perihelion and aphelion envelope the release zone).

For release from 67P's orbit the minimum  $C \approx 2.5$  au, occurring in particles released near perihelion

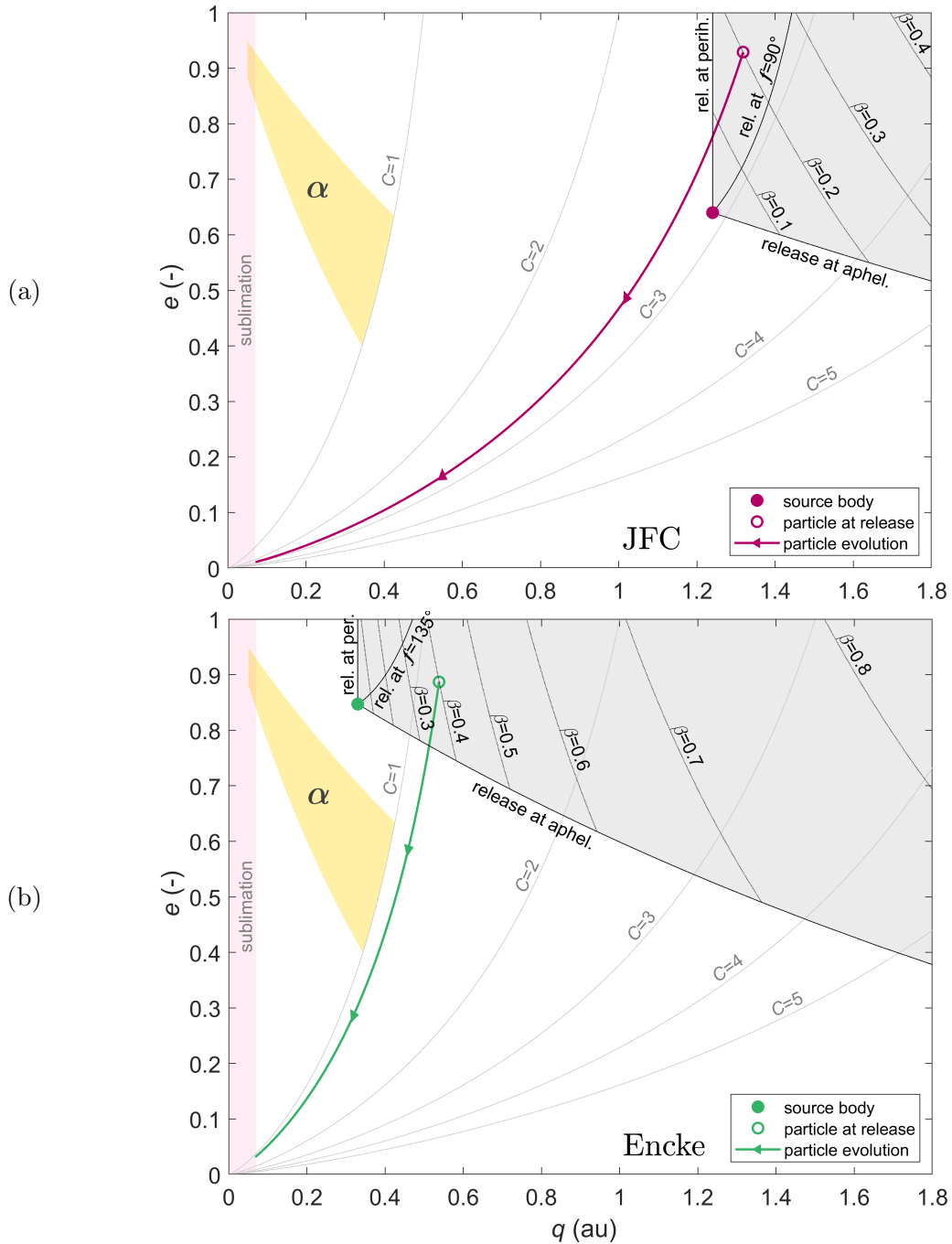


**Figure 5.18.:** Evolution of eccentricity and perihelion of exemplary particles released from different sources: (a) JFC (here 67P) and (b) Comet Encke. Particles may be released from the source body directly or generated from collisional fragmentation of larger released meteoroids that are still in the source body orbit. The release zone (grey) is the possible range of  $e$ - $q$  combinations that particles exhibit upon release from the source body, depending on their  $\beta$ -factor and on the release location along the orbit. Contours of  $\beta$  are shown within the release zone. The release zone is enclosed by solid lines indicating a release at the source body’s peri- & aphelion. Also shown is a contour corresponding to a release at a specific true anomaly  $f$ . Evolutionary tracks of the exemplary particles starting from the release zone are displayed, alongside contours of  $C$  (in units of au). The yellow zone labelled ‘ $\alpha$ ’ is set to span the  $e$ - $q$  combinations of the Pioneer 8/9-TOF-measured  $\alpha$ -meteoroids. At  $q < 15 R_\odot$  grains sublimate as indicated by the pink zone. Figure adapted from Sommer (2023).

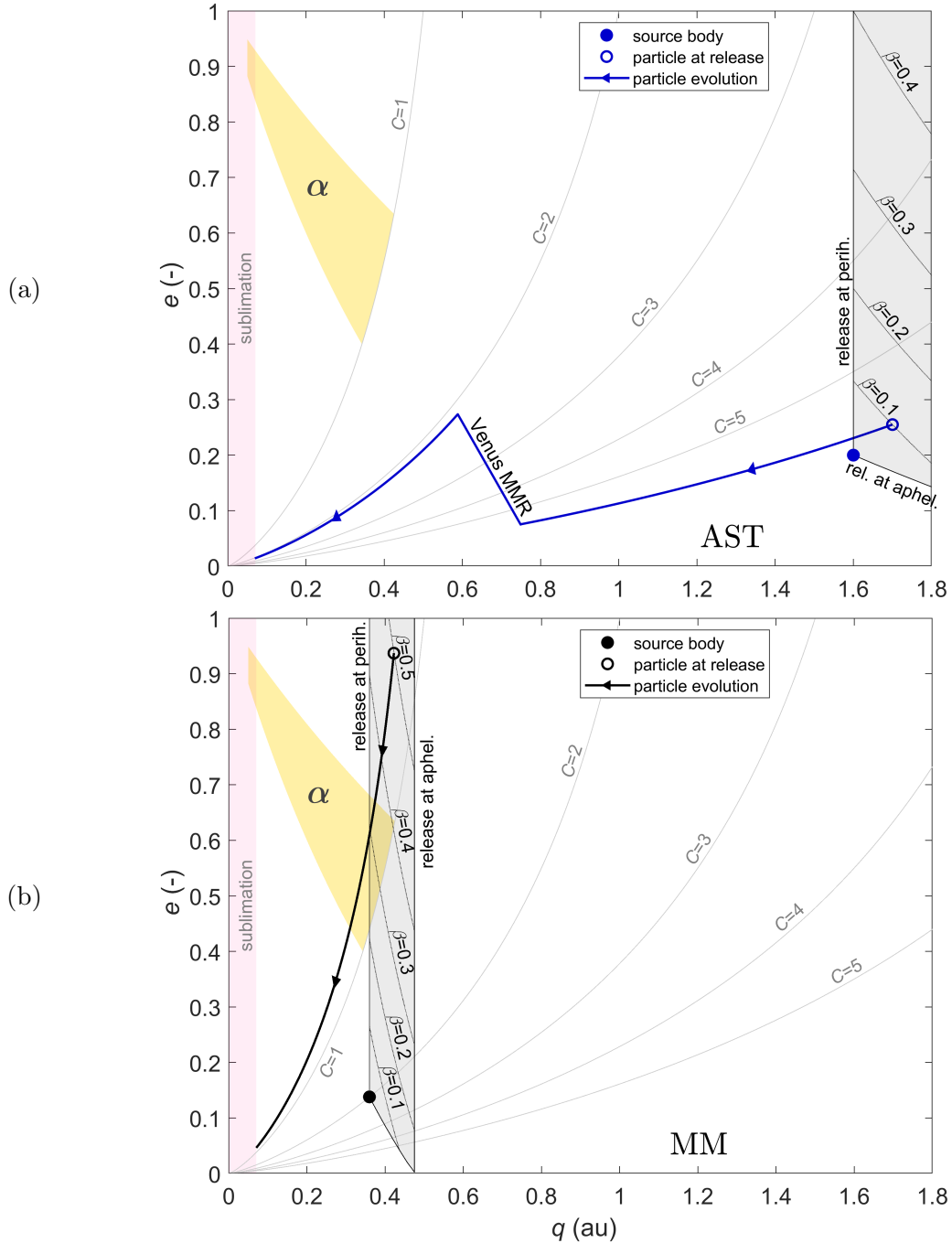


**Figure 5.19.:** Evolution of eccentricity and perihelion of exemplary particles released from different sources: (a) asteroidal and (b) a PR-evolved micrometeoroid (MM). Otherwise same as Figure 5.18. Figure adapted from Sommer (2023).

with  $\beta \approx 0.2$ . This is far from the  $C$ -value required for particles to PR-evolve through the  $\alpha$ -meteoroid  $e$ - $q$  region ( $C < 1$  au), as illustrated by the evolutionary track of an exemplary particle, making comets like 67P incapable of producing the  $\alpha$ -meteoroids.

**Comet Encke** One might suspect comets that themselves exhibit a semi-major axis and eccentricity combination that corresponds to a lower  $C$ -value of being able to produce bound, ‘low- $C$ ’ dust. Figure 5.18b shows the dust release zone from Comet Encke’s orbit ( $C_{Encke} \approx 0.7$  au), one of the lowest-perihelion periodic comets known to shed substantial amounts of material (e.g., Sarugaku et al., 2015). We see that the generation of dust from this type of orbit can yield low- $C$  particles if

---

their  $\beta$ -factor is sufficiently low ( $\beta \lesssim 0.3$ ), corresponding to the higher end of the  $\alpha$ -meteoroid mass range (i.e.,  $10^{-11}$  g). At  $\beta=0.4$ , particles can remain bound if released far from Encke’s perihelion, with achievable values of  $C \approx 1$  au. If release far from perihelion is acceptable, this creation pathway is borderline compatible with at least a fraction of the observed  $\alpha$ -meteoroids.

**Asteroidal dust in resonances** Another conceivable scenario is that of eccentricity pumping by mean-motion resonances (MMRs), and is depicted in Figure 5.19a. Here, a grain released from an asteroidal orbit evolves under PR drag until being trapped in an MMR with Venus. When trapped in an external MMR, particles affected by PR drag maintain a quasi-constant semi-major axis while their eccentricity steadily grows,<sup>30</sup> causing an effective lowering of their  $C$ -value. For each resonance there is a  $\beta$ -independent maximum eccentricity that particles may attain (e.g., Weidenschilling and Jackson, 1993; Beaugé and Ferraz-Mello, 1994), which therefore also limits their minimum attainable  $C$ -value. For the depicted particle with  $\beta=0.1$  in the 4:5 external Venus resonance that is  $C_{min} \approx 2.1$  au. This is far from the demanded  $C < 1$  au, notwithstanding the fact that trapping efficiency diminishes at such large  $\beta$  (Gomes, 1995; Dermott et al., 2001). On the other hand, more remote resonances (i.e., those of higher order or lower degree) theoretically allow lower  $C$ -values to be attained. However, these resonances have been shown to be effective in capturing particles in the absence of other planets and at larger particle sizes ( $\beta \lesssim 0.01$ ) only, and are entirely ineffective in the presence of a perturbing outer planet neighbour, such as Earth (Sommer et al., 2020). Thus, external MMRs can be ruled out as a mechanism to produce the  $\alpha$ -meteoroids.

Likewise, the  $\nu_6$  secular resonance and also various interior MMRs with Jupiter, which have been connected to eccentricity pumping in meteoroids (Morbidelli and Gladman, 1998), can be precluded as sources of  $\alpha$ -meteoroids by a similar argument as the external MMRs (see Sommer, 2023, for details).

**Fragmentation of evolved micrometeoroids** Figure 5.19b shows the scenario put forward by Grün and Zook (1980), in which collisions among evolved micrometeoroids give rise to the  $\alpha$ -meteoroids. In this example the progenitor is a meteoroid with  $C \approx 2$  au, compatible with a direct PR decay from a typical JFC orbit. Assuming that velocity components added by the collision are negligible, the release zone for the fragments of this meteoroid exhibits a narrow range for possible perihelia and wide range for possible eccentricities. Large eccentricities and thus values of  $C \lesssim 1$  au may be assumed by fragments with  $0.3 \lesssim \beta \lesssim 0.5$ . In this case, if fragmentation occurs near aphelion, even bound low- $C$  grains with  $\beta > 0.5$  may be created, due to the eccentricity of the progenitor. If not released directly into the ‘ $\alpha$  zone’, fragments released at higher eccentricities may cross it upon further PR migration, as shown by the indicated evolutionary track. Of the presented scenarios, release from a short heliocentric distance orbit thus poses the most reliable pathway for generating grains of the  $\alpha$ -meteoroid kind. Of course, the releasing body does not have to be a fragmenting meteoroid necessarily and could theoretically also be a dust shedding asteroid with comparable orbital parameters, that is, low heliocentric distance and moderate eccentricity. However, to date there is only a single known member of the dynamical class of minor bodies that revolve entirely within the orbit of Venus (‘Vatira asteroids’) and predictions for its population size are minuscule (Greenstreet et al., 2012; Sheppard et al., 2022).

---

<sup>30</sup>See Sections 2.2 and 5.3.6.

---

**Electromagnetic interaction** The Lorentz force resulting from the interaction of the charged particles with the interplanetary magnetic field (IMF) (see Sect. 2.2) may also be a relevant factor for the  $\alpha$ -meteoroids, especially for the smallest among them, due to its growing influence with decreasing particle size. As described by Parker (1964), this force acts largely perpendicular to the solar equatorial plane, due to the dominant in-plane component of the IMF, such that its principal effect on dust particles is a perturbation of their orbital inclination—a property where the  $\alpha$ -meteoroids show no strong characteristic. Since the actual magnetic field fluctuates such that there is also a minor field component normal to the solar equatorial plane present at all times, there is also a Lorentz force component within the orbital plane of affected particles, causing an analogous (yet less effective) perturbation of their semi-major axis and eccentricity (Parker, 1964).

At low latitudes, where the rotating IMF exhibits a structure of variable-length sectors of alternating field polarity, the Lorentz force acts effectively at random, thus, inducing a stochastic dispersion of the orbital elements of particles in the micron size range, also referred to as ‘Lorentz scattering’ (e.g., Consolmagno, 1979, 1980; Morfill and Grün, 1979b; Barge et al., 1982; Mukai and Giese, 1984; Wallis and Hassan, 1985; Fahr and Ripken, 1985; Morfill et al., 1986). The derived magnitude of this effect on particles in the  $\alpha$ -meteoroid size range, however, are inconsistent, ranging from a negligible dispersion in semi-major axis and eccentricities (Barge et al., 1982) to a scattering of semi-major axes strong enough to overcome PR drag (Consolmagno, 1979). Nonetheless, it is questionable whether a stochastic dispersion of orbital elements can produce  $\alpha$ -meteoroids efficiently enough as for them to constitute the dominant in-situ measured bound population, yet, it cannot be entirely ruled out either, within the scope of this work.

At high latitudes, the variable sector structure gives way to a unipolar magnetic field, which reverses polarity only once per 11-year solar cycle and reaches down to solar equatorial latitudes of  $15^\circ$  to  $20^\circ$  during solar minimum (e.g., Smith et al., 1993). Particles with considerable orbital inclination may enter this high-latitude field, where, due to the less frequent polarity fluctuations a more consistent Lorentz perturbation can take place (Morfill et al., 1986). However, given that the  $\alpha$ -meteoroids have been found to exhibit an average inclination  $\bar{i} < 30^\circ$ , it seems unlikely that the high-latitude Lorentz perturbations play a formative role in their creation.

Furthermore, by including a hypothetical, non-zero average normal component of the IMF, Lhotka et al. (2016) find that the Lorentz force could in principle induce a significant secular change of the semi-major axis, which (depending on the value and sign of a particle’s charge-to-mass ratio) can accelerate, compensate, or even overcome orbital decay due to PR drag. While they estimate that particles with radii as large as  $55\ \mu\text{m}$  could withstand PR decay at 1 au via this systematic Lorentz perturbation, a secular change of their eccentricity is not evident. However, in lack of a deeper understanding of the peculiarities of the IMF, such as a potential normal field component, we will not speculate on the relevance of this effect for the  $\alpha$ -meteoroids, only that it adds to the uncertainty about the degree to which the electromagnetic interaction plays a role in their formation.

**Sublimation** Besides collisional grinding, sublimation of dust is considered an effective mechanism for the creation of  $\beta$ -meteoroids (see review by Mann et al., 2004). As their orbits decay further toward the Sun, grains which survive the expulsion due to collisions are subject to an ever-higher solar thermal flux. When sublimation sets in at a material-specific heliocentric distance (typically below  $15 R_\odot$ , see Mann et al., 2004, Table 2), the mass loss of the particle steadily raises its  $\beta$ -factor.

---

The increasing effect of radiation pressure counteracts the decay due to PR drag and eventually causes the particle to maintain a quasi-constant perihelion distance. Yet, as the increase in  $\beta$  occurs around perihelion (where sublimation is strongest) the eccentricity starts to grow, raising the aphelion with each revolution. The further fate of the particle then depends on the material-specific maximum  $\beta$ -factor that particles can assume (Burns et al., 1979; Shestakova and Tambovtseva, 1995; Krivov et al., 1998): Once  $\beta$  surpasses a near-unity critical value (typically around radii of 100 to 200 nm), the particle may become hyperbolic, that is, a  $\beta$ -meteoroid. On the other hand, particles made up of materials that reach a maximum  $\beta$  below the threshold, orbitally collapse and sublimate entirely after the maximum  $\beta$  is passed.

One might think that, due to the incremental increase in eccentricity, particles will naturally surpass a stage with high aphelion before becoming hyperbolic, such that they can be detected at 1 au in the manner of the apex particles, as has been suggested by Shestakova and Tambovtseva (1995). However, due to the low perihelion, this would correspond to a narrow range of near-unity orbital eccentricity. If we demand an aphelion between 1 au and 1.5 au, the eccentricity range for a grain sublimating at  $10 R_{\odot}$  becomes 0.91 to 0.94. It is questionable whether an incremental increase in  $\beta$  at perihelion can efficiently generate grains within such a high, yet narrow eccentricity range. Moreover, a such created  $\alpha$ -meteoroid may remain in this state for only one revolution, given the sensitivity of the orbit to a changing  $\beta$  at the next perihelion. That is contrary to collisionally generated  $\alpha$ -meteoroids, which, once created, may remain in such orbits for many more revolutions.<sup>31</sup> However, whether sublimation can be ruled out as an  $\alpha$ -meteoroid-supplying mechanism must be left to further studies. If so, the presence of  $\alpha$ -meteoroids might be indicative of collisional grinding as the more effective loss-mechanism of the zodiacal cloud.

In this context it should be considered that recent findings of visible observations carried out by the Parker Solar Probe indicate a smooth decline in dust density starting from about  $19 R_{\odot}$  down to  $5 R_{\odot}$ , as well as a dust-free zone below  $5 R_{\odot}$  (Howard et al., 2019; Stenborg et al., 2021; Stenborg et al., 2022). The observed absence of dust bands speaks against a sublimation loss occurring only at specific heliocentric distances (see e.g., Kobayashi et al., 2009) and for a continuous process that gradually reduces the dust density (or for a process that dissolves the dust bands effectively, e.g., Isobe and Sateesh-Kumar, 1993).

Other loss mechanisms, erosive sputtering by solar wind particles and rotational bursting, may be also be relevant within a few  $R_{\odot}$  (Mann et al., 2004) and could thus also play a role in the creation of the  $\alpha$ -meteoroids.

**Origins Résumé** Given the above considerations, there remain some questions about the origins of the  $\alpha$ -meteoroids. In particular, a production from parent bodies in Encke-type orbits, a role of electromagnetic forces in their formation, and a production via sublimation are not entirely ruled out. Collisional grinding of the zodiacal cloud at short heliocentric distances, however, remains the favoured scenario for their creation, given its demonstrated ability to yield  $\alpha$ -meteoroid-typical orbits. Moreover, the creation of these bound, high-eccentricity grains alongside the hyperbolic  $\beta$ -meteoroids, is consequential, if the grinding occurs with a fragment size distribution that spans the  $\alpha$ -meteoroid-typical mass range.<sup>32</sup> Therefore, our analysis reinforces the argument for a collisional

---

<sup>31</sup>A typical  $\alpha$ -meteoroid with  $a=0.6$  au,  $e=0.6$ , and  $0.3 < \beta < 0.5$  has a PR lifetime of 200 to 300 years.

<sup>32</sup>Considering a colliding progenitor meteoroids of  $10 \mu\text{m}$  to  $100 \mu\text{m}$ , the creation of micron-sized fragments even in catastrophic collisions is a reasonable assumption. This is also compatible with constraints on the largest

---

origin made by Grün and Zook (1980).

## Study of $\alpha$ -meteoroids with DDA

For quantitative assessment of the  $\alpha$ -meteoroids observable with DDA, we may, again, resort to the DDA-converted Grün-flux incidence rates (see Figure 5.14). (See also Appendix C for a discussion on why more sophisticated dust environment models such as IMEM are unable to reproduce the  $\alpha$ -meteoroids.) With a minimum mass of the  $\alpha$ -meteoroids of  $m = 10^{-13}$  g, we find  $I_{\text{DDA,Grün,iso}} \approx 0.27 \text{ week}^{-1}$  and  $I_{\text{DDA,Grün,coll}} \approx 5 \text{ week}^{-1}$ . Due to their anisotropy, having approach directions broadly distributed around the apex direction, we may (for an apex-oriented DDA) expect an incidence rate in between the rates derived via the isotropic and via the collimated flux assumption, that is, in the order a one to a few detections per week. That is consistent with the (interplanetary) apex flux reported by HEOS-2 ( $\sim 10^{-4} \text{ m}^{-2} \text{ s}^{-1}$  at  $m > 10^{-13}$  g, Hoffmann et al., 1975b, Fig. 7), which converted to the nominal sensitive area of DDA yields 1.8 impacts per week. It should be stressed that, while the  $\alpha$ -meteoroids may be predominant flux-wise, there is a bias in sensors at 1 au to detect them (Weidenschilling, 1978; Altobelli et al., 2003). Hence, they do not necessarily have to be the most abundant density-wise, too.

DDA is inherently suited to give definitive answers on the nature of the  $\alpha$ -meteoroids, brought about by its ability to constrain the dynamics of particles larger than a few 100 nm to a degree significantly beyond that of the detectors flown on Helios, HEOS-2, and the Pioneers.<sup>33</sup> Its contactless trajectory sensing approach yields far more viable dynamical information than just the vector constraint via its instrument aperture—the only mean available to Helios and HEOS-2.<sup>34</sup> It also poses a significant improvement over the penetration-type TOF measurements of Pioneer 8/9, which, via deceleration at the front sensor, likely confounded the measured velocities of typical  $\alpha$ -meteoroid impactors.<sup>35</sup> Especially the constraining of their perihelion distance would be of high scientific value to possibly preclude the sublimation formation scenario.<sup>36</sup> A measurement of the particle charge, on the other hand, may yield a better assessment of the role electromagnetic forces play in their formation. Moreover, their chemical characterization at high mass resolution is unprecedented and may reveal valuable insights about the loss mechanisms of the zodiacal cloud. The prospect of finally uncovering the peculiar  $\alpha$ -meteoroids makes them a high priority target for the IPD science campaign of DDA.

---

fragment mass imposed by typically assumed fragment mass distributions, which are based on the scaling of impact experiment results (e.g., Grün et al., 1985b; Ishimoto, 2000; Krivov et al., 2005).

<sup>33</sup>Although Grün (1981) demonstrated that by ascribing probability distributions to the uncertain impactor trajectories and subsequent adding up of the resulting orbital elements distributions of all registered particles, a conclusive characterization of their dynamic properties is possible. (See also Schmidt and Grün, 1979, 1980; Schmidt, 1980; Grün et al., 1985a).

<sup>34</sup>Compare  $\Omega_{\text{eff,DDA,single-segment}} = 0.12 \text{ sr}$  ( $\sim 1\%$  of the entire sky) to  $\Omega_{\text{eff,Helios}} = 1.03 \text{ sr}$  and  $\Omega_{\text{eff,HEOS}} = 1.04 \text{ sr}$  (both,  $\sim 8\%$  of the entire sky), see Table 4.1.

<sup>35</sup>Impactors with a kinetic energy of 100 nJ (that is, e.g.,  $m = 10^{-12}$  g at  $v_{\text{impact}} = 10 \text{ km s}^{-1}$ ) may have been decelerated by 40% (Berg and Richardson, 1969). Also compare  $\Omega_{\text{eff,DDA,single-segment}} = 0.12 \text{ sr}$  to  $\Omega_{\text{eff,Pioneer,TOF,single-segment}} \approx 0.23 \text{ sr}$  (estimated from the anglr. sensitivity given in Grün et al., 1973).

<sup>36</sup>More speculative, a creation via sublimation may also be recognizable in a lack of certain (more volatile) elements, as well as, possibly, by indicators of partial melting (e.g., Belton, 1966)

---

### 5.3.4. The sporadic meteoroid complex

The third of group of in-situ-encountered IPD identified by Grün et al., contains grains larger than the  $\alpha$ -meteoroids, with typical masses  $>10^{-11}$  g.<sup>37</sup> In addition, they were characterized by their higher angular momentum orbits (for bound orbits, that is, effectively, higher perihelia)<sup>38</sup> than the  $\alpha$ -meteoroids, as well as a lower degree of anisotropy. Grün and Zook (1980) interpret these properties as indicative of a relation to the sporadic meteoroid complex (SMC). As the dust component of the SMC, these particles would be generated in the orbits of their source bodies (asteroids and comets),<sup>39</sup> and then disperse into the zodiacal cloud, while spiralling toward the Sun under PR drag. Such particles could exhibit dynamics similar to the larger meteoroids (10s to 100s of  $\mu\text{m}$  in size) observable as radar meteors. Thus, they may retain the dynamic linkage to their source body population and exhibit predominant flow directions akin to the meteor radar radiants.

However, assuming the radar-observed SMC dynamics to extend down to the in-situ measured masses of  $m = 10^{-11}$  g ( $s \approx 1 \mu\text{m}$ ) is not without caveats. The sudden onset of radiation pressure onto collisionally generated fragments can cause their trajectories to significantly differ from their progenitor orbits. If released along the inner arc of a highly eccentric orbit, even small  $\beta$ -factors are enough to cause the fragments to be ejected from the solar system. The  $\beta$ -factor above which this solar pressure ejection occurs is also referred to as the blowout limit, and may be calculated as

$$\beta = (1 - e) / 2 \quad (5.11)$$

where  $e$  is the parent body eccentricity. As a result, HTC-type progenitor orbits are only capable of producing bound dust of  $s > 10 \mu\text{m}$ , while JFC-type orbits may inject bound grains of  $s \gtrsim 3 \mu\text{m}$  into the zodiacal cloud (Moorhead, 2021). Smaller bound grains must be released far from perihelion, or from less eccentric orbits (either asteroidal sources or more PR-evolved cometary meteoroids). In either case, a deviation from the radar-observed SMC dynamics is expected, such as the disappearance of the apex and toroidal radiants, which are associated with material released from the highly eccentric HTC and Oort-cloud comets (Pokorný et al., 2014).

For a rough quantitative assessment, we again resort to the DDA-converted Grün-flux (Figure 5.14). Adopting the SMC dust minimum mass found by Grün et al. of  $m > 10^{-11}$  g, we obtain  $I_{\text{DDA,Grün,iso}} \approx 0.8 \text{ week}^{-1}$  and  $I_{\text{DDA,Grün,coll}} \approx 0.04 \text{ week}^{-1}$ . As aforementioned, less anisotropy is expected for the SMC dust based on the 1 au in-situ measurements. Thus, an incidence rate closer to the  $I_{\text{DDA,Grün,iso}}$  may be expected, that is, one impact every other week, even when pointed toward one of the SMC radiants.

## IMEM

In a next step, we employ the Interplanetary Meteoroid Environment Model (IMEM) tool to make more elaborate predictions. IMEM is a software package, developed by Dikarev et al. (2005a,b), that allows for the evaluation of dust models along a given spacecraft trajectory, and includes a physical model for dust released from asteroids and JFCs. Selecting a mass cut-off of  $10^{-11}$  g,

---

<sup>37</sup>Masses  $m > 10^{-11}$  g correspond to particle radii  $s > 1 \mu\text{m}$  at a density of  $2.5 \text{ g cm}^{-3}$ .

<sup>38</sup>The specific angular momentum is calculated as  $h = \sqrt{\mu a (1 - e^2)}$ , or, by insertion of  $a = q / (1 - e)$ ,  $h = \sqrt{\mu q (1 + e)}$ .

<sup>39</sup>Particles may be released from the source body directly or generated from collisional fragmentation of larger ejected meteoroids that are still in the source body orbit.

IMEM lets us compute the flux across the sky in angular bins. By dividing the fluxes by the solid angles spanned by their respective bins, we obtain a sky map of the directional flux. Figure 5.20a shows the thus-generated directional flux map for an observer in a heliocentric, circular orbit at 1 au. From the IMEM output one can also compute the resulting incidence rate onto DDA by convoluting the directional flux with the DDA angular sensitivity profile, that is, by cumulating the bin fluxes within the FOV at a certain instrument pointing, weighted by the effective sensitive area  $A(\theta)$  toward each direction. In that way, we can calculate the according incidence rate onto DDA for any pointing across the sky, as given in Figure 5.20b. The average velocity of impactors is shown in Figure 5.20c. Figures D.1 and D.2 show corresponding plots with only the asteroidal (AST) and JFC contributions.<sup>40</sup>

We find that, according to the IMEM (Dikarev) model, the flow of dust is concentrated in a ring-like structure roughly aligned with the plane spanned by the sunward, anti-sunward, and polar directions, with maximum intensities being reached near the sunward and anti-sunward direction. They are generated by the dominant JFC dust component in the Dikarev model, and correspond to the JFC-caused helion and anti-helion meteor radiants. The north/south apex and toroidal meteor radiants have no direct counterparts, due to the lack of HTC and long-period comets in the model. The minor visible apex radiant is caused by JFC dust scattered by Jupiter onto retrograde orbits.<sup>41</sup> Conversion to DDA incidence rates, yields a maxima of  $\sim 0.06 \text{ week}^{-1}$  in the direction of the helion and anti-helion radiants and minima of  $\sim 0.01 \text{ week}^{-1}$  at the apex and antapex. This is consistent with the DDA-converted Grün-flux for the isotropic case of  $\sim 0.04 \text{ week}^{-1}$  for an arbitrary direction.<sup>42</sup>

So far, we have considered the case of an observer in a circular orbit at 1 au, which is a practical approximation for the nominal phase of the DESTINY<sup>+</sup> interplanetary trajectory. Yet, taking into account the moderate eccentricity of the DESTINY<sup>+</sup> heliocentric orbit ( $e \approx 0.1$ ) has significant effects on the fluxes and incidence rates. Figure 5.21 shows the incidence rates onto DDA computed for certain boresight directions along the spacecraft trajectory. The pointings are chosen as equivalents of the major meteor radiants in the sky around DESTINY<sup>+</sup>.<sup>43</sup> Comparing Figures 5.21a and 5.21d, a strong correlation between the incidence rates of the various radiants and the spacecraft velocity is apparent: Most notably, the helion and anti-helion rates are strongly enhanced when the spacecraft moves toward and away from the Sun, respectively. A similar effect is observed for the toroidal, apex, and antapex rates, which are modulated by the spacecrafts absolute speed. The maximum amplification and attenuations factors of these rates over those emerging in a circular orbit (Figure 5.20b) is about 2 during the nominal mission phase (and 3 during the extended mission phase when the eccentricity is raised to 0.33), roughly consistent across the different radiants.

Figures 5.21b and 5.21c show how JFC and AST contribute to the modulation of the incidence rates: The modulation is, in relative terms, is more significant for the AST contribution. During unfavourable periods in the spacecraft orbit, the contributions from the respective radiants practically disappear (leading to infinite modulation factors). This is presumably due to the overall low

<sup>40</sup>Find also equivalent plots generated from the empirical Divine and Staubach models, the predecessors of the Dikarev model, in Figures D.3 and D.4 For more information on the Divine and Staubach models, see Appendix C.

<sup>41</sup>See the inclination distributions of Jupiter-scattered dust in Dikarev et al. (2005c), Figs. 4 & 5.

<sup>42</sup>This agreement is less surprising, considering that the Dikarev populations are fitted with lunar crater size distributions extracted from the Grün-flux model.

<sup>43</sup>Coordinates of the sensor pointings in the DON reference frame (see Appendix A): helion  $[350^\circ, 0^\circ]$ , anti-helion  $[190^\circ, 0^\circ]$ , north toroidal  $[270^\circ, 70^\circ]$ , south toroidal  $[270^\circ, -70^\circ]$ , apex  $[270^\circ, 0^\circ]$ , and anti-apex  $[90^\circ, 0^\circ]$ .

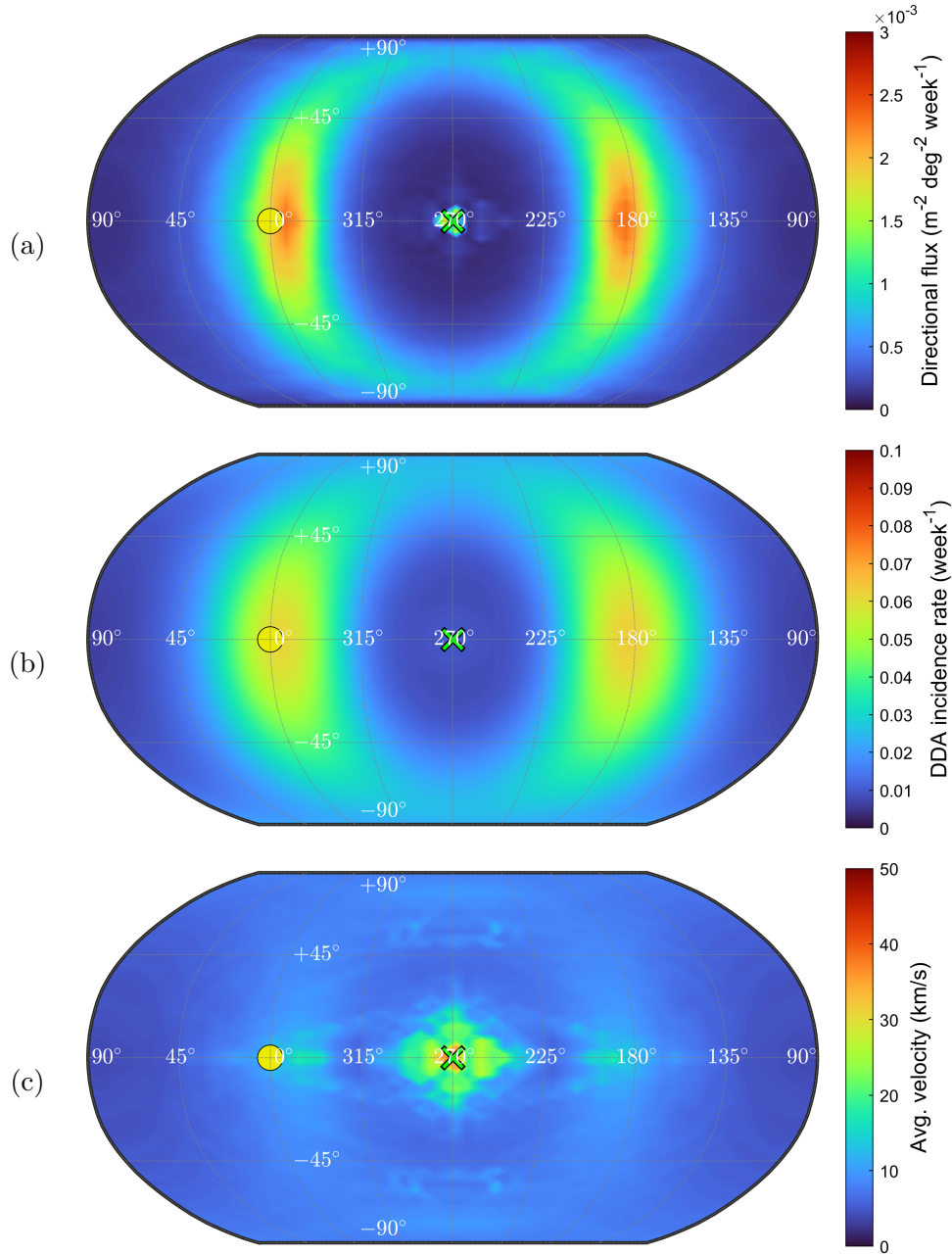


**Figure 5.20.:** Dikarev model sky maps of the IPD flux at 1 au: (a) directional flux, (b) DDA incidence rate, and (c) average velocity. The observer is in a heliocentric, circular orbit at 1 au. Directions of the Sun (0° longitude) and apex ( $\sim 270^\circ$  longitude) are indicated by the yellow circle and green cross, respectively. Data was generated with IMEM for a minimum particle mass of  $10^{-11}$  g.

eccentricities of AST dust, resulting in minimal relative velocities with respect to a spacecraft in a circular orbit. An added radial motion of the spacecraft causes the more effective intersecting of this dust population, which otherwise would seem to be flying ‘in formation’ with the spacecraft. Nevertheless, the AST contribution remains small compared to that of JFC dust, with a maximum incidence rate during the nominal mission of  $0.03 \text{ week}^{-1}$  (around 1/4th that of JFC dust), occurring at peak radial motion.

This ‘seasonal’ modulation of the directional flux is further illustrated in Figures 5.22, 5.23, and 5.24, showing the emerging sky maps at 4 different points along the DESTINY+ heliocentric

orbit: at the apsides, as well as at the points of peak radial velocity along its orbit. Corresponding figures showing the contribution of JFC and AST dust separately are given in Figures D.6 to D.11.<sup>44</sup> These show that the incidence onto DDA from a given radiant varies by a factor of 4 during the nominal mission (and a factor of 6 during the extended mission). The magnitude of this modulation is population-dependent, being (relatively) stronger for asteroidal dust, than for JFC dust. The predominant directions of asteroidal and JFC dust both lie in the helion and anti-helion directions, each being significantly enhanced during the spacecraft’s inbound and outbound orbital motion, respectively (asteroidal dust is detectable practically only during peak radial motion). According to the model predictions, asteroidal and JFC dust have different approach velocities with respect to the spacecraft, averaging at around  $5 \text{ km s}^{-1}$  and  $20 \text{ km s}^{-1}$ , respectively, which should facilitate their differentiation (compare Figures D.8 and D.11).

As the helion radiant remains unobservable for DDA (requiring a pointing close to the Sun direction), the anti-helion radiant offers the highest chances of detecting SMC dust, with a maximum incidence rate of  $0.14 \text{ week}^{-1}$  (of which 25% are asteroidal and 75% JFC dust), reached during peak anti-sunward motion of the spacecraft. At perihelion, the toroidal directions become comparable in strength to the anti-helion radiant, with rates of  $0.07 \text{ week}^{-1}$  and  $0.05 \text{ week}^{-1}$ , respectively.<sup>45</sup> Other directions are less favourable, regardless of the spacecraft’s position in its orbit, with incidence rates in the order of only  $1 \text{ yr}^{-1}$  or less.

## IMEM2

IMEM2 is the conceptual successor of the IMEM (Dikarev) model, in that, it is a physical model of dynamically evolving interplanetary dust and meteoroids that is fitted against various observational datasets. In contrast to the Dikarev model, IMEM2 includes HTCs as a grain producing population (in addition to asteroids and JFCs) and considers grain-grain collisions as a destructive mechanism. IMEM2 was developed by Soja et al. (2019), although the implementation of the adequate tooling for the evaluation of the model is still ongoing and currently continued by DDA Science Team member P. Strub. For comparison, preliminary sky maps generated with IMEM2 by Strub (priv. comm.) for an observer at 1 au are presented in Appendix E. These show the cumulative flux of particles larger than  $s_{\text{min}} = 1 \mu\text{m}$  (the smallest size considered by the model), which approximately equates to the threshold used in the above evaluation of the IMEM (Dikarev) model. Thus, the results are directly comparable.

Although the models produce similar absolute peak fluxes,<sup>46</sup> they yield generally different directional flux distributions. Most notably in the IMEM2 sky maps is the presence of strong flux radiants around the ecliptic poles, outshining only marginal helion and anti-helion radiants (see Figure E.1). This pattern is governed by the dominating JFC contribution (see Figure E.2), although the polar flux is also apparent in the asteroidal component (see Figure E.3). Only the HTC component shows a considerably different pattern, with prominent north/south apex and secondary north/south toroidal radiants (see Figure E.4), which matches the radar meteor radiants associated

<sup>44</sup>Find also the comparison of the Dikarev model with the Divine and Staubach models (Divine, 1993; Staubach et al., 1997) along the DESTINY+ trajectory in Figure D.5, yielding similar conclusions about the seasonal variation, yet, in the case of the Divine model, with notably stronger contributions from the apex and toroidal radiants.

<sup>45</sup>Note that, in the Divine model, the toroidal radiants produce the strongest overall incidence rates at perihelion of  $0.22 \text{ week}^{-1}$ , see Figure D.5.

<sup>46</sup>Both the Dikarev model and IMEM2 show absolute peak fluxes in the order of  $2 \times 10^{-3} \text{ m}^{-2} \text{ deg}^{-2} \text{ week}^{-1}$ .

---

with larger grains of the HTC population (e.g., Pokorný et al., 2014).

The reason for the discrepancy between the Dikarev model and the IMEM2, particularly for the JFC component, is not immediately clear. However, there remains some doubt about the validity of the Dikarev model in the evaluated particle size range. Most importantly, the orbit propagation used to generate the populations does not consider radiation pressure (as noted by Krüger et al., 2019) and thus effectively circumvents the blowout limit, which is in the order of a few microns in particle size for the JFC source. While direct release from JFCs of grains smaller than the blowout limit into bound orbits is still possible further from perihelion, these grains would be released into orbits with larger perihelion distances than their parent bodies, and would thus be given more time to circularize under PR drag before migrating to 1 au. It must be followed that dust of the sizes  $s > 1 \mu\text{m}$ , as examined here, is, to some extent, unphysically represented in the Dikarev model.

This may explain the discrepancy between the Dikarev model and IMEM2. In the IMEM2, which considers radiation pressure fully, only micron sized dust particles released further from perihelion remain bound to the Sun, which, as we have argued above, should exhibit more circularized orbits upon reaching 1 au. The velocity of such particles relative to an observer on a non-inclined, likewise circular orbit would be predominantly normal to the ecliptic caused by their differing orbital inclinations, which are unaffected by the PR migration (see Equation 2.3).<sup>47</sup> Thus, the flux of such evolved particles would be expected to be enhanced at directions near the ecliptic poles, which is indeed what the IMEM2 sky maps show. However, further analysis of the underlying dynamics of the IMEM2 populations is required to confirm this hypothesis.

Nevertheless, a modulation of the directional dust flux by the spacecraft's heliocentric motion, as we have investigated with the Dikarev model, should manifest also with IMEM2 and should be subject of further investigation as the tooling for evaluation of the model is further matured.

### SMC dust résumé

Considering the discrepancy between the directionality predicted by the Dikarev model and IMEM2, it is difficult to make a conclusive statement about the most promising directions for SMC dust detection. The mapping of the asteroidal and cometary dust flux across the sky and along the spacecraft orbit, would certainly be of high scientific value, to better constrain these models. Such an analysis, however, would require a statistically meaningful sample size, which, given the derived incidence rates in this particle size range (in the order of  $0.1 \text{ week}^{-1}$ ) seems difficult to achieve. It therefore stands to reason to focus on the directions of the highest incidence, as suggested by the two models. These are the anti-helion (from perihelion to aphelion) and the toroidal directions (during perihelion), according to the Dikarev model, and the ecliptic poles according to IMEM2.

Finally, given the concerns about the validity of the Dikarev model at smaller particle sizes, considerable reservations remain about earlier, provisional estimates for the IPD flux onto DDA by Krüger et al. (2019), which were based on the evaluation of the Dikarev model at even smaller particles, namely at a minimum mass of  $10^{-16} \text{ g}$ , corresponding to  $s \approx 20 \text{ nm}$ .

---

<sup>47</sup>The JFC source in IMEM2 has moderately broadly distributed inclinations, largely between  $0^\circ$  and  $30^\circ$ . It is the same population used by Nesvorný et al. (2010).

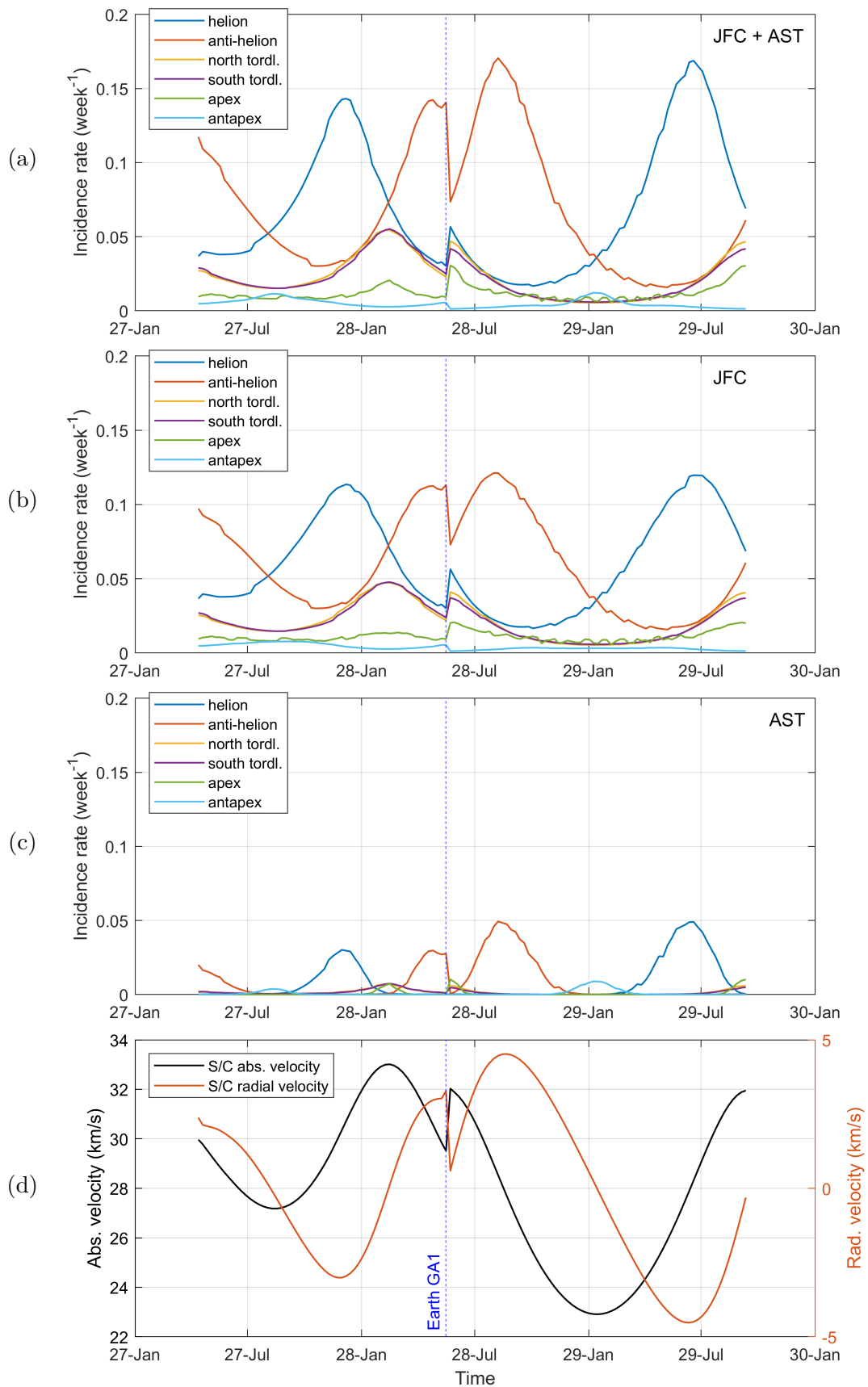


**Figure 5.21.:** DDA incidence rates at certain pointings along the DESTINY+ interplanetary trajectory generated from the Dikarev model: (a) - (c) rates caused by the JFC and AST population combined and separately, (d) spacecraft heliocentric absolute and radial velocity. In addition to the nominal phase trajectory, one full orbit of the extended mission phase is shown (period after EGA-1). Data was generated with IMEM for a minimum particle mass of  $10^{-11}$  g.

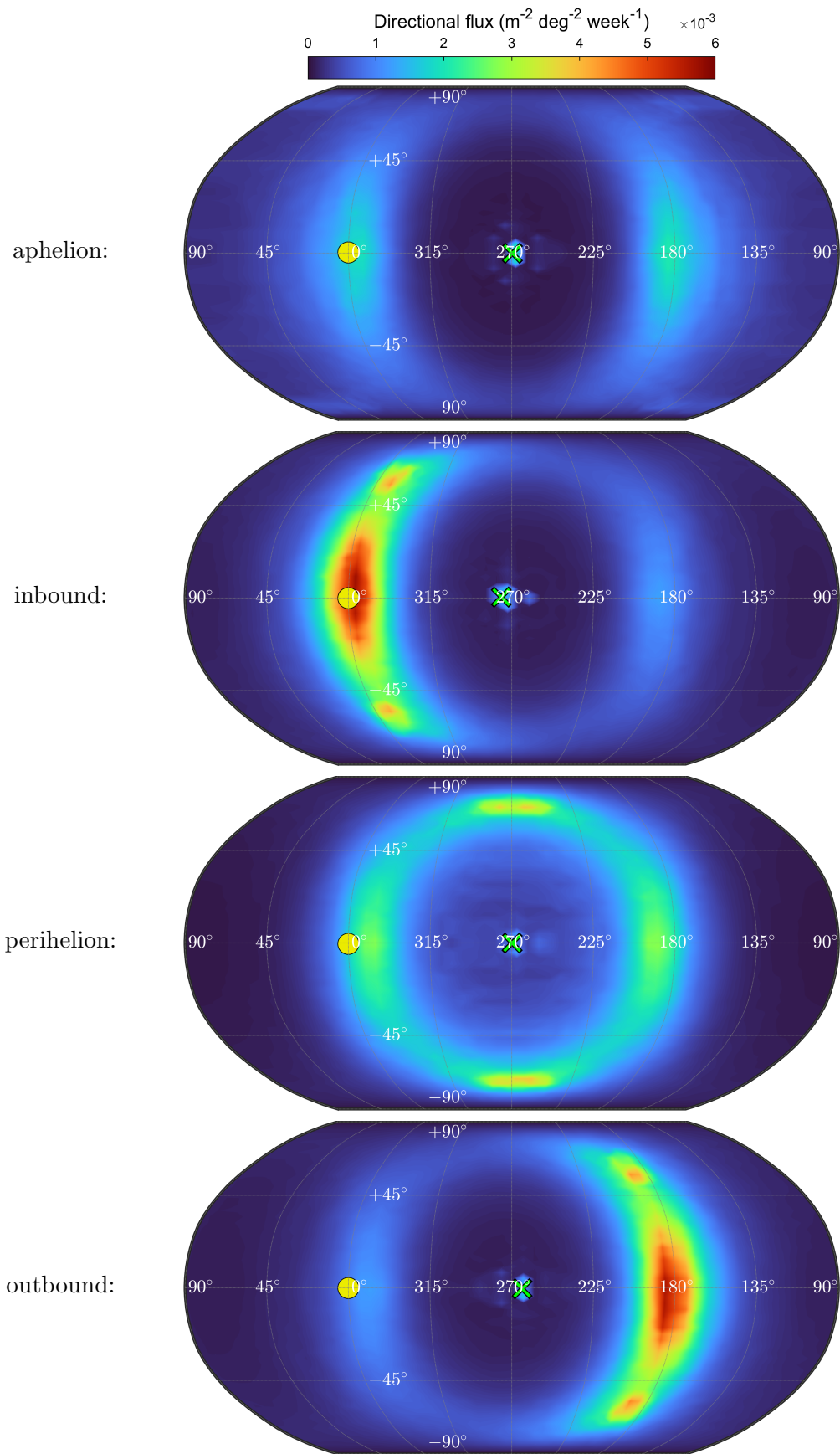


**Figure 5.22.:** Dikarev model seasonal sky maps of the directional flux of dust (JFC + AST) along the DESTINY+ interplanetary trajectory (nominal phase). Directions of the Sun and apex are indicated by the yellow circle and green cross, respectively. Data was generated with IMEM for a minimum particle mass of  $10^{-11}$  g.

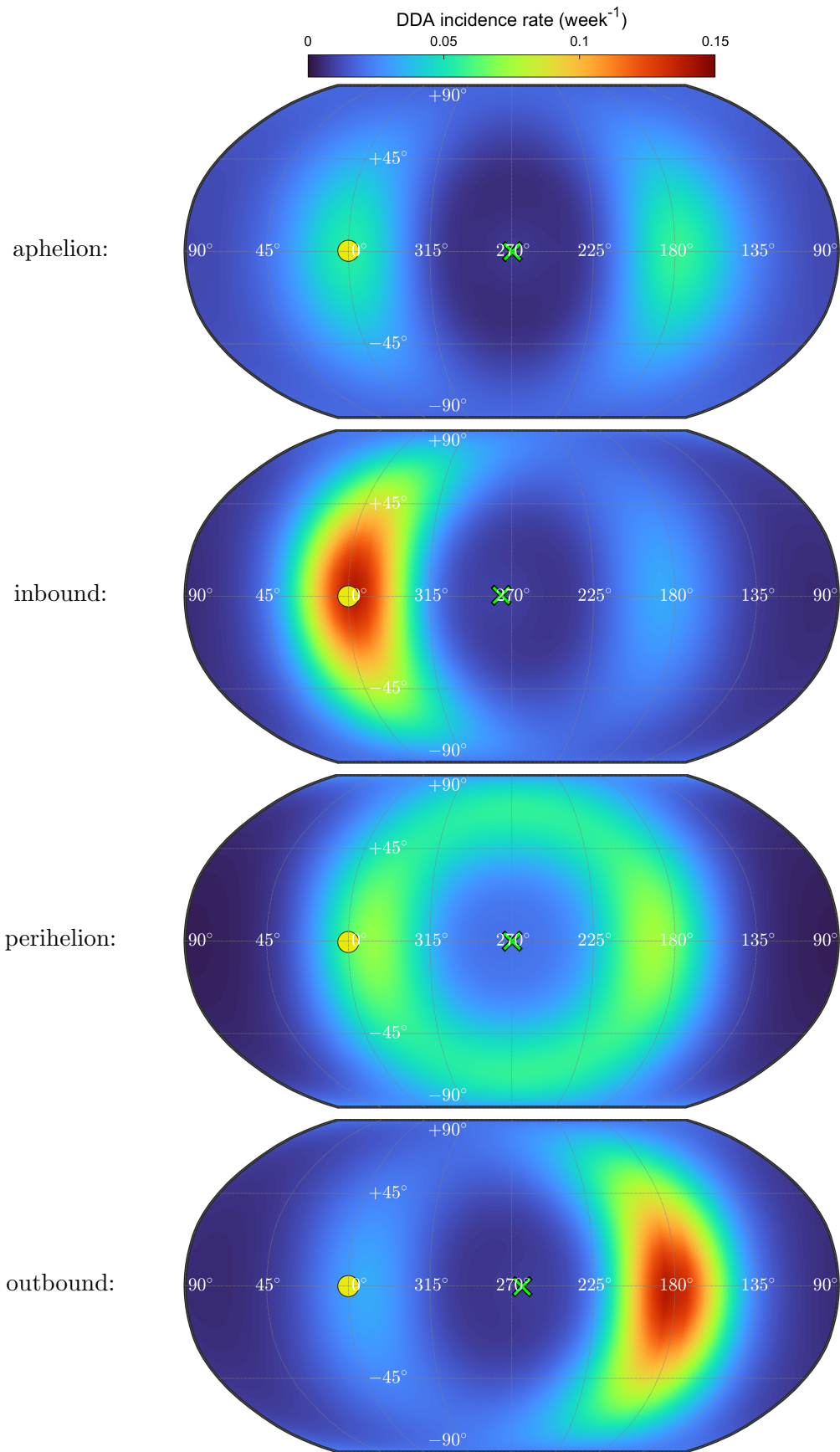


**Figure 5.23.:** Dikarev model seasonal sky maps of the DDA incidence rate of dust (JFC + AST) along the DESTINY<sup>+</sup> interplanetary trajectory (nominal phase). Directions of the Sun and apex are indicated by the yellow circle and green cross, respectively. Data was generated with IMEM for a minimum particle mass of  $10^{-11}$  g.

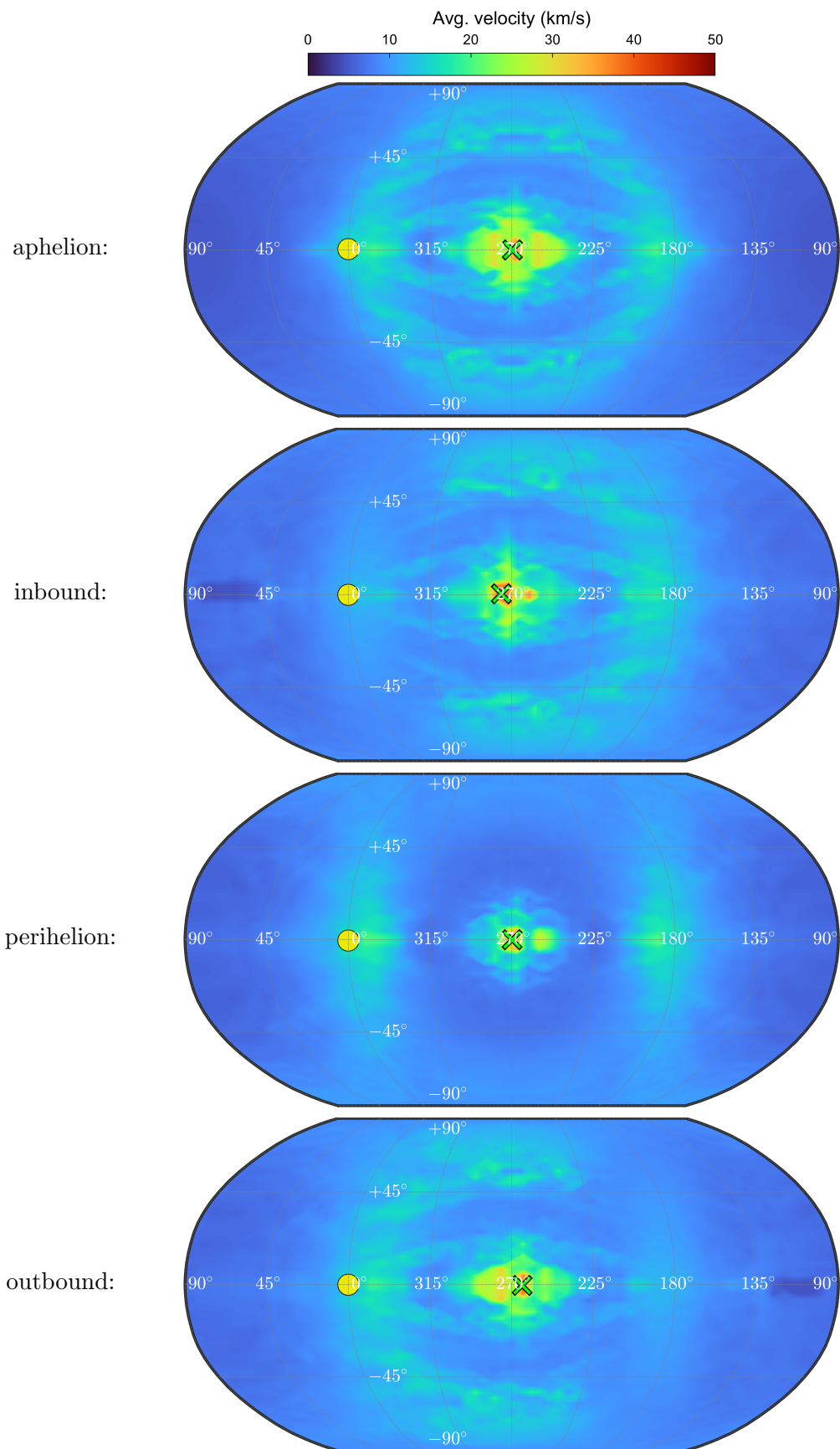


**Figure 5.24.:** Dikarev model seasonal sky maps of the directional flux of dust (JFC + AST) along the DESTINY+ interplanetary trajectory (nominal phase). Directions of the Sun and apex are indicated by the yellow circle and green cross, respectively. Data was generated with IMEM for a minimum particle mass of  $10^{-11}$  g.

---

### 5.3.5. Cometary streams

Besides the study of the diffuse constituents of the zodiacal cloud, one could also consider DDA's prospect of encountering denser formations of more recently released cometary dust, that is still part of its parent body's stream complex. In fact, clustered events recorded by in-situ detectors have, to some extent, been interpreted as cometary stream encounters before. We distinguish three different cometary dust structures (and according detection scenarios): The cometary trail, fresh trail filaments, and the dust tail.

#### Trail

The accumulation of debris along a comet orbit, dispersed enough to form a continuous, circumsolar toroidal stream, is referred to as a comet's trail. The annual meteor showers are generally associated with Earth's crossing of such cometary dust trails. Claims of direct detections of trail particles date back to the earliest days of in-situ dust research, made by studies with acoustic detectors onboard sub-orbital rockets and orbital spacecraft (e.g., Dubin et al., 1963; McCracken et al., 1967). For their high false detection rates, however, data from these types of detectors were later found to be spurious (see Section 1.2).

More reliable data retrieved by the later impact plasma detectors, such as that of the large-area GORID instrument, found no significant increases in impacts during known meteor shower (Drolshagen et al., 2001b). Impacts registered by the MDC onboard Nozomi that coincided with the spacecraft's encounter of the Leonids stream, could be ruled out to be trail particles by the sensor pointing (Sasaki et al., 2002; Senger, 2007).

These non-detections are consistent with expectations for the mass distribution of cometary trails: Smaller particles are more efficiently removed from a trail by their stronger dispersion, resulting from higher initial ejection speeds from the comet as well as a higher influence of the PR effect.<sup>48</sup> Effectively, this should lead to a flattening of the mass distribution of a trail (compared to the steep mass distribution of the sporadic background). This expectation is confirmed by visual and radar observations of meteor showers, showing that the ratio of stream flux to the sporadic flux decreases rapidly with decreasing particle size (Jenniskens, 2017). For the more sensitive radar observations, meteor showers virtually disappear in the background flux (Bruzzone et al., 2020). This vanishing of the stream contrast is also illustrated in Figure 5.25.

An argument that this trend is maintained or even increased for particles smaller than the typical meteor radar grains (i.e.,  $s < 10$ s of  $\mu\text{m}$ ) is given by Kresák (1976): With further decreasing particle size and increasing  $\beta$ -factor, particles begin to be removed from the trail upon release from the parent body via radiation pressure expulsion (i.e., they become hyperbolic). Effectively, this can be considered as an inability of a certain comet to inject particles smaller than a certain size into its trail. This blowout limit (largely depending on the parent body eccentricity, as already discussed in Section 5.3.4), is typically in the range of several  $\mu\text{m}$  for the annular meteor shower streams (Moorhead, 2021). Considering that shower contribution to the overall flux is vanishingly small at typical radar meteor grain sizes, it can thus be followed that the contribution is entirely absent in the few-micron (let alone sub-micron) size range. Therefore, it must be concluded that

---

<sup>48</sup>An additional factor for dispersion from the trail may be Lorentz scattering, as suggested by Consolmagno (1980).

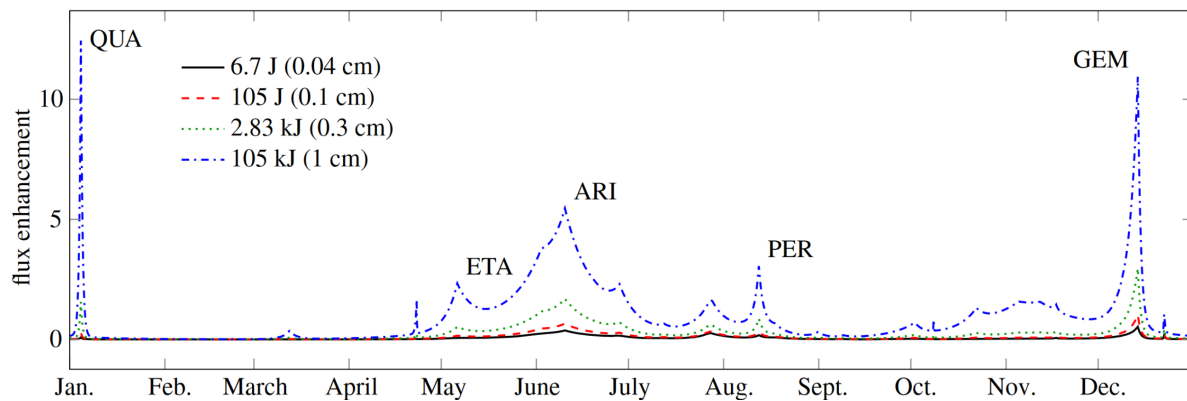


**Figure 5.25.:** Ratio of meteoroid stream flux to the sporadic flux of the annual meteor showers at different particle sizes. Taken from Moorhead et al. (2019).

trail detections by in-situ detectors such as DDA are virtually impossible.<sup>49</sup>

### Fresh trail filaments

After release from a comet, the material ejected during an apparition typically remains in an elongating formation for several revolutions, before eventually dispersing all around the comet orbit. These fresh filaments form regions of enhanced particle density, within the comet trail, which, if encountered by Earth, can cause meteor shower outbursts, accordingly referred to as meteor storms. A prominent example in recent history are the storms of the Leonids in 1999 and 2001, caused by the crossing of dense filaments generated by comet 55P/Tempel-Tuttle within just the last 300 years (e.g., McNaught and Asher, 1999). It is conceivable that such young stream filaments still hold enough small particles as to, if crossed, produce a meaningful flux enhancement over the sporadic flux, even at radar meteor grain sizes (as is the case for storm years of the Leonids, Brown et al., 1997), which could also enable their detection by large-area in-situ detectors.<sup>50</sup> During the 1999 Leonids outburst, the GORID experiment registered several impacts, which however, could be ruled out to stem from the Leonids by the instrument pointing (Drolshagen et al., 2001a).

While an extensive amount of research has been conducted concerning the occurrence of meteor storms at Earth, such dense filaments might also be encountered by spacecraft in interplanetary space. To build an understanding of these streams and to assess encounters with spacecraft, a model for young cometary streams was developed at IRS, as part of the ESA-funded Interplanetary Meteoroid Environment for eXploration (IMEX) project (Soja et al., 2014, 2015; Sommer et al., 2014). In essence, the IMEX-streams model is a large database holding the simulated trajectories of filament particles (with  $s \gtrsim 100 \mu\text{m}$ ) created since the year 1700 by over 400 known comets, including the according tools to query this database for encounters at any given location and time.<sup>51</sup> In the testcase of the Leonids, IMEX-Streams has been shown to reproduce the timings and meteor rates of the storms reasonably well (Soja et al., 2014; Sommer et al., 2014), as exemplified Figure 5.26.

<sup>49</sup>That excludes the indirect detection of trails, e.g., via the detection of an increased number of ejecta particles emitted by the Moon under the increased meteoroid bombardment.

<sup>50</sup>The dispersion of fresh filaments may, in certain cases, be additionally be slowed by mean-motion resonances, potentially creating so-called resonant swarms within the stream (e.g., Soja et al., 2011), although this is not expected to be particularly effective at smaller, i.e., PR-effect-prone, particle sizes, see also Section 5.3.6.

<sup>51</sup>The database holds only the parts of the trajectories between the years 1980 and 2080, to conserve storage space and query time (database size is around 2.5 TB).

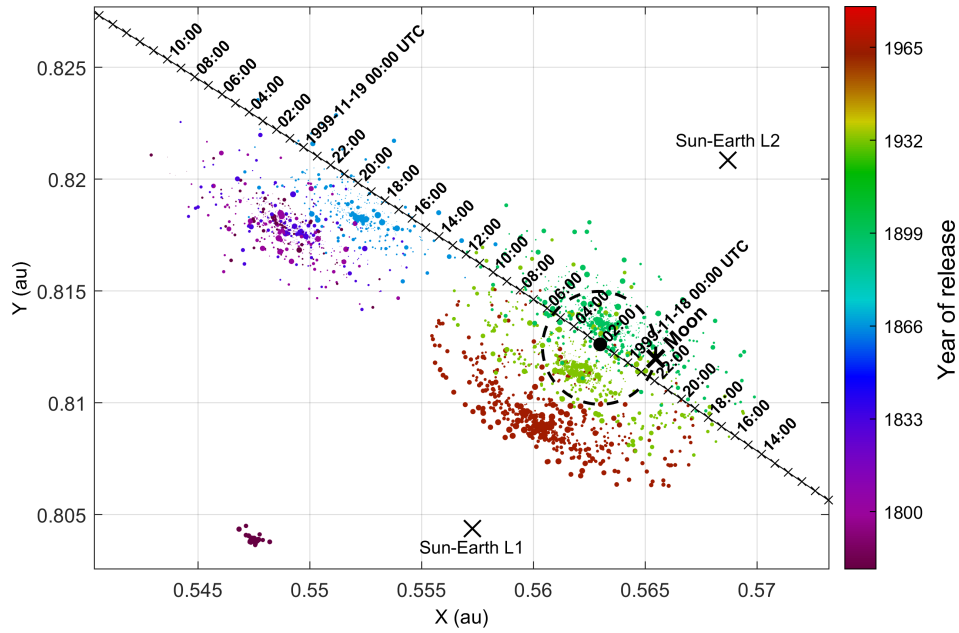


**Figure 5.26.:** Node distribution of stream particles during the 1999 Leonids storm, released during comet apparitions between 1800 and 1965, simulated with the IMEX-streams model. The black line indicates the path of the Earth where its hourly position is marked by crosses.

Krüger et al. have employed the IMEX-streams model to study the occurrence of ‘meteoroid storms’ along the trajectories of interplanetary missions: the Helios mission, which peculiarly registered recurrent particle impacts at a specific point along its orbit (Krüger et al., 2020), and the Martian Moons eXploration (MMX) mission, which will carry a 1 m<sup>2</sup> plate detector through interplanetary space to Mars (Krüger et al., 2021). Since IMEX-streams model only considers particle sizes  $s > 100 \mu\text{m}$ , Krüger et al. extrapolate the fluxes produced by the model down to radii of 10  $\mu\text{m}$ , based on an assumed trail size distributions.<sup>52</sup> However, this ignores the fact that a higher  $\beta$ -value increases the orbital period of particles, which can significantly delay the arrival times of smaller-sized constituents of the filament at a specific location. A particle released from a parent body at perihelion will obtain a  $\beta$ -factor-dependent semi-major axis  $a$ , calculated as:

$$\frac{a}{a_0} = \frac{(1 - \beta)(1 - e_0)}{1 - e_0 - 2\beta} \quad (5.12)$$

where  $a_0$  and  $e_0$  are the semi-major axis and eccentricity of the parent body (Kresák, 1976). With the orbital period of the parent body and the radiation-pressure-perturbed particle derived from Kepler’s third law of planetary motion:

$$T_0 = 2\pi\sqrt{\frac{a_0^3}{\mu}} \quad , \quad T = 2\pi\sqrt{\frac{a^3}{\mu(1 - \beta)}} \quad (5.13)$$

where  $\mu$  is the standard gravitational parameter of the Sun, we can find an expression for the

<sup>52</sup>The extrapolation down to 10  $\mu\text{m}$  is based on the assumption that the size distribution exhibits a constant power law exponent, using an exponent that was derived by Agarwal et al. (2010) for the trail of 67P/Churyumov-Gerasimenko at large particle sizes ( $> 100 \mu\text{m}$ ). Notwithstanding the changing orbital period of radiation-pressure-affected particles and thus delayed arrival times of smaller grains, this assumption is questionable, due to the loss of particles by blowout setting in at those sizes. See also Kresák (1976) for an analysis of the total mass distributions of cometary trails that takes into account the loss of smaller particles due to radiation pressure expulsion.

increase in orbital period of the released particle over that of the parent body:

$$\frac{T}{T_0} = \sqrt{\frac{(1 - \beta)^2(1 - e_0)^3}{(1 - e_0 - 2\beta)^3}} \quad (5.14)$$

For a typical JFC-type orbit with  $e_0 = 0.7$ , we find  $T/T_0 \approx 1.05$  for  $\beta = 0.005$  (corresponding to  $s \approx 100 \mu\text{m}$ , the smallest grains in IMEX-streams) and  $T/T_0 \approx 1.7$  for  $\beta = 0.05$  ( $s \approx 10 \mu\text{m}$ ).<sup>53</sup> That means that  $10 \mu\text{m}$  particles may return to the inner solar system only years after their  $100 \mu\text{m}$  counterparts, belonging to the same, drawn-out filament. We must therefore conclude, that an extrapolation from the IMEX-streams fluxes to smaller-than-modelled particle sizes is invalid, as it ignores the fact that smaller particles will arrive at the queried locations at substantially different times (that is, if they are not gravitationally perturbed during their extended aphelion excursions to miss the location altogether). We may thus consider the IMEX-streams flux predictions only for the particle sizes whose trajectories were simulated.

Nevertheless, the IMEX-streams model can be used to scout for stream traversals during the DESTINY+ nominal mission phase. After filtering streams of only marginal density or unobservable approach directions (due to DDA’s Sun-angle-requirement), IMEX-streams yielded one viable stream encounter during the near-Earth phase of the mission: the stream of 21P/Giacobini-Zinner encountered in October 2025, with a flux of up to  $0.11 \text{ m}^{-2} \text{ day}^{-1}$  at  $s > 100 \mu\text{m}$  (Krüger, priv. comm.). In fact, 21P is the parent body of the Draconids annual meteor shower and, indeed, a storm outburst has been predicted for the year 2025, due to an encounter of the young filament released during the comet’s 2012 apparition (Maslov, 2011; Ye et al., 2014; Egal et al., 2019). Even assuming that a continuous pointing toward the stream direction could be achieved, this would amount to a peak incidence rate onto DDA of merely  $0.003 \text{ day}^{-1}$ .<sup>54</sup> Taking into account that meteor storms are typically observed only for a matter of hours (see, for instance, Figure 5.26), it seems rather impossible for DDA to detect any of these particles, if not by severe luck. We therefore conclude that no detectable filament encounters, as predicted IMEX-streams, will occur along the DESTINY+ nominal mission. There may, however, exist short-lived yet dense-enough filaments of smaller particles ( $s \gtrsim 10 \mu\text{m}$ ), whose whereabouts are unknown to us. The extension of the IMEX model to such particle sizes is no mean feat, yet, the prospect of a high-mass-resolution analysis of grains whose parent body is definitely known, may warrant such efforts.

## Extended tail

The ‘dust tail’ is the (sometimes visually observable) curved arc extending from the comet in the anti-sunward direction, which is made up of small dust particles, affected by the solar radiation pressure enough to be promptly pushed away from the comet’s orbit, and potentially leave the solar system on hyperbolic trajectories. The unbound constituents of the dust tail are ‘flung away’ along the comet’s orbital plane, which we shall here refer to as the ‘extended tail’. A spacecraft could encounter a just-created extended tail upon crossing of a comet’s orbital plane thus conceivably

<sup>53</sup>Size-to- $\beta$  conversions assume  $\rho = 1 \text{ g cm}^{-3}$ , the value assumed for trail particles in IMEX-streams.

<sup>54</sup>For completeness: Adopting the conjectural extrapolation by Krüger et al. (2021) down to  $10 \mu\text{m}$  particles yields a peak incidence rate onto DDA of  $3.3 \text{ day}^{-1}$ , if pointed straight into the stream.

---

causing a cluster of impacts to be registered by an accordingly-pointed dust sensor.<sup>55</sup>

Such a detection has been speculated to have occurred during the crossing of the HEOS-2 spacecraft of the orbital plane of long-period comet Kohoutek (Hoffmann et al., 1976; Grün et al., 1976), which arrived in the inner solar system in 1973. That detection scenario is depicted in Figure 5.27: As the comet approaches the inner solar system, hyperbolic tail particles of certain sizes created during the onset of cometary activity at 3 au to 4 au may continue with near-linear motion, due to the gravity-cancelling effect of radiation pressure. Those particles, in this case moving with speeds of  $10 \text{ km s}^{-1}$  to  $15 \text{ km s}^{-1}$ , would then be overtaken by the Earth (and thus by HEOS-2) as they penetrate the ecliptic, with an apparent approach direction of  $43^\circ$  away from the apex direction toward the Sun. The apex-pointed HEOS-2 detector thus had around 20% detection efficiency toward that stream.<sup>56</sup> Around the time of the presumed encounter HEOS-2 record an increase of the impact rate over the background level by a factor of 3.5, which Hoffmann et al. (1976) and Grün et al. (1976) consider a strong indicator for the detection of the dust stream.

This scenario was further assessed by Kresák and Pittich (1976), arguing that long-period comets (such as Kohoutek) pose the best chance for such a detection, given their tendency to liberate much higher amounts of dust than their short-period counterparts. With an average of 1 to 2 long-period comets with perihelia below 1 au arriving in the inner solar system per year (Boe et al., 2019), the possibility of a deliberate extended tail detection by DDA should not be neglected. Therefore, special attention should be paid to comet discoveries once the DESTINY+ launch moves closer.

While the Kohoutek stream would have been unobservable by DDA (at least not without allowing sunlight to enter the aperture) due to its more constrained FOV, it is conceivable that more favourable detection geometries could be found for other comets, given the essentially isotropic inclination distribution of long-period comets. With its trajectory constraining capabilities, DDA could ascribe detected particles to a suspected comet with much higher certainty than HEOS-2 could. The compositional analysis of such particles would be of tremendous value to the field of solar system science, comparable with the prolific data obtained by the impact plasma mass spectrometers of comet flyby missions (e.g., by *Vega* and *Stardust*, Kissel et al., 1986, 2004).

---

<sup>55</sup>This detection scenario had been anticipated for the Pioneer 8/9 missions as a potential source for impact clusters in interplanetary space, yet was later ruled out as a frequently occurring (e.g., JFC-associated) phenomenon, due to the absence of such events in the measurements (Gerloff and Berg, 1971; Roosen et al., 1973).

<sup>56</sup>See Fig. 2b in Hoffmann et al. (1975b) showing the sensor's angular sensitive area.

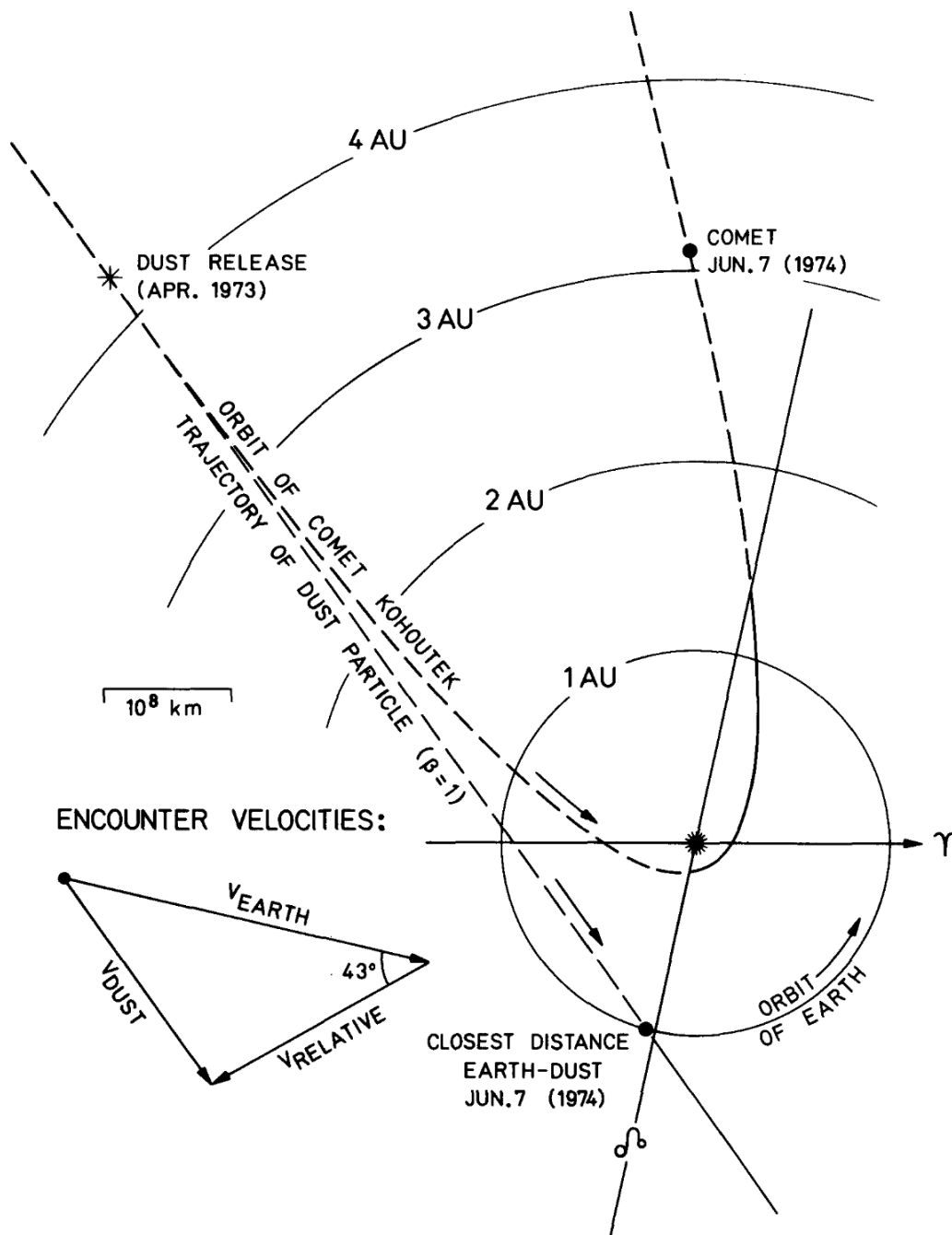


**Figure 5.27.:** Detection scenario of the Kohoutek extended tail particles by HEOS-2, taken from Hoffmann et al. (1976). The comet's line of nodes, marked by the  $\Omega$  symbol, is where its orbital plane intersects the ecliptic and, thus, that of Earth and HEOS-2.

### 5.3.6. Resonant dust

In this section, we discuss the relevance of mean-motion resonances (MMRs) for IPD particles measured by DDA. As outlined in Section 2.2, MMRs with the Earth are capable of locking dust particles into orbits of constant semi-major axis for considerable amounts of time, which gives rise to a ‘resonant ring’: a circumsolar, toroidal density enhancement near the Earth’s orbit. The most prominent structural features of this ring, as predicted by numerical models, include a sharp inner edge, a gap at the location of the Earth, as well as a density excess in the region trailing the Earth in its orbit (e.g., Stark and Kuchner, 2008).

Since the eccentric trajectory of DESTINY+ will lead the spacecraft to a trailing excursion behind the Earth, one could expect it being exposed to the highest density variations of the ring. This is illustrated in Figure 5.28, which shows the numerically modelled density distribution of the Earth’s resonant ring,<sup>57</sup> overlaid with the spacecraft’s trajectory (nominal and extended phase). This indicates that the spacecraft will indeed travel from the low density gap region into the trailing enhancement and back, which could lead one to suspect that this might be reflected in the measured IPD flux. However, we identify multiple reasons why this is not the case.

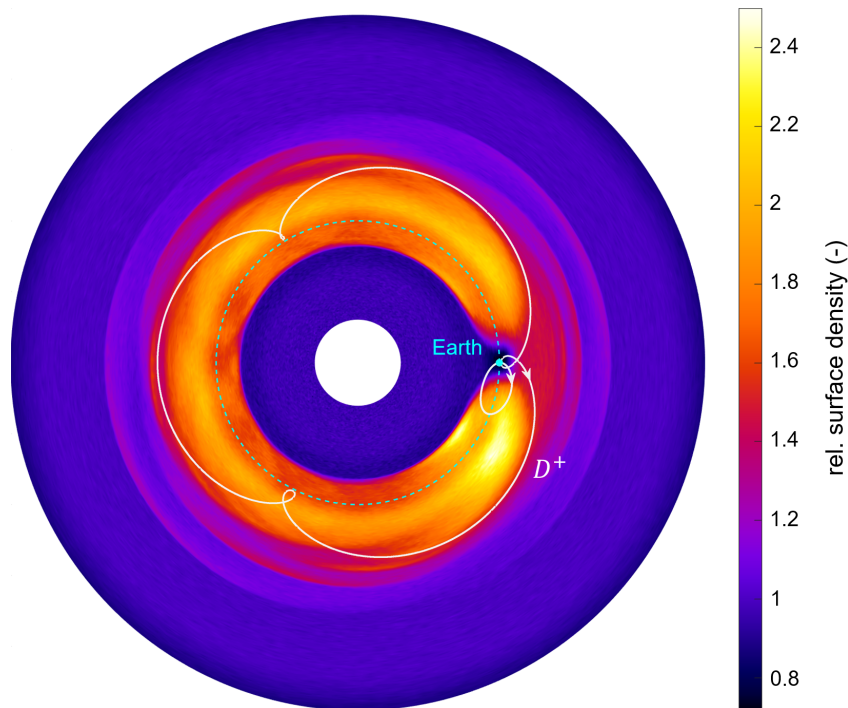


**Figure 5.28.:** The structure of Earth’s resonant ring overlaid with the DESTINY+ trajectory. The density distribution is modelled for  $\beta = 0.01$  ( $s \approx 25 \mu\text{m}$ ), in the absence of other planets. The DESTINY+ nominal phase corresponds only to the loop to the trailing side of the Earth. Plotted in a reference frame co-rotating with the Earth.

First, the ring overdensity is strongly dependent on the particle size. With higher  $\beta$ -factor the trapping efficacy decreases, due to a growing inability of resonances to counterbalance the particles’ PR-induced orbital decay (e.g., Dermott et al., 2001). Therefore, the contrast of the ring features vanishes at particle sizes of  $s < 10 \mu\text{m}$ , as seen by the radial density profiles for Earth’s modelled ring in Figure 5.29. In the size regime anticipated to be measured by DDA (submicron to few microns, see Section 5.3.1), only negligible resonance activity is expected to occur.

<sup>57</sup>For details on the numerical ring model, see Sommer et al. (2020).

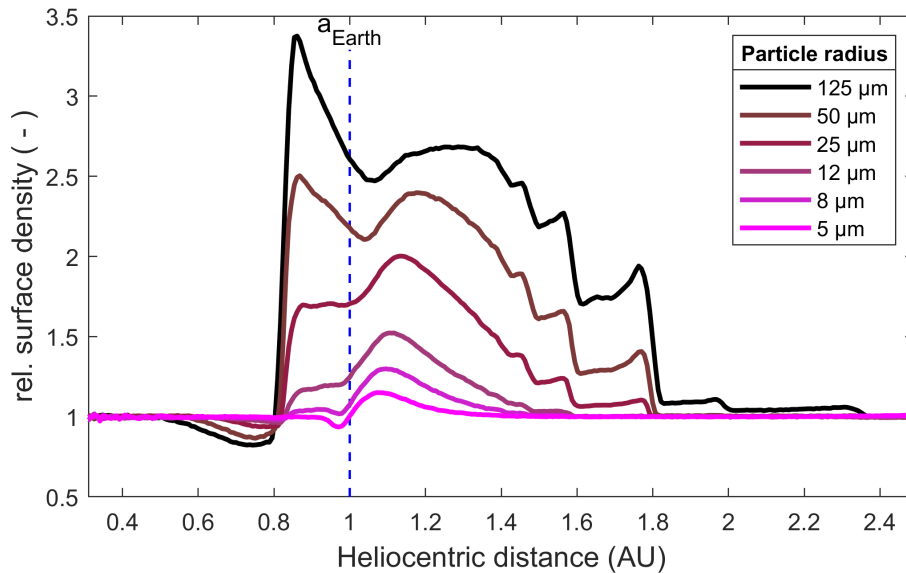


**Figure 5.29.:** Radial profiles of the density of Earth’s resonant ring at different particle sizes. (Simulated in the absence of other planets).

Secondly, models of the resonant ring typically only consider ‘dynamically cold’ particles, that is, particles with moderate eccentricities and inclinations (i.e., predominantly asteroidal dust). Their predicted overdensities are accordingly reduced by the contribution of ‘dynamically hot’ particles (i.e., particles with high eccentricities and inclinations, predominantly cometary dust), which is considered dominant in the solar system (Nesvorný et al., 2010; Rowan-Robinson and May, 2013; Soja et al., 2019, e.g.,). While a significant density variation in the zodiacal cloud might remain, this does not necessarily have to be reflected in the measured incident rate, as in-situ dust sensors are heavily biased to detect the dynamically hot component, i.e., particles with high relative velocities and accordingly amplified fluxes.<sup>58</sup>

Thirdly, Sommer et al. (2020) found that previous predictions for the Earth’s ring contrast were overestimated due to a disregard of the gravitationally perturbing influence of the other planets of the solar system. Especially Earth’s outer neighbours, Mars and Jupiter, were found to have a significant attenuating effect on the formation of the ring, in particular causing the dilution of the sharp structural features (see Figure 5.30).

For these reasons, we must conclude that in-situ instruments such as DDA are unable to investigate resonant dust in the inner solar system. Nevertheless, zodiacal light observations are being considered as additional science activities for the camera systems onboard DESTINY<sup>+</sup>, although technically being designed only for flyby science.<sup>59</sup> Unlike the particle flux, the local zodiacal light brightness directly correlates with the surrounding dust density, thus posing a viable chance for DESTINY<sup>+</sup> to detect a resonance-induced density variation.<sup>60</sup>

<sup>58</sup>Note that this is the case for in-situ dust instruments themselves deployed in a dynamically cold orbit. A detector moving in a highly eccentric orbit around the Sun, on the other hand, would also have an elevated probability of detecting dynamically cold particles (as e.g., onboard Helios, see Grün et al., 1980).

<sup>59</sup>A similar ‘reuse’ of instruments is currently being attempted in the Hayabusa2 extended mission, using the spacecraft’s navigational camera to conduct zodiacal light observations (Hirabayashi et al., 2021).

<sup>60</sup>Also conceivable (during the extended mission), would be the detection of a density variation associated with Mars, which may result from an apical alignment of particles, imposed on them upon migrating Mars’s moderately eccentric orbit, see Sommer et al. (2022).

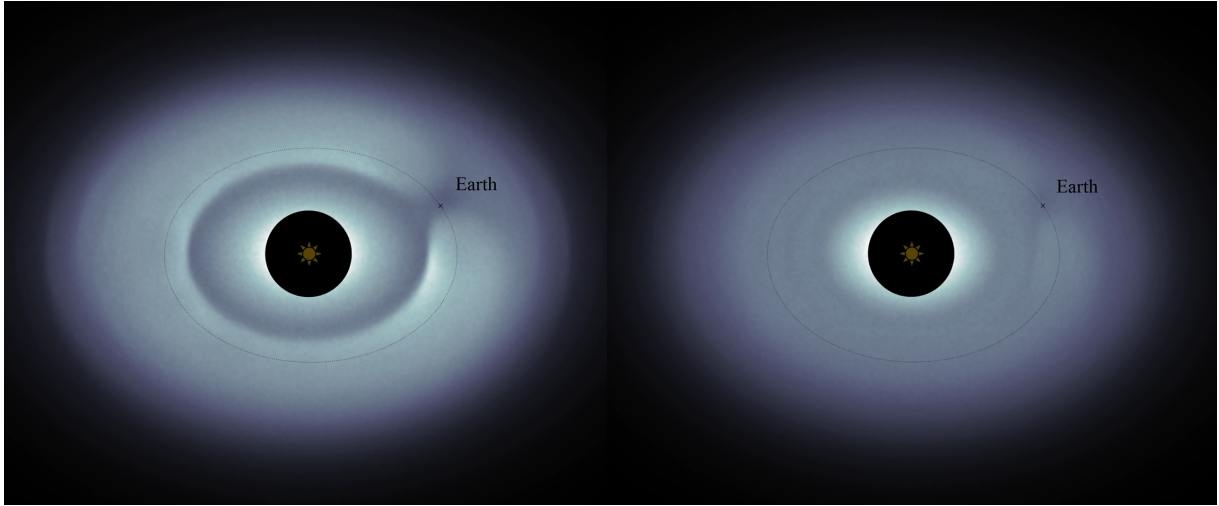


**Figure 5.30.:** Simulated infrared images of Earth’s resonant ring as seen by a distant observer. Left: the resonant ring arising in a simulation considering only the gravity of the Sun and Earth. Right: the resonant ring arising in a simulation considering the gravity of all planets of the solar system, showing a severe reduction of contrast as well as dilution of features (although the ring gap at Earth is still visible). Both images use the same (normalized, linear) colour scale. For details on how the densities distributions are modelled, see Sommer et al. (2020). These images were generated by calculating the emitted flux from each dust grain in a pixel, based on their thermal equilibrium following the method in Nesvorný et al. (2006). The contributions from various particle sizes were scaled according to a differential size distribution with slopes  $\alpha$  and  $\beta$  for sizes above and below a breakpoint  $D_{\text{mid}}$ , as outlined by Pokorný et al. (2014). In this simulation,  $\alpha = 4$ ,  $\beta = 3$ , and  $D_{\text{mid}} = 200 \mu\text{m}$ .

## 5.4. Interstellar dust

In Section 2.1.3, we have introduced interstellar dust (ISD) as the dust component of the interstellar medium, which flows into the solar system as a result of its motion through the local interstellar cloud. As a reference point for the primordial material of the solar system, ISD is a highly sought-after target for in-situ dust science, including DDA. To evaluate the corresponding observing conditions let us first consider the idealized ISD flow at Earth’s orbit, as illustrated in Figure 5.31.<sup>61</sup> Due to the directional motion of ISD, its relative velocity (and therefore its flux) with respect to an observer is modulated by that observer’s motion around the Sun. When the observer moves head-on to the flow of ISD, the ISD flux is highly elevated due to the added relative velocity (e.g., Altobelli et al., 2003; Hervig et al., 2022). This results in a kind of ‘interstellar season’, where the in-situ observation of ISD is most promising.

For an observer near Earth, this interstellar season occurs every year around vernal equinox. At the beginning of the interstellar season the ISD ram direction (that is, the upstream direction of flow relative to the observer), wanders from the solar hemisphere of the sky (the half of the sky facing the Sun) over the observer’s heliocentric apex direction for the duration of the highest relative velocity, and then continues into the anti-solar hemisphere. For DDA, the angular separation between the ISD ram direction and Sun’s direction, which we refer to as ram-Sun angle, is crucial for assessing overall observability. DDA can observe the ISD ram direction with full efficiency only when the ram-

<sup>61</sup>For the idealized flow, we assume particles with  $\beta = 1$ , unperturbed by electromagnetic forces, thus moving on linear trajectories through the solar system. Furthermore, an upstream direction at ecliptic longitude and latitude of  $259^\circ$  and  $8^\circ$  and a velocity of  $26 \text{ km s}^{-1}$  is assumed, see Section 2.1.3.

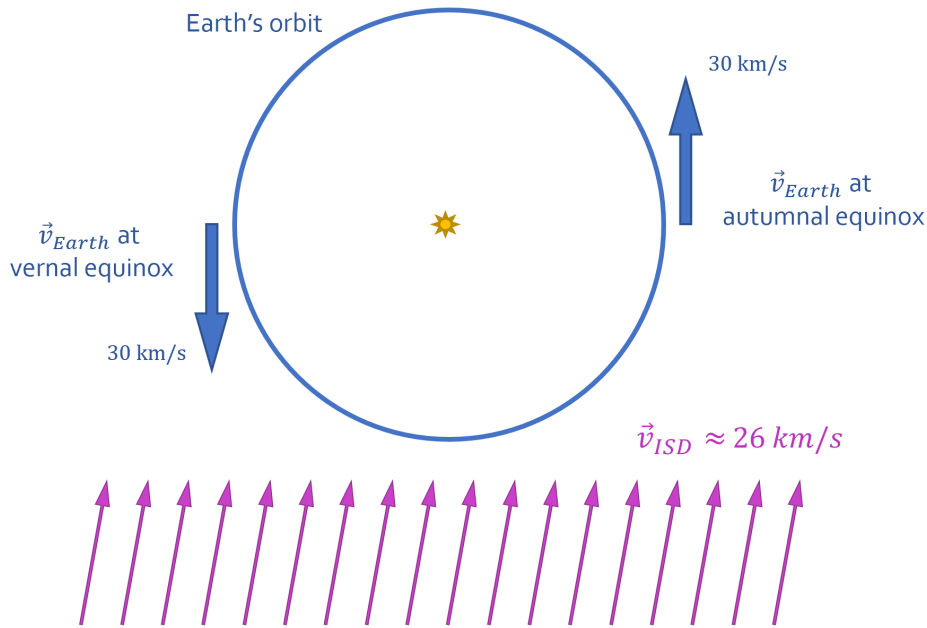


**Figure 5.31.:** The idealized flow of ISD ( $\beta=1$ ) at the Earth's orbit.

Sun angle is above  $90^\circ$ .<sup>62</sup> Figure 5.32 shows the ram-Sun angle and relative velocity of the idealized ISD flow with respect to DESTINY+. Periods favourable for ISD observation, meaning when the ram-Sun angle is above  $90^\circ$  and the relative velocity is high (e.g.,  $>30 \text{ km s}^{-1}$ ), are indicated in green. It is worth noting that during the interplanetary cruise phase (after April 2027), the interstellar season at the spacecraft begins only marginally later than when still in orbit around Earth, due to its continued proximity to Earth.

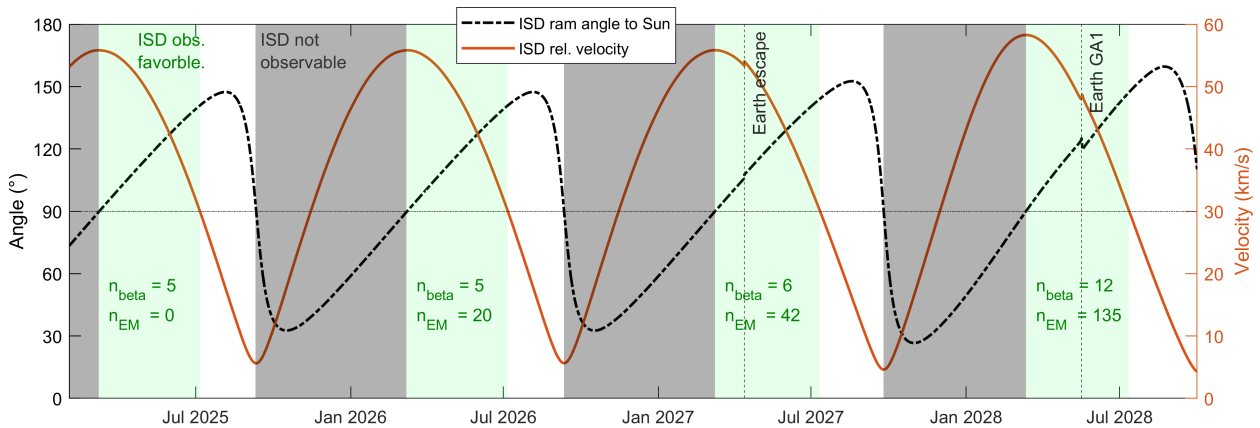


**Figure 5.32.:** Ram-Sun angle and relative velocity of the idealized ISD flow, with respect to DESTINY+. From launch to Earth escape, spacecraft position and velocity are assumed to be equal to that of the Earth. DDA may only be pointed toward the ISD flow when the ram-Sun angle is  $>90^\circ$ . The ISD flux is highest when the relative velocity is highest. Favourable periods for ISD observation (i.e., ram-Sun angle  $>90^\circ \wedge$  relative velocity  $>30 \text{ km s}^{-1}$ ) are indicated in green. The expected fluence for a DDA pointing constantly into the ram direction are shown within each favourable period (modelled with IMEX-ISD by Krüger, priv. comm.).

<sup>62</sup>However, observation with partial sensitivity can be conducted before that by pointing the boresight at an angle to the ram direction. For example, 50% of DDA's nominal sensitive area can be exposed to the ISD flow while the ram-Sun angle is still around  $70^\circ$ , see DDA's angular sensitivity in Figure 4.3.

---

### 5.4.1. Model predictions

For quantitative analysis as well as for considering the non-idealized ISD flow, we resort to the IMEX-ISD model. IMEX-ISD is a time-resolved representation of the flow of ISD up to heliocentric distances of 10 au, created from a Monte-Carlo-type simulations that take into account the changing configuration of the IMF over the course of the solar cycle. Developed by Strub et al. (2019) (taking up works of Sterken et al. (2012, 2013)), IMEX-ISD models 12 particle sizes within a range of  $0.05 \mu\text{m} \lesssim s \lesssim 5 \mu\text{m}$ , and is calibrated with data from the Ulysses dust detector. The evaluation of the IMEX-ISD model along the DESTINY+ trajectory, taking into account the DDA detector geometry, has been conducted by Krüger et al. (2019, 2022) and is summarized in the following.<sup>63</sup> We herein classify particles of the non-idealized ISD flow into three categories according to the force characterizing their motion (see Section 2.1.3).

- G-ISD, the larger considered particles with  $s \gtrsim 0.5 \mu\text{m}$  (whose trajectories are characterized by solar gravity), is too rare to be detected in the ‘undisturbed’ flow (i.e., on the upstream side of the sun). Downstream of the Sun they are gravitationally focussed such that they produce elevated fluxes, which however are unobservable by DDA due to an approach direction near the Sun’s direction.
- $\beta$ -ISD, particles within  $0.1 \mu\text{m} \lesssim s \lesssim 0.5 \mu\text{m}$  (whose trajectories are characterized by radiation pressure) are partially observable by DDA. Smaller particles with a  $\beta$  considerably above unity are ‘radiation-pressure filtered’, meaning they are deflected before reaching the inner solar system. On the other hand Larger  $\beta$ -ISD particles with  $\beta \approx 1$  ( $0.3 \mu\text{m} \lesssim s \lesssim 0.5 \mu\text{m}$ ) are observable more or less in the fashion of the idealized flow with a peak flux expected right at the beginning of the observation windows seen in Figure 5.32.
- EM-ISD, the smallest considered particles with  $s \lesssim 0.1 \mu\text{m}$  (where the  $\beta$ -factor returns to values around unity and the electromagnetic force dominates the motion), may be observable by DDA depending on the solar cycle: During the focussing configuration of the IMF (see Section 2.1.3), the flow of EM-ISD is concentrated towards the ecliptic plane. As with  $\beta$ -ISD, the EM-ISD flux is the highest around the time the observation window begins, with a ram direction near the observer’s apex. During the defocussing configuration of the IMF, EM-ISD does not reach the inner solar system. Over the course of the DESTINY+ mission the IMF will transition from an initially defocussing configuration to a focussing configuration, reaching its maximum focussing strength in the first half of the 2030s.

The fluences predicted by the model for  $\beta$ -ISD and EM-ISD for a DDA pointing constantly into the ram direction are shown in Figure 5.32 for each observation period. The number of observable  $\beta$ -ISD particles per year exhibit a moderate increase over the course of the mission (from 5 to 12).<sup>64</sup> For EM-ISD, on the other hand, an increase from zero detectable particles during the first observation period in 2025 to 135 particles in 2028 is predicted. For the timeframe of the extended mission the model predicts more or less steady  $\beta$ -ISD fluences in the order of 10 particles per observing period

---

<sup>63</sup>Whereas Krüger et al. (2019) used a now-obsolete trajectory corresponding to a mission launch date in 2022, Krüger et al. (2022) give a (yet unpublished) update on the IMEX-ISD evaluation for a trajectory corresponding to a launch date in 2024 (trajectory file name `BackUp1.bsp`). The trajectory of the current launch date in early 2025 resembles that of 2024 reasonably well, both featuring a Phaethon flyby in January 2028 and a proximity to Earth during the interplanetary cruise phase. Therefore, we can assume the results of Krüger et al. (2022) to be representative for the current baseline trajectory as well.

<sup>64</sup>This increase of the  $\beta$ -ISD is also caused by the focussing of the IMF, which is still partially effective at these particle sizes (Strub et al., 2019).

and a further increase of EM-ISD fluences to around 300 particles per season from 2029 onwards (Krüger et al., 2022).

We would like to point out, that the IMEX-ISD model uses an idealized solar cycle model with a period of 11 years, which might be slightly out of sync. Whereas IMEX-ISD assumes a maximum for Solar Cycle 25 maximum in 2022 and final minimum in mid 2029 (where the strongest focussing occurs), recent predictions suggest the maximum and the final minimum to be reached in early-to-mid 2024 and in 2030, respectively (e.g., Espuña Fontcuberta et al., 2023). This would result in a delayed focussing, such that the IMEX-ISD-predicted increase in EM-ISD fluences could occur later.

#### 5.4.2. Conflict with thrusting periods

As discussed in Section 3.1, the DESTINY<sup>+</sup> spacecraft will perform two extended ion engine thrusting periods during the interplanetary cruise phase, to adjust its course for the Phaethon flyby and then the Earth gravity assist manoeuvre. Here we discuss whether these thrusting periods will interfere with the DDA observation of ISD, due to the fixed thrusting vectors and, thus, inflexible spacecraft attitude.

The first thrusting period of about 5.5 months starts on June 3 2027, which is towards the end of the 2027 ISD observation window. With the thrusting vector in between the retrograde and ecliptic south direction, and a fixed roll angle around thrusting vector required for full illumination of the solar panels, the spacecraft assumes an attitude as indicated in Figure 5.33 (left). The PME achieves a pointing as close as 16° from the idealized ISD ram direction.<sup>65</sup> Thus, at the end of the 2027 observation window, the ISD flow may only be observed with about 50% detection efficiency. However, as previously noted, the ISD flux is expected to be already low at this time.

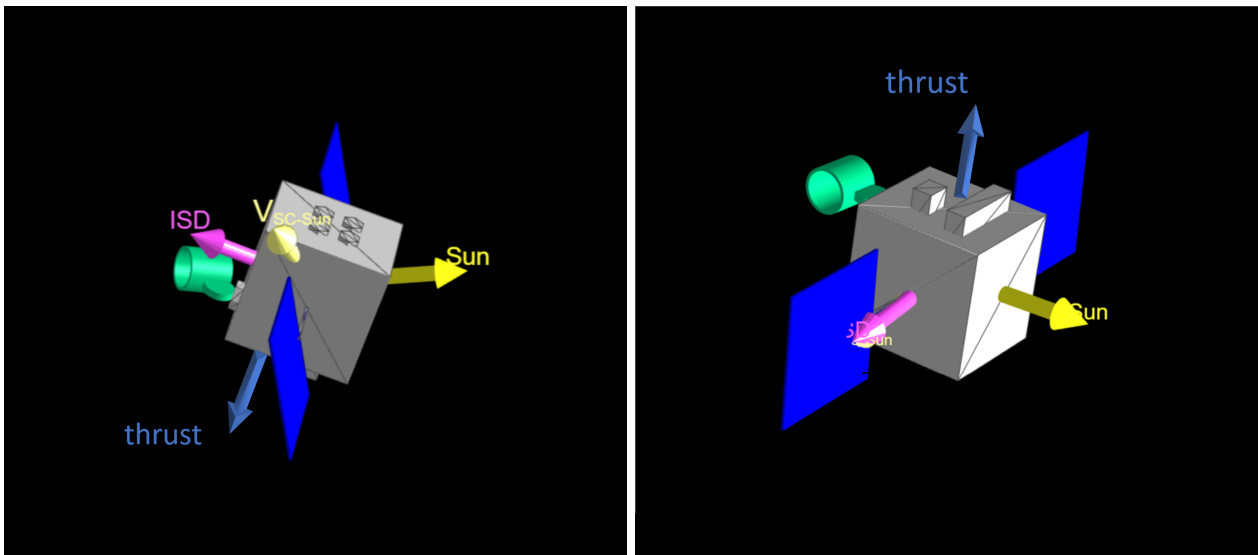


**Figure 5.33.:** Spacecraft attitude during interplanetary thrusting periods: Left: The beginning of the first thrusting period on June 3 2027. Right: The end of the second thrusting period on March 12 2028. Arrows indicate the direction of the Sun, the spacecraft’s heliocentric velocity vector (or apex, labelled ‘ $V_{SC-Sun}$ ’), and the ISD ram direction (magenta). In the right panel, the vectors of ISD ram and spacecraft velocity are nearly parallel. The renderings have been created with the DOPE tool, which is introduced in Section 6.4.

<sup>65</sup>At the beginning of the thrusting period the ISD ram direction has already veered off toward the anti-helion direction, which makes it easier to reach under the given spacecraft attitude.

---

The second thrusting period of about 1 month ends on March 12 2028, overlapping with the start of the 2028 observation window. At that time, the thrusting vector is close to the ecliptic north direction, with an according spacecraft attitude as indicated in Figure 5.33 (right). Here, the PME achieves nearly straight pointing towards the idealized ISD ram direction, with an offset of  $<10^\circ$ , when pointing along the spacecraft +Y axis. Therefore, around 70% of the nominal sensitive area may be exposed to the ISD flow (see DDA’s angular sensitivity profile, Figure 4.3). Since the overlap of thrusting period and observation window is only a few weeks, the impact on the above presented fluences is miniscule. However, should the PME not be available during this stage of the mission (either due to a malfunction, or a late descoping of the PME azimuth axis) a significant loss of fluence must be expected, since the overlap coincides with a peak in the ISD flux. This issue was discussed with the JAXA/DESTINY+ mission design office. In case of the PME functionality being insufficient for observing the start of the 2028 ISD window, a higher thrust level and thus earlier termination of the corresponding thrusting period by several weeks will likely be possible (Ozaki, priv. comm.) A change of the spacecraft’s coasting attitude could then potentially re-enable the full observation of the 2028 ISD window.

Assuming that the interplanetary trajectory of DESTINY+ will remain unchanged, we conclude that the thrusting periods will pose no hurdle for successful ISD observation campaigns with DDA. The situation during the Earth-bound spiralling phase, however, is more complicated. In Section 6.5.1, we analyse the time-averaged detection efficiency towards the flow of ISD that can be achieved under the constantly changing spacecraft attitude during this phase.

### 5.4.3. Distinguishing interstellar dust

As we have shown, the predominant parts of both the ISD flux and the IPD flux (in the form of  $\alpha$ -meteoroids) are expected to arrive at the spacecraft from the heliocentric apex direction. This poses the fundamental question of how to distinguish between the two dust populations. A straightforward way would be via their different velocities. From Figure 5.32 we can see that the impact velocities around the beginning of the ISD season (where most particles will be detected) are in the range of 40 to 60 km s<sup>-1</sup>, which agrees with the velocities of  $\beta$ -ISD and EM-ISD particles, as modelled with IMEX-ISD by Krüger et al. (2022). The  $\alpha$ -meteoroids, on the other hand, are expected to arrive with velocities  $<20$  km s<sup>-1</sup> (see Section 5.3.3). Differentiation could thus be achieved by recognition of these two velocity regimes.

DDA may accomplish this task with its charge-sensing entrance grids that allow for a TOF speed measurement of impacting grains larger than a few 100 nm (corresponding to  $\beta$ -ISD particle sizes). However, the smaller EM-ISD particles will not be registered by the charge-sensing entrance grids. This hinders straightforward differentiation, although it can be argued, that such small IPD particles may only be on hyperbolic trajectories (due to their large  $\beta$ -factor) and are unlikely to approach from the apex direction.

A similar differentiation scheme has been employed by Altobelli et al. (2003, 2005), who, in lack of an accurate speed measurement, evaluated the impactor energy instead (estimated from the measured ion impact charge  $QI$ ). An equivalent approach may also be suitable for DDA, in cases where TOF velocity measurements are lacking.

Impactor speed estimates derived from the signal shape of the measured ion impact charge,

---

as used by previous impact plasma detectors, are excluded for DDA, whose reflectron ion optic negates energy differences in the impact plasma. However, the recorded mass spectrum also contains information about the impactor's speed: The higher the speed, the more efficient the breakup of molecules into smaller molecules and atoms. Above  $20 \text{ km s}^{-1}$ , the impact plasma becomes dominated by neutrals and singly ionized atoms (Hillier et al., 2018). The absence of ionized molecules could be considered a (rather speculative) indicator for impactor speeds in the ISD-typical regime. Furthermore, the absence of specific atomic species in the mass spectra, which require certain velocity thresholds for their ionization, may provide additional indication for low impact speeds ( $\lesssim 10 \text{ km s}^{-1}$ , see Hillier et al., 2018).

## 6. Science and Operations Planning

In this chapter, we identify science objectives based on our considerations of the various types of dust possibly encountered by DESTINY+, and describe strategies and tools to effectively develop corresponding observation campaigns with the DDA instrument. Finally, we propose a coarse timeline of high-level science activities to be executed by DDA over the course of the mission, and demonstrate the design of granular pointing timelines for specific observation campaigns.

As a whole, this domain is commonly referred to as *science planning*. Its goal is to maximize the scientific return of the mission, by devising observation timelines that integrate the science objectives with the spacecraft and instrument capabilities and constraints. The transition from the high-level, so-called ‘science themes’ of a space exploration mission to machine-oriented timelines of instrument instructions is a challenging, interdisciplinary task, requiring extensive collaboration among scientists, operators, and engineers. Recognizing the operational commonalities among a growing number of planetary science missions, as well as the potential for optimization, space agencies such as ESA identified the need for a more standardized approach to science planning (Koschny et al., 2004; Hoofs et al., 2004). At ESA, structured science planning processes have since been employed for all planetary missions, as demonstrated for *Venus Express* (Titov et al., 2006), *Rosetta* (Koschny et al., 2007; Pérez-Ayúcar et al., 2018b), or *BepiColombo* (de la Fuente et al., 2016; Montagnon et al., 2021) among others. As far as applicable, we adapt principles of the ESA science planning process to the DDA instrument and take up the commonly used terminology.

### 6.1. The Science Themes concept

In our strategy to derive observation timelines for DDA, we will adhere to the ‘Science Themes’ concept, as proposed by Koschny et al. (2004). It is an ESA-established top-down approach to science planning, with the goal of linking any allocated observation time to the overarching science objectives of the mission. When adapting the Science Themes concept to the case of DESTINY+/DDA, it is important to once again emphasize the unique conditions of this planetary science mission:

- DDA is the only active instrument for the vast majority of the mission.<sup>1</sup>
- The spacecraft attitude is predetermined for large parts of the mission, yet, the instrument can be pointed autonomously, due to its two-axis mounting.

These conditions contrast to the typical case of a multi-instrument mission, where the Science Themes approach is also used to identify conflicts or capitalize on synergies between different instruments. Furthermore, planetary science missions usually involve conditions of a more flexible spacecraft attitude, which is controlled to adjust the pointing of the body-fixed instrument suites.<sup>2</sup>

---

<sup>1</sup>The two camera instruments onboard are designed for flyby science only. (Although other potential usages, such as occasional zodiacal light observations are being discussed).

<sup>2</sup>In the case of the Rosetta mission, even the spacecraft trajectory in the low-gravity field of comet 67P was flexible and constituted a part of the near-term science planning (Costa et al., 2016b; Vallat et al., 2017).

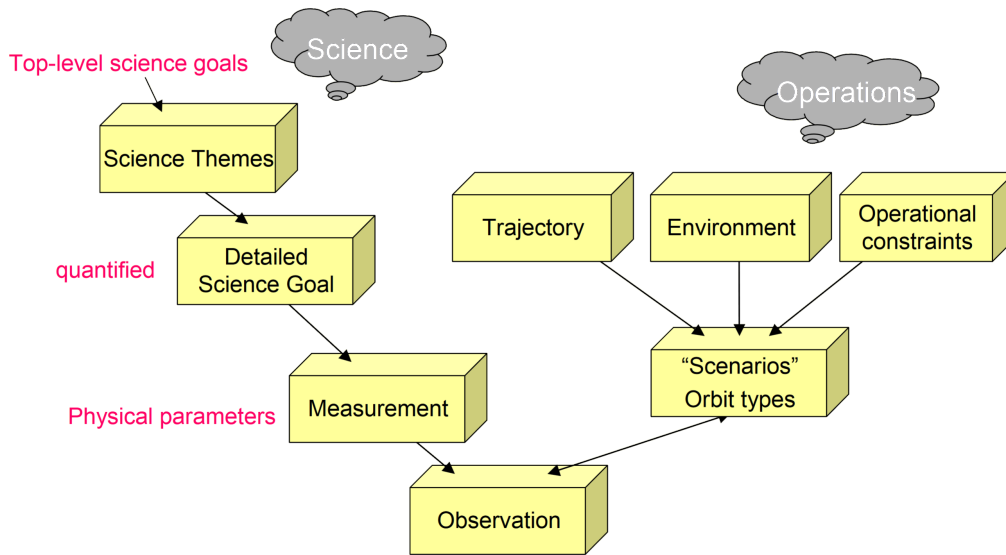


**Figure 6.1.:** Science Themes concept, taken from (Koschny et al., 2004).

There are two sides to the Science Themes concept, which is illustrated in Figure 6.1: the science side and the operations side. On the science branch (left), science themes define the overall domain of phenomena to be studied, which in our case are the different types of cosmic dust to be encountered by DDA. Within each science theme, more specific, quantifiable science objectives are then identified, such as the characterization of a certain dust property.<sup>3</sup> In the Science Themes concept, these objectives (goals) translate to measurements, which can be executed by one or more instruments to provide the necessary physical information to achieve the objective. In the case of DDA, however, the required measurement is virtually the same in all cases, namely, the dynamical, physical, and chemical analysis of individual dust particles.

The operations branch (right), on the other hand, takes into account the technical constraints of the mission. From the trajectory and corresponding operational aspects, ‘scenarios’ can be derived, which in our case correspond to the mission phases of DESTINY<sup>+</sup>, as discussed in Chapters 3 & 4.

By combining the science and operations sides, feasible and effective observation modes can be identified to achieve the science objectives. To some extent, this has already been done in Chapter 5, where we have identified certain observational requirements to study the different types of dust. Accordingly, Table 6.1 consolidates the science and operations sides for the dust types examined in Chapter 5 (excluding those deemed unobservable due to technical constraints) to compile the corresponding observations with respect to their applicable timing and instrument pointing mode.

Knowing the observational requirements for each dust type, one may now schedule the tackling of the various objectives over the course of the mission, while ensuring that all science themes are addressed in a balanced way. This will be done as part of the long-term preparation stage of the science operations, as described in the following section.

## 6.2. Planning cycles

To transition from the above defined science objectives to instrument command sequences, a three-step iterative planning process with increasing granularity is employed, as illustrated in Figure 6.2.

<sup>3</sup>The science objectives may also be called ‘science requirements’ in similar contexts (e.g., Koschny et al., 2010).

**Table 6.1.:** DDA science themes.

Science theme	Objectives	Observation		
		When	Pointing	
<b>Micro-debris</b>	Determine abundance of SRM dust	While within GEO altitudes	Close to the Earth-centric apex direction	
<b>Magnetospheric swarms</b>	<ul style="list-style-type: none"> <li>• Confirm the presence of particle swarms within the magnetosphere</li> <li>• Determine origin (artifcl. or natural) by dyn. &amp; chem. characterization</li> <li>• Determine swarm dimensions and size distribution</li> </ul>	While within 60,000 km from Earth	Probe various directions, with emphasis on the heliocentric apex	
<b>Lunar ejecta</b>	diffuse exosphere	Detect the dust exosphere at yet unexplored altitudes (200–5000 km) and regions (latitudes $>20^\circ$ )	While within 5000 km from the Moon	Exosphere ram direction (equiv. to the Moon-centric spacecraft velocity vector)
	roaming groups	Detect particle groups within EMS and dynamically confirm lunar origin	While within the EMS	Moon within FOV
<b>Alpha-meteoroids</b>	<ul style="list-style-type: none"> <li>• Confirm as the predominant bound dust population</li> <li>• Determine perihelion range to confirm collisional origin</li> </ul>	Anytime	Heliocentric apex within FOV	
<b>Sporadic meteoroid complex</b>	<ul style="list-style-type: none"> <li>• Determine validity of meteoroid models at dust sizes</li> </ul>	Anytime	5 principal directions: apex, antapex, N/S toroidal, anti-helion.	
	<ul style="list-style-type: none"> <li>• Analyse a meaningful number of SMC dust particles and establish a link with their source body type (asteroidal or cometary)</li> </ul>	During perihelion and outbound arc of interpl. trajectory	N/S toroidal (perihelion) and anti-helion (outbound)	
<b>Cometary streams</b>	Detect ‘extended tail’ particles	During orbital plane crossings of arriving long-period comets	Variable. Depends on velocity vector of comet during inner solar system approach.	
<b>Interstellar dust</b>	<ul style="list-style-type: none"> <li>• Determine variability of flux and size distribution from year to year</li> <li>• Analyse an unprecedented number (<math>\sim 100</math>) of EM-ISD</li> </ul>	During the interstellar season (roughly from February to May)	ISD ram direction (close to heliocentric apex)	

This includes the long-term (strategic) planning, the medium-term (pointing-oriented) planning, and the short-term (commanding-oriented) planning. The goal of each stage is the generation of planning products (e.g., pointing requests), which are used as inputs for the next stage, and, finally, for the mission operations centre controlling the spacecraft.

### 6.2.1. Long-term planning

In the broadest sense, the long-term planning stage takes place during the entire mission life-cycle, from the study phase, through the implementation phase, and until the end of the mission. More specifically, the long-term planning comprises the definition of science themes and objectives, and corresponding observational aspects (as done within the scope of this thesis), as well as the generation of the Science Activity Plan (SAP), which coarsely schedules the science activities throughout the mission. In the case of DDA, the priority with which observations are allocated to applicable time slots is largely determined by the uniqueness of opportunity of the corresponding measurements. For example, the study of interstellar dust takes precedence during the ‘interstellar season’, as it may be observed only during that time.

See Section 6.3 for the present working version of the DDA-SAP.

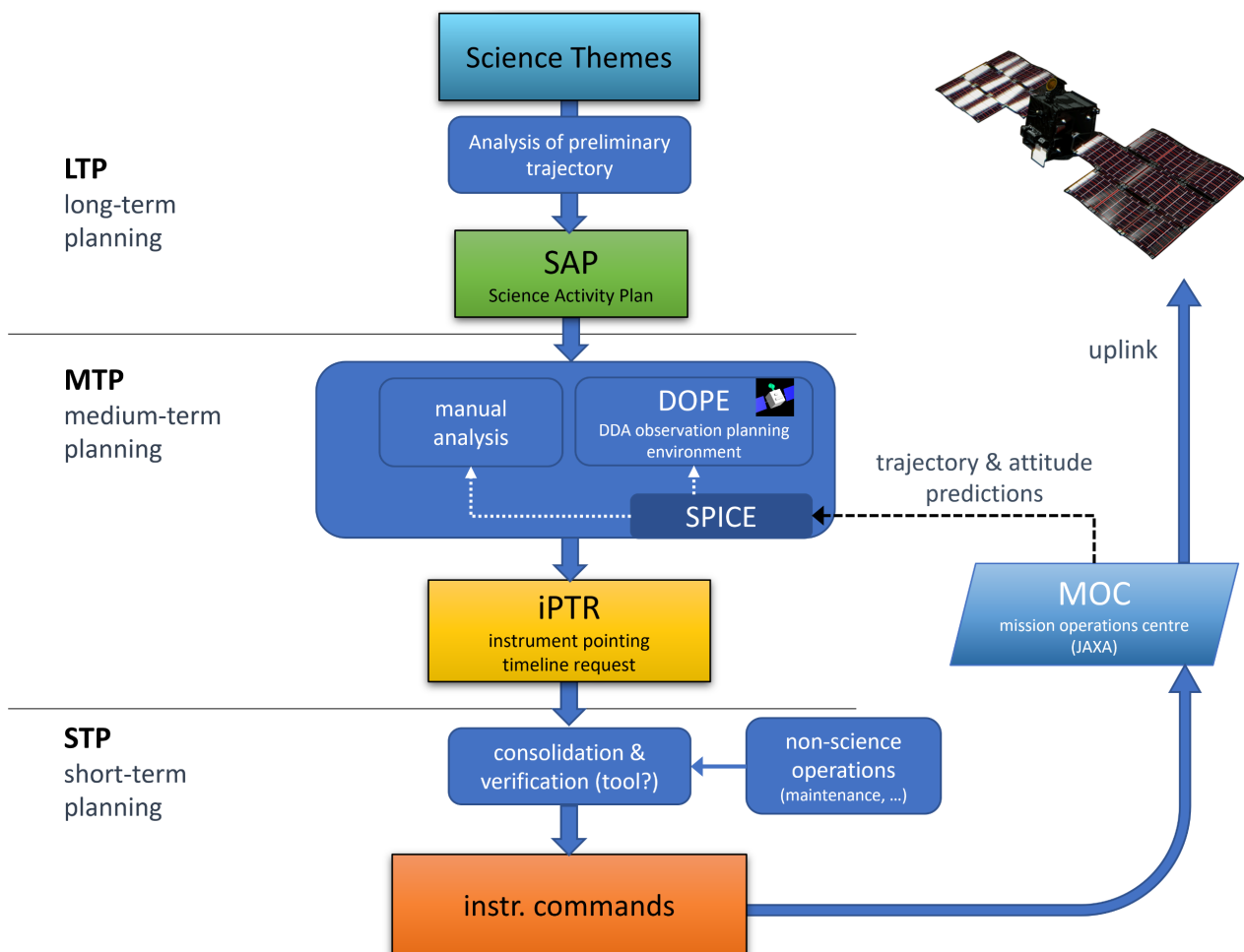


Figure 6.2.: DDA operations planning scheme.

---

### 6.2.2. Medium-term planning

The goal of the medium-term planning stage in the DDA operations preparation is to derive instrument pointing timelines based on the SAP and updates on the predicted spacecraft trajectory and attitude, which will be provided by the mission operations centre (JAXA/ISAS) during mission implementation. The medium-term planning is foreseen to occur up to months before the actual execution of the observations.

To accomplish this task, a software tool, DOPE was developed within the scope of this thesis project, which is described in Section 6.4. DOPE allows for the semi-automated generation of instrument pointing timeline requests (iPTRs), which hold the required sequence of angular states of the DDA pointing mechanism, based simply on specified observation targets.

At this point, no constraints regarding data volume and power consumption have been identified that would have to be considered in the medium-term planning.

Examples of medium-term planning with the DOPE tool are given in Section 6.5.

### 6.2.3. Short-term planning

Even closer to execution, on the order of weeks ahead, the short-term planning commences to generate the actual command sequences for the DDA instrument, to be provided to the mission operations centre for uplink to the spacecraft. These will be derived from the instrument pointing timeline requests (iPTRs) generated in the medium-term planning and shall also incorporate non-science operations, such as the instrument decontamination procedures (see Section 4.5).

This stage is not covered by the scope of this thesis, but is being addressed by the DDA instrument team and might be incorporated into the DOPE tool in the future.

## 6.3. Science Activity Plan (SAP) - proposal

Based on the results and considerations presented in this thesis, we propose a DDA-SAP, which schedules the high-level science activities over the course of the mission. The development of the SAP is an ongoing, iterative process that reflects the evolving understanding of the mission and its scientific potential, as well as updates in the trajectory design. Upon major changes, it is presented to and discussed with the DDA science team, which convenes bi-weekly.

The SAP is displayed in Figures 6.3–6.6, covering the years 2025 to 2028. Note that the second half of year 2028, following the gravity assist manoeuvre at Earth, already belongs to the (hypothetical) extended mission. Stated fluxes and fluences correspond to the pointings specified with each observation, notwithstanding the fact that only partial exposure may be achieved, particularly during the attitude-dynamic early mission phase.

The immovable annual ‘interstellar seasons’ build the backbone of the SAP, around which the study of planetary and interplanetary dust phenomena are scheduled. The ISD observations are named according to their corresponding year, e.g., ‘ISD C25’ (interstellar dust campaign 2025). The first ISD campaign, ISD C25, would occur right after launch, although it is heavily affected by the constraints of the early mission phase.<sup>4</sup> Subsequently, as long as within the magnetosphere,

---

<sup>4</sup>The delayed cover opening of DDA (see Section 4.4) prevents observation of the favourable first half of the ISD season. In addition, the ion detector might be switched off, due to the recurring passing of the Earth’s inner

---

observation of the magnetospheric swarms will be prioritized. The dynamic attitude of the spacecraft during this phase is compatible with this observation, which does not require a particular pointing direction to be maintained (although the heliocentric apex is preferred). While within GEO-altitudes, a secondary objective is the study of SRM dust, although the number of detectable particles is expected to be low (a few impacts over the entire period, as estimated with MASTER).

With the start of ISD C26, the spacecraft revolves mostly above an altitude of 60.000 km, where magnetospheric swarms stop to occur. Although the orbital period has increased to a few days, the spacecraft attitude is unfavourable, allowing only fractional coverage of the ISD ram direction (thus only a part of the ISD C26 fluence will be observable, see the exemplary MTP planning in Section 6.5.1). After the end of ISD C26, the spacecraft attitude will become more favourable for observations towards the heliocentric apex, therefore, observation of the  $\alpha$ -meteoroids will be prioritized. An alternative objective during the 2026 timeframe is the study of roaming lunar ejecta groups, which can be observed anytime the Moon is within the coverage zone of the pointing mechanism (see Section 6.5.3, for an example of lunar group observation MTP).

The start of 2027 marks the end of the spiralling phase and the beginning of the unthrusting lunar gravity assist phase. ISD C27 is thus the first viable, with static spacecraft attitude observable ISD campaign. Only towards the end of the season (when the flux has already subsided), an interplanetary thrusting period will commence, which reduces the detection efficiency towards the ISD ram direction by 50% (see Section 5.4.2). Further into the prolonged manoeuvre, the thrusting vector will increasingly prevent observations near the heliocentric apex. Therefore, this period is suited for surveying other directions, as is required for the study of SMC dust. The predominant radiants of SMC dust are not unambiguous. The IMEM (Dikarev) model predicts the highest fluxes from the anti-helion and ‘toroidal’ direction, while the IMEM2 model predicts the highest fluxes from directions around the ecliptic poles. The derived incidence rates onto DDA are generally below 0.1 per week, however, also few or non-detections are of interest, as valuable constraints on the directional distributions of particles.

2028 begins with the Phaethon flyby and a subsequent out-of-plane thrusting manoeuvre of around one month, which overlaps slightly with the beginning of ISD C28. However, the ISD ram direction is still within reach of the pointing mechanism (see Section 5.4.2). The nominal mission concludes with the Earth gravity assist manoeuvre during ISD C28. If the mission is extended, the time after the Earth flyby may be highly favourable for the study of SMC dust, as the gravity assist manoeuvre will accelerate the spacecraft to reach considerable outward radial motion (at least in the 2500 UD flyby scenario), thereby enhancing the anti-helion flux, according to the Dikarev model.

---

radiation belt (see Section 3.4). Lastly, the swiftly changing spacecraft attitude diminishes the achievable detection efficiency towards the ISD ram direction.

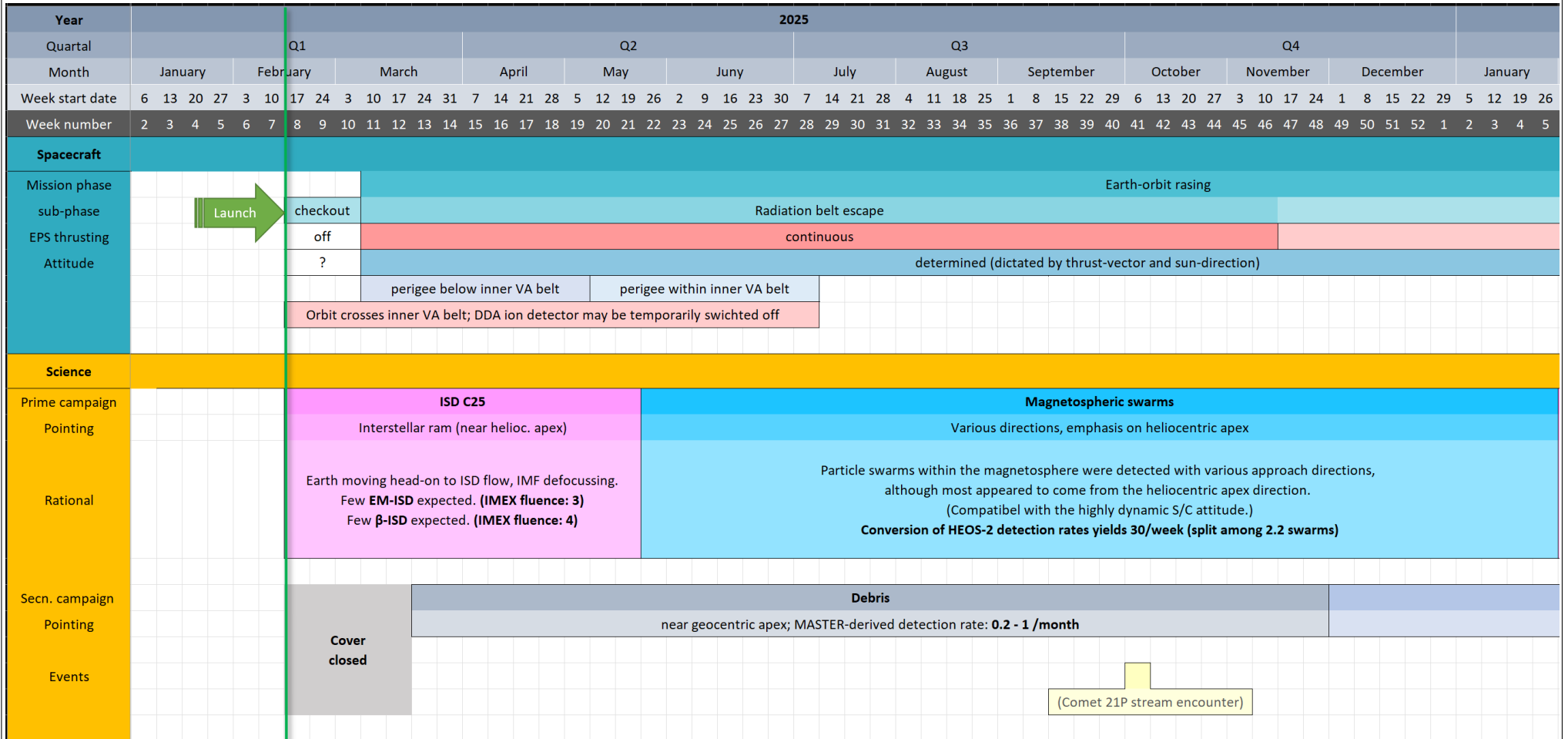


Figure 6.3.: SAP proposal for the year 2025.

Year	2026																																																							
Quartal	Q1				Q2				Q3				Q4																																											
Month	January		February		March		April		May		June		July		August		September		October		November		December		January																															
Week start date	5	12	19	26	2	9	16	23	2	9	16	23	30	6	13	20	27	4	11	18	25	1	8	15	22	29	6	13	20	27	3	10	17	24	31	7	14	21	28	5	12	19	26	2	9	16	23	30	7	14	21	28	4	11	18	25
Week number	2	3	4	5	6	7	8	9	10	11	12	13	14	15	16	17	18	19	20	21	22	23	24	25	26	27	28	29	30	31	32	33	34	35	36	37	38	39	40	41	42	43	44	45	46	47	48	49	50	51	52	53	1	2	3	4
Spacecraft																																																								
Mission phase	Earth-orbit raising																																																							
sub-phase	optimized orbit raising																								GA1																															
EPS thrusting	intermittent																																																							
Attitude	determined (dictated by thrust-vector and sun-direction)																																																							
Science																																																								
Prime campaign			ISD C26								Alpha-meteoroids																																													
Pointing			Interstellar ram (near helioc. apex)								Near heliocentric apex (within 30°)																																													
Rational			Earth moving head-on to ISD flow, IMF defocussing. Some <b>EM-ISD</b> expected. ( <b>IMEX fluence: 23</b> ) Few <b>β-ISD</b> expected. ( <b>IMEX fluence: 5</b> ) Highest flux in the first months of the campaign.								Apex-particles make up most of the IPD flux. Mass range: $1e-13 \text{ g} < m < 1e-11 \text{ g}$ ( $0.5 \mu\text{m} < D < 2 \mu\text{m}$ ). Approach direction is roughly from the ape; impact velocities 5-20 km/s. Expected flux onto DDA (for continuous apex pointing): <b>~ 1 / week</b>																																													
Secn. campaign																																																								
Pointing	Roaming lunar ejecta groups																																																							
Events	Moon within FOV; DDA-converted HEOS-2 detection rates: <b>~ 3 /week</b>																																																							

Figure 6.4.: SAP for the year 2026.

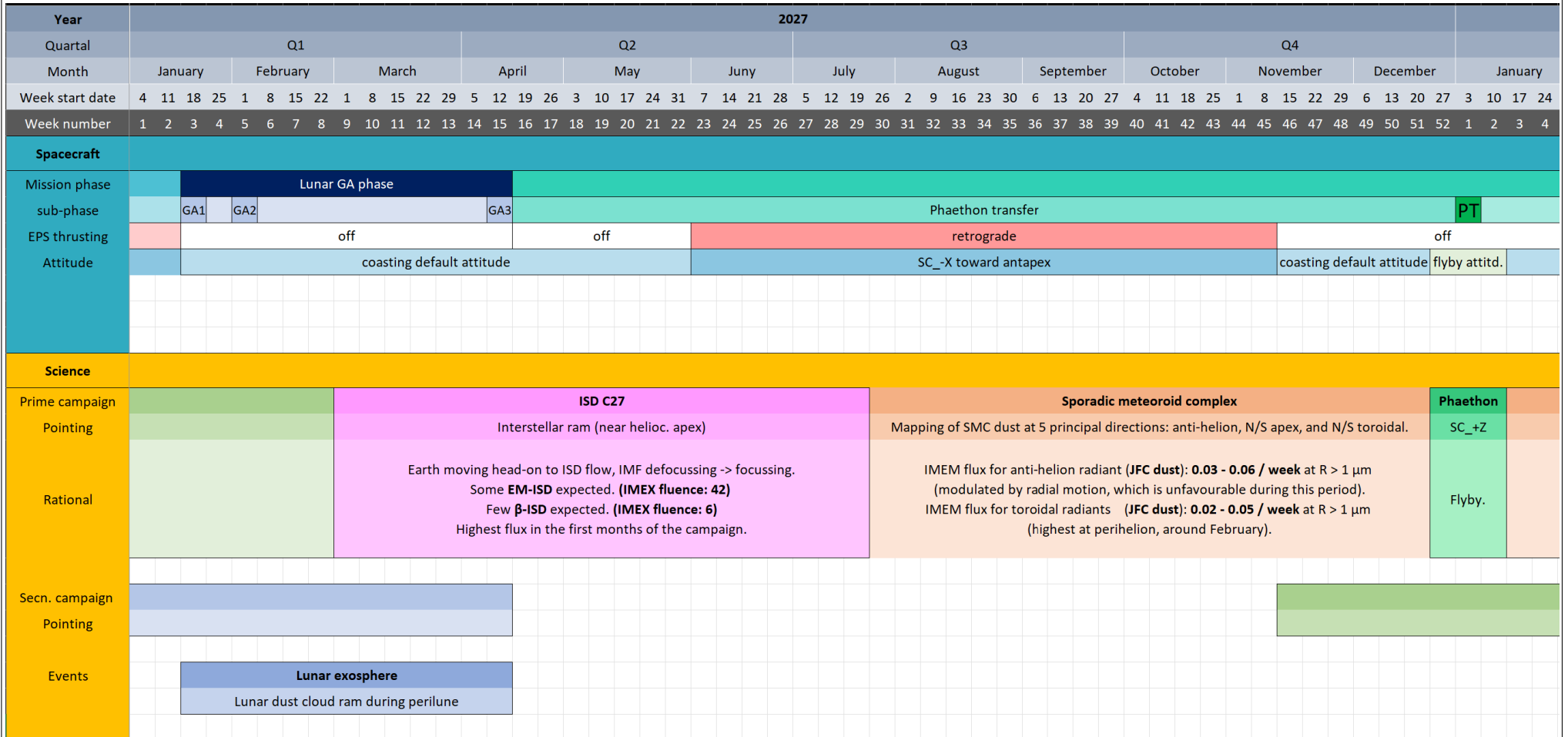


Figure 6.5.: SAP for the year 2027.

Year	2028																																																											
Quartal	Q1													Q2													Q3													Q4																				
Month	January					February					March					April					May					June					July					August					September					October					November					December				
Week start date	3	10	17	24	31	7	14	21	28	6	13	20	27	3	10	17	24	1	8	15	22	29	5	12	19	26	3	10	17	24	31	7	14	21	28	4	11	18	25	2	9	16	23	30	6	13	20	27	4	11	18	25								
Week number	1	2	3	4	5	6	7	8	9	10	11	12	13	14	15	16	17	18	19	20	21	22	23	24	25	26	27	28	29	30	31	32	33	34	35	36	37	38	39	40	41	42	43	44	45	46	47	48	49	50	51	52								
Spacecraft	Interplanetary cruise																																																											
Mission phase	Interplanetary cruise																																																											
sub-phase	PT																		EGA					extended mission													UD																							
EPS thrusting						out-of-plane																		off																																				
Attitude	y attitd.					-X toward ecl. north																		coasting default attitude																																				
Science																																																												
Prime campaign	aethon																		ISD C28													SMC					2500 UD																							
Pointing	C_+Z																		Interstellar ram (near helioc. apex)													Anti-helion direction					SC_+Z																							
Rational	flyby.																		Earth moving head-on to ISD flow, IMF focussing. Many <b>EM-ISD</b> expected. ( <b>IMEX fluence: 135</b> ) Some <b>β-ISD</b> expected. ( <b>IMEX fluence 12</b> ) Highest flux in the first months of the campaign.													High outward velocity due to Earth GA causes enhanced anti-helion fluxes. Best chance to detect JCF/AST dust with $R > 1\mu\text{m}$ at <b>~ 0.15 / week</b>					Flyby.																							
Secn. campaign																																																												
Pointing	Alpha-meteoroids																																																											
Events	Near heliocentric apex (within 30°), ~ 1 / week																																																											

Figure 6.6.: SAP for the year 2028.

---

## 6.4. Observation planning tool: DOPE

The generation of pointing timelines (instrument or spacecraft) is a complex task, that involves handling of trajectory and attitude data, and the complicated processing of geometrical information (like conversions between coordinate and time systems, FOV footprint calculations, etc.). This error-prone task warrants the development of tools that provide users with a more intuitive, interactive approach to designing pointing timelines, along with the possibility to visually verify the correctness of the observations. At ESA, such tools have had a long-standing role in aiding the operations planning of planetary science missions (e.g., Hoofs et al., 2004; Almeida, 2012; Costa et al., 2014; van der Plas et al., 2016; Pérez-Ayúcar et al., 2018a). Tools of this sort have come to unanimously draw on the SPICE astrometry library,<sup>5</sup> which, due to its reliability and adaptability, has established a significant user base across the mission-related space science community, including at ESA (Costa et al., 2016a, 2020).

Following that approach, the DDA Observation Planning Environment (DOPE) was developed within the scope of this thesis project. DOPE is a graphical tool that takes as inputs DESTINY+ spacecraft trajectory and attitude data (as SPICE kernels), and visualizes them in a 3D environment. It also displays the 2D projection of the sky around the spacecraft and indicates important regions and directions (such as the PME coverage range, the DDA FOV, or certain dust radiants). It allows the user to set the DDA pointing by specifying a direction to be aimed at, for instance towards the ISD ram direction or the heliocentric apex direction. DOPE then automatically calculates the corresponding PME angular states to achieve the desired pointing direction. If the target is not within reach of the PME, or if the angular separation of target and Sun is below  $90^\circ$ , the tool will find the closest feasible direction that respects the pointing constraints. (DOPE also allows the user to specify a secondary target direction, which will be used in case the primary target is not feasible to observe.) In that way, the tool can be used to automatically generate pointing timelines, given the desired observation targets and a time interval at which to reorient the sensor.<sup>6</sup>

Under the hood, DOPE relies on the SPICE library to perform all geometrical (or time-related) calculations. DOPE is a MATLAB-built app that requires at least the license-free MATLAB Runtime to be installed on the computer to be executed. (To develop the app, a full MATLAB installation is required.)

Figures 6.7 and 6.8 give an impression of the DOPE user interface, while the visualization panel is in focus. Overviews of the trajectory and attitude selection panels are given in Appendix F. In the following we demonstrate the use of DOPE through exemplary medium-term planning exercises.

---

<sup>5</sup>SPICE (Spacecraft, Planet, Instrument, Camera-matrix, Events) is a collection of APIs and smaller applications to work with geometrical (and temporal) data in the context of space missions. SPICE is developed and maintained by NASA's Navigation and Ancillary Information Facility (Acton, 1996; Acton et al., 2018), and is available freely for scientists and engineers to build applications upon it. The primary SPICE datasets are called 'kernels', which contain the time-resolved geometrical information on celestial bodies and spacecraft, usually generated by the mission operations centres.

<sup>6</sup>Alternatively, time points can also be specified individually with arbitrary intervals.

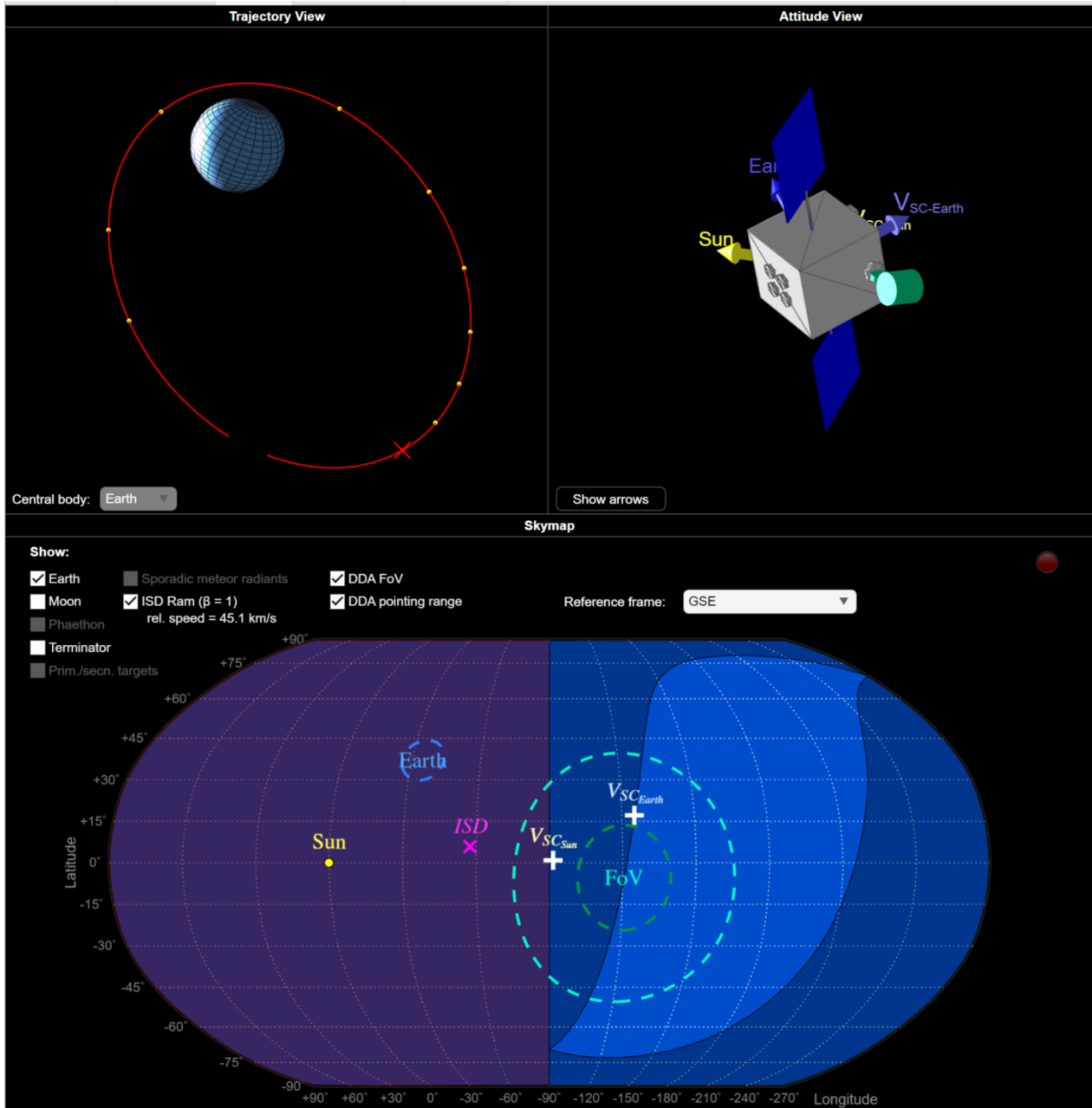


**Figure 6.7.:** DOPE geometry visualization, showing 3D displays of the spacecraft trajectory (top left) and attitude (top right), as well as a 2D projection of the sky around the spacecraft (bottom) with indicators for the DDA pointing range, FOV, and other relevant elements. This allows the user to get a better feeling for the geometrical conditions.

Time control / setting of time points

Visualization panels

Added time points appear here

The screenshot displays the DOPE application interface, which is divided into several functional panels:

- Top Left Panel:** Contains trajectory kernel information (EscapeRadBelt\_230x37000km\_40mN\_202409150600\_60sec), SPK time period (2024 SEP 15 06:00:00 - 2025 MAY 12 08:08:21), and S/C attitude definition (Rules-based).
- Left Panel (Time Control):** Features an "Add Timepoints" section with a date selector (2024-Dec-24), a time input (23.5 hours), and an "Apply time" button. Below this is an "Increment time by" section set to 60 minutes, with "Forward" and "Backward" navigation buttons. A "Selected time" field shows "2024 DEC 24 23:30:00" with "Add to sequence" and "Add 10 points to sequence with increment" buttons.
- Bottom Left Panel (DDA Pointing Control):** Includes "Set DDA Pointing" controls with sliders for Azimuth (23.0°) and Elevation (0.0°). It has a "Manual" toggle and an "Automatic" mode. Under "Automatic", there are dropdowns for "Primary target" (Apex) and "Secondary target" (Sun-Safe), along with a "Switchover angle" set to 50°. Buttons for "Select all timepoints" and "Assign pointing to selected timepoints" are at the bottom.
- Central Panel (Visualization):** Divided into three views: "Trajectory View" (top left) showing a red orbital path around Earth; "Attitude View" (top right) showing a 3D model of the spacecraft with its solar panels and instruments; and "Skymap" (bottom) showing a 2D projection of the sky with Earth, Sun, and various velocity vectors ( $V_{SC\ Earth}$ ,  $V_{SC\ Sun}$ ,  $V_{SC\ Earth}$ ) and fields of view (FoV) and ISD.
- Right Panel (Timepoint series):** A table listing time points with columns for UTC, Azimuth (°), Elevation (°), and Primary target. The first row is highlighted in yellow.

	UTC	Azimuth (°)	Elevation (°)	Primary target
1	24-Dec-2024 23:30:00	23	0	None
2	25-Dec-2024 00:30:00	NaN	NaN	None
3	25-Dec-2024 01:30:00	NaN	NaN	None
4	25-Dec-2024 02:30:00	NaN	NaN	None
5	25-Dec-2024 03:30:00	NaN	NaN	None
6	25-Dec-2024 04:30:00	NaN	NaN	None
7	25-Dec-2024 05:30:00	NaN	NaN	None
8	25-Dec-2024 06:30:00	NaN	NaN	None
9	25-Dec-2024 07:30:00	NaN	NaN	None
10	25-Dec-2024 08:30:00	NaN	NaN	None

Annotations on the screenshot include:

- A red arrow pointing from the "Time control / setting of time points" label to the "Add Timepoints" section.
- A red arrow pointing from the "Visualization panels" label to the central visualization area.
- A red arrow pointing from the "Added time points appear here" label to the "Timepoint series" table.
- Red text "The pointing timeline can be exported here" with an arrow pointing to the "Export sequence" button.
- Red text "An animation of the pointing timeline can be created here" with an arrow pointing to the "Capture sequence" button.
- An orange bracket at the bottom left encompasses the "DDA pointing control" label and the "Set DDA Pointing" panel.

Figure 6.8.: Screenshot of the DOPE application, showing the geometry visualization on the central panel.

## 6.5. Observation pointing timelines - examples

### 6.5.1. Observation of interstellar dust

This example demonstrates the planning of the observation of ISD during the 2026 interstellar season. Figure 6.9a shows the pointing timeline computed by DOPE, by setting the ISD ram direction as primary observation target with a reorientation interval of 60 min. To minimize the number of DDA reorientations, the tool was set to switch to the ‘Sun-safe’ position (see Section 4.3) if a pointing with the ISD ram direction within the sensor FOV is not possible. Figure 6.9b shows the resulting angular separation between the DDA boresight and the ISD ram and the Sun direction. Only for about half the orbit, the PME is able to keep the ISD ram direction within the FOV (illustrated by the blue line in Figure 6.9b being below  $45^\circ$ ). The time it can maintain nearly straight pointing toward the ISD ram direction is less than 1/5th of the orbit. From this pointing sequence we can derive the detection efficiency toward the ISD ram direction (i.e., the time-averaged exposed sensitive area as a fraction of  $A_0$ ), amounting to about 21%.

This low figure is particularly due to the spacecraft attitude profile during this phase, or more specifically, due to the orientation of the spacecraft orbit with respect to the Sun, which governs the spacecraft attitude profile. A few months later, coverage of the heliocentric apex direction is much more viable, as demonstrated in the next section.

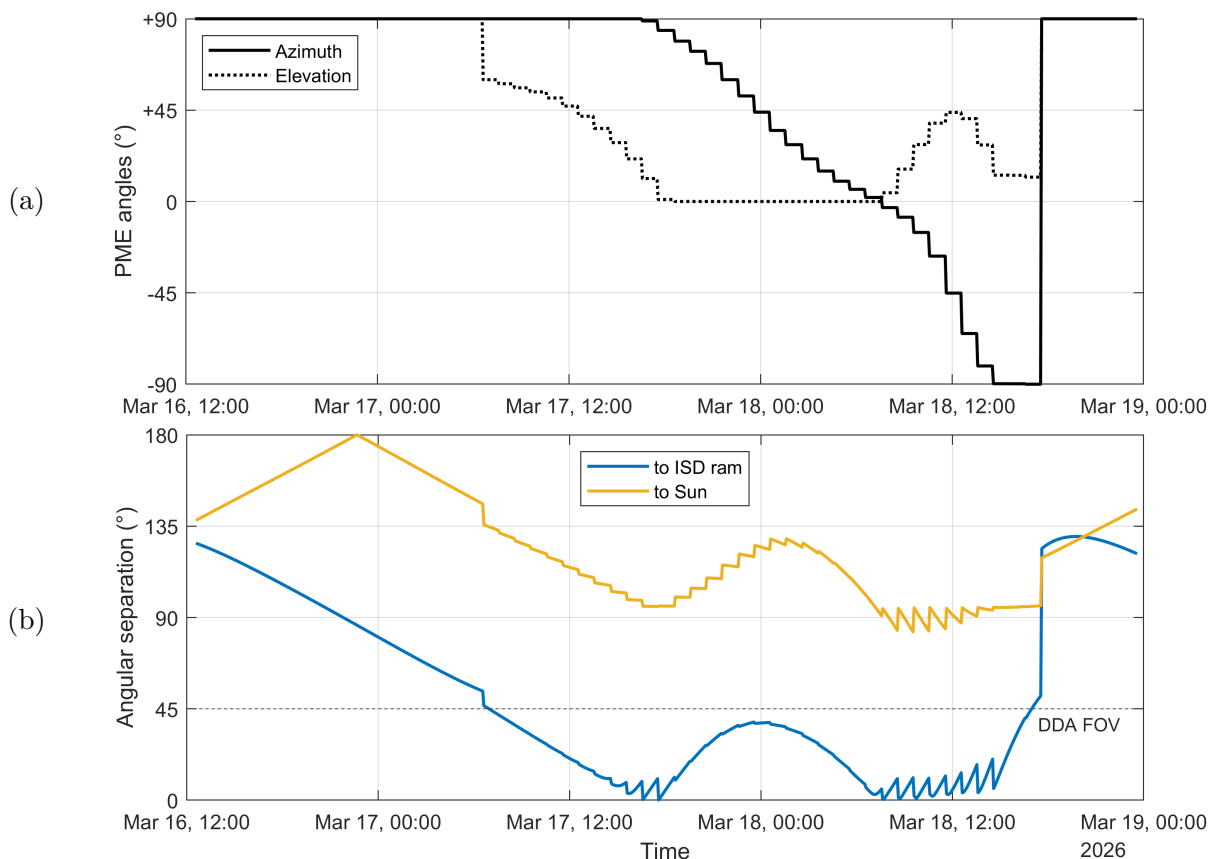


**Figure 6.9.:** Pointing timeline example for ISD C26. Observation sequence generated with DOPE, using the automatic pointing mode with the ISD ram direction as primary observation target (pointing interval of 60 min). The covered time period corresponds to one full geocentric orbit. (a): Sensor azimuth and elevation angles. (b): Angular separation between the DDA boresight and the ISD ram direction, as well as the Sun direction.

### 6.5.2. Observation of alpha-meteoroids

The planning of  $\alpha$ -meteoroid observation during the later spiralling phase in 2026 is demonstrated in this example. We have configured DOPE to automatically target the heliocentric apex direction (the predominant direction of  $\alpha$ -meteoroid impactors), switching to the Sun-safe position if the primary target cannot be kept within the sensor's FOV. As in the previous example, Figure 6.10 shows the angular state of the PME and angular separations of the DDA boresight to the apex direction and the Sun, for one full orbit. This observation sequence yields a time-averaged detection efficiency toward the apex direction of about 30%—a significant improvement over the previous example, despite the much longer reorientation interval of 6 h.

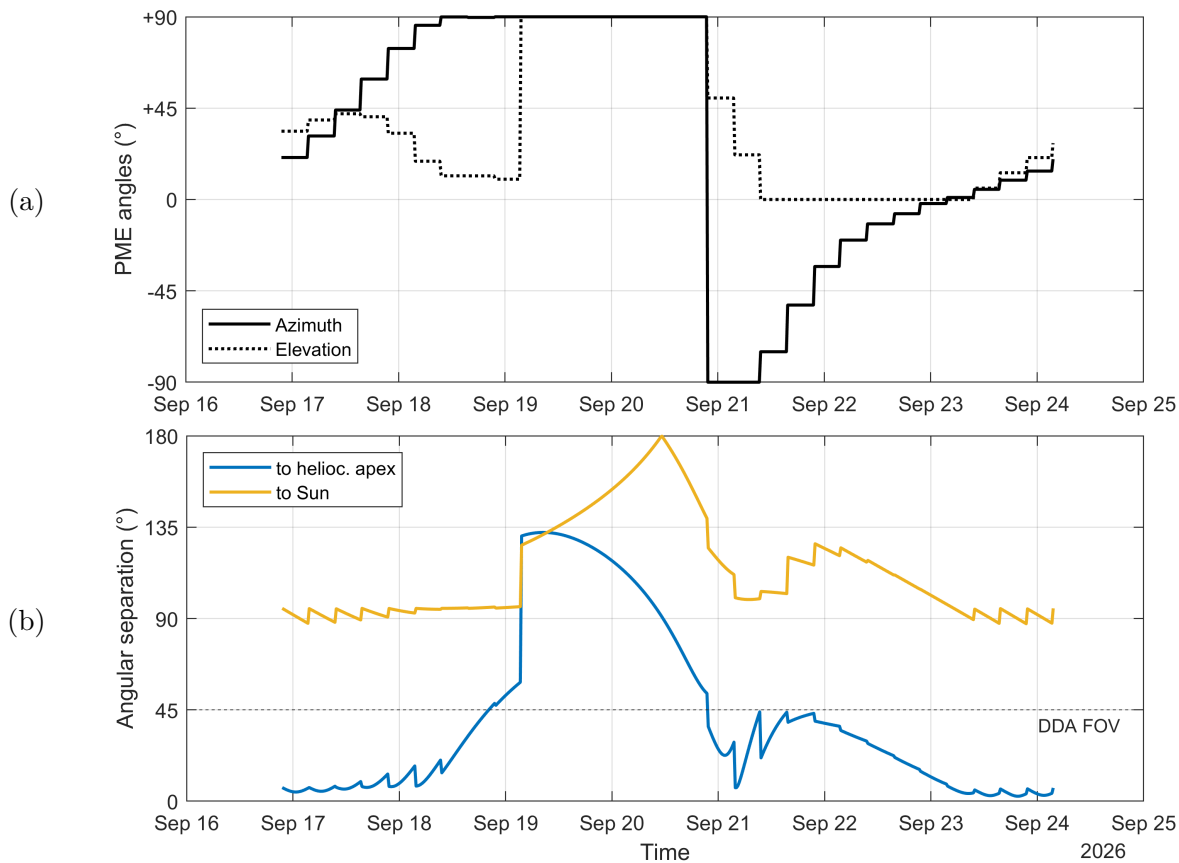


**Figure 6.10.:** Pointing timeline for the observation of  $\alpha$ -meteoroids. Observation sequence generated with DOPE, using the automatic pointing mode with the heliocentric apex direction as primary observation target (pointing interval of 6 h). The covered time period corresponds to one full geocentric orbit. (a): Sensor azimuth and elevation angles. (b): Angular separation between the DDA boresight and the heliocentric apex direction, as well as the Sun direction.

### 6.5.3. Observation of lunar ejecta groups

This last example demonstrates planning of the observation of the roaming lunar ejecta groups towards the end of the spiralling phase, during a favourable Moon passage. It also shows the automatic switching between two observation targets when the primary target is unreachable. Here, we assign the Moon direction (nadir) as the primary observation target and the heliocentric apex direction as the secondary target. A switchover distance of  $50^\circ$  is set, meaning that if the primary

target cannot be reached by at most  $50^\circ$ , DOPE will attempt to reach the secondary target instead.

Figure 6.11 presents the resulting timelines. DOPE toggles from the primary observation target (the direction of the Moon) to the secondary (the apex direction) around October 21/22, when the PME is unable to reach the primary target. This yields a time-averaged detection efficiency of about 51% for the Moon direction and about 7.5% for the apex direction, for the examined time period. This ‘dual target’ mode effectively maximizes the utilization of observation time.

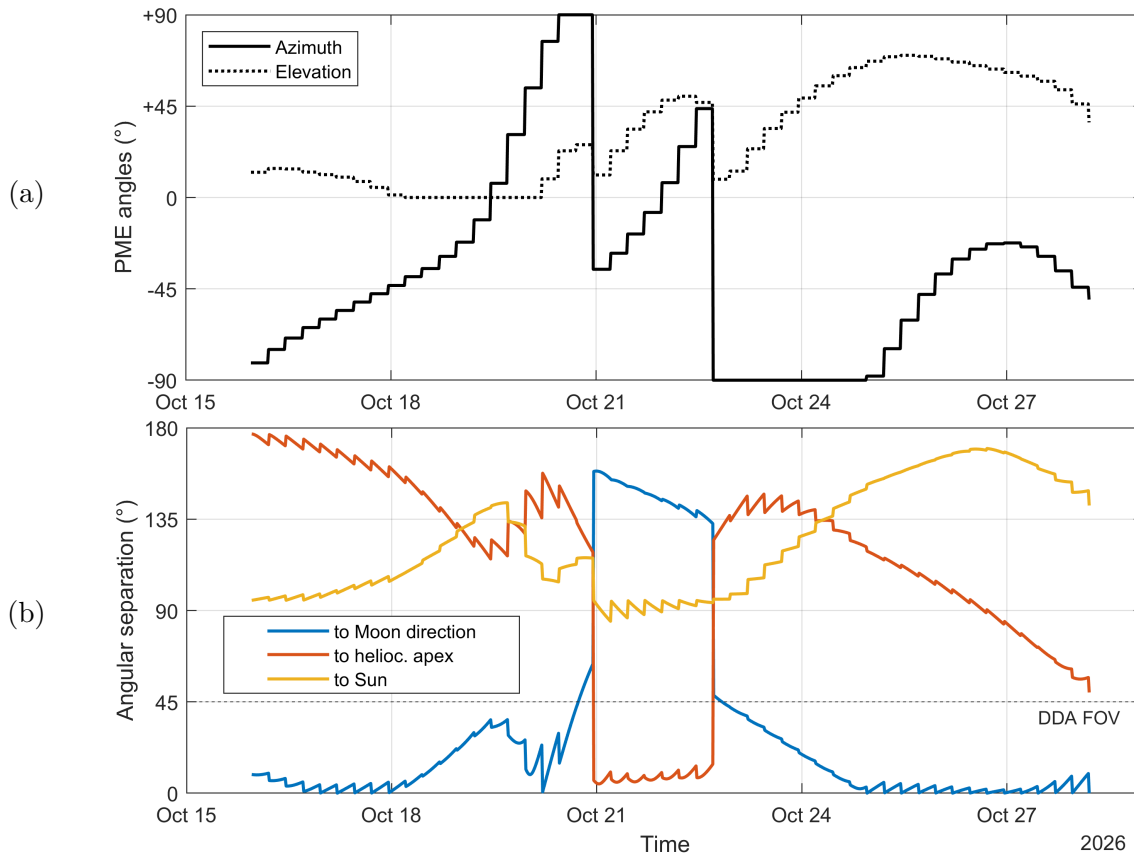


**Figure 6.11.:** Pointing timeline for lunar ejecta groups observation. Observation sequence generated with DOPE, using the automatic pointing mode with the Moon direction (nadir) and the heliocentric apex as secondary observation target (pointing interval of 6 h). The covered time period corresponds to one full geocentric orbit. (a): Sensor azimuth and elevation angles. (b): Angular separation between the DDA boresight and the primary and secondary observation targets, as well as the Sun direction.

---

## 6.6. Total dust fluences and significance

From the scheduled observation periods and with an understanding about the detection efficiencies during the spiralling phase, we can (based on the incidence rates derived in Chapter 5) give cautious estimates of the total fluences of the various dust types. Note that these fluences are highly uncertain, given our many assumptions and unknowns, yet, as current best estimates they are valuable figures, nonetheless:

- **Micro-debris:** Not more than a few impacts are anticipated, given the low (MASTER-predicted) flux and the relatively brief period spent within GEO-altitudes. The only debris population realistically detectable by DDA is that of SRM dust. However, little unambiguous data on this population exists, given the lack of chemical and conclusive dynamical information retrieved from previous experiments. A contamination of presumed debris-dust datasets (e.g., that of GORID) with the other near-Earth populations seems likely. The definitive differentiation of SRM dust enabled by DDA's chemical analysis will thus provide the first unequivocal constraint on this population—even if no such particles are detected.
- **Magnetospheric swarms:** Based on the incidence rates derived from HEOS-2 data, and considering that DESTINY<sup>+</sup> will spend approximately seven months within 60,000 km altitude (with open cover), several 100s of impacts from of this peculiar population can be anticipated. This statistically meaningful number of detections would allow for the thorough characterization of the magnetospheric swarms, whose existence has thus far only been indicated by dust-counter-type experiments. DDA is ideally equipped to illuminate the nature of these particles, and will likely uncover the origins of this population, which until now could only be speculated upon.
- **Lunar ejecta groups:** Assuming that observation of the Moon direction can be accomplished for a total of 15% of the allocated time (16 months as a secondary target), the incidence rates derived from HEOS-2 data suggest about 32 impacts, These would likely be registered in a few cluster events of multiple closely-timed impacts. With the chemical and dynamical information retrieved by DDA, definitive proof of the lunar origin of these particle groups can be obtained.
- **ISD:** C25 and C26 are unlikely to generate viable fluences, given the unfavourable operational constraints (see Section 6.5.1), in addition to the already low model predictions. Therefore, we expect almost all ISD detections to occur during C27 and C28, which are observable with nearly full detection efficiency. Together, these yield 147 EM-ISD and 18  $\beta$ -ISD particles, according to the IMEX-ISD model. This would constitute an unprecedented dataset of ISD detections, posing a significant advancement in terms of retrieved chemical and dynamical information over previous measurements. However, we want to stress that the IMEX-ISD solar cycle model might be on the order of 1–2 years early compared to the actual solar cycle (see Section 5.4.1). Notwithstanding other uncertainties of the model, this would mean that the ISD fluences during C27 and C28 could be significantly lower, and that comparable fluences will only be reached during a DESTINY<sup>+</sup> mission extension (i.e., C29 and C30). In any case, measuring the evolution of ISD flux over the onset of the focussing phase will be highly valuable, having many potential implications for our understanding of the heliosphere. Furthermore, it should be noted that even though the conditions for ISD detection are unfavourable,

---

vourable during C25 and C26, an observation attempt should still be made to constrain the year-to-year flux variability and thus confirm our current understanding of the ISD population.

- **$\alpha$ -meteoroids:** Considering a detection efficiency of 30% for the scheduled  $\alpha$ -meteoroid observation campaign during the late spiralling phase, and adding the observation time of ISD C27 and ISD C28 (which require a sensor pointing also favourable for  $\alpha$ -meteoroid detection), the herein derived incidence rates yield a total in the order of 50 impacts. This marks a significant improvement over the handful of  $\alpha$ -meteoroids that could dynamically be analysed by Pioneer 8/9 penetration TOF measurements, not to mention the chemical information that DDA will retrieve. This dataset could potentially reinstate the  $\alpha$ -meteoroids as a distinct dynamical population, which has been overlooked by contemporary studies due to a terminological confusion (see Section 5.3.3 and Sommer, 2023).
- **SMC dust:** The allocated observation time of about one year in the 2027/2028 timeframe, and the IMEM-predicted incidence rates yield not more than a few impacts of these larger grains. This is a particularly low number, considering that the chemical analysis of these particles, which have a chance of being dynamically correlated with their source body type (asteroidal or cometary) would be of great interest. An increase of this figure could be achieved by increasing the already extensive allocated observation time, at the cost of reduced observation times for the other populations. However, the low incidence rates of SMC dust hardly justify such a trade-off. Observation of the SMC dust population for the herein scheduled time period is still recommended, as it would provide a valuable constraint on the SMC dust flux. Such a constraint would be particularly valuable, considering the apparent discrepancy in the directional fluxes predicted by the IMEM (Dikarev) and IMEM2 models.

From the above, it is clear that in any of these domains, DDA holds the potential to provide illuminating insights, which will ultimately lead to a better understanding of near-Earth dust phenomena and the zodiacal cloud as a whole. Finally, it must be considered that the dynamical measurement capabilities of DDA might also uncover new dust populations, which could not be identified so far.

# 7. Conclusion

## 7.1. Summary

This dissertation presented a comprehensive study, tailoring and applying the principles and methods of science planning to DDA to support its scientific activities during the 3-year journey from Earth to Phaethon onboard the DESTINY+ spacecraft. Specifically, technical and practical considerations were combined with the scientific analysis of relevant dust populations, aiming to better understand and maximize the scientific potential of the DDA instrument.

The technical aspects were given due attention in Chapters 3 and 4. Chapter 3 focussed on spacecraft-related factors such as trajectory and attitude. Here we highlight the diverse conditions during the mission, that is, the spiral phase with its continuous thrusting and attitude changes—a unique setting for science operations of this sort—on the one hand, and the coasting phase with few thrusting arcs and a rather steady attitude, on the other. Chapter 4 then discussed relevant aspects of the DDA instrument, such as its two-axis mechanism mounting, which allows the sensor pointing to be incrementally adjusted. Most importantly, it provides an analysis of the sensor’s geometrical characteristics, which describe its gathering power and response to off-axis angles, necessary to gauge the incidence rates onto the instrument and, ultimately, to interpret the data collected. Compared to other instruments of this type, DDA exhibits a rather narrow angular response, which is a consequence of its rather elongated design, having to accommodate the mass analyser reflectron as well as the trajectory sensor stage. Although this geometry limits the instrument’s gathering power with respect to an isotropic flux, it allows for a better constraint on an impactor’s direction of incidence.

In Chapter 5, we presented a thorough investigation on the dust populations potentially encountered by DDA and estimated the theoretical incidence rates onto the instrument. While this analysis clarifies the observability of coveted populations, such as interstellar dust, it also spotlights various lesser-known dust phenomena, which DDA is in a unique position to study. These include the magnetospheric swarms and the (alleged) lunar ejecta groups roaming the Earth-Moon system, which have been reported by previous dust-counter-type instruments and whose origins DDA is poised to elucidate during its prolonged Earth-bound mission phase; as well as the  $\alpha$ -meteoroids as an overlooked yet particularly worthwhile target population, given their potential to provide insight into the processing of the zodiacal cloud in the vicinity of the Sun. On the other hand, we also provide arguments against the observability of certain populations: Particles belonging to the sporadic meteoroid complex (i.e., those which still hold their dynamical linkage to their parent body populations) are unlikely to be encountered by DDA in statistically meaningful numbers. Cometary streams must be expected to be unobservable, given their dwindling fluxes at in-situ-detectable grain sizes. An exception could be the cometary tail detections at orbit plane intersections of long-period comets, as may have occurred during the crossing of comet Kohoutek’s tail by the HEOS-2 probe.

---

In Chapter 6, we consolidate the findings of the previous chapters to set the ‘science themes’ scheme for the DDA, from which we derive a draft Science Activity Plan for the current baseline mission scenario. We further introduce the DOPE tool, which we developed to allow for intuitive and efficient planning of DDA pointing timelines. We demonstrate the functioning of the tool by means of a few example scenarios, which illustrate the significance of the attitude constraints during the spiral phase. For instance, only a detection efficiency in the order of 20% may be achieved during the 2026 interstellar dust season due to the unfavourable attitude of the spacecraft. Lastly, we collate the expectable fluences onto DDA of the various dust types considering both, the derived theoretical incidence rates and the inferred detection efficiencies under the operational constraints. This overview reiterates the most promising observation targets (in terms of numbers of detectable particles), which in the Earth-Moon-system-phase of the mission are the magnetospheric swarms and lunar ejecta groups, and in the interplanetary phase are the  $\alpha$ -meteoroids and interstellar dust. While other populations may also be detectable, their achievable fluences are expected to be too low to justify their observation as primary objectives. These include micro-debris (SRM dust) and ISD during the near-Earth phase, or SMC dust in general.

## 7.2. Outlook

Looking forward, there are several avenues to expand on the presented work. While the tools and methodologies developed in this dissertation are already a valuable asset for the DDA project, they are not without room for improvement. For instance, the DOPE tool could be extended to allow for more ‘intelligent’ pointing that anticipates the changing spacecraft attitude to optimize the coverage of certain directions instead of just finding and pointing to these directions at the requested time instants. This improvement could further increase the achievable detection efficiency toward a specific direction during the attitude-dynamic spiral phase. Another recommended addition to DOPE would be a panel that visualizes the sensor’s sensitivity with respect to particle orbital elements, based on the sensor geometry and pointing (as previously employed for other dust sensors, e.g., Schwanethal et al., 2002).

The next necessary step in the context of science planning for DDA will be the preparation of the short-term planning procedures, which will ultimately generate the instrument commands to be uploaded to the spacecraft. The implemented tools should work with the pointing timelines generated with DOPE and could be integrated into it, or developed as standalone tools to maintain the focus and simplicity of DOPE.

Furthermore, the analysis of cosmic dust populations near 1 au presented herein, is also relevant to other endeavours of in-situ dust astronomy to the inner solar system:

- IDEX, an impact plasma mass spectrometer onboard the IMAP mission, setting out for interstellar dust measurements at the Sun-Earth  $L_1$  point (McComas et al., 2018; Horanyi et al., 2023)
- considered dust instruments onboard the Lunar Gateway (Wozniakiewicz et al., 2021) or the proposed DOLPHIN mission (Sterken, 2022)
- dust detections via antenna measurements with the already-in-service Solar Orbiter and Parker Solar Probe (Mann et al., 2019)
- current and upcoming dust detectors in Earth orbit (Durin et al., 2022; Schweinfurth et al.,

---

2023), and in translunar space (Funase et al., 2020)

Especially noteworthy is also the potential for the joint investigation of single, larger lunar meteoroid impacts coordinated with other missions (e.g., LUMIO or PRISM-1b, Cervone et al., 2022; Panning et al., 2022). As described in Section 5.2.2, impacts sensed via impact flash detection or via lunar surface seismic measurements may allow for subsequent in-situ study of their unbound ejecta clouds, expanding into the Earth-Moon system.

### 7.3. Reflection and final thoughts

To conclude, let us first recapitulate the major challenges and opportunities presented by the DESTINY+/DDA mission, as spotlighted in this work, in the context of its predecessors: For in-situ dust astronomy, the operational setting is unprecedented. Other experiments often rely on spin-stabilized spacecraft (e.g., Pioneer 8/9, Helios, Ulysses, Galileo, IMAP), ensuring passive exposure to the dust fluxes from various directions. The next evolutionary step was taken by Cassini's CDA, being mounted on a three-axis stabilized spacecraft with a one-axis mechanism, that allowed for a more active and deliberate instrument pointing. Yet, DDA goes further still, employing a two-axis mechanism on an attitude-dynamic, ion-engine-driven spacecraft, thus calling for a vigorous operational scheme.

The sensor itself brings an auspicious set of capabilities to the table, warranting a foresighted planning effort to fully exploit its potential. One aspect we find particularly noteworthy: DDA will be the first dust instrument to deliver reliable dynamical data on a statistically meaningful number of cosmic grains, far exceeding previous attempts of TOF trajectory measurements. It has more than three times the sensitive area of the Pioneer 8/9 sensors, whose penetration-type TOF datasets (of 20 particles in total, Wolf et al., 1976) still represent the most accurate dynamical reference on cosmic dust in the one-micron size range. CDA's charge-sensing-type TOF measurements, on the other hand, were restricted to the biggest grains, sensitive only to particle masses well in excess of  $10^{-10}$  g (with a total of 6 particles measured in the inner solar system, Kempf et al., 2004). With its segmented trajectory sensor design, DDA achieves a charge sensitivity improvement of a factor of 5 over CDA (Li and Srama, priv. comm.), which will allow for TOF measurements down to submicron-sized particles. Together with its much-advanced mass resolution, DDA will be able to connect the dots put up by its predecessors, particularly for less explored dust phenomena, such as the uncanny groupings of particles in the Earth-Moon system or the peculiar  $\alpha$ -meteoroids.

This work aims to ensure that DDA will live up to its full potential. To that end, it provides a robust framework for DDA-specific science planning that remains valid even as the mission plan further evolves. The methodologies and tools developed in this dissertation not only enable more efficient and effective planning for the DDA instrument, they also contribute to the broader field of space mission planning, potentially informing the design and operations of future science missions.

Furthermore, the comprehensive investigation of dust populations presented herein serves as a valuable reference for understanding cosmic dust near 1 au. It highlights gaps in our knowledge and points to less understood phenomena that warrant further investigation. With these prerequisites in place, the DDA project is one step closer to a successful, and scientifically impactful mission that will be instrumental in our quest to achieve a holistic understanding of cosmic dust.



# Bibliography

- Ozaki, N. et al. (2022a). “Mission Design of DESTINY+ : Toward Active Asteroid (3200) Phaethon and Multiple Small Bodies”. In: *Acta Astronautica* 196, pp. 42–56.
- Dikarev, V. et al. (2005a). “The New ESA Meteoroid Model”. In: *Advances in Space Research*. Space Debris 35.7, pp. 1282–1289.
- Ozaki, N. et al. (2022b). “Asteroid Flyby Cyclor Trajectory Design Using Deep Neural Networks”. In: *Journal of Guidance, Control, and Dynamics* 45.8, pp. 1496–1511. eprint: [2111.11858](#) (astro-ph).
- Dikarev, V., E. Grün, M. Landgraf and R. Jehn (2005b). “Update of the ESA Meteoroid Model”. In: *4th European Conference on Space Debris, ESA SP-587*.
- Acton, C., N. Bachman, B. Semenov and E. Wright (2018). “A Look towards the Future in the Handling of Space Science Mission Geometry”. In: *Planetary and Space Science* 150, pp. 9–12.
- Acton, C. H. (1996). “Ancillary Data Services of NASA’s Navigation and Ancillary Information Facility”. In: *Planetary and Space Science*. Planetary Data System 44.1, pp. 65–70.
- Agarwal, J. et al. (2010). “The Dust Trail of Comet 67P/Churyumov-Gerasimenko between 2004 and 2006”. In: *Icarus* 207.2, pp. 992–1012.
- Akiba, R. and Y. Inatani (1990). “Alumina Particles Exhausted from Solid-Propellant Rocket Motor As a Potential Source of Space Debris”. In: *ISAS Science Report SP 11 - Proceedings of the Workshop on Space Debris*, pp. 51–59.
- Albin, T. (2019). “Machine Learning and Monte Carlo Based Data Analysis Methods in Cosmic Dust Research”. Doctoral Thesis. University of Stuttgart.
- Alexander, W. M., C. W. Arthur, J. L. Bohn and J. C. Smith (1973). “Four Years of Dust Particle Measurements in Cislunar and Selenocentric Space from Lunar Explorer 35 and OGO 3”. In: *Space Research XVIII, Proceedings of the Open Meetings of the Working Groups on Physical Sciences of the 15th Plenary Meeting of COSPAR*. Vol. 2, pp. 1037–1046.
- Alexander, W. M., O. E. Berg, C. W. Mc Cracken and L. Secretan (1963). “Review of Direct Measurements of Interplanetary Dust from Satellites and Probes”. In: *Space Research III, Proceedings of the 3rd International Space Science Symposium*, p. 891.
- Almeida, M. (2012). “Solar System Operations Lab for Constructing Optimized Science Observations”. In: *SpaceOps 2012 Conference*.
- Altobelli, N. et al. (2003). “Cassini between Venus and Earth: Detection of Interstellar Dust”. In: *Journal of Geophysical Research: Space Physics* 108.A10.
- Altobelli, N. et al. (2004). “Influence of Wall Impacts on the Ulysses Dust Detector on Understanding the Interstellar Dust Flux”. In: *Planetary and Space Science* 52.14, pp. 1287–1295.
- Altobelli, N. et al. (2005). “Interstellar Dust Flux Measurements by the Galileo Dust Instrument between the Orbits of Venus and Mars”. In: *Journal of Geophysical Research: Space Physics* 110.A7.
- Altobelli, N. et al. (2016). “Flux and Composition of Interstellar Dust at Saturn from Cassini’s Cosmic Dust Analyzer”. In: *Science* 352.6283, pp. 312–318.
- Arai, T. et al. (2019). “DESTINY+ Target Asteroid (3200) Phaethon: Recent Understandings from 2017 Observation Campaign and the Mission Science Overview”. In: *50th Lunar and Planetary Science Conference*, p. 3223.
- Arai, T. et al. (2018). “DESTINY+ Mission: Flyby of Geminids Parent Asteroid (3200) Phaethon and In-Situ Analyses of Dust Accreting on the Earth”. In: p. 2570.

- 
- Artymowicz, P. (1997). “BETA PICTORIS: An Early Solar System?” In: *Annual Review of Earth and Planetary Sciences* 25.1, pp. 175–219.
- Artymowicz, P. (2000). “Beta Pictoris and Other Solar Systems”. In: *Space Science Reviews* 92.1, pp. 69–86.
- Artymowicz, P. and M. Clampin (1997). “Dust around Main-Sequence Stars: Nature or Nurture by the Interstellar Medium?” In: *The Astrophysical Journal* 490.2, pp. 863–878.
- Asano, R. S., T. T. Takeuchi, H. Hirashita and A. K. Inoue (2013). “Dust Formation History of Galaxies: A Critical Role of Metallicity\* for the Dust Mass Growth by Accreting Materials in the Interstellar Medium”. In: *Earth, Planets and Space* 65.3, pp. 213–222.
- Auer, A. and K. Sitte (1968). “Detection Technique for Micrometeoroids Using Impact Ionization”. In: *Earth and Planetary Science Letters* 4.2, pp. 178–183.
- Auer, S. (1975). “Two High Resolution Velocity Vector Analyzers for Cosmic Dust Particles”. In: *Review of Scientific Instruments* 46.2, pp. 127–135.
- Auer, S. et al. (1968). “Studies on Simulated Micrometeoroid Impact”. In: *Space Research VIII*, pp. 606–616.
- Auer, S. et al. (2008). “Characteristics of a Dust Trajectory Sensor”. In: *Review of Scientific Instruments* 79.8, p. 084501.
- Bach, Y. P. and M. Ishiguro (2021). “Thermal Radiation Pressure as a Possible Mechanism for Losing Small Particles on Asteroids”. In: *Astronomy & Astrophysics* 654, A113.
- Baguhl, M. et al. (1995). “Dust Measurements at High Ecliptic Latitudes”. In: *Science* 268.5213, pp. 1016–1019.
- Barge, P., R. Pellat and J. Millet (1982). “Diffusion of Keplerian Motions by a Stochastic Force. II - Lorentz Scattering of Interplanetary Dusts”. In: *Astronomy and Astrophysics* 115.1, pp. 8–19.
- Bariteau, M. and J.-C. Mandeville (2000). “Modelling of Ejecta as a Space Debris Source”. In: *Space Debris* 2.2, pp. 97–107.
- Beaugé, C. and S. Ferraz-Mello (1994). “Capture in Exterior Mean-Motion Resonances Due to Poynting-Robertson Drag”. In: *Icarus* 110.2, pp. 239–260.
- Bedford, D. K., N. G. Adams and D. Smith (1975). “The Flux and Spatial Distribution of Micrometeoroids in the Near-Earth Environment”. In: *Planetary and Space Science* 23.10, pp. 1451–1456.
- Belton, M. J. S. (1966). “Dynamics of Interplanetary Dust”. In: *Science* 151.3706, pp. 35–44.
- Berezhnoy, A. A. et al. (2019). “Detection of Impact-Produced Dust Clouds near the Lunar Terminator”. In: *Planetary and Space Science* 177, p. 104689.
- Berg, O. E. and U. Gerloff (1971). “More than Two Years of Micrometeorite Data from Two Pioneer Satellites”. In: *Space Research XI, Proceedings of Open Meetings of Working Groups of the 13th Plenary Meeting of COSPAR*. Vol. 1, pp. 225–235.
- Berg, O. E. and E. Grün (1973). “Evidence of Hyperbolic Cosmic Dust Particles.” In: *Space Research XVIII, Proceedings of the Open Meetings of the Working Groups on Physical Sciences of the 15th Plenary Meeting of COSPAR*. Vol. 2, pp. 1047–1055.
- Berg, O. E. and U. Gerloff (1970). “Orbital Elements of Micrometeorites Derived from Pioneer 8 Measurements”. In: *Journal of Geophysical Research* 75.34, pp. 6932–6939.
- Berg, O. E. and L. H. Meredith (1956). “Meteorite Impacts to Altitude of 103 Kilometers”. In: *Journal of Geophysical Research (1896-1977)* 61.4, pp. 751–754.
- Berg, O. E. and F. F. Richardson (1969). “The Pioneer 8 Cosmic Dust Experiment”. In: *Review of Scientific Instruments* 40.10, pp. 1333–1337.
- Bernardoni, E., M. Horányi and J. Szalay (2021). “Formation of the Lunar Dust Ejecta Cloud”. In: *The Planetary Science Journal* 2.2, p. 67.
- Bertoldi, F. et al. (2003). “Dust Emission from the Most Distant Quasars”. In: *Astronomy & Astrophysics* 406.3, pp. L55–L58.
- Boe, B. et al. (2019). “The Orbit and Size-Frequency Distribution of Long Period Comets Observed by Pan-STARRS1”. In: *Icarus* 333, pp. 252–272.

- 
- Boice, D. C. (2017). “SUISEI—A Versatile Global Model of Comets with Applications to Small Solar System Bodies”. In: *Journal of Applied Mathematics and Physics* 5.2, pp. 311–320.
- Braun, V. et al. (2021). “Recent Developments in Space Debris Environment Modelling, Verification and Validation with MASTER”. In: *Proceedings of the 8th European Conference on Space Debris*.
- Brown, P., M. Simek and J. Jones (1997). “Radar Observations of the Leonids: 1964-1995.” In: *Astronomy and Astrophysics* 322, pp. 687–695.
- Brownlee, D. E. (1978). “Microparticle Studies by Sampling Techniques”. In: *Cosmic Dust*, pp. 295–336.
- Bruzzzone, J. S. et al. (2020). “A Comparative Study of Radar and Optical Observations of Meteor Showers Using SAAMER-OS and CAMS”. In: *Planetary and Space Science* 188, p. 104936.
- Bunte, K. D. and G. Drolshagen (2005). “Detection and Simulation of Debris Cloud Impacts”. In: *ESA SP-587*, p. 201.
- Bunte, K. D. (2003). “The Detectability of Debris Particle Clouds”. In: *54th IAC of the IAF*, IAA-5.1.07.
- Burchell, M. J., M. J. Cole, J. A. M. McDonnell and J. C. Zarnecki (1999). “Hypervelocity Impact Studies Using the 2 MV Van de Graaff Accelerator and Two-Stage Light Gas Gun of the University of Kent at Canterbury”. In: *Measurement Science and Technology* 10.1, p. 41.
- Burchell, M. J., G. Graham and A. Kearsley (2006). “Cosmic Dust Collection in Aerogel”. In: *Annual Review of Earth and Planetary Sciences* 34.1, pp. 385–418.
- Burns, J. A., P. L. Lamy and S. Soter (1979). “Radiation Forces on Small Particles in the Solar System”. In: *Icarus* 40.1, pp. 1–48.
- Burns, J. A., P. L. Lamy and S. Soter (2014). “Radiation Forces on Small Particles in the Solar System: A Re-Consideration”. In: *Icarus* 232, pp. 263–265.
- Burns, J. A. et al. (1999). “The Formation of Jupiter’s Faint Rings”. In: *Science* 284.5417, pp. 1146–1150.
- Callas, J. L., M. P. Golombek and A. A. Fraeman (2019). *Mars Exploration Rover Opportunity End of Mission Report*. Tech. rep. JPL-CL-19-7647.
- Campbell-Brown, M. D. (2008). “High Resolution Radiant Distribution and Orbits of Sporadic Radar Meteoroids”. In: *Icarus* 196.1, pp. 144–163.
- Carpenter, J. D., A. Wells, A. F. Abbey and R. M. Ambrosi (2008). “Meteoroid and Space Debris Impacts in Grazing-Incidence Telescopes”. In: *Astronomy & Astrophysics* 483.3, pp. 941–947.
- Caswell, R. D., N. McBride and A. Taylor (1995). “Olympus End of Life Anomaly — a Perseid Meteoroid Impact Event?” In: *International Journal of Impact Engineering*. Hypervelocity Impact 17.1, pp. 139–150.
- Ceplecha, Z. (1977). “Meteoroid Populations and Orbits”. In: *IAU Colloquium 39*, pp. 143–152.
- Ceplecha, Z. et al. (1998). “Meteor Phenomena and Bodies”. In: *Space Science Reviews* 84.3, pp. 327–471.
- Cervone, A. et al. (2022). “LUMIO: A CubeSat for Observing and Characterizing Micro-Meteoroid Impacts on the Lunar Far Side”. In: *Acta Astronautica* 195, pp. 309–317.
- Chen, H., Y. Kawakatsu and T. Hanada (2016). “Earth Escape from a Sun-Earth Halo Orbit Using Unstable Manifold and Lunar Swingbys”. In: *Transactions of the Japan Society for Aeronautical and Space Sciences* 59.5, pp. 269–277.
- Colombo, G., I. I. Shapiro and D. A. Lautman (1966). “The Earth’s Dust Belt: Fact or Fiction?: 3. Lunar Ejecta”. In: *Journal of Geophysical Research (1896-1977)* 71.23, pp. 5719–5731.
- Consolmagno, G. J. (1979). “Lorentz Scattering of Interplanetary Dust”. In: *Icarus* 38.3, pp. 398–410.
- Consolmagno, G. J. (1980). “Influence of the Interplanetary Magnetic Field on Cometary and Primordial Dust Orbits: Applications of Lorentz Scattering”. In: *Icarus* 43.2, pp. 203–214.
- Costa, M., N. Altobelli, M. Almeida and A. Cardesin Moinelo (2014). “The Solar System Science Operations Laboratory: A Planetary Science Lab Simulator Supporting the JUpiter Icy Moons Explorer (JUICE) Science Operations Development”. In: *SpaceOps 2014 Conference*.
- Costa, M., A. E. López and C. Arviset (2020). “An Update of SPICE for ESA Solar System Exploration Missions”. In: *EPSC Abstracts*. Vol. 14, EPSC2020–204.
-

- 
- Costa, M., A. C. Moinelo, D. Frew and C. Arviset (2016a). “Solar System Geometry Tools with SPICE for ESA’s Planetary Missions”. In: *Proceedings of the 6th International Conference on Astrodynamics Tools and Techniques (ICATT)*, p. 6.
- Costa, M. et al. (2016b). “Rosetta: Rapid Science Operations for a Dynamic Comet”. In: *SpaceOps 2016 Conference*.
- D’Aiotolo, C. T., W. H. Kinard and R. J. Naumann (1967). “Recent NASA Meteoroid Penetration Results from Satellites”. In: *Smithsonian Contributions to Astrophysics* 11, p. 239.
- Dainty, A. M., S. Stein and M. N. Toksöz (1975). “Variation in the Number of Meteoroid Impacts on the Moon with Lunar Phase”. In: *Geophysical Research Letters* 2.7, pp. 273–276.
- Dalman, B. .-, E. Grün, J. Kissel and H. Dietzel (1977). “The Ion-Composition of the Plasma Produced by Impacts of Fast Dust Particles”. In: *Planetary and Space Science* 25.2, pp. 135–147.
- de la Fuente, S., J. McAuliffe and M. Casale (2016). “Science Operations Planning Concept for BepiColombo Mercury Planetary Orbiter”. In: *SpaceOps 2016 Conference*.
- Deiries/ESO, S. (2007). *Comet McNaught*. Licensed under CC BY 4.0. URL: [https://www.eso.org/public/images/mc\\_naught34/](https://www.eso.org/public/images/mc_naught34/).
- Delbo, M. et al. (2014). “Thermal Fatigue as the Origin of Regolith on Small Asteroids”. In: *Nature* 508.7495, pp. 233–236.
- Dermott, S. F., P. D. Nicholson, J. A. Burns and J. R. Houck (1984). “Origin of the Solar System Dust Bands Discovered by IRAS”. In: *Nature* 312.5994, pp. 505–509.
- Dermott, S. F. et al. (1994). “A Circumsolar Ring of Asteroidal Dust in Resonant Lock with the Earth”. In: *Nature* 369.6483, pp. 719–723.
- Dermott, S. F. et al. (2001). “Orbital Evolution of Interplanetary Dust”. In: *Interplanetary Dust*, pp. 569–639.
- Devogèle, M. et al. (2018). “The Phase-Polarization Curve of Asteroid (3200) Phaethon†”. In: *Monthly Notices of the Royal Astronomical Society* 479.3, pp. 3498–3508.
- Devogèle, M. et al. (2020). “New Evidence for a Physical Link between Asteroids (155140) 2005 UD and (3200) Phaethon\*”. In: *The Planetary Science Journal* 1.1, p. 15.
- Dietzel, H. et al. (1973). “The HEOS 2 and HELIOS Micrometeoroid Experiments”. In: *Journal of Physics E: Scientific Instruments* 6.3, pp. 209–217.
- Dietzel, H., G. Neukum and P. Rauser (1972). “Micrometeoroid Simulation Studies on Metal Targets”. In: *Journal of Geophysical Research (1896-1977)* 77.8, pp. 1375–1395.
- Dikarev, V. V. et al. (2005c). “A Single Physical Model for Diverse Meteoroid Data Sets”. In: *arXiv e-prints*.
- Divine, N. (1993). “Five Populations of Interplanetary Meteoroids”. In: *Journal of Geophysical Research: Planets* 98.E9, pp. 17029–17048.
- DLR (2020). *DLR and JAXA Sign Cooperation Agreement*. News article. URL: [https://www.dlr.de/content/en/articles/news/2020/04/20201112\\_destiny-germany-and-japan-begin-new-asteroid-mission.html](https://www.dlr.de/content/en/articles/news/2020/04/20201112_destiny-germany-and-japan-begin-new-asteroid-mission.html) (visited on 28/03/2023).
- Dohnanyi, J. S. (1970). “On the Origin and Distribution of Meteoroids”. In: *Journal of Geophysical Research (1896-1977)* 75.17, pp. 3468–3493.
- Dohnanyi, J. S. (1971). “Current Evolution of Meteoroids”. In: *International Astronomical Union Colloquium* 13, pp. 363–374.
- Dohnanyi, J. S. (1977). “Groups of Micrometeoroids in the Earth-Moon System”. In: *Space Research XVII, Proceedings of the Open Meetings of Working Groups on Physical Sciences*, pp. 623–625.
- Drolshagen, G. (2006). “In-Situ Observations of Space Debris at ESA”. In: *Advanced Maui Optical and Space Surveillance Technologies Conference*, E68.
- Drolshagen, G., H. Svedhem and E. Grün (2001a). “Measurements of Cosmic Dust and Micro-Debris with the GORID Impact Detector in GEO”. In: *Proceedings of the Third European Conference on Space Debris (ESA SP-473)*, pp. 177–184.

- 
- Drolshagen, G., H. Svedhem, E. Grün and K. D. Bunte (2001b). “Measurements of Cosmic Dust and Micro-Debris in GEO”. In: *Advances in Space Research* 28.9, pp. 1325–1333.
- Dubin, M., W. M. Alexander and O. E. Berg (1963). “Cosmic Dust Showers by Direct Measurements”. In: *Smithsonian Contributions to Astrophysics* 7, p. 109.
- Dubin, M. (1960). “Meteoritic Dust Measured from Explorer I”. In: *Planetary and Space Science* 2.2, pp. 121–129.
- Duennebieer, F. K., Y. Nakamura, G. V. Latham and H. J. Dorman (1976). “Meteoroid Storms Detected on the Moon”. In: *Science* 192.4243, pp. 1000–1002.
- Durin, C., J. C. Mandeville and J. M. Perrin (2016). “System for an Active Detection of Orbital Debris in Space”. In: *Journal of Spacecraft and Rockets* 53.6, pp. 1178–1184.
- Durin, C. and J. C. Mandeville (2009). “SODAD: First Results and Post-Flight Analysis”. In: *Proceedings of ISMSE*. Vol. 11.
- Durin, C., J. C. Mandeville and J. M. Perrin (2022). “Active Detection of Micrometeoroids and Space Debris SODAD-2 Experiment on SAC-D Satellite”. In: *Advances in Space Research* 69.10, pp. 3856–3863.
- Egal, A. et al. (2019). “Meteor Shower Modeling: Past and Future Draconid Outbursts”. In: *Icarus* 330, pp. 123–141.
- Ehrenfreund, P. et al. (2002). “Astrophysical and Astrochemical Insights into the Origin of Life”. In: *Reports on Progress in Physics* 65.10, p. 1427.
- Elvis, M., M. Marengo and M. Karovska (2002). “Smoking Quasars: A New Source for Cosmic Dust”. In: *The Astrophysical Journal* 567.2, p. L107.
- Emmert, J. T. (2015). “Thermospheric Mass Density: A Review”. In: *Advances in Space Research* 56.5, pp. 773–824.
- Espuña Fontcuberta, A. et al. (2023). “Forecasting Solar Cycle 25 with Physical Model-Validated Recurrent Neural Networks”. In: *Solar Physics* 298.1, p. 8.
- Exle, A. (2023). “Lightweight design of space mechanisms on the example of the DESTINY+ Dust Analyzer”. Submitted for examination. Doctoral Thesis. University of Stuttgart.
- Fahr, H. J. and H. W. Ripken (1985). “Dust-Plasma-Gas Interactions in the Heliosphere”. In: *International Astronomical Union Colloquium* 85, pp. 305–323.
- Fechtig, H., E. Grün and G. Morfill (1979). “Micrometeoroids within Ten Earth Radii”. In: *Planetary and Space Science* 27.4, pp. 511–531.
- Flynn, B. C., J. V. Vallerga, G. R. Gladstone and J. Edelstein (1998). “Lunar Reflectivity from Extreme Ultraviolet Explorer Imaging and Spectroscopy of the Full Moon”. In: *Geophysical Research Letters* 25.17, pp. 3253–3256.
- Freistetter, F., A. V. Krivov and T. Löhne (2007). “Planets of  $\beta$  Pictoris Revisited”. In: *Astronomy & Astrophysics* 466.1, pp. 389–393.
- Friichtenicht, J. F. (1964). “Micrometeoroid Simulation Using Nuclear Accelerator Techniques”. In: *Nuclear Instruments and Methods* 28.1, pp. 70–78.
- Frisch, P. C., S. Redfield and J. D. Slavin (2011). “The Interstellar Medium Surrounding the Sun”. In: *Annual Review of Astronomy and Astrophysics* 49.1, pp. 237–279.
- Frisch, P. C. et al. (1999). “Dust in the Local Interstellar Wind”. In: *The Astrophysical Journal* 525.1, p. 492.
- Fröhlich, P. (2021). “Determining Flight Vectors and Orbital Elements of Micro-Meteoroids Measured by the DESTINY+ Dust Analyzer”. MSc thesis. University of Stuttgart.
- Fujimoto, M. and E. J. Tasker (2019). “Unveiling the Secrets of a Habitable World with JAXA’s Small-Body Missions”. In: *Nature Astronomy* 3.4, pp. 284–286.
- Fukushima, Y. (2012). “Onboard Mission Replanning Using Operation Script and Orthogonal Design Algorithm”. In: *International Symposium on Artificial Intelligence, Robotics and Automation in Space*.
-

- 
- Fukushima, Y. and M. Mita (2011). “A New Approach to Autonomous Onboard Mission Replanning Using Orthogonal Array Design”. In: *2011 IEEE Fourth International Conference on Space Mission Challenges for Information Technology*, pp. 43–50.
- Funase, R. et al. (2016). “One-Year Deep Space Flight Result of the World’s First Full-scale 50kg-Class Deep Space Probe PROCYON and Its Future Perspective”. In: *Small Satellite Conference*.
- Funase, R. et al. (2020). “Mission to Earth–Moon Lagrange Point by a 6U CubeSat: EQUULEUS”. In: *IEEE Aerospace and Electronic Systems Magazine* 35.3, pp. 30–44.
- Ganushkina, N. Y., I. Dandouras, Y. Y. Shprits and J. Cao (2011). “Locations of Boundaries of Outer and Inner Radiation Belts as Observed by Cluster and Double Star”. In: *Journal of Geophysical Research: Space Physics* 116.A9.
- Gault, D. E., H. J. Moore and E. M. Shoemaker (1963). *Spray Ejected from the Lunar Surface by Meteoroid Impact*. NASA Technical Note NASA-TN-D-1767. Ames Research Center.
- Geem, J. et al. (2022). “(3200) Phaethon Polarimetry in the Negative Branch: New Evidence for the Anhydrous Nature of the DESTINY+ Target Asteroid”. In: *Monthly Notices of the Royal Astronomical Society: Letters* 516.1, pp. L53–L57.
- Geisler, R. (2002). “A Global View of the Use of Aluminum Fuel in Solid Rocket Motors”. In: *38th AIAA Joint Propulsion Conference & Exhibit*, p. 3748.
- Gerloff, U. and O. E. Berg (1971). “A Model for Predicting the Results of in Situ Meteoroid Experiments: Pioneer 8 and 9 Results and Phenomenological Evidence”. In: *Space Research XI, Proceedings of Open Meetings of Working Groups of the 13th Plenary Meeting of COSPAR*. Vol. 1, pp. 397–413.
- Goel, A. and S. Close (2015). “Electrical Anomalies on Spacecraft Due to Hypervelocity Impacts”. In: *2015 IEEE Aerospace Conference*, pp. 1–7.
- Gold, T. (1975). “Resonant Orbits of Grains and the Formation of Satellites”. In: *Icarus* 25.3, pp. 489–491.
- Göller, J. and E. Grün (1989). “Calibration of the Galileo/Ulysses Dust Detectors with Different Projectile Materials and at Varying Impact Angles”. In: *Planetary and Space Science* 37.10, pp. 1197–1206.
- Gomes, R. (1995). “Resonance Trapping and Evolution of Particles Subject to Poynting-Robertson Drag: Adiabatic and Non-Adiabatic Approaches”. In: *Celestial Mechanics and Dynamical Astronomy* 61.1, pp. 97–113.
- Goode, W., S. Kempf and J. Schmidt (2021). “Detecting the Surface Composition of Geological Features on Europa and Ganymede Using a Surface Dust Analyzer”. In: *Planetary and Space Science* 208, p. 105343.
- Graham, G. A. et al. (2001). “Microparticle Impacts upon HST Solar Cells”. In: *Advances in Space Research* 28.9, pp. 1341–1346.
- Graps, A. L. et al. (2004). “GEO Debris and Interplanetary Dust: Fluxes and Charging Behavior”. In: *35th COSPAR Scientific Assembly*, p. 2717.
- Graps, A. L. et al. (2007). “GEO Debris and Interplanetary Dust: Fluxes and Charging Behavior”. In: *ESA SP-643*, pp. 97–102.
- Green, S. F., A. J. Meadows and J. K. Davies (1985). “Infrared Observations of the Extinct Cometary Candidate Minor Planet (3200) 1983TB”. In: *Monthly Notices of the Royal Astronomical Society* 214.1, 29P–36P.
- Greenstreet, S., H. Ngo and B. Gladman (2012). “The Orbital Distribution of Near-Earth Objects inside Earth’s Orbit”. In: *Icarus* 217.1, pp. 355–366.
- Grew, G. W. and C. A. Gurtler (1971). *The Lunar Orbiter Meteoroid Experiments - Description and Results from Five Spacecraft*. NASA Technical Note NASA TN D-6266.
- Grossman, E., I. Gouzman and R. Verker (2010). “Debris/Micrometeoroid Impacts and Synergistic Effects on Spacecraft Materials”. In: *MRS Bulletin* 35.1, pp. 41–47.
- Grün, E., O. E. Berg and J. S. Dohnanyi (1973). “Reliability of Cosmic Dust Data from Pioneers 8 and 9”. In: *Space Research XVIII, Proceedings of the Open Meetings of the Working Groups on Physical Sciences of the 15th Plenary Meeting of COSPAR*. Vol. 2, pp. 1057–1062.

- 
- Grün, E., H. Fechtig and J. Kissel (1985a). “Orbits of Interplanetary Dust Particles Inside 1 AU as Observed by Helios”. In: *Properties and Interactions of Interplanetary Dust*. Astrophysics and Space Science Library, pp. 105–111.
- Grün, E., J. Kissel and H.-J. Hoffmann (1976). “Dust Emission from Comet Kohoutek (1973f) at Large Distances from the Sun”. In: *Interplanetary Dust and Zodiacal Light, Proc. of the IAU-Colloq. 31*. Vol. 31, pp. 334–338.
- Grün, E., N. Pailer, H. Fechtig and J. Kissel (1980). “Orbital and Physical Characteristics of Micrometeoroids in the Inner Solar System as Observed by Helios 1”. In: *Planetary and Space Science* 28.3, pp. 333–349.
- Grün, E. and P. Staubach (1996). “Dynamic Populations of Dust in Interplanetary Space”. In: *IAU Colloquium*. Vol. 150, pp. 3–14.
- Grün, E. and H. A. Zook (1980). “Dynamics of Micrometeoroids”. In: *IAU Symposium*. Vol. 90, pp. 293–298.
- Grün, E., H. Zook, H. Fechtig and R. Giese (1985b). “Collisional Balance of the Meteoritic Complex”. In: *Icarus* 62.2, pp. 244–272.
- Grün, E. et al. (1992a). “The Ulysses Dust Experiment”. In: *Astronomy and Astrophysics Supplement Series* 92.2, pp. 411–423.
- Grün, E. et al. (1993). “Discovery of Jovian Dust Streams and Interstellar Grains by the Ulysses Spacecraft”. In: *Nature* 362.6419, pp. 428–430.
- Grün, E. et al. (1995a). “Reduction of Galileo and Ulysses Dust Data”. In: *Planetary and Space Science* 43.8, pp. 941–951.
- Grün, E. et al. (1995b). “Three Years of Galileo Dust Data”. In: *Planetary and Space Science* 43.8, pp. 953–969.
- Grün, E. et al. (1997). “South–North and Radial Traverses through the Interplanetary Dust Cloud”. In: *Icarus* 129.2, pp. 270–288.
- Grün, E. (1981). *Physikalische Und Chemische Eigenschaften Des Interplanetaren Staubes - Messungen Des Mikrometeoritenexperimentes Auf Helios*. Bundesministerium Für Forschung Und Technologie, Forschungsbereich W81-034. BMFT.
- Grün, E., M. Baguhl, H. Svedhem and H. A. Zook (2001). “In Situ Measurements of Cosmic Dust”. In: *Interplanetary Dust*, pp. 295–346.
- Grün, E. and M. Horányi (2013). “A New Look at Apollo 17 LEAM Data: Nighttime Dust Activity in 1976”. In: *Planetary and Space Science* 89, pp. 2–14.
- Grün, E., H. Krüger and R. Srama (2019). “The Dawn of Dust Astronomy”. In: *Space Science Reviews* 215.7, p. 46.
- Grün, E. et al. (1992b). “The Galileo Dust Detector”. In: *Space Science Reviews* 60.1, pp. 317–340.
- Grün, E. et al. (2005). “2002 Kuiper Prize Lecture: Dust Astronomy”. In: *Icarus* 174.1, pp. 1–14.
- Gustafson, B. A. S. (1994). “Physics of Zodiacal Dust”. In: *Annual Review of Earth and Planetary Sciences* 22, pp. 553–595.
- Gustafson, B. Å. S. et al. (2001). “Interactions with Electromagnetic Radiation: Theory and Laboratory Simulations”. In: *Interplanetary Dust*. Astronomy and Astrophysics Library, pp. 509–567.
- Halliday, I., A. A. Griffin and A. T. Blackwell (1996). “Detailed Data for 259 Fireballs from the Canadian Camera Network and Inferences Concerning the Influx of Large Meteoroids”. In: *Meteoritics & Planetary Science* 31.2, pp. 185–217.
- Hasegawa, S. et al. (2001). “Microparticle Acceleration for Hypervelocity Experiments by A 3.75MV van de Graaff Accelerator and a 100KV Electrostatic Accelerator in Japan”. In: *International Journal of Impact Engineering* 26.1, pp. 299–308.
- Hedman, M. M. et al. (2009). “Three Tenuous Rings/Arcs for Three Tiny Moons”. In: *Icarus* 199.2, pp. 378–386.
- Henry, R. C. et al. (1995). “Ultraviolet Albedo of the Moon with the Hopkins Ultraviolet Telescope”. In: *The Astrophysical Journal* 454.1, p. L69.
-

- 
- Herranen, J. (2020). “Rotational Disruption of Nonspherical Cometary Dust Particles by Radiative Torques”. In: *The Astrophysical Journal* 893.2, p. 109.
- Hervig, M. E. et al. (2022). “Decadal and Annual Variations in Meteoric Flux From Ulysses, Wind, and SOFIE Observations”. In: *Journal of Geophysical Research: Space Physics* 127.10, e2022JA030749.
- Hillier, J. K. et al. (2018). “Impact Ionisation Mass Spectrometry of Platinum-Coated Olivine and Magnesite-Dominated Cosmic Dust Analogues”. In: *Planetary and Space Science. Dust, Atmosphere, and Plasma Environment of the Moon and Small Bodies* 156, pp. 96–110.
- Hirabayashi, M. et al. (2021). “Hayabusa2 Extended Mission: New Voyage to Rendezvous with a Small Asteroid Rotating with a Short Period”. In: *Advances in Space Research* 68.3, pp. 1533–1555.
- Hirabayashi, M. et al. (2023). “Electrostatic Dust Remediation for Future Exploration of the Moon”. In: *Acta Astronautica* 207, pp. 392–402.
- Hirai, T. et al. (2014). “Microparticle Impact Calibration of the Arrayed Large-Area Dust Detectors in Interplanetary Space (ALADDIN) Onboard the Solar Power Sail Demonstrator IKAROS”. In: *Planetary and Space Science. Cosmic Dust VI* 100, pp. 87–97.
- Hirashita, H., A. Ferrara, P. Dayal and M. Ouchi (2014). “Constraining Dust Formation in High-Redshift Young Galaxies”. In: *Monthly Notices of the Royal Astronomical Society* 443.2, pp. 1704–1712.
- Hoffmann, H.-J., H. Fechtig, E. Grün and J. Kissel (1975a). “First Results of the Micrometeoroid Experiments 215 on the HEOS 2 Satellite”. In: *Planetary and Space Science* 23.1, pp. 215–224.
- Hoffmann, H.-J., H. Fechtig, E. Grün and J. Kissel (1975b). “Temporal Fluctuations and Anisotropy of the Micrometeoroid Flux in the Earth-Moon System Measured by HEOS 2”. In: *Planetary and Space Science* 23.6, pp. 985–991.
- Hoffmann, H.-J., H. Fechtig, E. Grün and J. Kissel (1976). “Particles from Comet Kohoutek Detected by the Micrometeoroid Experiment On HEOS 2”. In: *International Astronomical Union Colloquium* 25.2, pp. 949–961.
- Hoffmann, H.-J. (1971). “Entwicklung Eines Detektors Zur Massen-und Geschwindigkeitsanalyse von Kosmischen Staubteilchen”. PhD thesis. Heidelberg University.
- Hönig, S. F. et al. (2017). “Cosmology with AGN Dust Time Lags—Simulating the New VEILS Survey”. In: *Monthly Notices of the Royal Astronomical Society* 464.2, pp. 1693–1703.
- Hoofs, R. M., D. Koschny and P. van der Plas (2004). “Planning Strategy and Supporting Tools for the Science Operations of ESA’s Planetary Science Missions”. In: *Space OPS 2004 Conference*.
- Horálek, P., L. L. Christensen, D. Nesvorný and R. Davies (2016). “Light Phenomena over the ESO Observatories III: Zodiacal Light”. In: *The Messenger* 164, pp. 45–47.
- Horanyi, M., H. L. F. Houpis and D. A. Mendis (1988). “Charged Dust in the Earth’s Magnetosphere”. In: *Astrophysics and Space Science* 144.1, pp. 215–229.
- Horanyi, M. et al. (2023). “Inventory of Interstellar (ISD) and Interplanetary Dust (IDP) at 1 AU”. In: *EGU General Assembly 2023*, EGU23–8649.
- Horányi, M. et al. (2008). “The Student Dust Counter on the New Horizons Mission”. In: *Space Science Reviews* 140.1, pp. 387–402.
- Horányi, M. et al. (2014). “The Lunar Dust Experiment (LDEX) Onboard the Lunar Atmosphere and Dust Environment Explorer (LADEE) Mission”. In: *Space Science Reviews* 185.1-4, pp. 93–113.
- Horányi, M. et al. (2015). “A Permanent, Asymmetric Dust Cloud around the Moon”. In: *Nature* 522.7556, pp. 324–326.
- Horányi, M. (1996). “Charged Dust Dynamics in the Solar System”. In: *Annual Review of Astronomy and Astrophysics* 34.1, pp. 383–418.
- Horstmann, A. and E. Stoll (2017). “Investigation of propagation accuracy effects within the modeling of space debris”. In: *7th European Conference on Space Debris*.

- 
- Horstmann, A., S. Hesselbach and C. Wiedemann (2020). *MASTER-8 Final Report: Enhancement of S/C Fragmentation and Environment Evolution Models*. Technical Report DD-0045. TU Braunschweig, Institute of Space Systems.
- Howard, R. A. et al. (2019). “Near-Sun Observations of an F-corona Decrease and K-corona Fine Structure”. In: *Nature* 576.7786, pp. 232–236.
- Hsieh, H. H. (2017). “Asteroid–Comet Continuum Objects in the Solar System”. In: *Philosophical Transactions of the Royal Society A: Mathematical, Physical and Engineering Sciences* 375.2097, p. 20160259.
- Hui, M.-T. (2023). “Perihelion Activity of (3200) Phaethon Is Not Dusty: Evidence from STEREO/COR2 Observations”. In: *The Astronomical Journal* 165.3, p. 94.
- Hui, M.-T. and J. Li (2016). “RESURRECTION OF (3200) PHAETHON IN 2016”. In: *The Astronomical Journal* 153.1, p. 23.
- Igenbergs, E. et al. (1991). “The Present Status of the Munich Dust Counter Experiment on Board of the Hiten Spacecraft”. In: *Origin and Evolution of Interplanetary Dust*. Astrophysics and Space Science Library, pp. 15–20.
- Iglseder, H., R. Münzenmayer, H. Svedhem and E. Grün (1993). “Cosmic Dust and Space Debris Measurements with the Munich Dust Counter on Board the Satellites Hiten and Brem-Sat”. In: *Advances in Space Research* 13.8, pp. 129–132.
- Iglseder, H., K. Uesugi and H. Svedhem (1996). “Cosmic Dust Measurements in Lunar Orbit”. In: *Advances in Space Research* 17.12, pp. 177–182.
- Isella, A. et al. (2018). “The Disk Substructures at High Angular Resolution Project (DSHARP). IX. A High-definition Study of the HD 163296 Planet-forming Disk”. In: *The Astrophysical Journal* 869.2, p. L49.
- Ishibashi, K. et al. (2018). “Telescopic CAMERA for Phaethon (TCAP) and Multiband CAMERA for Phaethon (MCAP) to Be Installed on the DESTINY+ Spacecraft”. In: *49th Lunar and Planetary Science Conference*, p. 2126.
- Ishibashi, K. et al. (2022). “Development Status of DESTINY+ Onboard Cameras for Flyby Imaging of (3200) Phaethon”. In: 2678, p. 1729.
- Ishimoto, H. (2000). “Modeling the Number Density Distribution of Interplanetary Dust on the Ecliptic Plane within 5AU of the Sun”. In: *Astronomy and Astrophysics* 362, pp. 1158–1173.
- Isobe, S. and A. Sateesh-Kumar (1993). “An Effect of Lorenz Force on Interplanetary Dust”. In: *Meteoroids and Their Parent Bodies*, p. 381.
- Iwata, T. et al. (2016). “Studies on Solar System Explorations Using DESTINY: The Demonstration and Experiment of Space Technology for Interplanetary Voyage”. In: *Transactions of the Japan Society for Aeronautical and Space Sciences, Aerospace Technology Japan* 14.ists30, Pk.111–Pk.116.
- Jackson, A. A. and H. A. Zook (1989). “A Solar System Dust Ring with the Earth as Its Shepherd”. In: *Nature* 337.6208, pp. 629–631.
- Janches, D. et al. (2021). “Meteoroids as One of the Sources for Exosphere Formation on Airless Bodies in the Inner Solar System”. In: *Space Science Reviews* 217.4, p. 50.
- Jenniskens, P. (2017). “Meteor Showers in Review”. In: *Planetary and Space Science*. SI:Meteoroids 2016 143, pp. 116–124.
- Jennison, R. C. (1969). “The Detection of Micrometeorites in Space”. In: *Physics Bulletin* 20.8, pp. 321–325.
- Jennison, R. C. and J. A. M. McDonnell (1964). “A Technique for the Detection and Determination of the Velocity, Mass, Radiant, Charge and Flux of Micrometeorite Particles in Space”. In: *Planetary and Space Science* 12.6, pp. 627–635.
- Jennison, R. C., J. A. M. McDonnell and I. Rodger (1967). “The Ariel II Micrometeorite Penetration Measurements”. In: *Proceedings of the Royal Society of London Series A* 300, pp. 251–269.
- Jewitt, D. (2012). “THE ACTIVE ASTEROIDS”. In: *The Astronomical Journal* 143.3, p. 66.
- Jewitt, D., D. Asmus, B. Yang and J. Li (2019). “High-Resolution Thermal Infrared Imaging of 3200 Phaethon”. In: *The Astronomical Journal* 157.5, p. 193.
-

- 
- Jewitt, D. and J. Li (2010). “[ACTIVITY IN GEMINID PARENT \(3200\) PHAETHON](#)”. In: *The Astronomical Journal* 140.5, p. 1519.
- Jewitt, D., J. Li and J. Agarwal (2013). “[THE DUST TAIL OF ASTEROID \(3200\) PHAETHON](#)”. In: *The Astrophysical Journal Letters* 771.2, p. L36.
- Johnson, N. and H. Klinkrad (2009). “[The International Space Station and the Space Debris Environment: 10 Years On](#)”. In: *5th European Conference on Space Debris*.
- Jones, A. P. (1997). “[The Lifecycle of Interstellar Dust](#)”. In: *ASP Conference Series, Vol. 122: From Stardust to Planetesimals*. Vol. 122, p. 97.
- Jones, J. and P. Brown (1993). “[Sporadic Meteor Radiant Distributions: Orbital Survey Results](#)”. In: *Monthly Notices of the Royal Astronomical Society* 265.3, pp. 524–532.
- Jones, J., M. Campbell and S. Nikolova (2001). “[Modelling of the Sporadic Meteoroid Sources](#)”. In: *Proceedings of the Meteoroids 2001 Conference, ESA SP-495*, pp. 575–580.
- Jones, M. H., D. Bewsher and D. S. Brown (2013). “[Imaging of a Circumsolar Dust Ring Near the Orbit of Venus](#)”. In: *Science* 342.6161, pp. 960–963.
- Juhász, A. and M. Horányi (1997). “[Dynamics of Charged Space Debris in the Earth’s Plasma Environment](#)”. In: *Journal of Geophysical Research: Space Physics* 102.A4, pp. 7237–7246.
- Kareta, T. et al. (2021). “[Investigating the Relationship between \(3200\) Phaethon and \(155140\) 2005 UD through Telescopic and Laboratory Studies](#)”. In: *The Planetary Science Journal* 2.5, p. 190.
- Katzan, C. M. and J. L. Edwards (1991). *Lunar Dust Transport and Potential Interactions with Power System Components*. Tech. rep. NAS 1.26:4404.
- Kawaguchi, J., I. Nakatani, T. Uesugi and K. Tsuruda (2003). “[Synthesis of an Alternative Flight Trajectory for Mars Explorer, Nozomi](#)”. In: *Acta Astronautica*. Selected Proceedings of the 4th IAA International Conference on Low Cost Planetary Missions 52.2, pp. 189–195.
- Kawakatsu, Y. and T. Iwata (2013). “[Destiny Mission Overview: A Small Satellite Mission for Deep Space Exploration Technology Demonstration](#)”. In: *Advances in the Astronautical Sciences* 146, pp. 727–739.
- Kearsley, A. T. et al. (2005). “[Impacts on Hubble Space Telescope Solar Arrays: Discrimination between Natural and Man-Made Particles](#)”. In: *Advances in Space Research*. Space Debris 35.7, pp. 1254–1262.
- Keller, L. P. and G. J. Flynn (2022). “[Evidence for a Significant Kuiper Belt Dust Contribution to the Zodiacal Cloud](#)”. In: *Nature Astronomy* 6.6, pp. 731–735.
- Kempf, S. et al. (2004). “[Cassini between Earth and Asteroid Belt: First in-Situ Charge Measurements of Interplanetary Grains](#)”. In: *Icarus* 171.2, pp. 317–335.
- Kempf, S. (2018). “[The Surface Dust Analyzer \(SUDA\) on Europa Clipper](#)”. In: *European Planetary Science Congress 2018*, EPSC2018–462.
- Kempf, S. et al. (2012). “[Linear High Resolution Dust Mass Spectrometer for a Mission to the Galilean Satellites](#)”. In: *Planetary and Space Science* 65.1, pp. 10–20.
- Kempf, S. et al. (2023). “[Micrometeoroid Infall onto Saturn’s Rings Constrains Their Age to No More than a Few Hundred Million Years](#)”. In: *Science Advances* 9.19, eadf8537.
- Kennedy, G. M. and M. C. Wyatt (2013). “[The Bright End of the Exo-Zodi Luminosity Function: Disc Evolution and Implications for Exo-Earth Detectability](#)”. In: *Monthly Notices of the Royal Astronomical Society* 433.3, pp. 2334–2356.
- Kim, M.-J. et al. (2018). “[Optical Observations of NEA 3200 Phaethon \(1983 TB\) during the 2017 Apparition](#)”. In: *Astronomy & Astrophysics* 619, A123.
- Kimura, H. et al. (2022). “[Electrostatic Dust Ejection from Asteroid \(3200\) Phaethon with the Aid of Mobile Alkali Ions at Perihelion](#)”. In: *Icarus* 382, p. 115022.
- Kiselev, N. N. et al. (2022). “[Asteroid \(3200\) Phaethon: Results of Polarimetric, Photometric, and Spectral Observations](#)”. In: *Monthly Notices of the Royal Astronomical Society* 514.4, pp. 4861–4875.
- Kissel, J., F. R. Krueger, J. Silén and B. C. Clark (2004). “[The Cometary and Interstellar Dust Analyzer at Comet 81P/Wild 2](#)”. In: *Science* 304.5678, pp. 1774–1776.

- 
- Kissel, J. et al. (1986). “Composition of Comet Halley Dust Particles from Vega Observations”. In: *Nature* 321.6067, pp. 280–282.
- Klačka, J., J. Petržala, P. Pástor and L. Kómar (2014). “The Poynting–Robertson Effect: A Critical Perspective”. In: *Icarus* 232, pp. 249–262.
- Kobayashi, H., S.-i. Watanabe, H. Kimura and T. Yamamoto (2009). “Dust Ring Formation Due to Sublimation of Dust Grains Drifting Radially Inward by the Poynting–Robertson Drag: An Analytical Model”. In: *Icarus* 201.1, pp. 395–405.
- Kortenkamp, S. J., S. F. Dermott, D. Fogle and K. Grogan (2001). “Sources and Orbital Evolution of Interplanetary Dust Accreted by Earth”. In: *Accretion of Extraterrestrial Matter Throughout Earth’s History*, pp. 13–30.
- Koschny, D. et al. (2004). “Science Operations for Planetary Missions in the European Space Agency”. In: *Space OPS 2004 Conference*.
- Koschny, D. et al. (2007). “Scientific Planning and Commanding of the Rosetta Payload”. In: *Space Science Reviews* 128.1-4, pp. 167–188.
- Koschny, D. et al. (2010). “The European BepiColombo Science Ground Segment—Overview and Tasks”. In: *Planetary and Space Science*. Comprehensive Science Investigations of Mercury: The Scientific Goals of the Joint ESA/JAXA Mission BepiColombo 58.1, pp. 319–326.
- Kouyama, T. et al. (2021). “Post-Arrival Calibration of Hayabusa2’s Optical Navigation Cameras (ONCs): Severe Effects from Touchdown Events”. In: *Icarus* 360, p. 114353.
- Kral, Q. et al. (2017). “Exozodiacal Clouds: Hot and Warm Dust around Main Sequence Stars”. In: *Astronomical Review* 13.2, pp. 69–111.
- Kresák, L. (1976). “Orbital Evolution of the Dust Streams Released from Comets”. In: *Bulletin of the Astronomical Institutes of Czechoslovakia* 27, p. 35.
- Kresák, L. and E. M. Pittich (1976). “On the Structure of Hyperbolic Interplanetary Dust Streams”. In: *Interplanetary Dust and Zodiacal Light, Proc. of the IAU-Colloq. 31* 31, pp. 396–399.
- Krivov, A. V., T. Löhne and M. Sremčević (2006). “Dust Distributions in Debris Disks: Effects of Gravity, Radiation Pressure and Collisions”. In: *Astronomy & Astrophysics* 455.2, pp. 509–519.
- Krivov, A. V., I. Mann and N. A. Krivova (2000). “Size Distributions of Dust in Circumstellar Debris Discs”. In: *Astronomy and Astrophysics, v.362, p.1127-1137 (2000)* 362, p. 1127.
- Krivov, A., H. Kimura and I. Mann (1998). “Dynamics of Dust near the Sun”. In: *Icarus* 134.2, pp. 311–327.
- Krivov, A. V. (2010). “Debris Disks: Seeing Dust, Thinking of Planetesimals and Planets”. In: *Research in Astronomy and Astrophysics* 10.5, p. 383.
- Krivov, A. V. and D. P. Hamilton (1997). “Martian Dust Belts: Waiting for Discovery”. In: *Icarus* 128.2, pp. 335–353.
- Krivov, A. V., M. Sremčević and F. Spahn (2005). “Evolution of a Keplerian Disk of Colliding and Fragmenting Particles: A Kinetic Model with Application to the Edgeworth–Kuiper Belt”. In: *Icarus* 174.1, pp. 105–134.
- Krivova, N. A., A. V. Krivov and I. Mann (2000a). “Size Distribution of Dust in the Disk of  $\beta$  Pictoris”. In: *Disks, Planetesimals, and Planets, ASP Conference Series*. Vol. 219, p. 387.
- Krivova, N. A., A. V. Krivov and I. Mann (2000b). “The Disk of  $\beta$  Pictoris in the Light of Polarimetric Data”. In: *The Astrophysical Journal* 539.1, pp. 424–434.
- Krüger, H., D. P. Hamilton, R. Moissl and E. Grün (2009). “Galileo In-Situ Dust Measurements in Jupiter’s Gossamer Rings”. In: *Icarus* 203.1, pp. 198–213.
- Krüger, H., A. V. Krivov, D. P. Hamilton and E. Grün (1999). “Detection of an Impact-Generated Dust Cloud around Ganymede”. In: *Nature* 399.6736, pp. 558–560.
- Krüger, H., M. Landgraf, N. Altobelli and E. Grün (2007). “Interstellar Dust in the Solar System”. In: *Space Science Reviews* 130.1-4, pp. 401–408.
-

- 
- Krüger, H., P. Strub and the DDA Science Team (2022). *Interstellar Dust Detection Conditions for the DESTINY+ Dust Analyzer (DDA)*. Internal Report.
- Krüger, H. et al. (2019). “Modelling DESTINY+ Interplanetary and Interstellar Dust Measurements En Route to the Active Asteroid (3200) Phaethon”. In: *Planetary and Space Science* 172, pp. 22–42.
- Krüger, H. et al. (2020). “Helios Spacecraft Data Revisited: Detection of Cometary Meteoroid Trails by Following in Situ Dust Impacts”. In: *Astronomy & Astrophysics* 643, A96.
- Krüger, H. et al. (2021). “Modelling Cometary Meteoroid Stream Traverses of the Martian Moons eXploration (MMX) Spacecraft En Route to Phobos”. In: *Earth, Planets and Space* 73.1, p. 93.
- Kuninaka, H. and J. Kawaguchi (2011). “Lessons Learned from Round Trip of Hayabusa Asteroid Explorer in Deep Space”. In: *2011 Aerospace Conference*, pp. 1–8.
- Landgraf, M. (2000). “Modeling the Motion and Distribution of Interstellar Dust inside the Heliosphere”. In: *Journal of Geophysical Research: Space Physics* 105.A5, pp. 10303–10316.
- Laurance, M. R. and D. E. Brownlee (1986). “The Flux of Meteoroids and Orbital Space Debris Striking Satellites in Low Earth Orbit”. In: *Nature* 323.6084, pp. 136–138.
- Lazzarin, M. et al. (2019). “Phaethon Variability during December 2017 Closest Approach to Earth”. In: *Planetary and Space Science* 165, pp. 115–123.
- Lee, N. et al. (2012). “Measurements of Freely-Expanding Plasma from Hypervelocity Impacts”. In: *International Journal of Impact Engineering* 44, pp. 40–49.
- Leinert, C. and B. Moster (2007). “Evidence for Dust Accumulation Just Outside the Orbit of Venus”. In: *Astronomy & Astrophysics* 472.1, pp. 335–340.
- Leinert, C. and E. Grün (1990). “Interplanetary Dust”. In: *Physics of the Inner Heliosphere I: Large-Scale Phenomena*. Physics and Chemistry in Space, Space and Solar Physics, pp. 207–275.
- León, J. de et al. (2010). “Origin of the Near-Earth Asteroid Phaethon and the Geminids Meteor Shower”. In: *Astronomy & Astrophysics* 513, A26.
- Lhotka, C., P. Bourdin and Y. Narita (2016). “CHARGED DUST GRAIN DYNAMICS SUBJECT TO SOLAR WIND, POYNTING–ROBERTSON DRAG, AND THE INTERPLANETARY MAGNETIC FIELD”. In: *The Astrophysical Journal* 828.1, p. 10.
- Li, J. and D. Jewitt (2013). “RECURRENT PERIHELION ACTIVITY IN (3200) PHAETHON”. In: *The Astronomical Journal* 145.6, p. 154.
- Li, Y. et al. (2014). “Instrument Study of the Lunar Dust eXplorer (LDX) for a Lunar Lander Mission”. In: *Advances in Space Research*. Lunar Science and Exploration 54.10, pp. 2094–2100.
- Li, Y. et al. (2015). “Instrument Study of the Lunar Dust eXplorer (LDX) for a Lunar Lander Mission II: Laboratory Model Calibration”. In: *Advances in Space Research* 56.8, pp. 1777–1783.
- Li, Y. et al. (2017). “Instrument Concept of a Single Channel Dust Trajectory Detector”. In: *Advances in Space Research* 59.6, pp. 1636–1641.
- Li, Y. et al. (2021). “The Advances of Dust Detection Techniques and Dust Acceleration Facilities”. In: *43rd COSPAR Scientific Assembly. Held 28 January - 4 February*. Vol. 43, p. 833.
- Li, Y. et al. (2022). “Measurement of Fragments Generated by Hypervelocity Impacts of Micron-Sized Iron Particles at Grazing Incidents”. In: *Advances in Space Research* 69.6, pp. 2629–2635.
- Liakos, A. et al. (2020). “NELIOTA: Methods, Statistics, and Results for Meteoroids Impacting the Moon”. In: *Astronomy & Astrophysics* 633, A112.
- Lin, Z.-Y. et al. (2020). “A Study of Photometric Observations of (3200) Phaethon from Lulin Observatory”. In: *Planetary and Space Science* 194, p. 105114.
- Linnarsson, D. et al. (2012). “Toxicity of Lunar Dust”. In: *Planetary and Space Science*. Scientific Preparations For Lunar Exploration 74.1, pp. 57–71.
- Lisse, C. M. and J. K. Steckloff (2022). “Thermal Alteration and Differential Sublimation Can Create Phaethon’s “Rock Comet” Activity and Blue Color”. In: *Icarus* 381, p. 114995.

- 
- Liu, X. and J. Schmidt (2021). “Configuration of the Martian Dust Rings: Shapes, Densities, and Size Distributions from Direct Integrations of Particle Trajectories”. In: *Monthly Notices of the Royal Astronomical Society* 500.3, pp. 2979–2985.
- Liu, Y. et al. (2018). “The Far Ultraviolet Wavelength Dependence of the Lunar Phase Curve as Seen by LRO LAMP”. In: *Journal of Geophysical Research: Planets* 123.10, pp. 2550–2563.
- Lorenz, R. D. et al. (2021). “Lander and Rover Histories of Dust Accumulation on and Removal from Solar Arrays on Mars”. In: *Planetary and Space Science* 207, p. 105337.
- Love, S. G. and D. E. Brownlee (1993). “A Direct Measurement of the Terrestrial Mass Accretion Rate of Cosmic Dust”. In: *Science* 262.5133, pp. 550–553.
- Maas, D. et al. (1986). “Impact Simulation Experiments with Nano- to Microgram Particles at the Munich Plasma Drag Accelerator”. In: 250, pp. 337–340.
- MacLennan, E. and M. Granvik (2023). “Thermal Decomposition as the Activity Driver of Near-Earth Asteroid (3200) Phaethon”. In: *Nature Astronomy*, pp. 1–9.
- MacLennan, E., A. Toliou and M. Granvik (2021). “Dynamical Evolution and Thermal History of Asteroids (3200) Phaethon and (155140) 2005 UD”. In: *Icarus* 366, p. 114535.
- Mann, I. and A. Czechowski (2021). “Dust Observations from Parker Solar Probe: Dust Ejection from the Inner Solar System”. In: *Astronomy & Astrophysics* 650, A29.
- Mann, I. et al. (2004). “Dust Near The Sun”. In: *Space Science Reviews* 110.3, pp. 269–305.
- Mann, I. et al. (2006). “Dust in the Solar System and in Extra-Solar Planetary Systems”. In: *The Astronomy and Astrophysics Review* 13.3, pp. 159–228.
- Mann, I. et al. (2010). “Dust in the Interplanetary Medium”. In: *Plasma Physics and Controlled Fusion* 52.12, p. 124012.
- Mann, I. et al. (2019). “Dust Observations with Antenna Measurements and Its Prospects for Observations with Parker Solar Probe and Solar Orbiter”. In: *Annales Geophysicae* 37.6, pp. 1121–1140.
- Manring, E. R. (1959). “Micrometeorite Measurements from 1958 Alpha and Gamma Satellites”. In: *Planetary and Space Science* 1.1, pp. 27–31.
- Manyapu, K. K. et al. (2017). “Proof of Concept Demonstration of Novel Technologies for Lunar Spacesuit Dust Mitigation”. In: *Acta Astronautica* 137, pp. 472–481.
- Masiero, J. R. et al. (2021). “Volatility of Sodium in Carbonaceous Chondrites at Temperatures Consistent with Low-perihelion Asteroids”. In: *The Planetary Science Journal* 2.4, p. 165.
- Maslov, M. (2011). “Future Draconid Outbursts (2011 - 2100)”. In: *WGN, Journal of the International Meteor Organization* 39, pp. 64–67.
- Mattsson, L. (2011). “Dust in the Early Universe: Evidence for Non-Stellar Dust Production or Observational Errors?”. In: *Monthly Notices of the Royal Astronomical Society* 414.1, pp. 781–791.
- May, B. H. (2007). “A Survey of Radial Velocities in the Zodiacal Dust Cloud”. PhD thesis. Imperial College London.
- McComas, D. J. et al. (2018). “Interstellar Mapping and Acceleration Probe (IMAP): A New NASA Mission”. In: *Space Science Reviews* 214.8, p. 116.
- McCracken, C. W., W. M. Alexander and M. Dubin (1967). “Direct Measurements of the Mass Distribution and Time Variations in the Flux of Small Dust Particles”. In: *Smithsonian Contributions to Astrophysics* 11, p. 259.
- McDonnell, J. A. M. (1978). “Microparticle Studies by Space Instrumentation”. In: *Cosmic Dust*, pp. 337–426.
- McDonnell, T. et al. (2001). “Near Earth Environment”. In: *Interplanetary Dust. Astronomy and Astrophysics Library*, pp. 163–231.
- McNaught, R. H. and D. J. Asher (1999). “Leonid Dust Trails and Meteor Storms”. In: *WGN, Journal of the International Meteor Organization* 27, pp. 85–102.
- Melosh, H. J. et al. (1993). “Remote Visual Detection of Impacts on the Lunar Surface”. In: p. 975.

- 
- Ménard, B., M. Kilbinger and R. Scranton (2010). “On the Impact of Intergalactic Dust on Cosmology with Type Ia Supernovae”. In: *Monthly Notices of the Royal Astronomical Society* 406.3, pp. 1815–1820.
- Menicucci, A. et al. (2013). “In-Flight and Post-Flight Impact Data Analysis from DEBIE2 (Debris In-Orbit Evaluator) on Board of ISS”. In: *Proceedings of the 6th European Conference on Space Debris*.
- Merisio, G. and F. Topputo (2023). “Present-Day Model of Lunar Meteoroids and Their Impact Flashes for LUMIO Mission”. In: *Icarus* 389, p. 115180.
- Misconi, N. Y. (1993). “The Spin of Cosmic Dust: Rotational Bursting of Circumsolar Dust in the F Corona”. In: *Journal of Geophysical Research: Space Physics* 98.A11, pp. 18951–18961.
- Mocker, A. et al. (2011). “A 2 MV Van de Graaff Accelerator as a Tool for Planetary and Impact Physics Research”. In: *Review of Scientific Instruments* 82.9, p. 095111.
- Molaro, J. L., S. Byrne and J. -. Le (2017). “Thermally Induced Stresses in Boulders on Airless Body Surfaces, and Implications for Rock Breakdown”. In: *Icarus* 294, pp. 247–261.
- Montagnon, E. et al. (2021). “BepiColombo Ground Segment and Mission Operations”. In: *Space Science Reviews* 217.2, p. 32.
- Moorhead, A. V. (2021). “Forbidden Mass Ranges for Shower Meteoroids”. In: *Icarus* 354, p. 113949.
- Moorhead, A. V. et al. (2019). “Meteor Shower Forecasting in Near-Earth Space”. In: *Journal of Spacecraft and Rockets* 56.5, pp. 1531–1545.
- Morbidelli, A. and B. Gladman (1998). “Orbital and Temporal Distributions of Meteorites Originating in the Asteroid Belt”. In: *Meteoritics & Planetary Science* 33.5, pp. 999–1016.
- Morfill, G. E. and E. Grün (1979a). “The Motion of Charged Dust Particles in Interplanetary Space—II. Interstellar Grains”. In: *Planetary and Space Science* 27.10, pp. 1283–1292.
- Morfill, G. E., E. Grün and C. Leinert (1986). “The Interaction of Solid Particles with the Interplanetary Medium”. In: *The Sun and the Heliosphere in Three Dimensions, Proceedings of the 19th ESLAB Symposium, Astrophysics and Space Science Library*. Vol. 123. Astrophysics and Space Science Library, pp. 455–474.
- Morfill, G. and E. Grün (1979b). “The Motion of Charged Dust Particles in Interplanetary Space—I. The Zodiacal Dust Cloud”. In: *Planetary and Space Science* 27.10, pp. 1269–1282.
- Mueller, A. C. and D. J. Kessler (1985). “The Effects of Particulates from Solid Rocket Motors Fired in Space”. In: *Advances in Space Research* 5.2, pp. 77–86.
- Mukai, T. (1981). “On the Charge Distribution of Interplanetary Grains”. In: *Astronomy and Astrophysics* 99, pp. 1–6.
- Mukai, T. and R. H. Giese (1984). “Modification of the Spatial Distribution of Interplanetary Dust Grains by Lorentz Forces”. In: *Astronomy and Astrophysics* 131.2, pp. 355–363.
- Mukai, T. and T. Yamamoto (1979). “A Model of the Circumsolar Dust Cloud”. In: *Publications of the Astronomical Society of Japan* 31, pp. 585–596.
- Nakano, R. and M. Hirabayashi (2020). “Mass-Shedding Activities of Asteroid (3200) Phaethon Enhanced by Its Rotation”. In: *The Astrophysical Journal Letters* 892.2, p. L22.
- NASA (2006). *In Saturn’s Shadow - the Pale Blue Dot*. CICLOPS. URL: <https://ciclops.org/view.php%3fid=2230.html> (visited on 15/05/2023).
- NASA (2017). *Arecibo radar images of asteroid 3200 Phaethon*. Image. URL: <https://www.jpl.nasa.gov/news/arecibo-radar-returns-with-asteroid-phaethon-images> (visited on 24/03/2023).
- NASA (2021). *NASA Selects New Science Investigations for Future Moon Deliveries*. Press Release. URL: <https://www.nasa.gov/press-release/nasa-selects-new-science-investigations-for-future-moon-deliveries> (visited on 15/04/2023).
- NASA (2023). *Cassini spacecraft viewer*. URL: <https://solarsystem.nasa.gov/missions/cassini/the-journey/the-spacecraft/> (visited on 01/06/2023).
- NASA/Adler/U. Chicago/Wesleyan (2012). *NASA’s IBEX Spacecraft Reveals New Observations of Interstellar Matter*. URL: <https://svs.gsfc.nasa.gov/10906> (visited on 01/06/2023).
-

- 
- Naumann, R. J. (1965). *Pegasus Satellite Measurements of Meteoroid Penetration*. Technical Report NASA TM X-1192.
- Neish, M., T. Goka and K. Imagawa (2004). “Numerical Analysis of a Debris Swarm of Solid Rocket Motor Dust Particles”. In: *35th COSPAR Scientific Assembly*, p. 1794.
- Nesvorný, D., D. Vokrouhlický, W. Bottke and M. Sykes (2006). “Physical Properties of Asteroid Dust Bands and Their Sources”. In: *Icarus* 181.1, pp. 107–144.
- Nesvorný, D., D. Vokrouhlický, P. Pokorný and D. Janches (2011a). “DYNAMICS OF DUST PARTICLES RELEASED FROM OORT CLOUD COMETS AND THEIR CONTRIBUTION TO RADAR METEORS”. In: *The Astrophysical Journal* 743.1, p. 37.
- Nesvorný, D. et al. (2010). “COMETARY ORIGIN OF THE ZODIACAL CLOUD AND CARBONACEOUS MICROMETEORITES. IMPLICATIONS FOR HOT DEBRIS DISKS”. In: *The Astrophysical Journal* 713.2, pp. 816–836.
- Nesvorný, D. et al. (2011b). “DYNAMICAL MODEL FOR THE ZODIACAL CLOUD AND SPORADIC METEORS”. In: *The Astrophysical Journal* 743.2, p. 129.
- Nilsson, C. S., F. W. Wright and D. Wilson (1969). “Attempts to Measure Micrometeoroid Flux on the OGO 2 and OGO 4 Satellites”. In: *Journal of Geophysical Research (1896-1977)* 74.22, pp. 5268–5276.
- Nilsson, C. S. et al. (1965). “Measured Velocities of Interplanetary Dust Particles”. In: *Nature* 208.5011, pp. 673–674.
- Nilsson, C. (1966). “Some Doubts about the Earth’s Dust Cloud”. In: *Science* 153.3741, pp. 1242–1246.
- Oberst, J. and Y. Nakamura (1991). “A Search for Clustering among the Meteoroid Impacts Detected by the Apollo Lunar Seismic Network”. In: *Icarus* 91.2, pp. 315–325.
- Ogawa, N. et al. (2022). “Sensitivity Degradation of Optical Navigation Camera and Attempts for Dust Removal”. In: *Hayabusa2 Asteroid Sample Return Mission*, pp. 415–431.
- Ohtsuka, K. et al. (2006). “Apollo Asteroid 2005 UD: Split Nucleus of (3200) Phaethon?” In: *Astronomy & Astrophysics* 450.3, pp. L25–L28.
- Oliver, J. P. et al. (1995). “LDEF Interplanetary Dust Experiment (IDE) Results”. In.
- Osman, O., K. Bekki and L. Cortese (2020). “The Role of Dust Destruction and Dust Growth in the Evolution of the Interstellar Medium”. In: *Monthly Notices of the Royal Astronomical Society* 497.2, pp. 2002–2017.
- Pailer, N. and E. grün (1980). “The Penetration Limit of Thin Films”. In: *Planetary and Space Science* 28.3, pp. 321–331.
- Panning, M. et al. (2022). “Farside Seismic Suite (FSS): First-ever Seismology on the Farside of the Moon and a Model for Long-Lived Lunar Science”. In: *EPSC Abstracts*. Vol. 16, EPSC2022–672.
- Parker, E. N. (1964). “The Perturbation of Interplanetary Dust Grains by the Solar Wind.” In: *The Astrophysical Journal* 139, p. 951.
- Pérez-Ayúcar, M., F. Nespoli, M. Costa and P. van der Plas (2018a). “MAPPS 3D Tool: Use for Rosetta Science Operations”. In: *2018 SpaceOps Conference*. SpaceOps Conferences.
- Pérez-Ayúcar, M. et al. (2018b). “The Rosetta Science Operations and Planning Implementation”. In: *Acta Astronautica* 152, pp. 163–174.
- Perko, H. A., J. D. Nelson and J. R. Green (2012). “Review of Martian Dust Composition, Transport, Deposition, Adhesion, and Removal”. In: pp. 176–189.
- Pokorný, P. et al. (2014). “DYNAMICAL MODEL FOR THE TOROIDAL SPORADIC METEORS”. In: *The Astrophysical Journal* 789.1, p. 25.
- Pokorný, P. et al. (2019). “Meteoroids at the Moon: Orbital Properties, Surface Vaporization, and Impact Ejecta Production”. In: *Journal of Geophysical Research: Planets* 124.3, pp. 752–778.
- Poppe, A. R. et al. (2019). “Constraining the Solar System’s Debris Disk with In Situ New Horizons Measurements from the Edgeworth–Kuiper Belt”. In: *The Astrophysical Journal Letters* 881.1, p. L12.
- Poppe, A. R. (2016). “An Improved Model for Interplanetary Dust Fluxes in the Outer Solar System”. In: *Icarus* 264, pp. 369–386.
-

- 
- Postberg, F. et al. (2023). “Detection of Phosphates Originating from Enceladus’s Ocean”. In: *Nature* 618.7965, pp. 489–493.
- Pusack, A. et al. (2021). “Dust Directionality and an Anomalous Interplanetary Dust Population Detected by the Parker Solar Probe”. In: *The Planetary Science Journal* 2.5, p. 186.
- Reach, W. T. et al. (1995). “Observational Confirmation of a Circumsolar Dust Ring by the COBE Satellite”. In: *Nature* 374.6522, pp. 521–523.
- Reach, W. T., B. A. Franz and J. L. Weiland (1997). “The Three-Dimensional Structure of the Zodiacal Dust Bands”. In: *Icarus* 127.2, pp. 461–484.
- Rigley, J. (2022). “The Origin and Evolution of Warm Exozodiacal Dust”. Thesis. University of Cambridge.
- Roosen, R. G., O. E. Berg and N. H. Farlow (1973). “Dust Storms in Space?” In: *IAU Colloquium 13, NASA SP-319*, pp. 223–226.
- Rowan-Robinson, M. and B. May (2013). “An Improved Model for the Infrared Emission from the Zodiacal Dust Cloud: Cometary, Asteroidal and Interstellar Dust”. In: *Monthly Notices of the Royal Astronomical Society* 429.4, pp. 2894–2902.
- Ryabova, G. O., V. A. Avdyushev and I. P. Williams (2019). “Asteroid (3200) Phaethon and the Geminid Meteoroid Stream Complex”. In: *Monthly Notices of the Royal Astronomical Society* 485.3, pp. 3378–3385.
- Sarli, B. V. and Y. Kawakatsu (2017). “Selection and Trajectory Design to Mission Secondary Targets”. In: *Celestial Mechanics and Dynamical Astronomy* 127.2, pp. 233–258.
- Sarli, B. V., Y. Kawakatsu and T. Arai (2015). “Design of a Multiple Flyby Mission to the Phaethon–Geminid Complex”. In: *Journal of Spacecraft and Rockets* 52.3, pp. 739–745.
- Sarli, B. V. et al. (2018). “DESTINY+ Trajectory Design to (3200) Phaethon”. In: *The Journal of the Astronautical Sciences* 65.1, pp. 82–110.
- Sarugaku, Y. et al. (2015). “INFRARED AND OPTICAL IMAGINGS OF THE COMET 2P/ENCKE DUST CLOUD IN THE 2003 RETURN”. In: *The Astrophysical Journal* 804.2, p. 127.
- Sasaki, S. et al. (2002). “Observation of Interplanetary and Interstellar Dust Particles by Mars Dust Counter (MDC) on Board NOZOMI”. In: *Advances in Space Research* 29.8, pp. 1145–1153.
- Schmidt, J. (2020). *NGC 4826*. <https://flickr.com/photos/54209675@N00/49659407432>. Accessed: 06/03/2023. Licensed under CC BY 2.0.
- Schmidt, K. D. (1980). *Bahnelemente von Mikrometeoriten: Analyse von Messungen Der Sonnensonde Helios 1*. Bundesministerium Für Forschung Und Technologie, Forschungsbreicht W 80-036. BMFT.
- Schmidt, K. D. and E. Grün (1979). “The Distribution of Orbital Elements of Interplanetary Dust in the Inner Solar System as Detected by the Helios Spaceprobe.” In: *Space Research XIX, Proceedings of the Open Meetings of the Working Groups on Physical Sciences of the 21st Plenary Meeting of COSPAR*, pp. 439–442.
- Schmidt, K. D. and E. Grün (1980). “Orbital Elements of Micrometeoroids Detected by the Helios 1 Space Probe in the Inner Solar System”. In: *IAU Symposium No. 90*. Vol. 90, pp. 321–324.
- Schobert, D. and K. G. Paul (1997). “Al<sub>2</sub>O<sub>3</sub> Particle Fluxes from the ECS 2 Apogee Maneuver—Witnessed by the LDEF Interplanetary Dust Experiment”. In: *Advances in Space Research*. Space Debris 19.2, pp. 271–274.
- Schwanethal, J. P., N. McBride and S. F. Green (2002). “Detecting Interplanetary and Interstellar Dust with the DEBIE Sensor”. In: *Proceedings of Asteroids, Comets, Meteors. ESA SP-500*, pp. 75–78.
- Schwanethal, J. P. et al. (2005). “Analysis of Impact Data from the Debie (debris In-Orbit Evaluator) Sensor in Polar Low Earth Orbit”. In: *Proceedings of the 4th European Conference on Space Debris, ESA SP-587*, p. 177.
- Schweinfurth, A. G., F. S. Firsch, P. Pucknus and N. Zorbach (2023). “MOVE-III and DEDRA: In Situ Sub-millimetric Space Debris and Micrometeoroid Detection and Characterisation”. In: *2nd NEO and Debris Detection Conference*.

- 
- Senger, R. (2007). “Data Handling and Evaluation for Autonomous Experiments in Interplanetary Missions”. PhD thesis. Technische Universität München.
- Sharma, R. et al. (2009). “Experimental Evaluation and Analysis of Electrodynamic Screen as Dust Mitigation Technology for Future Mars Missions”. In: *IEEE Transactions on Industry Applications* 45.2, pp. 591–596.
- Sheppard, S. S. et al. (2022). “A Deep and Wide Twilight Survey for Asteroids Interior to Earth and Venus”. In: *The Astronomical Journal* 164.4, p. 168.
- Shestakova, L. I. and L. V. Tambovtseva (1995). “Dynamics of Dust Grains near the Sun”. In: *Astronomical & Astrophysical Transactions* 8.1, pp. 59–81.
- Shu, A. et al. (2012). “3 MV Hypervelocity Dust Accelerator at the Colorado Center for Lunar Dust and Atmospheric Studies”. In: *Review of Scientific Instruments* 83.7, p. 075108.
- Simpson, J. A. and A. J. Tuzzolino (1985). “Polarized Polymer Films as Electronic Pulse Detectors of Cosmic Dust Particles”. In: *Nuclear Instruments and Methods in Physics Research Section A: Accelerators, Spectrometers, Detectors and Associated Equipment* 236.1, pp. 187–202.
- Smith, E. J. et al. (1993). “Disappearance of the Heliospheric Sector Structure at Ulysses”. In: *Geophysical Research Letters* 20.21, pp. 2327–2330.
- Soberman, R. K. and L. della Lucca (1963). “Micrometeorite Measurements from Midas II (Satellite 1960 ζ 1)”. In: *Smithsonian Contributions to Astrophysics* 7, p. 85.
- Soja, R. H., W. J. Baggaley, P. Brown and D. P. Hamilton (2011). “Dynamical Resonant Structures in Meteoroid Stream Orbits”. In: *Monthly Notices of the Royal Astronomical Society* 414.2, pp. 1059–1076.
- Soja, R. H. et al. (2014). “The Interplanetary Meteoroid Environment for eXploration - (IMEX) Project”. In: *Proceedings of the International Meteor Conference*, pp. 146–149.
- Soja, R. H. et al. (2015). “Characteristics of the Dust Trail of 67P/Churyumov-Gerasimenko: An Application of the IMEX Model”. In: *Astronomy & Astrophysics* 583, A18.
- Soja, R. H. et al. (2019). “IMEM2: A Meteoroid Environment Model for the Inner Solar System”. In: *Astronomy & Astrophysics* 628, A109.
- Sommer, M., H. Yano and R. Srama (2020). “Effects of Neighbouring Planets on the Formation of Resonant Dust Rings in the Inner Solar System”. In: *Astronomy & Astrophysics* 635, A10.
- Sommer, M. et al. (2023). “Measuring Micro-Debris In-Situ with the DESTINY+ Dust Analyzer”. In: *2nd NEO and Debris Detection Conference*.
- Sommer, M. (2023). “Alpha-Meteoroids Then and Now: Unearthing an Overlooked Micrometeoroid Population”. In: *Planetary and Space Science* 236, p. 105751.
- Sommer, M., P. Pokorný, H. Yano and R. Srama (2022). “Apsidal Alignment in Migrating Dust - Crescent Features Caused by Eccentric Planets”. In: *Proceedings IAU Symposium No. 364*, pp. 259–261.
- Sommer, M. et al. (2014). “Meteoroid Stream Modelling Using Distributed Computing to Define the Impact Hazard to Spacecraft Caused by Natural Space Debris”. In: *65th IAC, IAC-14-A6.P.16*.
- Spahn, F. et al. (2006). “Cassini Dust Measurements at Enceladus and Implications for the Origin of the E Ring”. In: *Science* 311.5766, pp. 1416–1418.
- Spahn, F. et al. (2019). “Circumplanetary Dust Populations”. In: *Space Science Reviews* 215.1, p. 11.
- Srama, R. et al. (2004a). “Dust Astronomy with a Dust Telescope”. In: *Proceedings of the 37th ESLAB Symposium*. Vol. ESA SP-543, pp. 73–78.
- Srama, R. et al. (2004b). “The Cassini Cosmic Dust Analyzer”. In: *Space Science Reviews* 114, pp. 465–518.
- Srama, R. et al. (2007). “A Trajectory Sensor for Sub-micron Sized Dust”. In: 643, pp. 213–217.
- Srama, R. et al. (2011). “The Cosmic Dust Analyser Onboard Cassini: Ten Years of Discoveries”. In: *CEAS Space Journal* 2.1-4, pp. 3–16.
- Srama, R. (2010). “Micrometeoroids”. In: *Encyclopedia of Aerospace Engineering*, eae326.
- Stabroth, S. et al. (2007). “Explanation of the “May Swarm” Signature in the LDEF IDE Impact Data”. In: *Aerospace Science and Technology* 11.2, pp. 253–257.
-

- 
- Stabroth, S. et al. (2008). “The Influence of Solid Rocket Motor Retro-Burns on the Space Debris Environment”. In: *Advances in Space Research* 41.7, pp. 1054–1062.
- Stark, C. C. and M. J. Kuchner (2008). “The Detectability of Exo-Earths and Super-Earths Via Resonant Signatures in Exozodiacal Clouds”. In: *The Astrophysical Journal* 686.1, pp. 637–648.
- Staubach, P., E. Grün and R. Jehn (1997). “The Meteoroid Environment near Earth”. In: *Advances in Space Research*. Space Debris 19.2, pp. 301–308.
- Stenborg, G., R. A. Howard, P. Hess and B. Gallagher (2021). “PSP/WISPR Observations of Dust Density Depletion near the Sun: I. Remote Observations to  $8 R_{\odot}$  from an Observer between 0.13 and 0.35 AU”. In: *Astronomy & Astrophysics* 650, A28.
- Stenborg, G., R. A. Howard, A. Vourlidis and B. Gallagher (2022). “PSP/WISPR Observations of Dust Density Depletion near the Sun. II. New Insights from within the Depletion Zone”. In: *The Astrophysical Journal* 932.2, p. 75.
- Sterken, V. J. et al. (2012). “The Flow of Interstellar Dust into the Solar System”. In: *Astronomy & Astrophysics* 538, A102.
- Sterken, V. J. et al. (2013). “The Filtering of Interstellar Dust in the Solar System”. In: *Astronomy & Astrophysics* 552, A130.
- Sterken, V. (2022). “The DOLPHIN Mission and Unique Opportunities in 2030 to Probe the Dust-Heliosphere Interactions”. In: *44th COSPAR Scientific Assembly*. Vol. 44, p. 1016.
- Sternovsky, Z. et al. (2011). “Novel Instrument for Dust Astronomy: Dust Telescope”. In: *2011 Aerospace Conference*, pp. 1–8.
- Strub, P. et al. (2019). “Heliospheric Modulation of the Interstellar Dust Flow on to Earth”. In: *Astronomy & Astrophysics* 621, A54.
- Stübig, M. (2002). “New Insights in Impact Ionization and in Time-Of-Flight Mass Spectroscopy With Micrometeoroid Detectors by Improved Impact Simulations in the Laboratory”. PhD thesis. Heidelberg University.
- Svedhem, H. et al. (2000). “New Results from in Situ Measurements of Cosmic Dust — Data from the GORID Experiment”. In: *Advances in Space Research*. Sample Return Missions to Small Bodies 25.2, pp. 309–314.
- Szalay, J. R. et al. (2019a). “Impact Ejecta and Gardening in the Lunar Polar Regions”. In: *Journal of Geophysical Research: Planets* 124.1, pp. 143–154.
- Szalay, J. R. et al. (2021). “Collisional Evolution of the Inner Zodiacal Cloud”. In: *The Planetary Science Journal* 2.5, p. 185.
- Szalay, J. R. and M. Horányi (2015a). “Annual Variation and Synodic Modulation of the Sporadic Meteoroid Flux to the Moon”. In: *Geophysical Research Letters* 42.24, pp. 10, 580–10, 584.
- Szalay, J. R. and M. Horányi (2015b). “The Search for Electrostatically Lofted Grains above the Moon with the Lunar Dust Experiment”. In: *Geophysical Research Letters* 42.13, pp. 5141–5146.
- Szalay, J. R. and M. Horányi (2016a). “Detecting Meteoroid Streams with an In-Situ Dust Detector above an Airless Body”. In: *Icarus* 275, pp. 221–231.
- Szalay, J. R. and M. Horányi (2016b). “Lunar Meteoritic Gardening Rate Derived from in Situ LADEE/LDEX Measurements”. In: *Geophysical Research Letters* 43.10, pp. 4893–4898.
- Szalay, J. R. et al. (2019b). “Impact Ejecta Environment of an Eccentric Asteroid: 3200 Phaethon”. In: *Planetary and Space Science* 165, pp. 194–204.
- Szalay, J. R. (2015). “The Lunar Dust Environment”. PhD thesis. University of Colorado Boulder.
- Tabeshian, M. et al. (2019). “Asteroid (3200) Phaethon: Colors, Phase Curve, Limits on Cometary Activity, and Fragmentation”. In: *The Astronomical Journal* 158.1, p. 30.
- Takir, D. et al. (2020). “Near-Infrared Observations of Active Asteroid (3200) Phaethon Reveal No Evidence for Hydration”. In: *Nature Communications* 11.1, p. 2050.
- Taylor, A. D. and W. G. Elford (1998). “Meteoroid Orbital Element Distributions at 1 AU Deduced from the Harvard Radio Meteor Project Observations”. In: *Earth, Planets and Space* 50.6, pp. 569–575.

- 
- Taylor, P. A. et al. (2019). “Arecibo Radar Observations of Near-Earth Asteroid (3200) Phaethon during the 2017 Apparition”. In: *Planetary and Space Science* 167, pp. 1–8.
- Titov, D. et al. (2006). “Venus Express Science Planning”. In: *Planetary and Space Science* 54.13-14, pp. 1279–1297.
- Toyota, H., K. Nishiyama, Y. Kawakatsu and the DESTINY+ Team (2017). “DESTINY+: Deep Space Exploration Technology Demonstrator and Explorer to Asteroid 3200 Phaethon”. In: *12th Low-Cost Planetary Missions Conference*.
- Triani, D. P. et al. (2020). “The Origin of Dust in Galaxies across Cosmic Time”. In: *Monthly Notices of the Royal Astronomical Society* 493.2, pp. 2490–2505.
- Tuzzolino, A. J. et al. (2003). “Dust Flux Monitor Instrument for the Stardust Mission to Comet Wild 2”. In: *Journal of Geophysical Research: Planets* 108.E10.
- Tuzzolino, A. et al. (2005). “Final Results from the Space Dust (SPADUS) Instrument Flown Aboard the Earth-Orbiting ARGOS Spacecraft”. In: *Planetary and Space Science* 53.9, pp. 903–923.
- Ueda, T. et al. (2017). “Size Dependence of Dust Distribution around the Earth Orbit”. In: *The Astronomical Journal* 153.5, p. 232.
- Vallat, C. et al. (2017). “The Science Planning Process on the Rosetta Mission”. In: *Acta Astronautica* 133, pp. 244–257.
- Van Allen, J. A. (1959). “Radiation Belts around the Earth”. In: *Scientific American* 200.3, pp. 39–47. JSTOR: 24944942.
- van der Plas, P., B. García-Gutiérrez, F. Nespoli and M. Pérez-Ayúcar (2016). “MAPPS: A Science Planning Tool Supporting the ESA Solar System Missions”. In: *SpaceOps 2016 Conference*. SpaceOps Conferences.
- Venemans, B. P. et al. (2017). “Copious Amounts of Dust and Gas in a  $z = 7.5$  Quasar Host Galaxy”. In: *The Astrophysical Journal Letters* 851.1, p. L8.
- Wagner, S. (2006). *The Apollo Experience Lessons Learned for Constellation Lunar Dust Management*. Technical Report NASA/TP-213726. Johnson Space Center.
- Wallis, M. K. and M. H. A. Hassan (1985). “Stochastic Diffusion of Interplanetary Dust Grains Orbiting under Poynting-Robertson Forces”. In: *Astronomy and Astrophysics* 151.2, pp. 435–441.
- Wehry, A., H. Krüger and E. Grün (2004). “Analysis of Ulysses Data: Radiation Pressure Effects on Dust Particles”. In: *Astronomy & Astrophysics* 419.3, pp. 1169–1174.
- Wehry, A. and I. Mann (1999). “Identification of  $\beta$ -Meteoroids from Measurements of the Dust Detector Onboard the ULYSSES Spacecraft”. In: *Astronomy and Astrophysics* 341, pp. 296–303.
- Weidenschilling, S. J. (1978). “The Distribution of Orbits of Cosmic Dust Particles Detected by Pioneers 8 and 9”. In: *Geophysical Research Letters* 5.7, pp. 606–608.
- Weidenschilling, S. J. and A. A. Jackson (1993). “Orbital Resonances and Poynting-Robertson Drag”. In: *Icarus* 104.2, pp. 244–254.
- Westphal, A. J. et al. (2014). “Evidence for Interstellar Origin of Seven Dust Particles Collected by the Stardust Spacecraft”. In: *Science* 345.6198, pp. 786–791.
- Wiegert, P., J. Vaubaillon and M. Campbell-Brown (2009). “A Dynamical Model of the Sporadic Meteoroid Complex”. In: *Icarus* 201.1, pp. 295–310.
- Williams, I. P. and Z. Wu (1993). “The Geminid Meteor Stream and Asteroid 3200 Phaethon”. In: *Monthly Notices of the Royal Astronomical Society* 262.1, pp. 231–248.
- Wolf, H., J. Rhee and O. E. Berg (1976). “Orbital Elements of Dust Particles Intercepted by Pioneers 8 and 9”. In: *Interplanetary Dust and Zodiacal Light, Proc. of the IAU-Colloq. 31*. Lecture Notes in Physics, pp. 165–169.
- Wozniakiewicz, P. J. et al. (2021). “A Cosmic Dust Detection Suite for the Deep Space Gateway”. In: *Advances in Space Research* 68.1, pp. 85–104.
- Wyatt, S. P. and F. L. Whipple (1950). “The Poynting-Robertson Effect on Meteor Orbits”. In: *The Astrophysical Journal* 111, pp. 134–141.
-

- 
- Yang, H. and M. Ishiguro (2015). “ORIGIN OF INTERPLANETARY DUST THROUGH OPTICAL PROPERTIES OF ZODIACAL LIGHT”. In: *The Astrophysical Journal* 813.2, p. 87.
- Yang, K., J. Schmidt, W. Feng and X. Liu (2022). “Distribution of Dust Ejected from the Lunar Surface into the Earth-Moon System”. In: *Astronomy & Astrophysics* 659, A120.
- Ye, Q. et al. (2014). “The Unexpected 2012 Draconid Meteor Storm”. In: *Monthly Notices of the Royal Astronomical Society* 437.4, pp. 3812–3823.
- Ye, Q. et al. (2021). “A Deep Search for Emission from “Rock Comet” (3200) Phaethon at 1 Au”. In: *The Planetary Science Journal* 2.1, p. 23.
- Yoshikawa, M., J. Kawaguchi, A. Fujiwara and A. Tsuchiyama (2021). “The Hayabusa Mission”. In: *Sample Return Missions*, pp. 123–146.
- Yu, L. L., W. H. Ip and T. Spohn (2019). “What Mechanisms Dominate the Activity of Geminid Parent (3200) Phaethon?” In: *Monthly Notices of the Royal Astronomical Society* 482.3, pp. 4243–4252.
- Zhang, Q. et al. (2023). “Sodium Brightening of (3200) Phaethon near Perihelion”. In: *The Planetary Science Journal* 4.4, p. 70.
- Zimbardo, G. et al. (2010). “Magnetic Turbulence in the Geospace Environment”. In: *Space Science Reviews* 156.1, pp. 89–134.
- Zook, H. A. and O. E. Berg (1975). “A Source for Hyperbolic Cosmic Dust Particles”. In: *Planetary and Space Science* 23.1, pp. 183–203.
- Zubko, E. et al. (2022). “On the Dust Production of Active Asteroid (3200) Phaethon in 2009: What the DESTINY+ Spaceprobe Could Encounter”. In: *Journal of Quantitative Spectroscopy and Radiative Transfer* 286, p. 108224.
- Zuiani, F., Y. Kawakatsu and M. Vasile (2013). “Multi-Objective Optimisation of Many-Revolution, Low-Thrust Orbit Raising for Destiny Mission”. In: *23rd AAS/AIAA Space Flight Mechanics Conference*.

# Appendices



# A. Coordinate Systems

Within the scope of this project, a number of coordinate systems CS were defined to standardize the description of positions and orientations of various components, as well as to avoid mistakes that could arise from using different conventions. These CS were adopted consistently throughout the DDA project and thus, they established a common language throughout not only in the domain of science planning, but also in instrument and spacecraft interface design.

Where applicable, SPICE naming conventions and notations were adopted.

## Ecliptic CS

The ecliptic CS is widely used in interplanetary missions and space sciences. Its fundamental plane is the ecliptic, the system's origin can be the centre of either the Sun or Earth, its primary vector is towards the vernal equinox, and it has a right-hand convention (see Figure A.1). For the CS to be fixed in space, the referenced ecliptic/equinox must be specified at a particular date (epoch). Following SPICE conventions, the DDA project uses the standard epoch J2000.0 to define the ecliptic CS, which is thus referred to as ECLIPJ2000.

Within the DDA project, the ecliptic CS shall be used when handling trajectory data of heliocentric and geocentric spacecraft orbits.

**Identifier (SPICE name):**

ECLIPJ2000

**Abbreviation:**

None.

**Origin:**

Can be used Sun-centred or Earth-centred, depending on usage.

**Axes definition:**

+**X**: Points towards the vernal equinox (primary vector).

+**Z**: Points towards the north ecliptic pole.

+**Y**: Completes the right-handed frame, such that  $X \times Y = Z$ .

**Parametrization:**

**Ecliptic Longitude:** angle from the +X axis to the projection of a position vector on the X-Y plane (increases in counter-clockwise direction).

**Ecliptic Latitude:** angle between a position vector and the X-Y plane (positive on the northern hemisphere, negative on the southern hemisphere).

## Equatorial CS

The equatorial CS is widely used in Earth-orbiting missions. Its fundamental plane is formed by projection of Earth's equator onto the celestial sphere, the system's origin is the centre of Earth

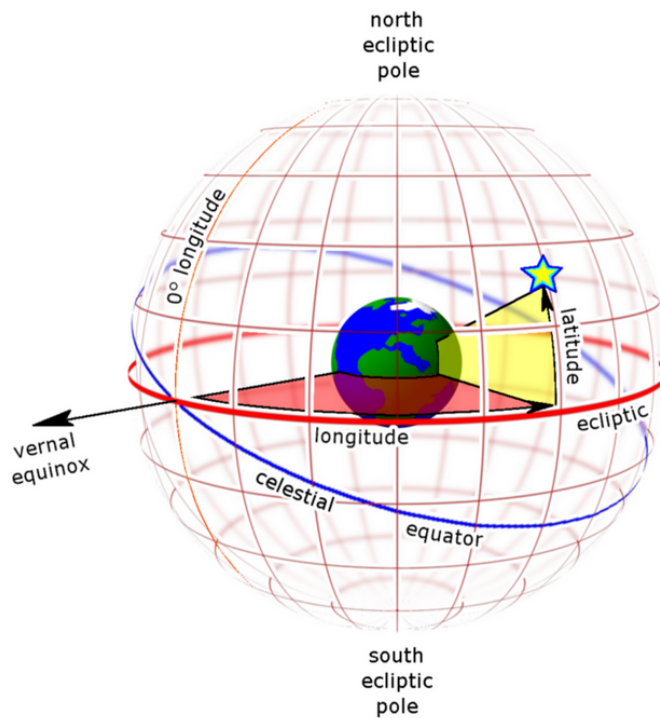


**Figure A.1.:** Scheme of the Ecliptic CS (Earth-centred). The X axis points towards the vernal equinox and Z axis towards the north ecliptic pole. Also indicated is the celestial equator (projection of the Earth's equator onto the celestial sphere), which is the fundamental plane of the Equatorial CS. Image from *Wikipedia*: [https://commons.wikimedia.org/wiki/File:Ecliptic\\_grid\\_globe.png](https://commons.wikimedia.org/wiki/File:Ecliptic_grid_globe.png) licensed under CC BY-SA 3.0.

its primary vector is towards the vernal equinox, and it has a right-hand convention. For the CS to be fixed in space, the referenced equator/equinox must be specified at a particular date (epoch). Following SPICE conventions, the DDA project uses the standard epoch J2000.0 to define the equatorial CS, which is simply referred to as J2000. Within the DDA project, the equatorial CS can be used alongside the ecliptic CS, when handling geocentric spacecraft orbits.

**Identifier (SPICE name):**

J2000

**Abbreviation:**

None.

**Origin:**

Earth-centred.

**Axes definition:**

- +X: Points towards the vernal equinox (primary vector).
- +Z: Points towards the north celestial pole.
- +Y: Completes the right-handed frame, such that  $X \times Y = Z$ .

**Parametrization:**

**Right Ascension:** angle from the +X axis to the projection of a position vector on the X-Y plane (is defined in hours, not degrees, from 0h to 24h; increases in counter-clockwise direction).

**Declination:** angle between a position vector and the X-Y plane (positive on the northern hemisphere, negative on the southern hemisphere).

## Spacecraft-fixed CS

This is the spacecraft-fixed CS as implemented by the spacecraft manufacturer, see Figure A.2.

### Identifier (SPICE name):

DESTINY\_SPACECRAFT

### Abbreviation:

SC

### Origin:

-

### Axes definition:

+**X**: Points normal from the ion-engine bus panel, away from the S/C.

+**Z**: Points normal from the launch adapter bus panel, towards the centre of the S/C.

+**Y**: Completes the right-handed frame, such that  $X \times Y = Z$ .

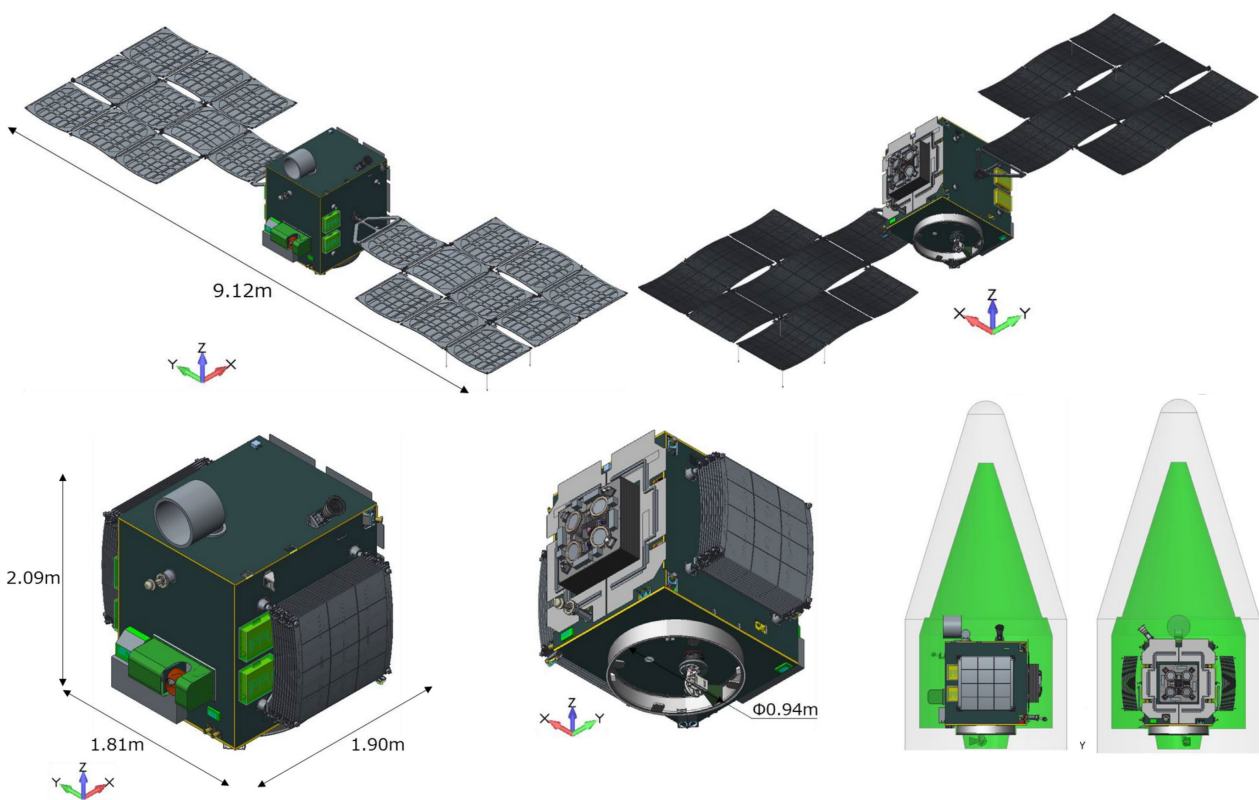


**Figure A.2.:** The DESTINY+ spacecraft, deployed (top) and launch configuration (bottom). Note that the DDA pointing in the stowed configuration is outdated in this figure (compare with Figure 4.1). Figure received from JAXA/ISAS (Toyota, priv. comm.).

## DDA Base CS

The DDA Base system remains fixed with respect to the non-moving part of the DDA Pointing Mechanism (see Figure A.3). The pointing of the DDA Sensor is defined in this CS. In accordance with the fundamental design of the PM, it is parametrized as is conventional in an altazimuth mount: rotation about the vertical axis varies the azimuth of the pointing direction of the instrument, rotation about the horizontal axis varies its elevation. The pointing of the sensor boresight shall be

defined in the DDA\_BASE CS, using the azimuth/elevation parametrization.

**Identifier (SPICE name):**

DESTINY\_DDA\_BASE

**Abbreviation:**

DDA\_BASE

**Origin:**

Crossing of the azimuth rotation axis with the mounting panel surface plane.

**Axes definition:**

+**X**: Points normal to the TCAP/MCAP bus panel, away from the S/C.

+**Z**: Points parallel to the DDA Pointing Mechanism azimuth rotation axis, away from the S/C.

+**Y**: Completes the right-handed frame, such that  $X \times Y = Z$ .

**Parametrization:**

**Azimuth (*a*):** angle from the +X axis to the projection of a position vector on the X-Y plane (increases in clockwise direction).

**Elevation (*h*):** angle between a position vector and the X-Y plane (positive on the +Z hemisphere, negative on the -Z hemisphere).

The angular representation of a vector is transferred into the Cartesian representation via the following transformation:

$$\begin{pmatrix} x \\ y \\ z \end{pmatrix}_{SC} = \begin{pmatrix} -x \\ -y \\ z \end{pmatrix}_{DDA\_BASE} = \begin{pmatrix} -\cos h \cdot \cos a \\ \cos h \cdot \sin a \\ \sin h \end{pmatrix} \quad (\text{A.1})$$

**Table A.1.:** Exemplary pointings (angles) and their corresponding boresight vectors.

Azimuth	Elevation	Vector in SC	Vector in DDA_BASE	Note
-90°	0°	(0, -1, 0)	(0, 1, 0)	-
-45°	0°	(-0.7, -0.7, 0)	(0.7, 0.7, 0)	-
0°	0°	(-1, 0, 0)	(1, 0, 0)	to thrust vector
+45°	0°	(-0.7, 0.7, 0)	(0.7, -0.7, 0)	-
+90°	0°	(0, 1, 0)	(0, -1, 0)	-
-90°	45°	(0, -0.7, 0.7)	(0, 0.7, 0.7)	-
-45°	45°	(-0.5, -0.5, 0.7)	(0.5, 0.5, 0.7)	-
0°	45°	(-0.7, 0, 0.7)	(0.7, 0, 0.7)	-
+45°	45°	(-0.5, 0.5, 0.7)	(0.5, -0.5, 0.7)	-
+90°	45°	(0, 0.7, 0.7)	(0, -0.7, 0.7)	-
any	90°	(0, 0, 1)	(0, 0, 1)	Flyby dust ram
-90°	90°	(0, 0, 1)	(0, 0, 1)	Launch lock position

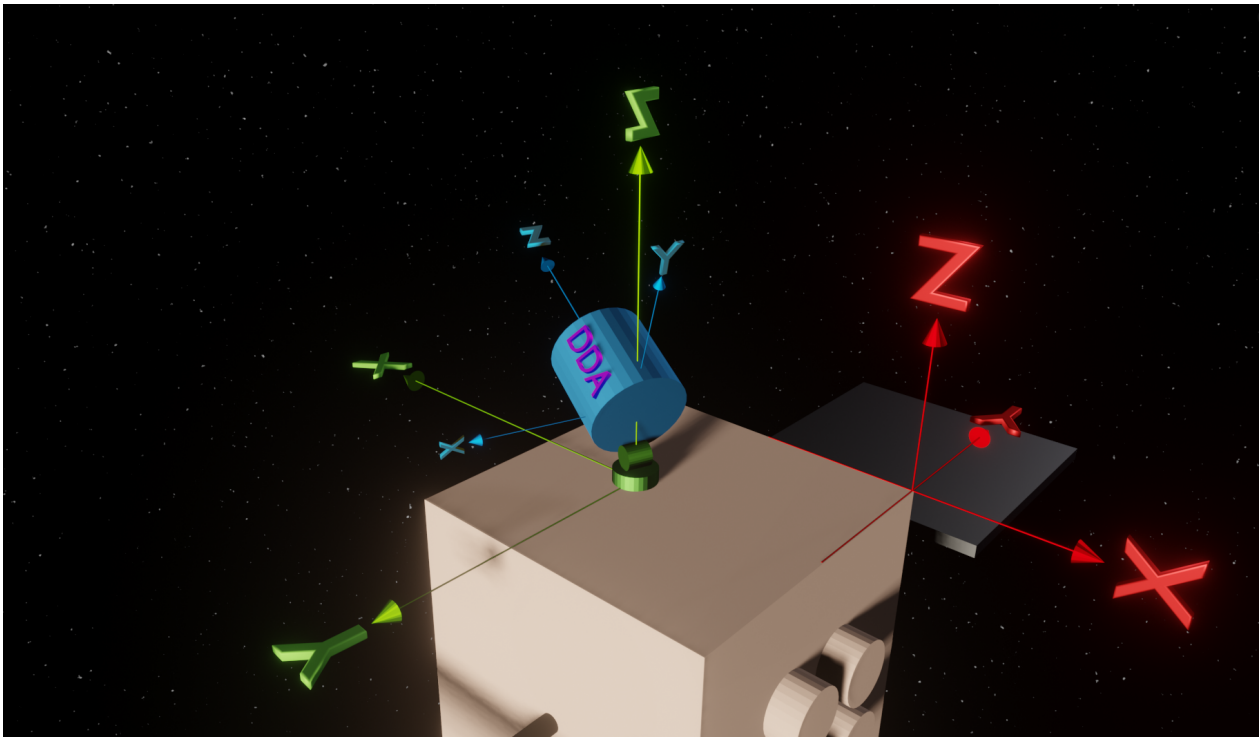


**Figure A.3.:** DDA Instrument coordinate systems. The DDA\_BASE is shown in green. The sensor-fixed system DDA\_SENS is shown in blue. Also shown is the spacecraft-fixed system DESTINY\_SPACECRAFT in red.

## DDA Sensor CS

The DDA Sensor system remains fixed with respect to the sensor head (see Figure A.3) and shall be used when reconstructing directionality of measured particles. The primary vector is the instrument boresight vector, which is the rotation axis of the instrument body, pointing from impact target plane towards the aperture.

**Identifier (SPICE name):**

DESTINY\_DDA\_SENSOR

**Abbreviation:**

DDA\_SENS

**Origin:**

Crossing of boresight vector with the impact target plane.

**Axes definition:**

+**Z**: Points parallel to the instrument boresight vector.

+**Y**: Is antiparallel to the vector that points radially from the Z axis to the centre of the sensor head amplifier housing.

+**X**: Completes the right-handed frame, such that  $X \times Y = Z$ .

---

## Destiny-centric Orbit Normal CS

The Destiny-centric Orbit Normal (DON) system is a dynamic frame, whose primary vector points to the Sun, whereas the Z axis points normal to the S/C's orbital plane (see Figure A.4).

The DON system shall be used when planning observations campaigns with DDA when in interplanetary space. The DON system allows for easy and invariant separation of the hemisphere unobservable by DDA (the solar hemisphere) and the observable hemisphere (the anti-solar hemisphere), at its Y-Z plane (see Figure A.5). In addition, the directionality of interplanetary dust sources (e.g., N/S apex, N/S toroidal, solar/anti-solar) remains relatively constant in the DON system, given the moderate eccentricity and inclination of the DESTINY<sup>+</sup> heliocentric orbit.

### Identifier (SPICE name):

DESTINY\_ORBITNORMAL

### Abbreviation:

DON

### Origin:

S/C centre of mass.

### Axes definition:

+X: Points towards the Sun (*primary vector*).

+Y: The inertially referenced velocity vector of the Sun relative to the DESTINY<sup>+</sup> spacecraft is the *secondary vector*. The Y axis points parallel to the component of the secondary vector that is orthogonal to the X axis.

+Z: Completes the right-handed frame, such that  $X \times Y = Z$ .

### Parametrization:

**DON Longitude:** angle from the +X axis to the projection of a position vector on the X-Y plane (increases in counter-clockwise direction).

**DON Latitude:** angle between a position vector and the X-Y plane (positive on the +Z hemisphere, negative on the -Z hemisphere).

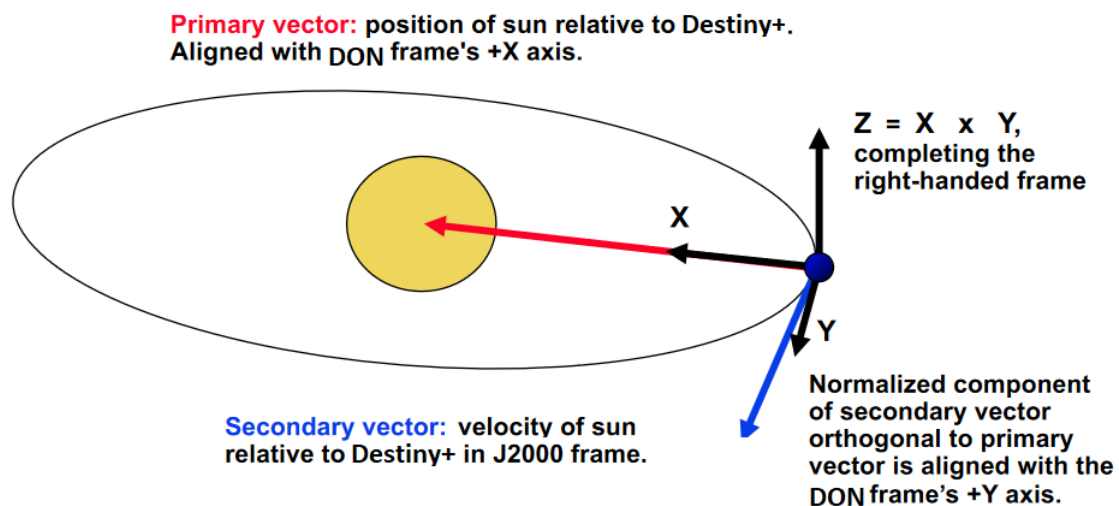


**Figure A.4.:** Definition of the Destiny-centric Orbit Normal CS. The figure is an adapted version of NAIF's definition of the Geocentric Solar Ecliptic: [https://naif.jpl.nasa.gov/pub/naif/toolkit\\_docs/Tutorials/pdf/individual\\_docs/24\\_dynamic\\_frames.pdf](https://naif.jpl.nasa.gov/pub/naif/toolkit_docs/Tutorials/pdf/individual_docs/24_dynamic_frames.pdf)

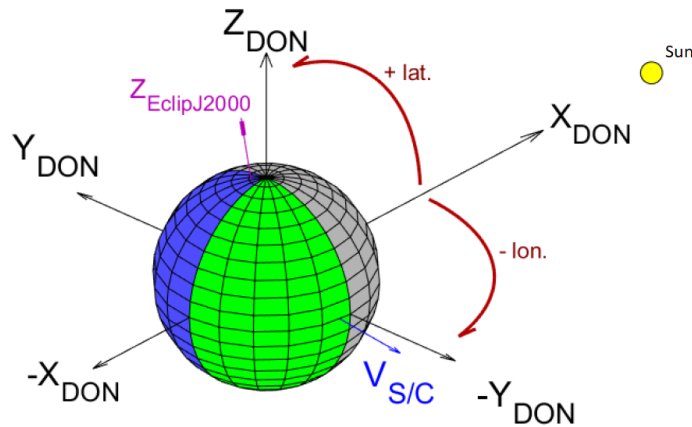


**Figure A.5.:** Destiny-centric Orbit Normal (DON) CS. The  $Z_{ECLIPJ2000}$  and  $V_{S/C}$  directions are exemplary. The sphere depicts the sky around the spacecraft. Viewing directions with a separation angle to the Sun  $< 90^\circ$  form the solar (i.e., sun-facing) hemisphere (grey) and are unobservable by DDA. The observable anti-solar hemisphere is divided into the prograde *apex quadrant* (green) and a retrograde *antapex quadrant* (blue).

## Geocentric Solar Ecliptic CS

The Geocentric Solar Ecliptic (GSE) system is a dynamic frame, whose primary and secondary vectors point to the Sun and the ecliptic north, respectively (see Figure A.6). It shall be used when planning observations campaigns with DDA when still in the Earth-Moon system. The GSE CS allows for easy and invariant separation of the hemisphere unobservable by DDA (the solar hemisphere) and the observable hemisphere (the anti-solar hemisphere), at its Y-Z plane. In addition, the directionality of interplanetary dust sources (e.g., N/S apex, N/S toroidal, solar/anti-solar) remains relatively constant in the GSE system.

### Identifier (SPICE name):

GSE

### Abbreviation:

None.

### Origin:

Earth-centred.

### Axes definition:

+X: Points towards the Sun (*primary vector*).

+Y: The inertially referenced velocity vector of the Sun relative to the Earth is the *secondary vector*. The Y axis points parallel to the component of the secondary vector that is orthogonal to the X axis.

+Z: Completes the right-handed frame, such that  $X \times Y = Z$ .

### Parametrization:

**GSE Longitude:** angle from the +X axis to the projection of a position vector on the X-Y plane (increases in counter-clockwise direction).

**GSE Latitude:** angle between a position vector and the X-Y plane (positive on the +Z hemisphere, negative on the -Z hemisphere).

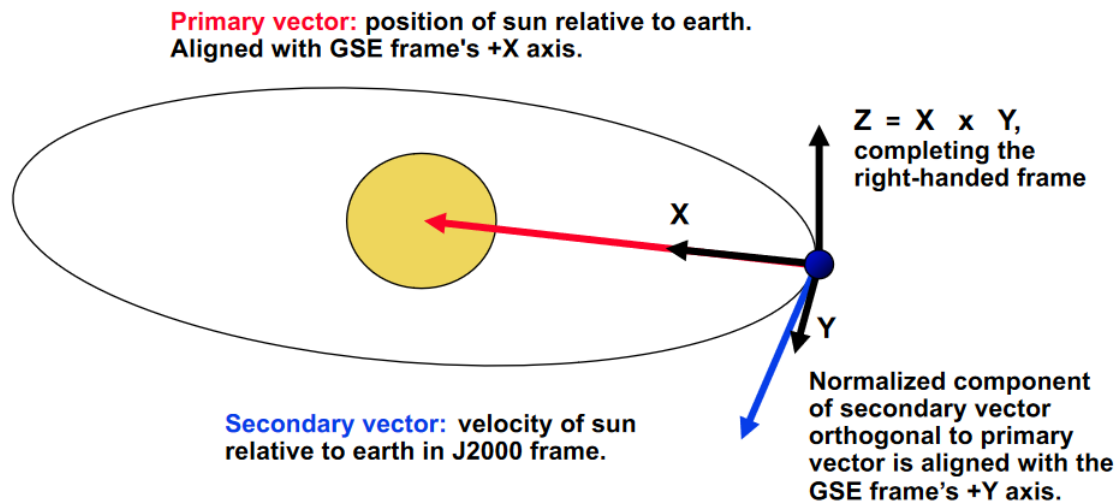


**Figure A.6.:** Definition of the Geocentric Solar Ecliptic CS. Taken from NAIF's definition of the Geocentric Solar Ecliptic frame: [https://naif.jpl.nasa.gov/pub/naif/toolkit\\_docs/Tutorials/pdf/individual\\_docs/24\\_dynamic\\_frames.pdf](https://naif.jpl.nasa.gov/pub/naif/toolkit_docs/Tutorials/pdf/individual_docs/24_dynamic_frames.pdf)

## Selenocentric Solar Ecliptic CS

The Selenocentric Solar Ecliptic (SSE) system is a Moon-centred dynamic frame. It shall be used when planning observations campaigns when in proximity of the Moon. The SSE system allows for easy and invariant separation of the hemisphere unobservable by DDA (the solar hemisphere) and the observable hemisphere (the anti-solar hemisphere), at its Y-Z plane. In addition, the directionality of interplanetary dust sources (e.g., N/S apex, N/S toroidal, solar/anti-solar) remains relatively constant in the SSE system. It has previously been used in the context of Lunar exosphere modelling (e.g., Szalay et al., 2019a).

### Identifier (SPICE name):

SSE

### Abbreviation:

None.

### Origin:

Moon-centred.

### Axes definition:

- +X: Points towards the Sun (*primary vector*).
- +Z: Points towards the north ecliptic pole (*secondary vector*).
- +Y: Completes the right-handed frame, such that  $X \times Y = Z$ .

### Parametrization:

- SSE Longitude:** angle from the +X axis to the projection of a position vector on the X-Y plane (increases in counter-clockwise direction).
- SSE Latitude:** angle between a position vector and the X-Y plane (positive on the +Z hemisphere, negative on the -Z hemisphere).

## B. Correction of Lunar Ejecta Cloud Model

The equations given by Szalay et al. (2019a) that describe their geometric density model for the lunar ejecta cloud appears to exhibit typos (confirmed by Szalay, priv. comm.).

The corrected versions of the erroneous equations are given below. For the particle number density  $n$  dependent on altitude  $h$ , local time  $\phi$ , latitude  $\lambda$ , and the particle radius  $a$ , that is:

$$n(h, \phi, \lambda, a) = e^{-h/h_0} a_\mu^{-q} n_w \sum_s w_s \cos^3(\Delta\varphi_s) \Theta(\pi/2 - \Delta\varphi_s)$$

where  $h_0 = 200$  km,  $q = 2.7$ ,  $n_w$  is the normalization density scaled to match LDEX measurements,  $s$  is the source index,  $w_s$  is the relative weight of each source,  $\Theta$  is the Heaviside function, and  $\Delta\varphi_s$  is the angular distance to a given source. The LDEX-derived values for  $n_w$  and  $w_s$  are given in Szalay et al. (2019a). Note that here, the symbol  $a$  denotes the particle radius, whereas throughout the rest of this thesis, the particle radius is denoted by  $s$ .

For  $\Delta\varphi_s$  the corrected version is:

$$\Delta\varphi_s = \cos^{-1} [\cos \lambda \cos \lambda_s + \sin \lambda \sin \lambda_s \cos(\phi - \phi_s)]$$

where  $\phi_s$  and  $\lambda_s$  are the radiant angles of a given source, as likewise given in Szalay et al. (2019a).



## C. Absence of $\alpha$ -meteoroid in Dust Models

One may consider employing various dust environment models for assessing the flow of dust at 1 au of particles of the  $\alpha$ -meteoroids size range. None of the existing models, however, include a corresponding population that could adequately represent the  $\alpha$ -meteoroids, as we shall show. Here, we consider those notable examples of dust environment model that cover the relevant particle sizes, specifically the models of Divine (1993), Staubach et al. (1997), and Dikarev et al. (2005a,b).

### The Divine model

The first of these, the Divine model, is an empirical model with five particle populations of different orbital elements distributions and particle sizes, purely designed to fit various observational datasets (including data on radar meteors, zodiacal light, the Grün-flux, and in-situ measurements retrieved by Helios and Pioneer 10 & 11 as well as by Ulysses and Galileo during their early operational phases). The populations with considerable contributions in the  $\alpha$ -meteoroid mass-range are the ‘core’ and the ‘eccentric’ population,<sup>1</sup> The ‘core’ population is designed to match most datasets reasonably well, including that of the Helios ecliptic sensor (which predominantly detected  $\alpha$ -meteoroids Grün, 1981), while the ‘eccentric’ population is introduced to fit the dataset of the Helios south sensor. Although the ‘eccentric’ population appears to cover the  $\alpha$ -meteoroid-typical orbital elements, it is unable to reproduce the azimuthal distribution of impacts observed by the Helios ecliptic sensor, as noted by Divine (1993). We presume this to be due to the omission of radiation pressure in the model, which, as a key defining factor for the  $\alpha$ -meteoroids, would effectively cause a decrease of orbital speeds of such small particles, thus skewing their azimuthal distribution of impacts onto a spacecraft towards its apex direction. To resolve the incompatibility of the ‘eccentric’ population with the azimuthal distribution observed by the ecliptic sensor, Divine (1993) set its particle bulk density to  $0.25 \text{ g cm}^{-3}$  (10% of the density used in the other populations), which, due to a sunlight reflecting thin foil covering the aperture, the ecliptic sensor would have been insensitive to (Pailer and grün, 1980; Grün et al., 1980). This only leaves the ‘core’ population to represent the particles observed by the ecliptic sensor. Yet, as the backbone population of the model, designed to match other datasets as well, it exhibits broad orbital elements distributions, covering both asteroidal and cometary orbits. It is thus also unable to produce the distinct predominance of the  $\alpha$ -meteoroids, at the corresponding particle masses. Divine notes, however, that the poor fit of the Helios directional dataset may be improved by the inclusion of radiation pressure in the model.<sup>2</sup>

---

<sup>1</sup>The ‘core’ and the ‘eccentric’ populations of the Divine model represent particles down to  $m = 10^{-18} \text{ g}$ .

<sup>2</sup>See Divine (1993), p. 17,042. This deficiency of the model is also discussed by Grün and Staubach (1996) who also give an outlook on the upcoming ‘Staubach model’.

---

## The Staubach model

The Staubach model addresses this issue, curtailing Divine’s ‘core’ population to masses unaffected by radiation pressure, as well as introducing new populations to replace those populations that are radiation-pressure-prone (see also Grün et al., 1997). These new, empirical populations, however, are designed to fit the datasets of the Galileo and Ulysses dust detectors, which, due to their outer-solar-system and out-of-ecliptic voyages, were largely insensitive to the  $\alpha$ -meteoroids. Although Galileo could have been significantly exposed to  $\alpha$ -meteoroids, during its roughly three years tour of inner solar system, the sensor covered predominantly the anti-sunward hemisphere.<sup>3</sup> As a result, it seems unlikely that the apex-dominated  $\alpha$ -meteoroids could constitute a meaningful, let alone a salient, contribution to the recorded dataset. Consequently, it must be inferred that the Staubach populations also do not represent the  $\alpha$ -meteoroids.

## The Dikarev model

The Dikarev model, on the other hand, adopts a bottom-up physical approach, where the particle populations are constructed from the orbital evolution of meteoroids originating in source body populations (JFCs and asteroids),<sup>4</sup> before being fitted to various observational datasets. Yet, as the source of the  $\alpha$ -meteoroids (presumably PR-drag-evolved progenitor meteoroids close to the Sun) is not considered, and since they cannot be created efficiently from cometary or asteroidal orbits from PR drag alone (as demonstrated in Section 5.3.3), the  $\alpha$ -meteoroids cannot possibly be reproduced by Dikarev’s populations. On the other hand, the representation of JFC and asteroidal dust is misguided, as their size distribution is effectively fitted with the Grün-flux, which arguably includes a contribution from  $\alpha$ -meteoroids. Therefore, these populations yield unphysically high contributions of JFC and asteroidal dust at sizes that may be well below the radiation pressure blowout limit for those sources (e.g., Moorhead, 2021). Thus, they must be considered inadequate to make predictions for fluxes of grains smaller than a few microns.

Dikarev et al. (2005a,b) also provide the software framework to evaluate synthetic dust populations (such as those of the Divine-, Staubach-, and Dikarev model) with respect to a moving observer/spacecraft, called the Interplanetary Meteoroid Environment Model (IMEM). Figure C.1 shows the flux sky maps of the different models, (data generated with IMEM) for  $m > 10^{-13}$  g. Evidently, none of the three models can reproduce an apex radiant caused by the  $\alpha$ -meteoroids, confirming our presumptions. Nevertheless, we shall consider these models for assessing the flux of dust of the sporadic meteoroid complex (i.e., a particle size regime where they can be expected to be more reliable) in Section 5.3.4.

---

<sup>3</sup>The Galileo detector pointed at an angle of  $55^\circ$  to the anti-sunward direction, about which the spacecraft rotated (Grün et al., 1995b).

<sup>4</sup>The orbital propagation in the Dikarev model considers solar and planetary gravity as well as the Poynting-Robertson drag (Dikarev et al., 2005a).

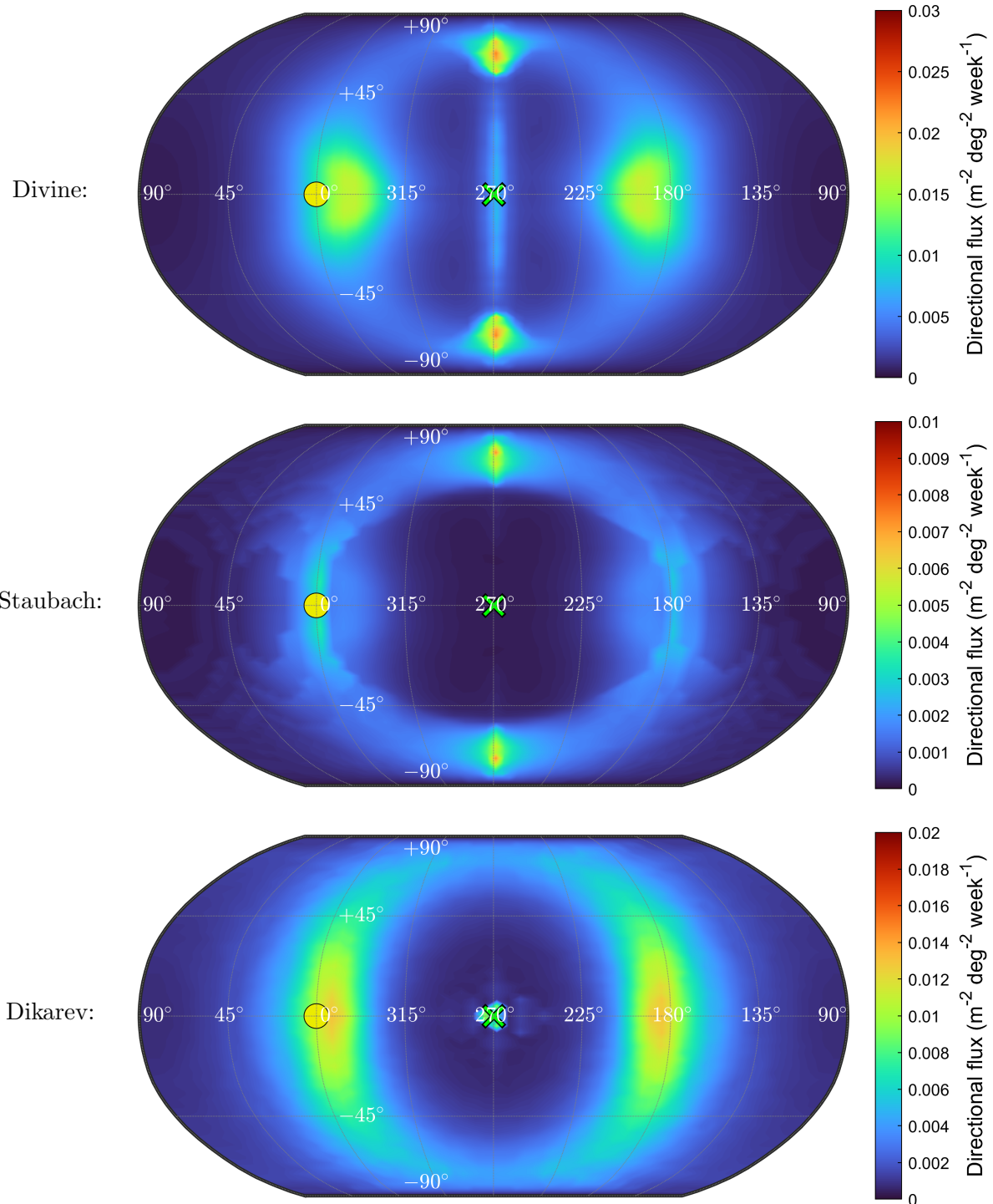


**Figure C.1.:** Flux sky maps for the Divine, Staubach, and Dikarev model, showing the absence of  $\alpha$ -meteoroids. The observer is in a heliocentric, circular orbit at 1 au. The presence  $\alpha$ -meteoroids would be apparent in a distinct apex radiant. (The minor apex radiant in the Divine model is caused by retrograde JFC dust). Direction of the Sun and apex are indicated by the yellow circle and green cross, respectively. Data was generated with IMEM for a minimum particle mass of  $10^{-13}$  g.



## D. Supplementary IMEM Sky Maps

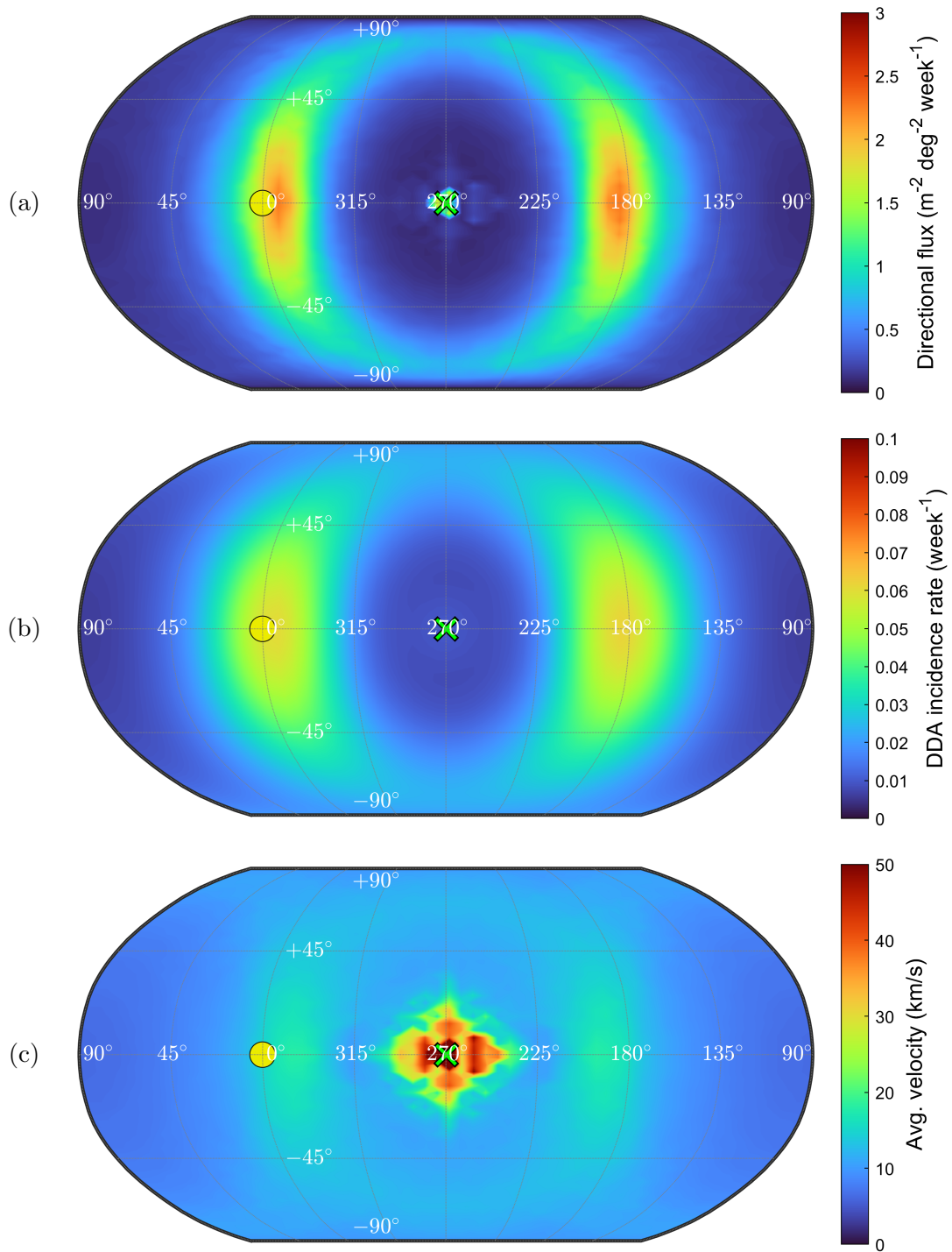


**Figure D.1.:** Dikarev model sky maps of the JFC flux at 1 au: (a) directional flux, (b) DDA incidence rate, and (c) average velocity. The observer is in a heliocentric, circular orbit at 1 au. Direction of the Sun and apex are indicated by the yellow circle and green cross, respectively. Data was generated with IMEM for a minimum particle mass of  $10^{-11}$  g.

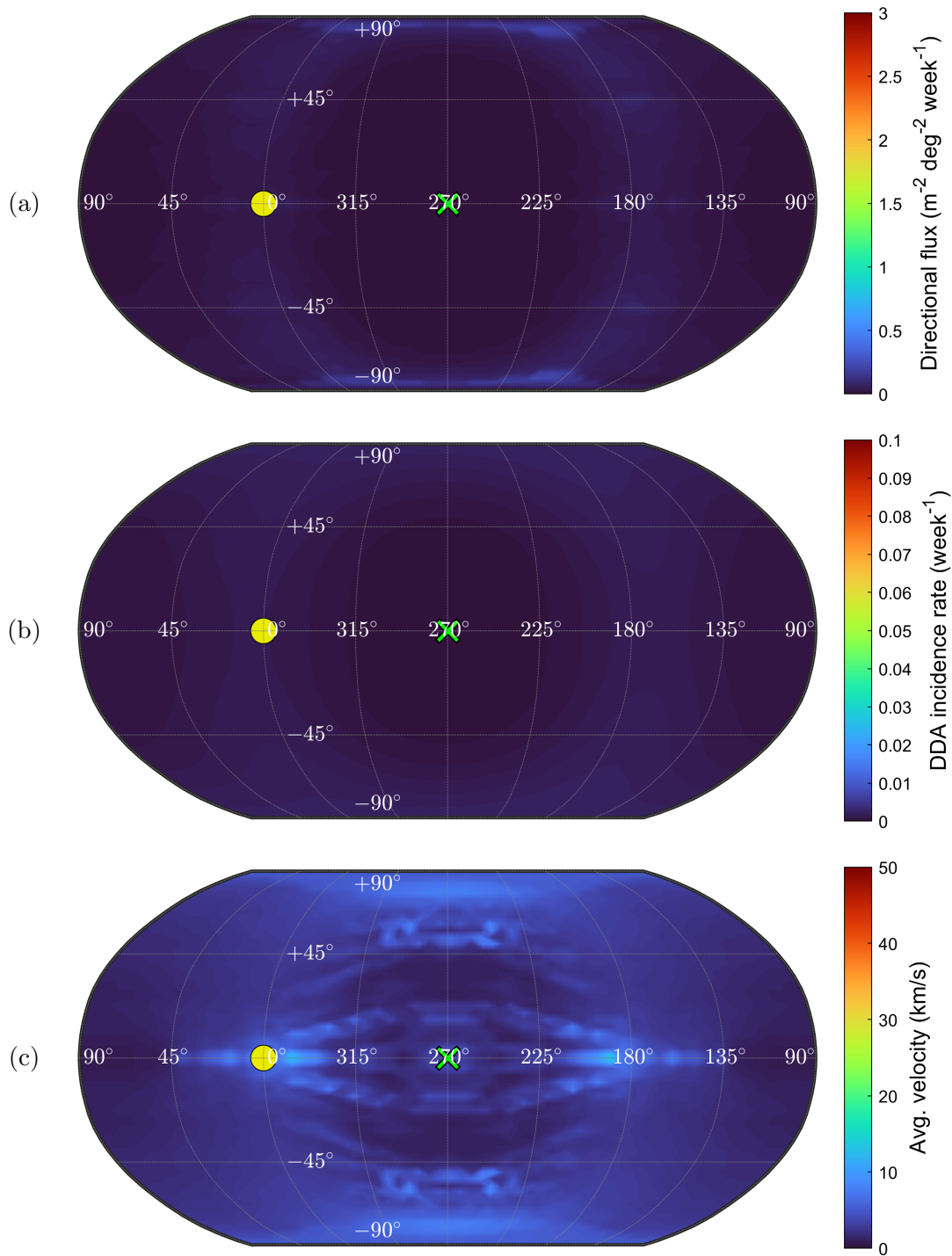


**Figure D.2.:** Dikarev model sky maps of the AST flux at 1 au: (a) directional flux, (b) DDA incidence rate, and (c) average velocity. The observer is in a heliocentric, circular orbit at 1 au. Direction of the Sun and apex are indicated by the yellow circle and green cross, respectively. Data was generated with IMEM for a minimum particle mass of  $10^{-11}$  g.

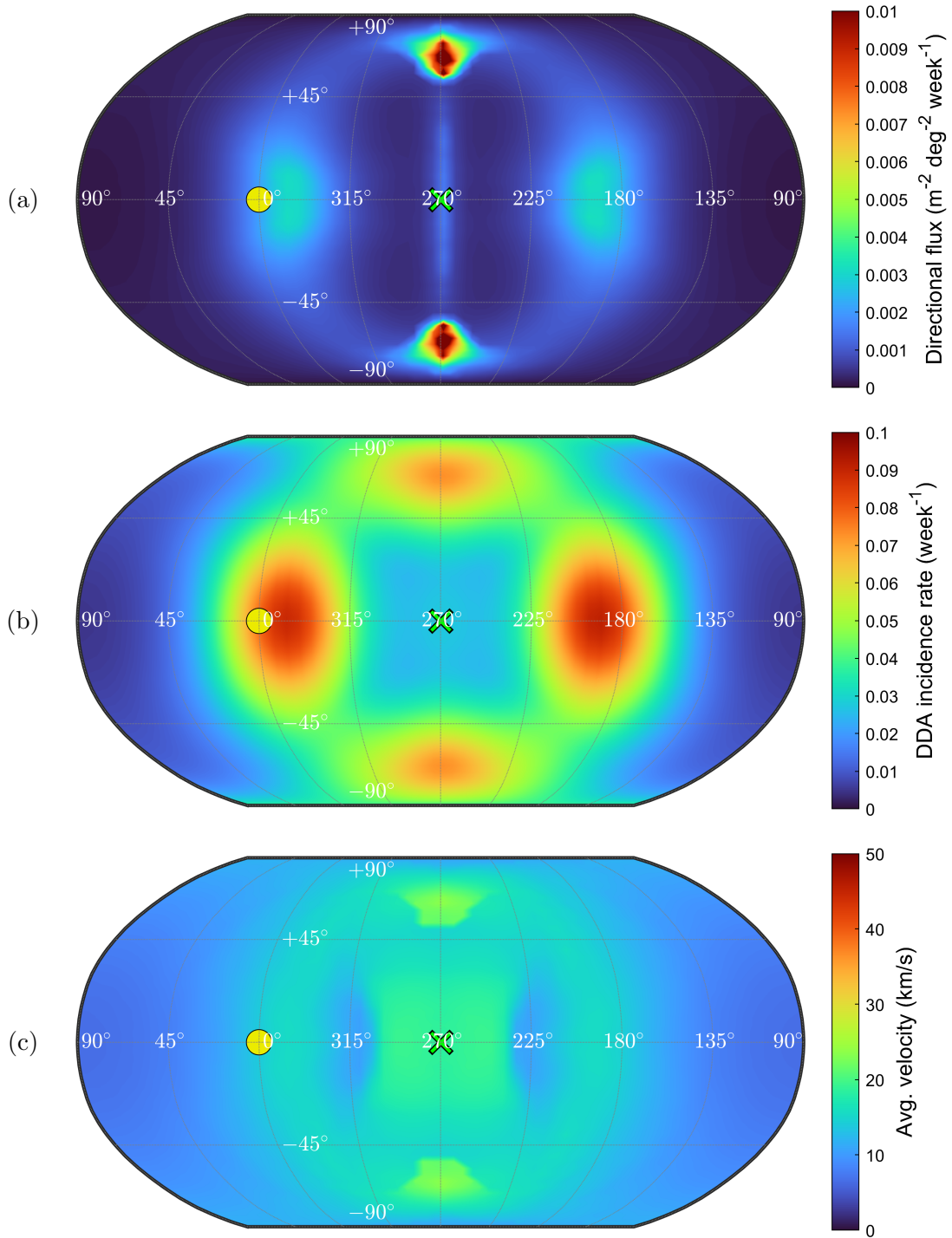


**Figure D.3.:** Divine model sky maps of the IPD flux at 1 au: (a) directional flux, (b) DDA incidence rate, and (c) average velocity. The observer is in a heliocentric, circular orbit at 1 au. Direction of the Sun and apex are indicated by the yellow circle and green cross, respectively. Data was generated with IMEM for a minimum particle mass of  $10^{-11}$  g.

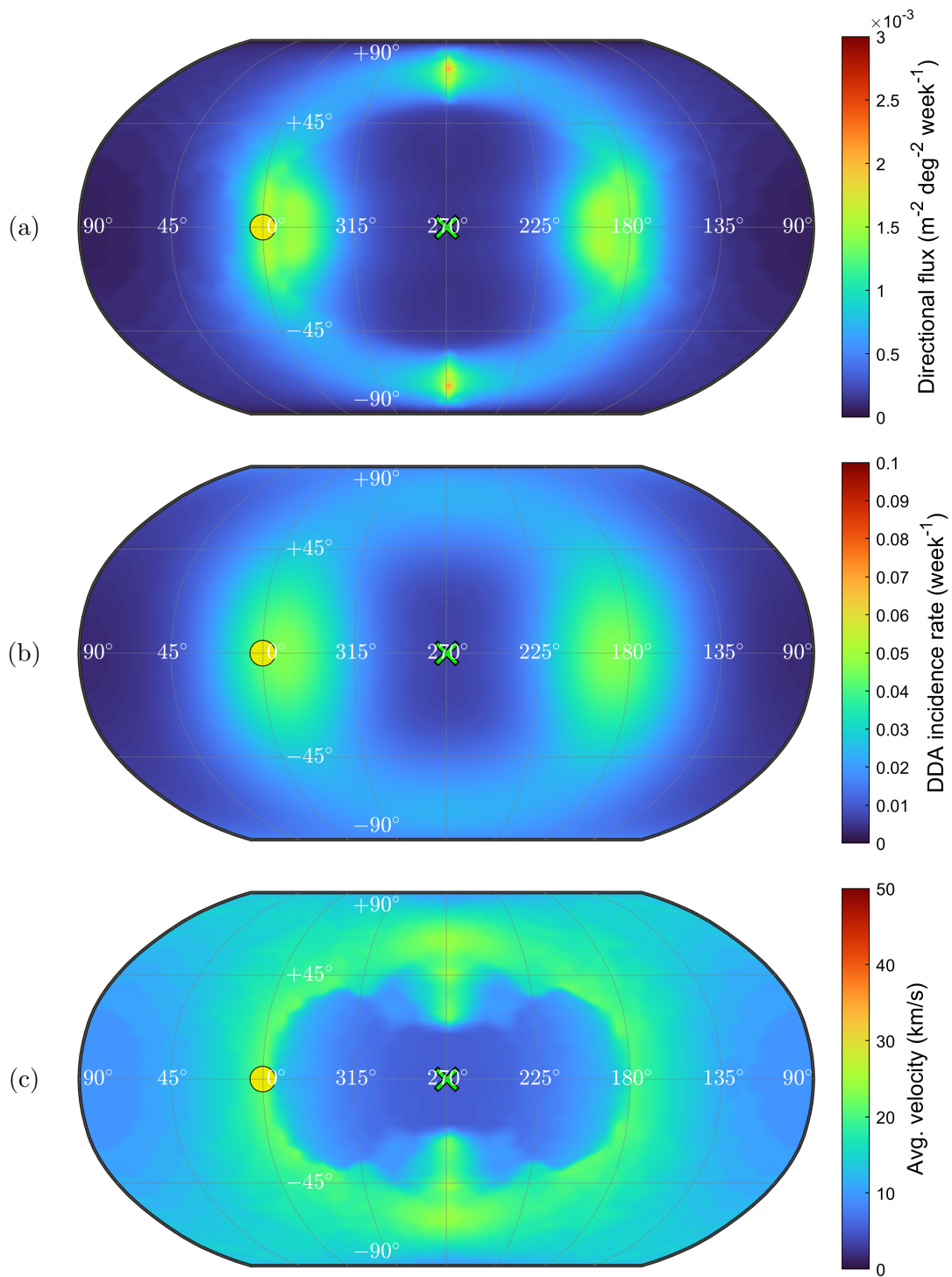


**Figure D.4.:** Staubach model sky maps of the IPD flux at 1 au: (a) directional flux, (b) DDA incidence rate, and (c) average velocity. The observer is in a heliocentric, circular orbit at 1 au. Direction of the Sun and apex are indicated by the yellow circle and green cross, respectively. Data was generated with IMEM for a minimum particle mass of  $10^{-11}$  g.

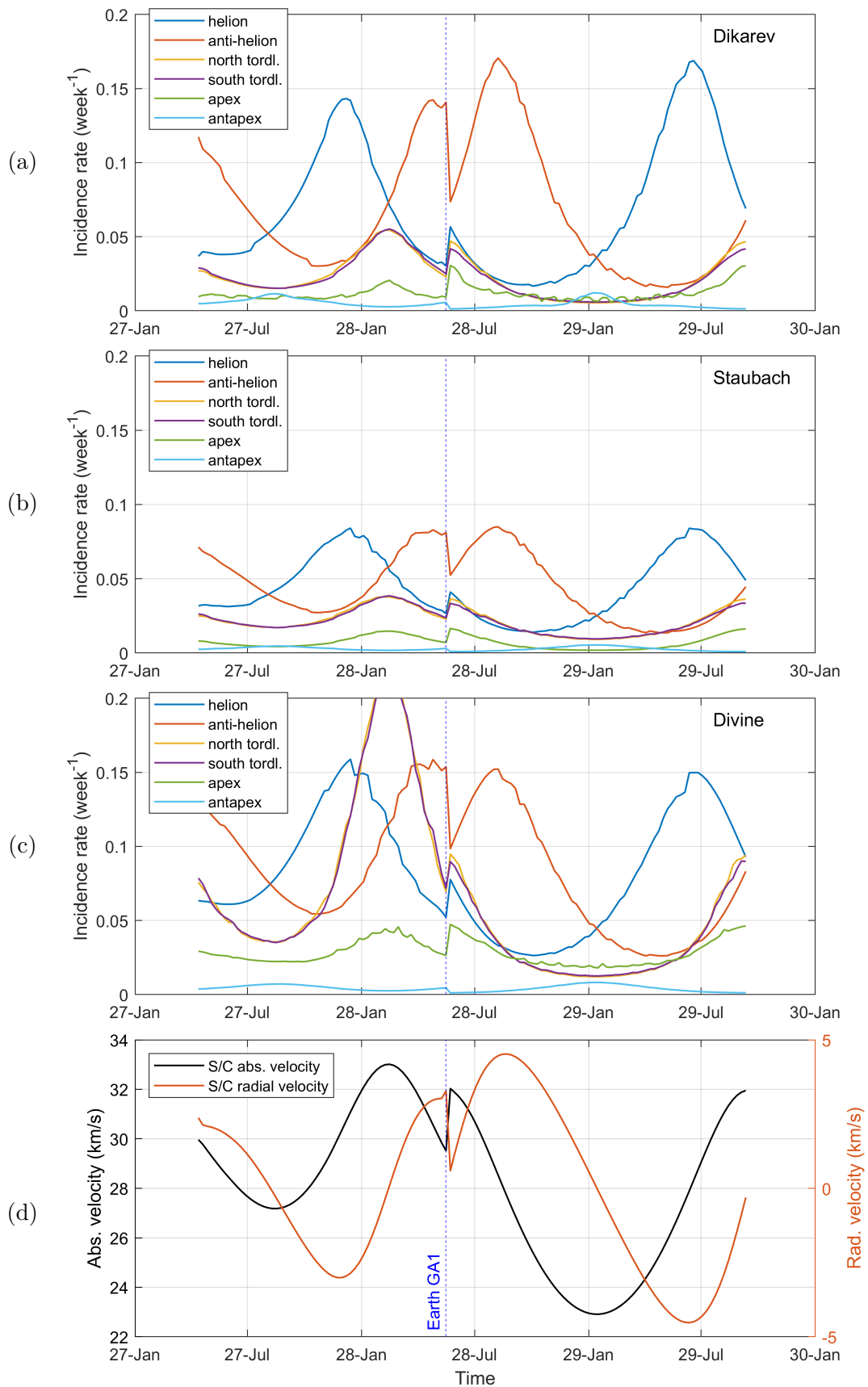


**Figure D.5.:** DDA incidence rates at certain pointings along the DESTINY+ interplanetary trajectory generated from the (a) Dikarev, (b) Staubach, and (c) Divine models. (d) shows the spacecraft heliocentric absolute and radial velocity. In addition to the nominal phase trajectory, one full orbit of the extended mission phase is shown (period after EGA-1). Data was generated with IMEM for a minimum particle mass of  $10^{-11}$  g.

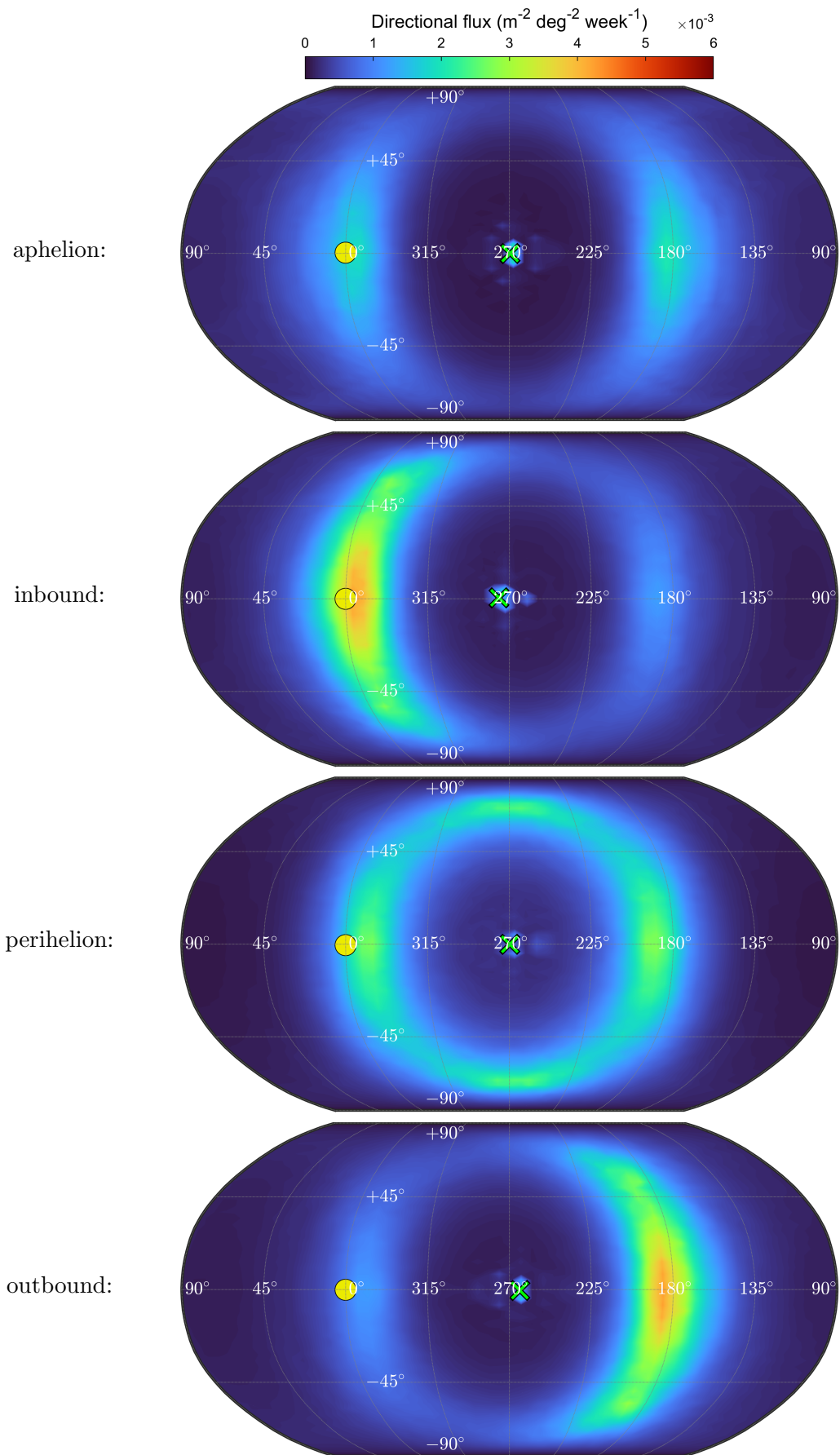


**Figure D.6.:** Dikarev model seasonal sky maps of the directional flux of JFC dust along the DESTINY+ interplanetary trajectory (nominal phase). Direction of the Sun and apex are indicated by the yellow circle and green cross, respectively. Data was generated with IMEM for a minimum particle mass of  $10^{-11}$  g.

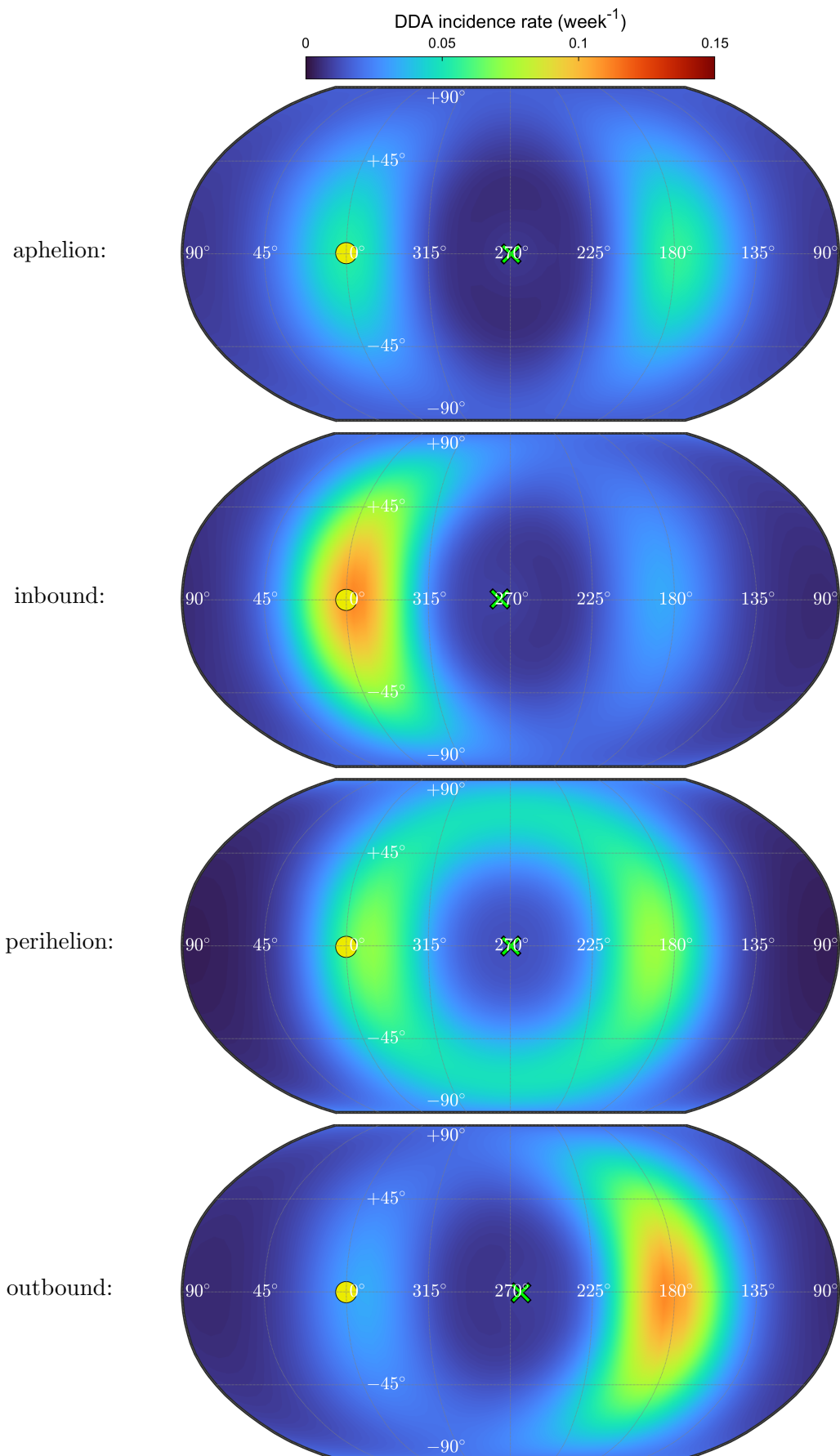


**Figure D.7.:** Dikarev model seasonal sky maps of the DDA incidence rate of JFC dust along the DESTINY<sup>+</sup> interplanetary trajectory (nominal phase). Direction of the Sun and apex are indicated by the yellow circle and green cross, respectively. Data was generated with IMEM for a minimum particle mass of  $10^{-11}$  g.

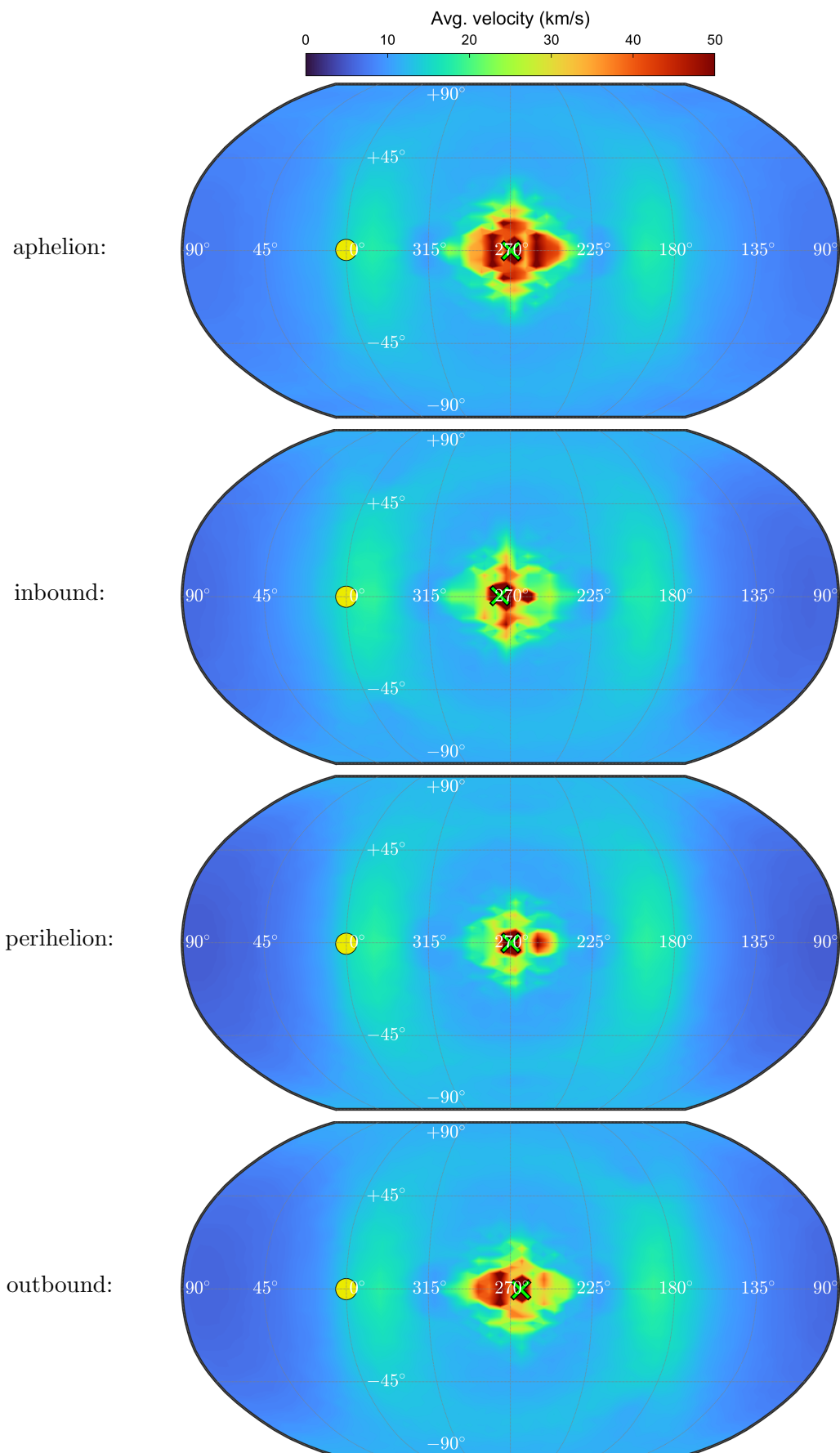


**Figure D.8.:** Dikarev model seasonal sky maps of the directional flux of JFC dust along the DESTINY<sup>+</sup> interplanetary trajectory (nominal phase). Direction of the Sun and apex are indicated by the yellow circle and green cross, respectively. Data was generated with IMEM for a minimum particle mass of  $10^{-11}$  g.

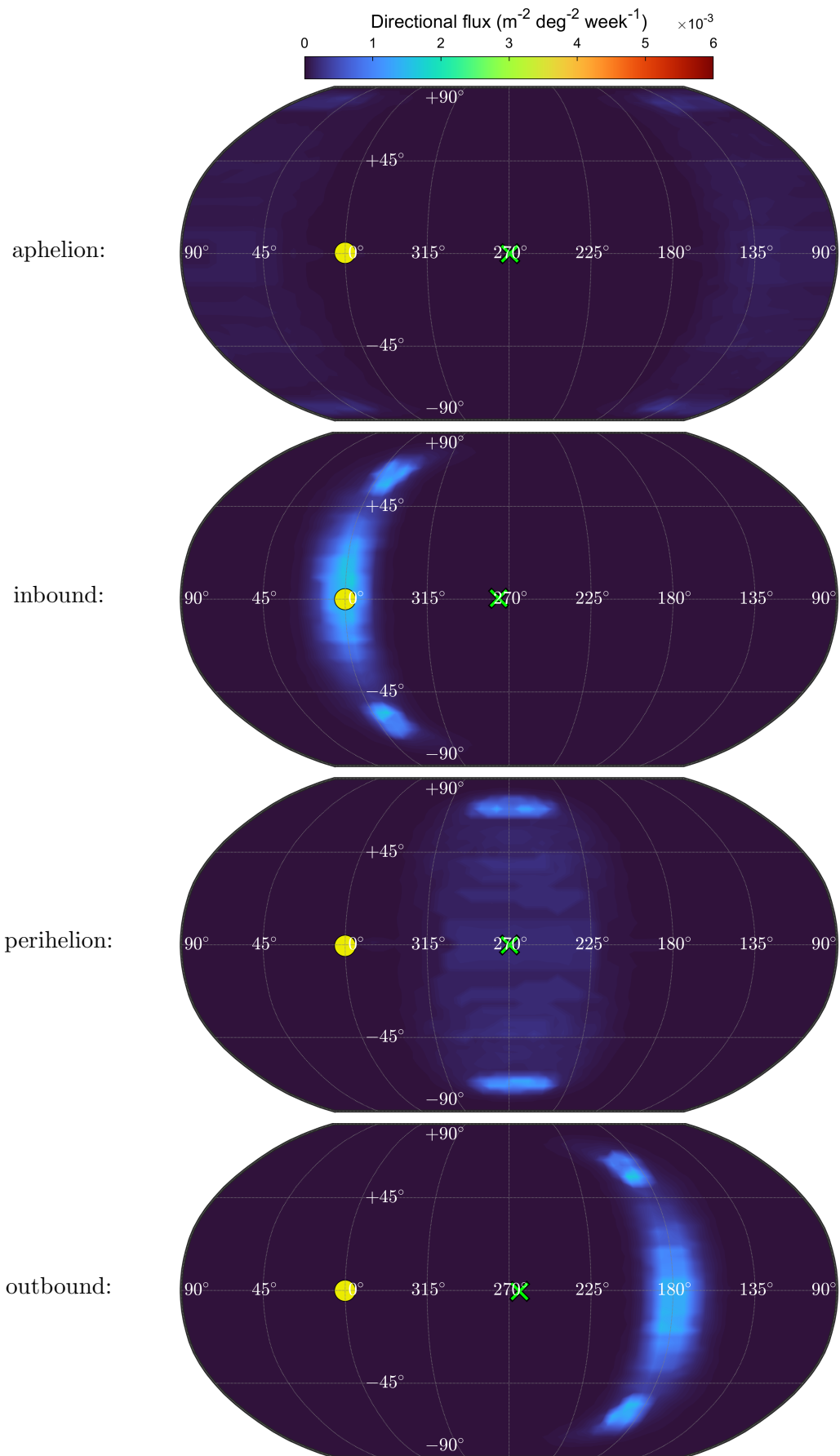


**Figure D.9.:** Dikarev model seasonal sky maps of the directional flux of AST dust along the DESTINY<sup>+</sup> interplanetary trajectory (nominal phase). Direction of the Sun and apex are indicated by the yellow circle and green cross, respectively. Data was generated with IMEM for a minimum particle mass of  $10^{-11}$  g.

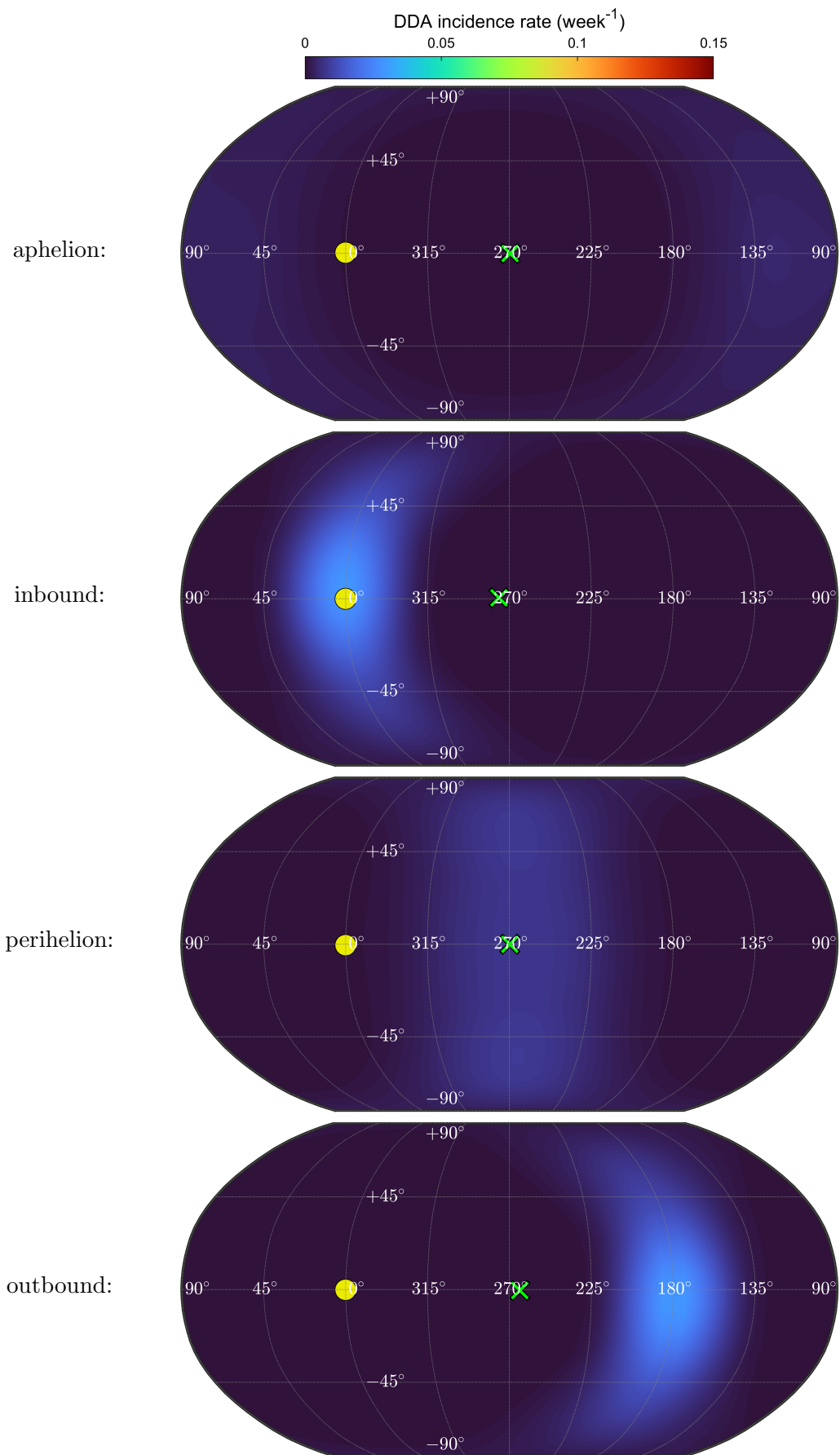


**Figure D.10.:** Dikarev model seasonal sky maps of the DDA incidence rate of AST dust along the DES-TINY<sup>+</sup> interplanetary trajectory (nominal phase). Direction of the Sun and apex are indicated by the yellow circle and green cross, respectively. Data was generated with IMEM for a minimum particle mass of  $10^{-11}$  g.

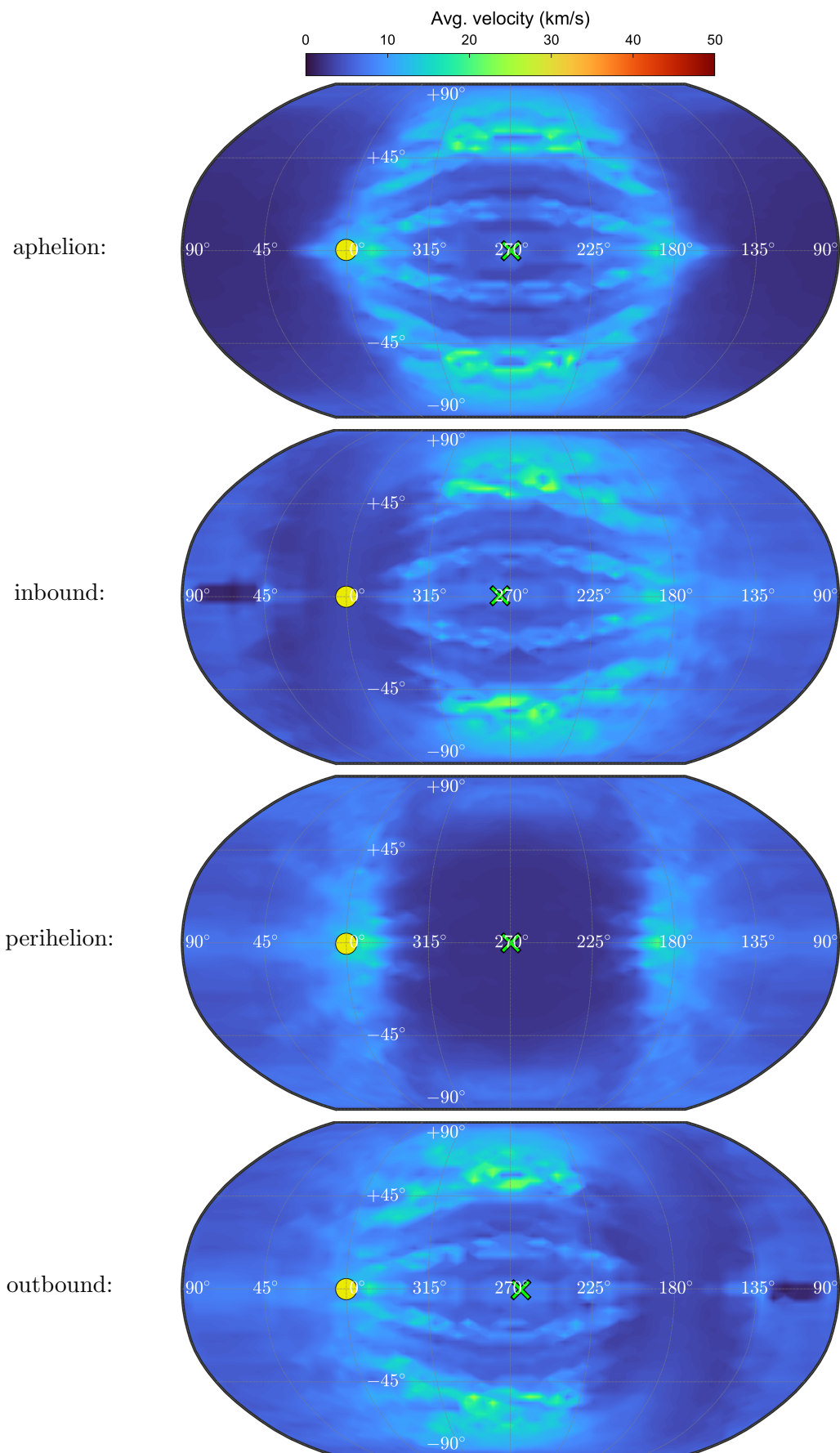


**Figure D.11.:** Dikarev model seasonal sky maps of the directional flux of AST dust along the DESTINY+ interplanetary trajectory (nominal phase). Direction of the Sun and apex are indicated by the yellow circle and green cross, respectively. Data was generated with IMEM for a minimum particle mass of  $10^{-11}$  g.

## E. Supplementary IMEM2 Sky Maps

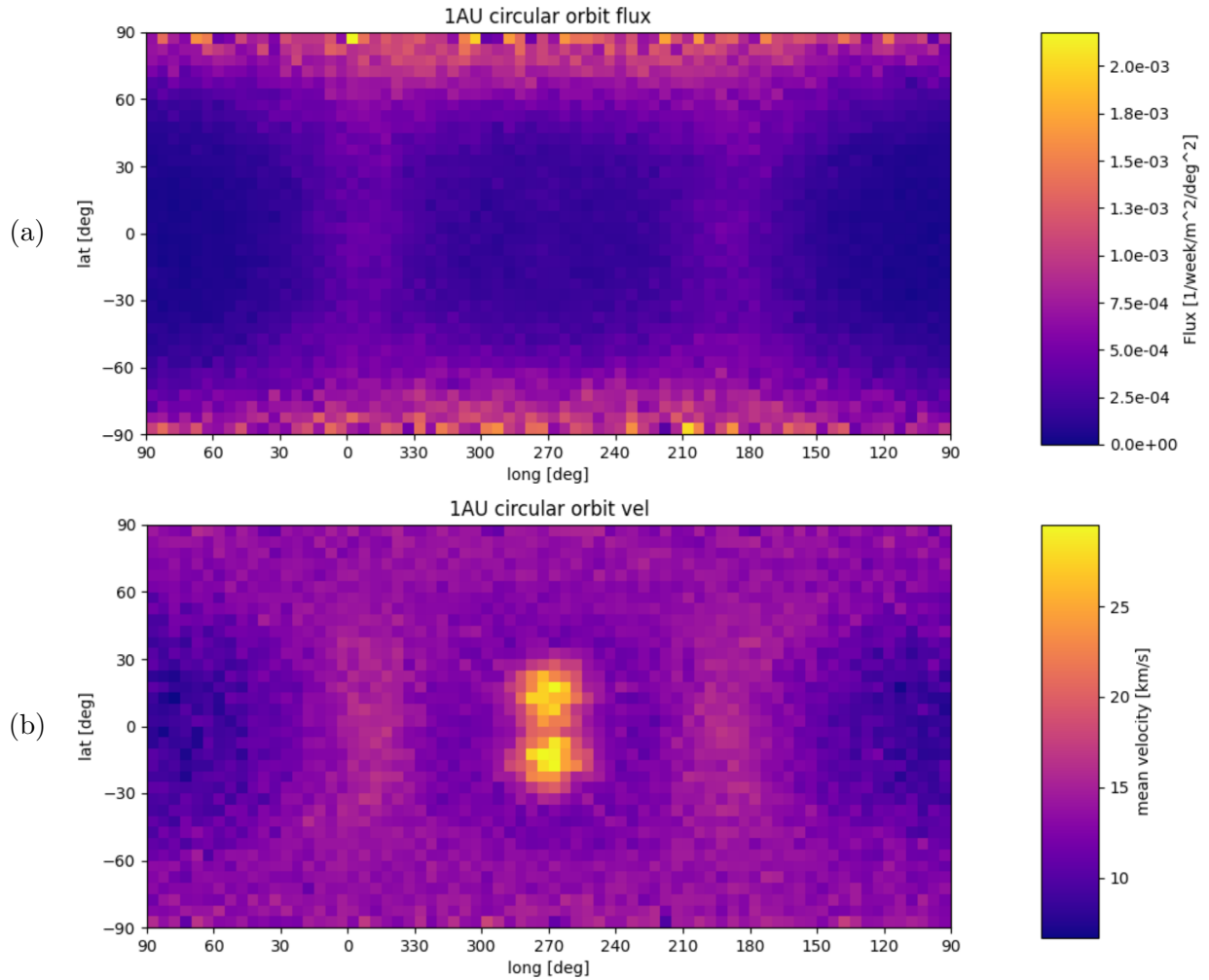


**Figure E.1.:** IMEM2 sky maps of the total flux at 1 au(all populations): (a) directional flux and (b) average velocity. The observer is in a heliocentric, circular orbit at 1 au. Direction of the Sun is at 0° long. & 0° lat. and the apex is at the centre at 270° long. & 0° lat.. Plots were generated with IMEM2 by Strub (priv. comm.) for a minimum particle radius  $s_{\min} = 1 \mu\text{m}$ , which corresponds to  $m_{\min} \approx 10^{-11} \text{g}$  at  $\rho = 2.5 \text{g cm}^{-3}$ .

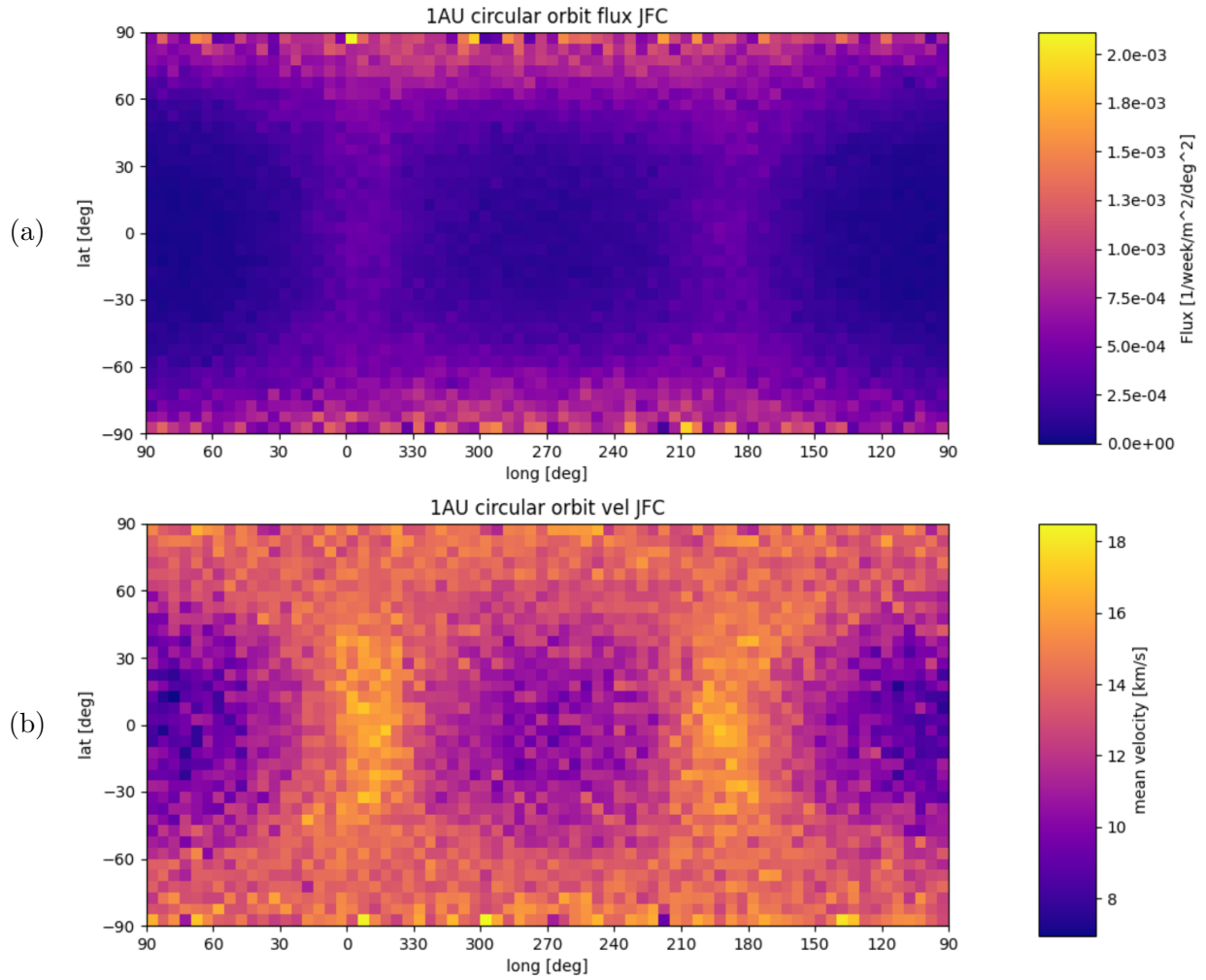


**Figure E.2.:** IMEM2 sky maps of the JFC flux at 1 au: (a) directional flux and (b) average velocity. The observer is in a heliocentric, circular orbit at 1 au. Direction of the Sun is at  $0^\circ$  long. &  $0^\circ$  lat. and the apex is at the centre at  $270^\circ$  long. &  $0^\circ$  lat.. Plots were generated with IMEM2 by Strub (priv. comm.) for a minimum particle radius  $s_{\min} = 1 \mu\text{m}$ , which corresponds to  $m_{\min} \approx 10^{-11} \text{g}$  at  $\rho = 2.5 \text{g cm}^{-3}$ .

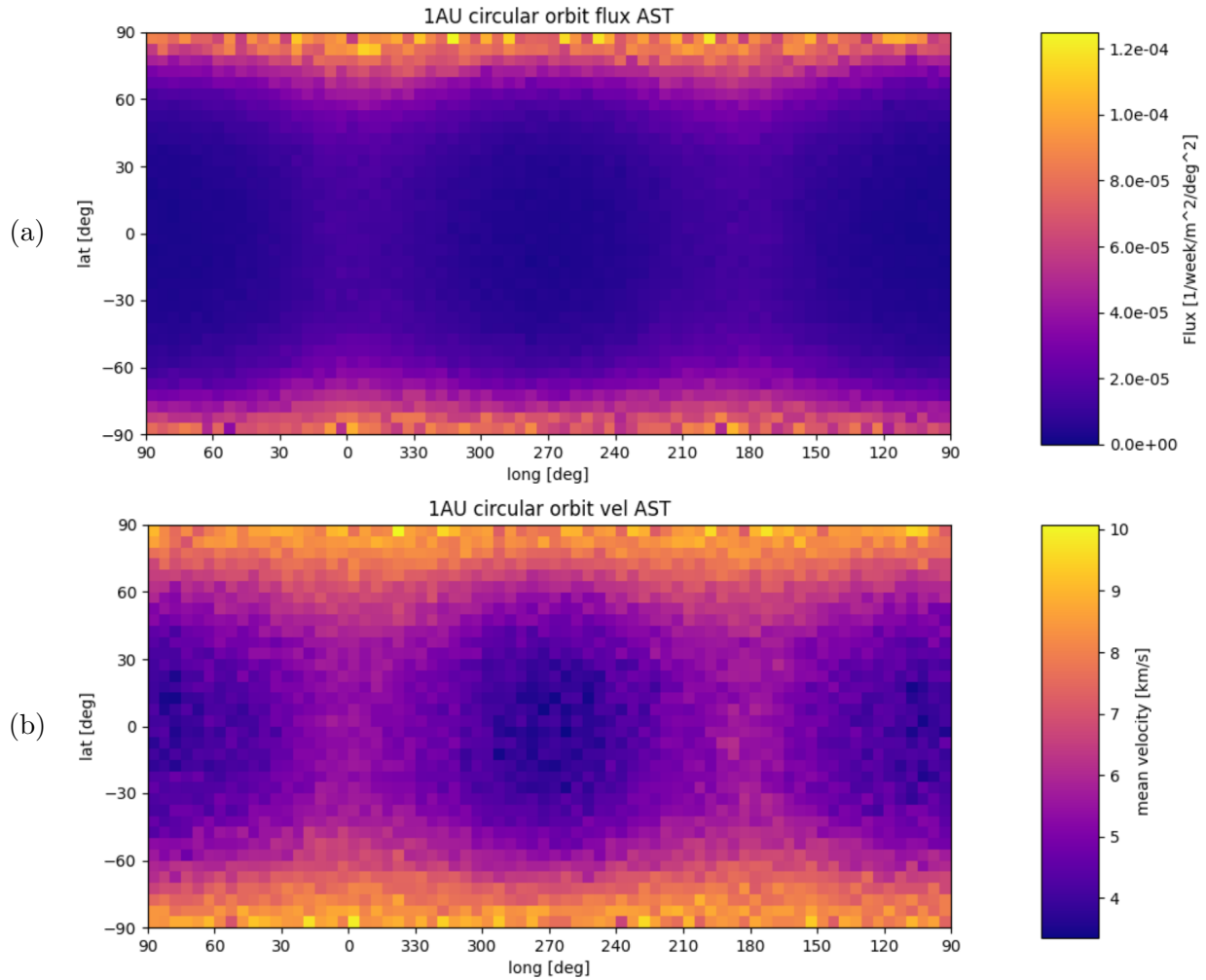


**Figure E.3.:** IMEM2 sky maps of the AST flux at 1 au: (a) directional flux and (b) average velocity. The observer is in a heliocentric, circular orbit at 1 au. Direction of the Sun is at  $0^\circ$  long. &  $0^\circ$  lat. and the apex is at the centre at  $270^\circ$  long. &  $0^\circ$  lat.. Plots were generated with IMEM2 by Strub (priv. comm.) for a minimum particle radius  $s_{\min} = 1 \mu\text{m}$ , which corresponds to  $m_{\min} \approx 10^{-11} \text{g}$  at  $\rho = 2.5 \text{g cm}^{-3}$ .

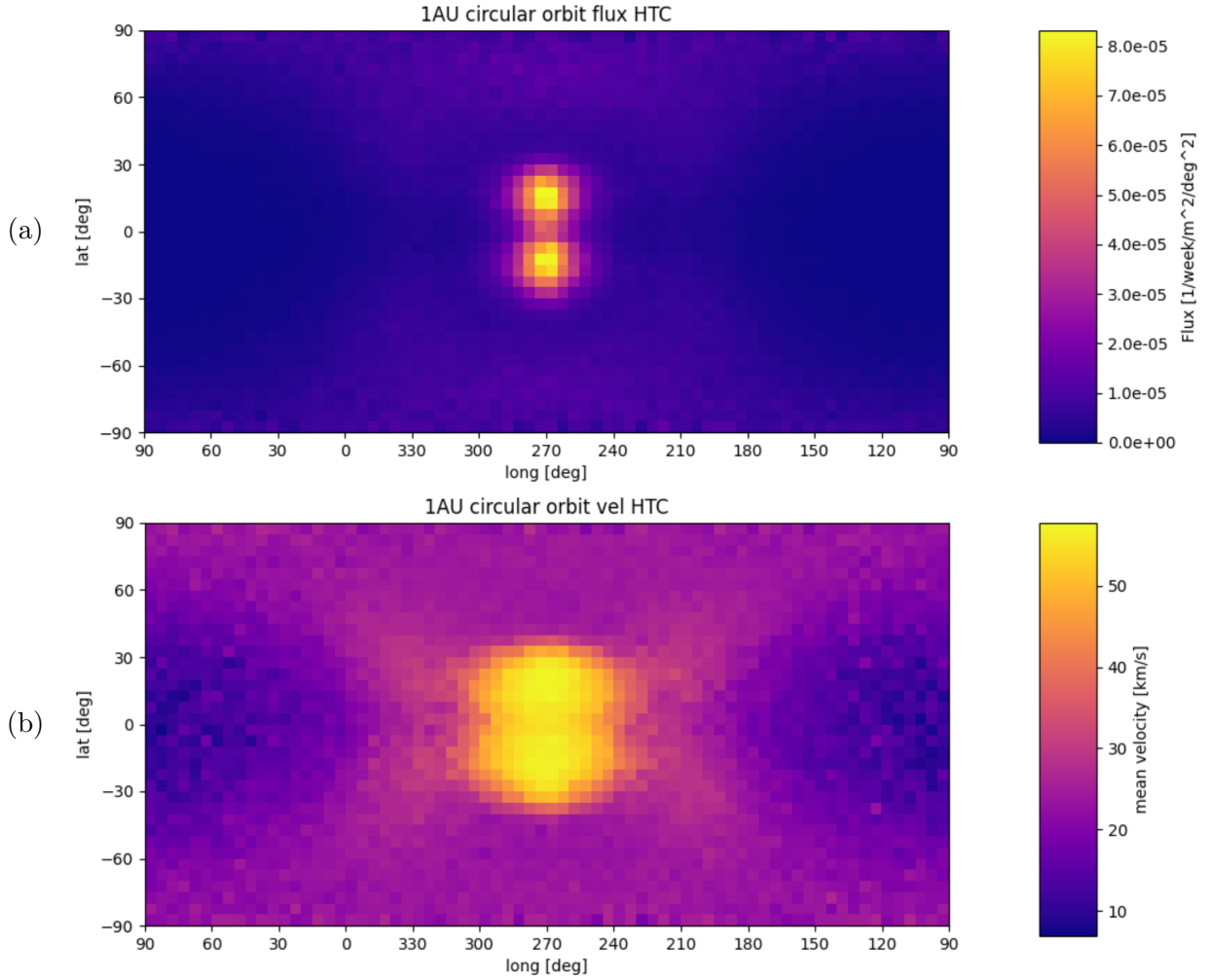


**Figure E.4.:** IMEM2 sky maps of the HTC flux at 1 au: (a) directional flux and (b) average velocity. The observer is in a heliocentric, circular orbit at 1 au. Direction of the Sun is at  $0^\circ$  long. &  $0^\circ$  lat. and the apex is at the centre at  $270^\circ$  long. &  $0^\circ$  lat.. Plots were generated with IMEM2 by Strub (priv. comm.) for a minimum particle radius  $s_{\min} = 1 \mu\text{m}$ , which corresponds to  $m_{\min} \approx 10^{-11} \text{ g}$  at  $\rho = 2.5 \text{ g cm}^{-3}$ .

## F. DOPE Instructions: Setting Spacecraft Trajectory and Attitude

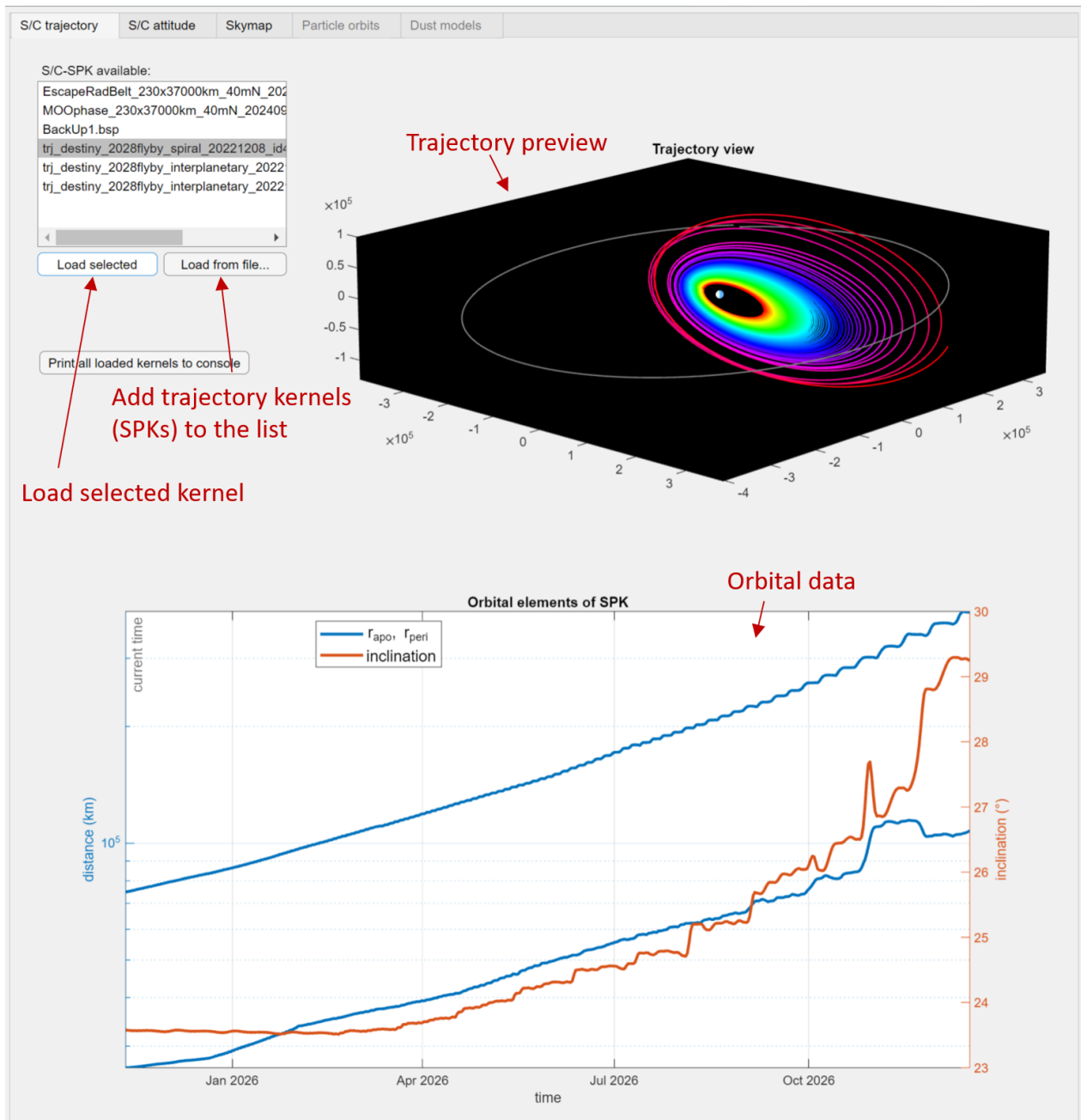


**Figure F.1.:** DOPE trajectory selection panel. Only SPICE trajectory kernels (SPKs) can be used. Alternatively, kernels can also be loaded on application start-up by adding their paths to the meta kernel (‘.tm’) file in the application folder.

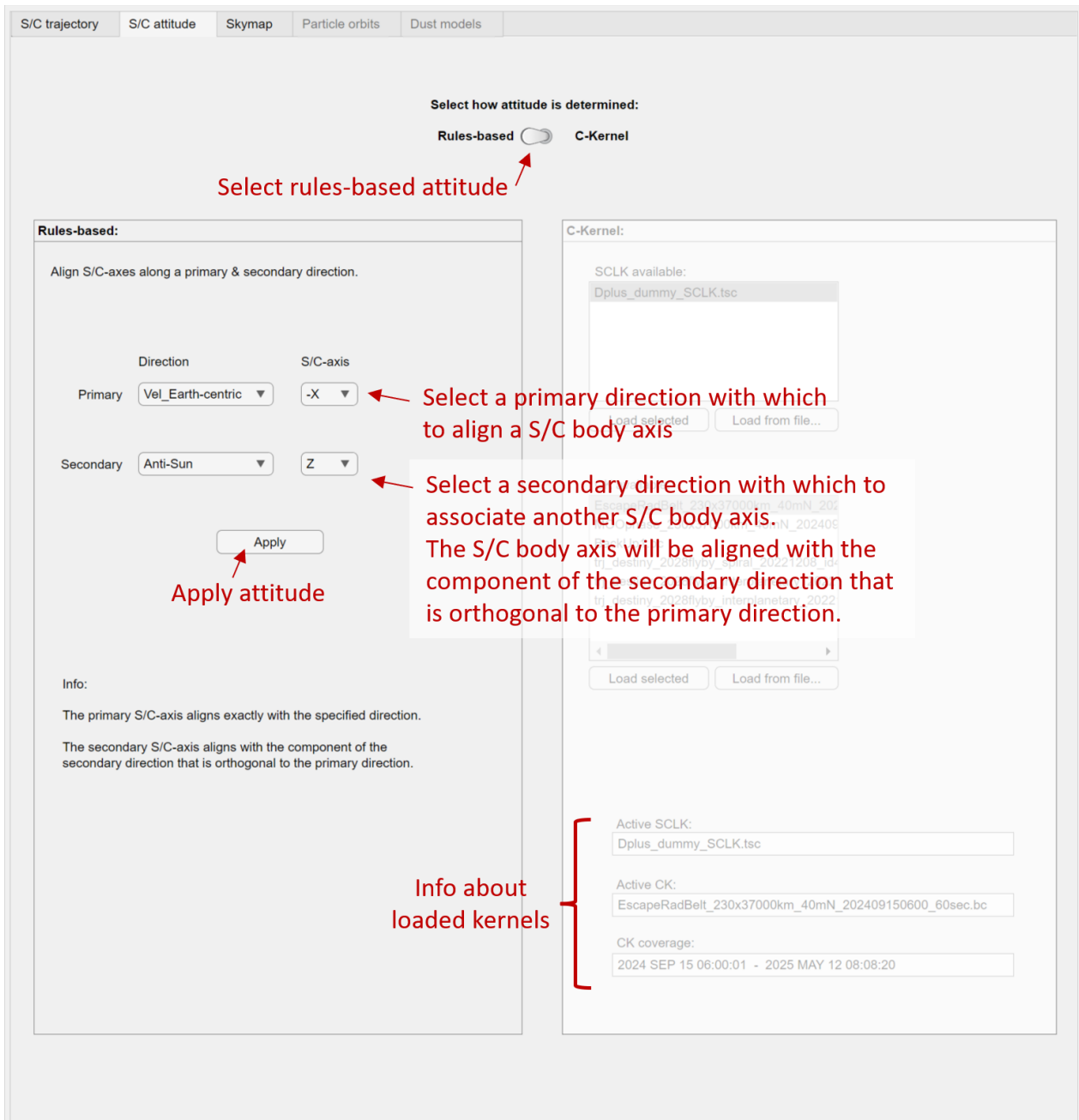


**Figure F.2.:** DOPE attitude selection panel (rules-based). Set the spacecraft attitude according to a primary and secondary direction. In the above example the primary direction is the Earth-centric apex (to be aligned with the spacecraft  $-X$  axis) and the secondary direction is the anti-sunward direction (to be aligned as closely as possible with the spacecraft  $+Z$  axis), which is the default attitude during the powered spiralling phase.

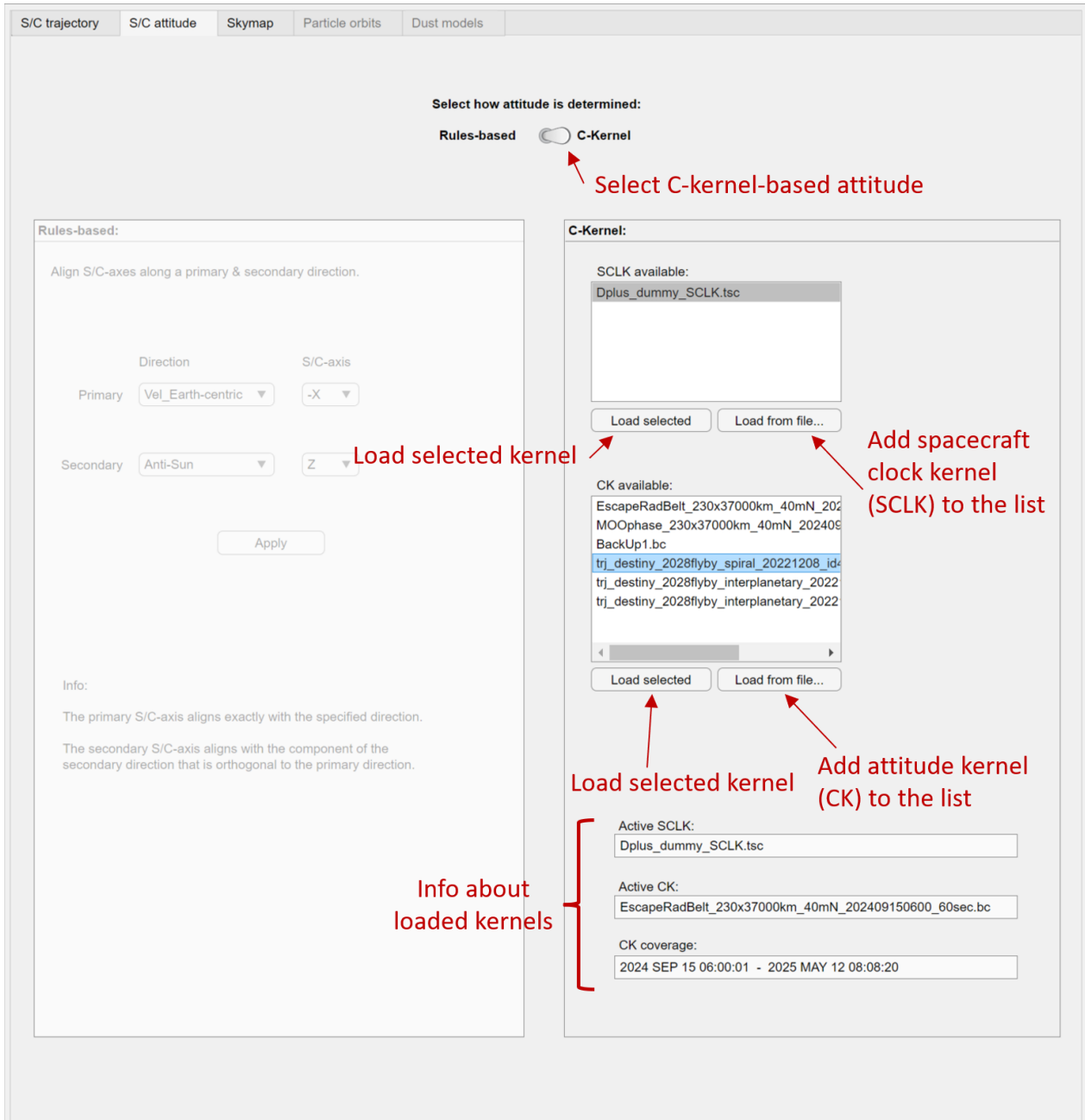


**Figure F.3.:** DOPE attitude selection panel (kernel-based). Only SPICE spacecraft clock and camera-matrix kernels (SCLKs and CKs) can be used. Alternatively, kernels can also be loaded on application start-up by adding their paths to the meta kernel (‘.tm’) file in the application folder.